SYNTHESIS AND LIGAND ENGINEERING OF COLLOIDAL METAL CHALCOGENIDE NANOPARTICLES FOR SCALABLE SOLUTION PROCESSED PHOTOVOLTAICS

by

Ryan Gupta Ellis

A Dissertation

Submitted to the Faculty of Purdue University

In Partial Fulfillment of the Requirements for the degree of

Doctor of Philosophy

Davidson School of Chemical Engineering

West Lafayette, Indiana

August 2020

THE PURDUE UNIVERSITY GRADUATE SCHOOL

STATEMENT OF COMMITTEE APPROVAL

Dr. Rakesh Agrawal, Chair

Davidson School of Chemical Engineering

Dr. Bryan Boudouris

Davidson School of Chemical Engineering

Dr. Letian Dou

Davidson School of Chemical Engineering

Dr. Hilkka Kenttämaa

Department of Chemistry

Approved by:

Dr. John Morgan

Dedicated to my friends and family

ACKNOWLEDGMENTS

The decision to pursue a PhD subjects the candidate to long and arduous journey of higher learning that would be an impossible task if not for a large support network of mentors, peers, friends, and family. The unwavering support from these individuals and groups enables a candidate to persevere through times of hardship and enable times of success. As such, I will attempt to acknowledge all of those who have been there to enable my success throughout my time as a PhD candidate at Purdue University.

I was extremely fortunate to join the solar energy research group of Prof. Rakesh Agrawal in my first year at Purdue. Prof. Agrawal has continually astounded me through his unwavering excitement and passion for his work. This passion has provided a basis of emulation for the entire research group, instilling the same excitement for my research that he continually displayed. Prof. Agrawal has provided continued mentorship at all stages of my PhD that have enabled me to learn a new field of research, professionally network, and greatly expand my professional skillset. In addition to Prof. Agrawal's mentorship, the research group was a continued source of inspiration and learning. My time in the solar energy research group began with training by group alumni, Dr. Caleb Miskin, who established the foundation of my research skills through excellent teaching and leading by example with unparalleled work ethic and systematic research. I owe significant thanks to Dr. Miskin for his valuable mentorship. I would also like to acknowledge fellow group member Swapnil Deshmukh, with whom I worked closely and collaborated throughout my PhD. I would also to like to acknowledge my other close collaborators within the group, Jonathan Turnely, David Rokke, and Essam Alruqobah for their various expertise and contributions to my work. Furthermore, I'd like to acknowledge the undergraduate researchers who worked under me, Jacob Fields and Dwi Sutandar, for their inquisitive nature and their role in teaching me about being a mentor. I would also like to acknowledge all of the group members and group alumni who have been there for fruitful discussion about my work and the group's research at large, Dr. Steven Mcleod, Dr. Brian Graeser, Dr. Mark Koeper, Dr. Xin Zhao, Dr. Scott McClary, Dr. Xianyi Hu, Robert Boyne, Dr. Joseph Andler, Kyle Weideman, Apurva Pradhan, and Anna Murray.

Next, I would like to thank my committee members for their continued expert advice and guidance. I would like to thank Prof. Bryan Boudouris for his electronic materials expertise and ability to ask both detailed and broad questions to guide my research direction and think about

broader impact. I would like to thank Prof. Letian Dou for providing expertise in photovoltaic material synthesis and characterization. Finally, I would like to thank Prof. Hilkka Kenttämaa for providing expertise in chemistry and characterization, encouraging me to think like a chemist and understand underlying chemical phenomena in our systems. I would also like to thank my collaborators, Dr. Doojin Vak and Dr. Anthony Chesman for giving me the opportunity to perform research at the Commonwealth Scientific and Industrial Research Organization (CSIRO) in Melbourne, Australia for 4 months. It was a phenomenal experience and allowed to greatly expand my research and professional skillset.

I have also had the support of family and a great friend group during my PhD who have always been there for encouragement and destressing. I would like to acknowledge my mother and father for always encouraging my inquisitive nature and promoting an interest in math and science from a young age. Both of my parents played a crucial role in my decision to pursue higher education and provided the support I needed to be successful. My father, Dr. Mark Ellis, a fellow chemical engineer, was pivotal in my decision to pursue a PhD and offered continued advice throughout the journey based on his experiences in graduate school. I would also like to acknowledge fellow chemical engineering graduate students Aidan Coffey, Claire Nimlos, Joe Oliva, and Laura Wilcox for their friendship and support throughout my PhD.

Finally, I would like to acknowledge my fiancé, Heather Ostertag, for her immense patience, support, and encouragement throughout my PhD. Whether it was long nights in the lab, or my sudden departure for Australia, she remained supportive and offered unwavering encouragement through my most stressful times and helped me celebrate my successes. A large part of my sanity during my PhD is owed to her and I struggle to articulate the thanks she is owed during these last five years. I will summarize these acknowledgments with one last thank you to all of those who have supported me through these last five years.

TABLE OF CONTENTS

LIST OF TABLES

LIST OF FIGURES

ABSTRACT

As global population continue to rise, the demand for energy is slated to increase substantially. To combat climate change, large amounts of renewable energy will be needed to feed this growing demand. Of renewable energy sources, photovoltaics are well positioned to meet this increasing demand due to the immense abundance of solar energy incident on earth. However, existing energy intensive, low throughput, and costly manufacturing techniques for photovoltaics may pose a barrier to continued large scale implementation.

Solution processing has emerged as a promising photovoltaics fabrication technique with high throughput, high materials utilization, and lower cost than existing vacuum-based methods. Thin film photovoltaic materials such as $Cu(In,Ga)(S,Se)_2$ and CdTe have both been fabricated using various solution processing methods. Of the various solution processing routes, colloidal metal chalcogenide nanoparticles have demonstrated promise as a hydrazine-free route for the solution processing of high efficiency $Cu(In,Ga)(S,Se)_2$ solar cells. However, conventional solution processing with colloidal nanoparticles has long suffered from anionic and carbonaceous impurities, stemming from legacy synthesis methods. The work in this dissertation aims to solve these issues through the development of novel synthetic methods, ligand engineering, and ultimately improved scalability through slot-die coating.

Typical colloidal syntheses rely on the use of metal salts as precursors such as metal halides, nitrates, acetates, and so forth, where the anions may incorporate and alter the electrical properties of the targeted nanomaterials. In this work, the recent advances in amine-thiol chemistry and its unique ability to solubilize many metal containing species are expanded upon. Alkylammonium metal thiolate species are easily formed upon addition of monoamine and dithiol to elemental Cu, In, Ga, Sn, Zn, Se, or metal chalcogenides such as Cu_2S and Ag_2S. These species were then used directly for the synthesis of colloidal nanoparticles without the need for any additional purification. The metal thiolate thermal decomposition pathway was studied, verifying that only metal chalcogenides and volatile byproducts are formed, providing a flexible route to compositionally uniform, phase pure, and anionic impurity-free colloidal nanoparticles including successful syntheses of In_2S_3, $(In_xGa_{1-x})_2S_3$, $CuInS_2$, $CuIn(S_xSe_{1-x})_2$, $Cu(In_xGa_{1-x})S_2$, Cu_2ZnSnS_4, and $AgInS_2$.

However, further impurities from deleterious carbonaceous residues originating from long chain native ligands were still a persistent problem. This impurity carbon has been observed to hinder grain formation during selenization and leave a discrete residue layer between the absorber layer and the back contact. An exhaustive hybrid organic/inorganic ligand exchange was developed in this work to remove tightly bound oleyalmine ligands through a combination of microwave-assisted solvothermal pyridine ligand stripping followed by inorganic capping with diammonium sulfide, yielding greater than 98% removal of native ligands via a rapid process. Despite the aggressive ligand removal, the nanoparticle stoichiometry remained largely unaffected when making use of the hybrid ligand exchange. Scalable blade coating of the ligand exchanged nanoparticle inks from non-toxic dimethyl sulfoxide inks yielded remarkably smooth and crack free films with RMS roughness less than 7 nm. Selenization of ligand exchanged nanoparticle films afforded substantially improved grain growth as compared to conventional non-ligand exchanged methods yielding an absolute improvement in device efficiency of 2.8%. Hybrid ligand exchange nanoparticle-based devices reached total-area power conversion efficiencies of 12.0%.

While extremely effective in ligand removal, ligand exchange pathways increase process complexity and solvent usage substantially, which may limit the cost advantage solution processing aims to provide. Further synthesis improvement was developed through a ligand exchange free, direct sulfide capped strategy. Using sulfolane as a benign solvent, $CuInS_2$ nanoparticles with thermally degradable thioacetamide ligands were synthesized using thermal decomposition of isolated metal thiolates from Cu_2S and In precursors. Through gentle thermal treatment, these ligands decomposed into non-contaminating gaseous byproducts leaving carbon free nanoparticle films without the need for ligand exchange.

With the development of virtually contamination free colloidal nanoparticle inks, focus was shifted to scalability using slot die coating. Unlike typical lab-scale coating techniques such as spin coating, slot die coating is a widely used industrial coating technique with nearly 100% materials utilization, and high throughput roll-to-roll compatibility. A custom lab-scale slot-die coater was used to rapidly proof coating conditions, which were rapidly analyzed for uniformity using absorbance scanning in conjunction with profilometry. A cosolvent chlorobenzene/dichlorobenzene ink was developed to yield highly uniform, crack free thin films from non-ligand-exchanged $Cu(In,Ga)S_2$ nanoparticles, which were finished into devices with champion total are efficiencies of 10.7%. To the best of our knowledge, this represents the first

report of slot die coated $Cu(In,Ga)(S,Se)_2$ photovoltaics. The methods presented in this work offer a pathway towards low impurity, high efficiency, scalable solution processed $Cu(In,Ga)(S,Se)_2$ photovoltaics to enable low cost renewable energy.

1. INTRODUCTION TO PHOTOVOLTAICS

1.1 The Case for Photovoltaics

With rapid population growth, increasing standards of living, increasing energy demands, and the ever-growing concerns of global warming driven by fossil fuel greenhouse gas emissions, renewable energy has been thrust into the limelight to aid in the new demand for clean energy. Global energy consumption is projected to increase 48%, from 549 quadrillion BTUs in 2012 to 815 quadrillion BTUs in 2040. Of this projected 815 quadrillion BTUs, 78% is estimated to be sourced by fossil fuels.[1] In a promising turn, domestic use of some of the worst fossil fuel offenders such as coal have largely stagnated. However, a large boom in natural gas usage has taken over and is projected to continually increase, dominating the energy landscape in the United States.

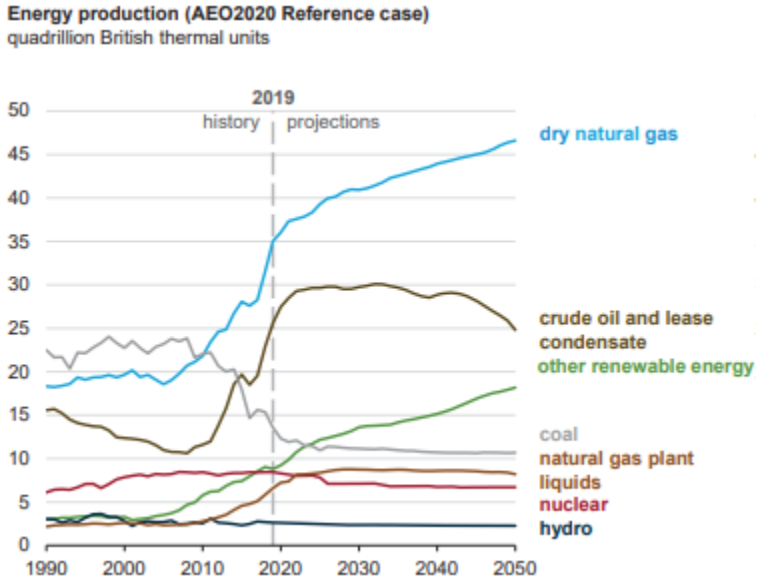

Figure 1.1. U.S. Energy Information Administration (EIA) Annual Energy Outlook 2020 historical and projected energy production by type under the reference case of strong domestic energy production with slow growth in domestic energy demand.[2]

While less polluting than its legacy counterpart, coal, CO_2 emissions and accidental CH_4 release pose a continued threat to the global climate.[3] With increased usage comes increased CO_2 emissions as shown in Figure 2.

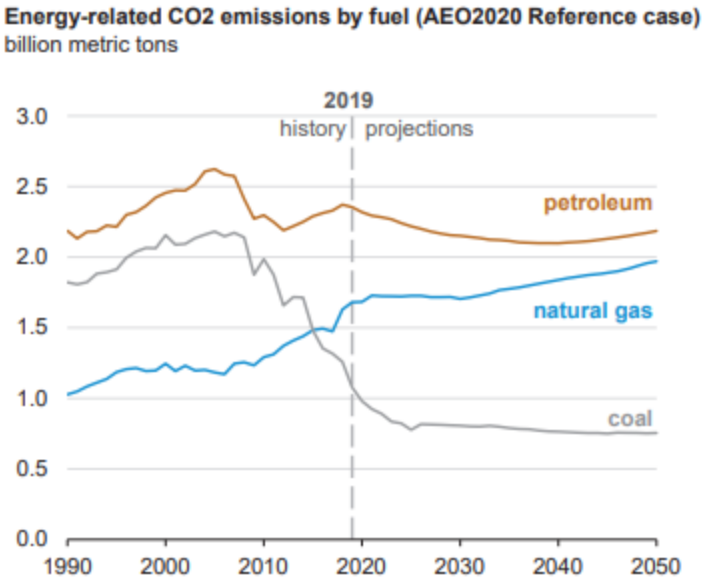

Figure 1.2. U.S. Energy Information Administration (EIA) Annual Energy Outlook 2020 historical and projected CO_2 emission by type under the reference case of strong domestic energy production with slow growth in domestic energy demand.[2]

While renewable energy is a prime component of energy production for a low-greenhouse gas future and is projected to rise dramatically in usage, it is still dwarfed by the dominant natural gas technologies. A paradigm shift is needed to cut off greenhouse gas emissions to prevent further increases in global temperatures, which come with numerous ill effects such as more severe weather, increased prevalence of drought, increasing sea levels, and many other dire consequences.[4–8]

The renewable sector of energy production is largely dominated by hydroelectric, wind, and biomass/biofuels. However, there has been a recent and dramatic increase in solar energy consumption, doubling from 0.427 quadrillion Btu in 2015 to 0.917 quadrillion Btu in 2018, whereas other renewables have remained much more stagnant as seen in Table 1.[9]

Table 1.1. U.S. Renewables consumption in quadrillion BTU from 2015-2018.[9]

	2015	2016	2017	2018
Hydroelectric power	2.321	2.472	2.767	2.667
Geothermal	0.212	0.210	0.210	0.209
Solar	0.427	0.570	0.777	0.917
Wind	1.777	2.096	2.343	2.486
Wood biomass	2.312	2.224	2.278	2.360
Biofuels	2.153	2.287	2.304	2.283
Waste biomass	0.518	0.503	0.495	0.487
Total	9.720	10.362	11.173	11.409

Of these renewables, solar energy stands unique with an immense excess of potential production capacity as compared to current energy demands. The estimated amount of solar energy incident on earth daily is over 10^5 TW, where up to 600 TW can feasibly be captured. When compared to annual global power consumption of 17 TW, the magnitude of potential solar energy production is abundantly clear.[10] As such, solar energy is well positioned for a dominant role in a renewable dominated energy future. Of the various solar technologies, there are two primary methods in which solar radiation is converted to electricity: solar thermal and photovoltaics (PV).[10] Solar thermal uses solar energy to heat and vaporize a working fluid and turn a turbine to generate electricity, whereas PVs convert solar energy directly into electricity in a solid-state semiconductor device. Of the two technologies, PVs have emerged as the more cost-effective technology and will be the topic of this report.

1.2 Photovoltaic Device Physics

The device physics of photovoltaics are well documented in a variety of sources; however, a brief overview is presented in this section.[11–13] PVs operate by extracting electrons generated by light striking a semiconductor. When light reaches the solar cell absorber layer, an electron from the valence band can be promoted to the conduction band if the energy of the absorbed light is equal to or greater than the energy difference between the valence and conduction band, known as the bandgap. The bandgap is generally a fundamental property of a given semiconductor. When an electron is promoted to the conduction band, a positively charged energy state in the valence

band called a hole is left behind. In the case that the energy absorbed is greater than the bandgap, a process known as thermalization occurs where the electron must lose energy until it reaches the conduction band. This process is extremely rapid, normally occurring on the order of femtoseconds. Thermalization is one of the largest losses present within a PV device and cannot be avoided in conventional solar cells. Once the electron reaches the conduction band, it can then relax back to the valence band to recombine with a hole. This process occurs within nano to microseconds for high quality semiconductors. In order to extract electrical work, the electrons need to be shuttled through an external circuit before relaxing to the valence band. In a full PV device, the charge separation is generally facilitated by a p-n junction.[12]

Before discussing the function of the p-n junction, an understanding of doping is needed. Doping of semiconductors refers to the introduction of impurity atoms or presence of naturally occurring defects. The nomenclature n-type and p-type refers to the specific type of doping and defines the majority carrier type. For p-type semiconductors, the majority carrier is positively charge holes and for n-type semiconductors, the majority carrier in negatively charged electrons. The carrier type of the material is defined by the nature of its dopants.[13] For example, for n-type silicon semiconductors, an atom with free electrons such as the pentavalent atoms phosphorus and arsenic are added into the semiconductor. These atoms have one extra valence electron compared to quadrivalent silicon thus imparting n-type doping. In p-type silicon semiconductors, an atom with electron deficiencies such as the trivalent atoms boron, aluminum, or gallium is added into the semiconductor. The one less valence electron in these atoms therefore imparts p-type conductivity. The addition of dopant atoms to a material is known as extrinsic doping, which is needed for materials such as silicon, which is naturally intrinsic when highly purified. An intrinsic material is a material without either p or n-type characteristic and therefore a low carrier concentration below ~10^{12}.[12] However, not all materials achieve their doping through extrinsic dopants. For example, CIGSSe naturally forms copper vacancies when grown at copper poor conditions (Cu/(In+Ga) <1) which creates additional holes in the material giving it naturally p-type doping on the order of 10^{15}-10^{17}.[14] These dopants create energy levels within the bandgap, where n-type dopants create energy states just above the conduction band and where p-type dopants create energy states just below the valence band. The n-type dopants are considered donors, where they donate electrons to the conduction band and p-type dopants are considered acceptors, accepting electrons from the valence band.[12]

Joining a p-type and n-type semiconductor results in a p-n junction. When the p-type and n-type material are first contacted, the higher concentration of electrons from the n-type material begin to flow to the p-type region leaving behind positively charged ions in the n-region, while the higher concentration holes from the p-type material flow to the n-type material leaving behind negatively charge ions in the p-region. The buildup of opposing charges in the region around the p-n junction begins to build an electric field that opposes the diffusion occurring until the electric field and diffusion come to an equilibrium. The resulting field is known as the built-in electric field and opposes any further diffusion. The physical region encompassed by the field is known as the space charge region. When equilibrium is disturbed by sunlight striking the semiconductor and creating electron hole pairs within the space charge region, the built-in electric field will sweep electron and holes to opposite ends of the device allowing for extraction of electrons to an external circuit.[12]

In an idealized case, a solar cell can be modeled using an equivalent circuit that places a constant current generator in parallel with a diode. To account for imperfections, present in the device, two resistances are added: Series resistance and shunt resistance. Series resistance is the resistance that an electron encounters as it passes through the device, typically occurring in the window and absorber layers. It is desirable to have the lowest possible series resistance. Shunt resistance occurs in parallel to the diode and constant current generator. Shunt is caused by alternative pathways in which an electron may pass through the device, such as pinholes, that leads to recombination. As such, high shunt resistance is desirable as to inhibit unfavorable pathways for parasitic shunt losses. Figure 2 shows the circuit diagram for an idealized solar cell.

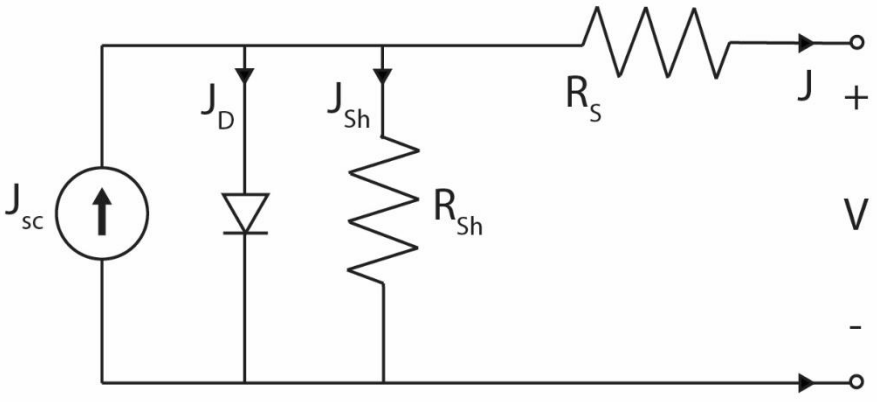

Figure 1.3. Equivalent circuit diagram for modeling a photovoltaic device.

The current in a solar cell is derived using Kirchhoff's circuit rules. When this current is combined with the parasitic losses caused by shunt and series resistances, Equation 1.1 is obtained

$$J = J_{sc} - J_0\left(e^{\frac{q(V+JAR_S)}{kT}} - 1\right) - \frac{V+JAR_S}{R_{SH}} \quad \textbf{(}\text{Equation 1.1}\textbf{)}$$

where R_{SH} and R_S are as described in Figure 2, J_{sc} is the short circuit current, J_0 is the reverse saturation current, and T is the temperature of the device. The short circuit current can be calculated by integrating the solar spectrum along with the quantum efficiency of the cell as shown in Equation 1.2

$$J_{sc} = q\int b_s(E)QE(E)dE \quad \textbf{(}\text{Equation 1.2}\textbf{)}$$

where q is the fundamental charge of an electron, $b_s(E)$ is the number of photons incident at a given energy, E, and $QE(E)$ is the quantum efficiency at a given energy, E. The quantum efficiency describes the probability that an incident photon will create an electron that is extracted to the external circuit, with $QE(E) = 1$ being the ideal case of one electron extracted per incident photon.

The performance of a solar cell is typically measured using current density-voltage measurements. A typical J-V curve is shown in Appendix A. The quantities used to measure the performance of a PV device include fill factor (FF), open circuit voltage (V_{OC}), J_{sc} and efficiency (η). The fill factor is the ratio of the maximum power to the product of J_{sc} and V_{OC}, and is visually a measure of the "squareness" of the J-V curve with a corner at the maximum power point as a percentage of the square formed by intersections of J_{sc} and V_{OC}. The open circuit voltage is defined as the voltage at zero current density. The efficiency is the most common measure of device performance and is defined as the ratio of inlet power to outlet power as shown in Equation 1.3:

$$\eta = (J_{SC}V_{OC}FF)/P_{in} \quad \textbf{(}\text{Equation 1.3}\textbf{)}$$

where P_{in} is the incident power on the solar cell.[12] Typically, a calibrated simulated spectrum is used known as AM1.5G, such that comparisons can be directly made between laboratories across the world. The fundamental principles of photovoltaics were applied to determine the efficiency

limits of photovoltaic devices in groundbreaking work from William Shockley and Hans-Joachum Queisser. In their analysis, a number of major assumptions were made. First, they assumed for each incident photon, one electron-hole pair is generated (a quantum efficiency of one) and only photons with energy at or above the bandgap are absorbed. Further it was assumed all photons above the bandgap are absorbed (infinite absorption coefficient). The only recombination mode present in their assumption was radiative recombination. Additionally, they assumed infinite mobility of charge carriers. Finally, they assumed non-concentrated sunlight was incident on the cell from a black body sun at 6000 K where the solar cell is a black body at 300 K. The resulting limits obtained in their analysis are known as the Shockley-Queisser limit. The theoretical maximum efficiency of a single junction solar cell is estimated to be 33.7% at a bandgap of 1.34 eV using their analysis.[15] It should be noted that various methods have been developed that can invalidate these assumptions such as multiple p-n junctions, solar concentration, bandgap grading, etc. It is also worth noting that while the Shockley-Queisser limit is an upper limit, it neglects many real-world factors such as Shockley-Read-Hall recombination, auger recombination, optical losses, and series and shunt resistance loses. In the goal of improving photovoltaic materials, an overarching goal of photovoltaics research is reducing the prevalence of these real-world effects and driving efficiencies closer and closer to the efficiency limits.

1.3 Overview of Photovoltaic Technologies

PV technologies are typically classified into three generations.[13] First generation PVs are dominant in today's market, making up approximately 90% installed PV, and are based on crystalline silicon.[16] Efficiencies of commercial modules vary between 15-21%.[5] A major shortcoming of crystalline silicon is the rigidity and large energy consumption needed in production. There are a variety of crystalline silicon PV types and corresponding manufacturing techniques depending on if the cheaper but lower efficiency multicrystalline silicon (mc-Si) or more costly but higher efficiency crystal silicon is desired. A commonality among silicon manufacturing processes is a relatively large energy demand for processing. For single crystal silicon-based photovoltaics, this is exemplified by the commonly used Czochralski (Cz) process. In this method, a melt of crystalline silicon is formed at temperatures in excess of 1400℃. A seed silicon single crystal is slowly rotated and drawn out of the melt pulling molten silicon along with it, which cools and continues the single crystal in an initially conical shape followed by a cylinder.

Various dopants can be added to the melt such as boron for p-type doping or phosphorus for n-type doping. Following the formation of the single crystal ingot, sawing is performed to form wafers 100-300 μm in thickness which are used for the further fabrication of the silicon photovoltaic cells.[17] Throughout the process, careful control of contaminants must be maintained due to silicon's extreme sensitivity towards defects. This often necessitates use of clean rooms during processing, which can increase initial capital costs and further increase energy expenditure. While economies of scale and process optimization have increased throughput and lowered energy demands, the process is fundamentally limited by the high temperatures needed to melt silicon. The energy intensity and batch nature of the process increases the manufacturing cost of the modules and can act as a barrier to the further cost reductions needed to displace fossil fuels. Additionally, silicon photovoltaics are inherently rigid and brittle due to their relatively large thickness of 100-300 μm which is needed due to silicon's indirect bandgap and low absorption coefficient.[17] This large thickness leads to increased module weight and thereby module shipping and installation costs.

Second generation PVs, also known as thin film PVs have recently began approaching the efficiencies of silicon modules on the commercial scale with 12-15% module efficiency. These second-generation PVs and their processing alleviate some of the limitations of silicon photovoltaics while being cost competitive with silicon PVs.[16] Thin film materials make use of materials with high absorption coefficients and direct bandgaps, allowing for complete light absorption with absorber layer thicknesses below 2-3 μm.[14] Due to the extremely thin layers, these PVs can be prepared on flexible substrates such as polymers or metal foils and manufactured on roll-to-roll lines, increasing manufacturing throughput and potentially decreasing manufacturing, shipping, and installation costs.[18] Additionally, the extremely small amount of material needed for the absorber layer can allow for use of traditionally rare elements without significant supply and cost bottlenecks such as indium, selenium, tellurium, and silver. Currently, copper indium gallium sulfoselenide (CIGSSe) and cadmium telluride (CdTe) dominate the thin film PV market. Figure 1.4 shows the device architecture for a typical thin film CIGSSe PV device.

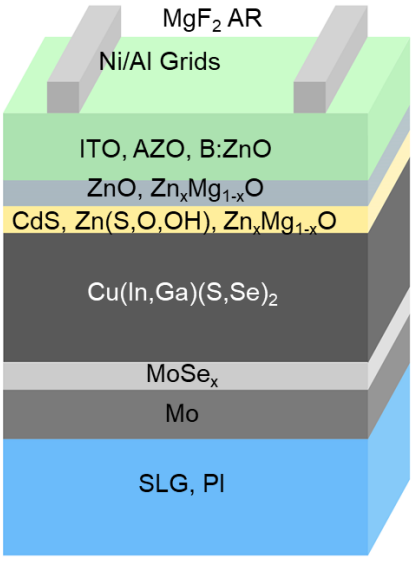

Figure 1.4. Diagram of a typical CIGSSe photovoltaic device stack. Layers with multiple materials seperated by commas are commonly used varients.

However, a shortcoming of thin film photovoltaics is that vacuum processing is the primary method of absorber layer deposition. While vacuum processing has demonstrated its ability to fabricated high efficiency laboratory scale devices of 22.1% and 23.35% for CdTe and CIGSSe respectively,[19] vacuum processing suffers from several drawbacks which have prevented thin films from reaching large levels of PV market penetration that silicon has. To date, thin film PVs have only reached market shares of around 10%.[16] The initial capital cost associated with setting up a vacuum processing line is also very large due to the complex nature of specialty vacuum equipment needed to deposit high quality absorbers. Additionally, vacuum processing suffers from poor large area uniformity due to conical evaporation plumes and limitations of feasible chamber sizes. The poor uniformity of vacuum absorbers has led to a large cell to module efficiency gap.[20] Thin film PVs make use of monolithic series interconnects between cells generally facilitated through laser scribing, which has reduced module costs. However, with poor uniformity and the need for current matching between the series interconnected cells, lower efficiency cells will detriment the entire module.[20] Vacuum processing also suffers from poor materials utilization due to deposition of materials on vacuum chamber walls or poor utilization and reusability of sputtering targets.

Third generation photovoltaics are made up of a variety of different emerging technologies including, organic, perovskite, dye-sensitized, quantum dot, and multijunction PVs. While a number of these technologies have reached extremely promising efficiencies,[19] they generally have

not yet reached the stages of commercialization or are used in only niche application. For example, perovskites and organic photovoltaics suffer from instability due to ambient moisture, oxygen, ion migration, and a variety of other factors during operation or even storage.[21,22] As such, their ability to meet the 25-year warranties that are commonplace with silicon and thin film photovoltaics is still in question. In the case of many of the multijunction photovoltaics based on III-V absorber stacks, the extremely high cost of cells has relegated this technology to primarily space use, where high efficiencies are desired, and cost is less of a factor.[23]

1.4 References

(1) Energy Information Administration, U. *International Energy Outlook 2016*; 2016.

(2) EIA. *Overview of Energy Markets*; 2020.

(3) Bluestein, J. *Life Cycle Greenhouse Gas Analysis of Natural Gas Extraction & Delivery in the United States*; 1990; Vol. 6.

(4) Bachelet, D.; Neilson, R. P.; Lenihan, J. M.; Drapek, R. J. Climate Change Effects on Vegetation Distribution and Carbon Budget in the United States. *Ecosystems* **2001**, *4* (3), 164–185. https://doi.org/10.1007/s10021-001-0002-7.

(5) Durance, I.; Ormerod, S. J. Climate Change Effects on Upland Stream Macroinvertebrates over a 25-Year Period. *Glob. Chang. Biol.* **2007**, *13* (5), 942–957. https://doi.org/10.1111/j.1365-2486.2007.01340.x.

(6) Nelson, G. C.; Valin, H.; Sands, R. D.; Havlík, P.; Ahammad, H.; Deryng, D.; Elliott, J.; Fujimori, S.; Hasegawa, T.; Heyhoe, E.; Kyle, P.; Von Lampe, M.; Lotze-Campen, H.; Mason d'Croz, D.; van Meijl, H.; van der Mensbrugghe, D.; Müller, C.; Popp, A.; Robertson, R.; Robinson, S.; Schmid, E.; Schmitz, C.; Tabeau, A.; Willenbockel, D. Climate Change Effects on Agriculture: Economic Responses to Biophysical Shocks. *Proc. Natl. Acad. Sci.* **2014**, *111* (9), 3274–3279. https://doi.org/10.1073/pnas.1222465110.

(7) Pörtner, H. O.; Peck, M. A. Climate Change Effects on Fishes and Fisheries: Towards a Cause-and-Effect Understanding. *J. Fish Biol.* **2010**, *77* (8), 1745–1779. https://doi.org/10.1111/j.1095-8649.2010.02783.x.

(8) Garrett, K. A.; Dendy, S. P.; Frank, E. E.; Rouse, M. N.; Travers, S. E. Climate Change Effects on Plant Disease: Genomes to Ecosystems. *Annu. Rev. Phytopathol.* **2006**, *44* (1), 489–509. https://doi.org/10.1146/annurev.phyto.44.070505.143420.

(9) EIA. U.S. Energy Information Administration (EIA) - Renewable & Alternative Fuels https://www.eia.gov/renewable/ (accessed Jun 24, 2020).

(10) Wolden, C. A.; Kurtin, J.; Baxter, J. B.; Repins, I.; Shaheen, S. E.; Torvik, J. T.; Rockett, A. A.; Fthenakis, V. M.; Aydil, E. S. Photovoltaic Manufacturing: Present Status, Future Prospects, and Research Needs. *J. Vac. Sci. Technol. A Vacuum, Surfaces, Film.* **2011**, *29* (3), 030801. https://doi.org/10.1116/1.3569757.

(11) Pierret, R. F. *Semiconductor Device Fundamentals*; New York, 1996. https://doi.org/10.1007/BF00198606.

(12) Nelson, J. *The Physics of Solar Cells*; Imperial College Press, 2003. https://doi.org/10.1142/p276.

(13) Tiwari, G. N.; Dubey, S. *RSC Energy Series: Fundamentals of Photovoltaic Modules and Their Applications*; Hunt, J., Ed.; RSC Publishing: Cambridge, 2010.
(14) Rau, U.; Schock, H. W. Cu(In,Ga)Se_2 Thin-Film Solar Cells. In *Solar Cells*; Elsevier Ltd, 2013; pp 261–304. https://doi.org/10.1016/B978-0-12-386964-7.00009-3.
(15) Shockley, W.; Queisser, H. J. Detailed Balance Limit of Efficiency of P-n Junction Solar Cells. *J. Appl. Phys.* **1961**, *32* (3), 510–519. https://doi.org/10.1063/1.1736034.
(16) Schmalensee, R.; Bulovic, V.; Armstrong, R.; Batlle, C.; Brown, P.; Deutch, J.; Jacoby, H.; Faffe, R.; Jean, J.; Miller, R.; O'Sullivan, F.; Parsons, J.; Perez-Arriaga, J. I.; Seifkar, N.; Stoner, R.; Vergara, C.; Amatya, R.; Brushett, F.; Ampanella, A.; Kavlak, G.; Macko, J.; Maurano, A.; McNerney, J.; Osedach, T.; Ridukkam Oavki; Rose, A.; Sakti, A.; Steinfeld, E.; Trancik, J.; Tuller, H. *The Future of Solar Energy*; Cambridge, 2015.
(17) McEvoy, A.; Markvart, T.; Castañer, L. *Solar Cells*; Elsevier Ltd, 2013. https://doi.org/10.1016/C2011-0-07789-X.
(18) Reinhard, P.; Chirila, A.; Blosch, P.; Pianezzi, F.; Nishiwaki, S.; Buechelers, S.; Tiwari, A. N. Review of Progress toward 20% Efficiency Flexible CIGS Solar Cells and Manufacturing Issues of Solar Modules. In *2012 IEEE 38th Photovoltaic Specialists Conference (PVSC) PART 2*; IEEE, 2012; pp 1–9. https://doi.org/10.1109/PVSC-Vol2.2012.6656789.
(19) NREL. Best Research-Cell Efficiencies https://www.nrel.gov/pv/assets/pdfs/best-research-cell-efficiencies.20200406.pdf.
(20) Bermudez, V.; Perez-Rodriguez, A. Understanding the Cell-to-Module Efficiency Gap in Cu(In,Ga)(S,$Se)_2$ Photovoltaics Scale-Up. **2018**. https://doi.org/10.1038/s41560-018-0177-1.
(21) Mesquita, I.; Andrade, L.; Mendes, A. Perovskite Solar Cells: Materials, Configurations and Stability. *Renewable and Sustainable Energy Reviews*. Elsevier Ltd February 1, 2018, pp 2471–2489. https://doi.org/10.1016/j.rser.2017.09.011.
(22) Cheng, P.; Zhan, X. Stability of Organic Solar Cells: Challenges and Strategies. *Chemical Society Reviews*. Royal Society of Chemistry May 7, 2016, pp 2544–2582. https://doi.org/10.1039/c5cs00593k.
(23) Miles, R. W.; Zoppi, G.; Forbes, I. Inorganic Photovoltaic Cells. *Materials Today*. Elsevier November 1, 2007, pp 20–27. https://doi.org/10.1016/S1369-7021(07)70275-4.

2. SOLUTION PROCESSING OF CU(IN,GA)(S,SE)$_2$ PHOTOVOLTAICS FROM COLLOIDAL NANOPARTICLES

2.1 Introduction to Solution Processing

With ever growing concerns regarding climate change and its ill effects on the environment and society, a shift to renewable energy technologies such as photovoltaics has drawn considerable interest. Due to the existing commercial success of thin film technologies, they are well poised to aid in the displacement of greenhouse gas emitting fossil fuel technologies. However, the costly and low-throughput vacuum processing methods currently used could constitute a substantial barrier to further cost reductions and remain the dominant factor in the existing module to cell efficiency gap, prevalent in materials like Cu(In,Ga)(S,Se)$_2$ (CIGSSe).[1] In order to alleviate these shortcomings, a paradigm shift in manufacturing is needed. Solution processing is an alternative manufacturing technique that aims to solve a wide variety of the shortcomings associated with vacuum processing. In solution processing, liquid solutions of precursor materials are cast at atmospheric pressure using scalable coatings techniques including spray coating, blade coating, slot-die coating, and inkjet printing. Through various thermal treatments, device quality absorber layers can be formed from the solution deposited precursor films. This method bypasses the need for vacuum processing and is easily scaled to accommodate large width and lengths needed for modules. Further, a vast increase in materials utilization can be realized. For instance, in slot-die coating, all material that exits the coating head is deposited on the substrate, realizing nearly 100% materials utilization.[2] An envisioned roll-to-roll solution processing line for Cu(In,Ga)(S,Se)$_2$ photovoltaics in shown in Figure 2.1.

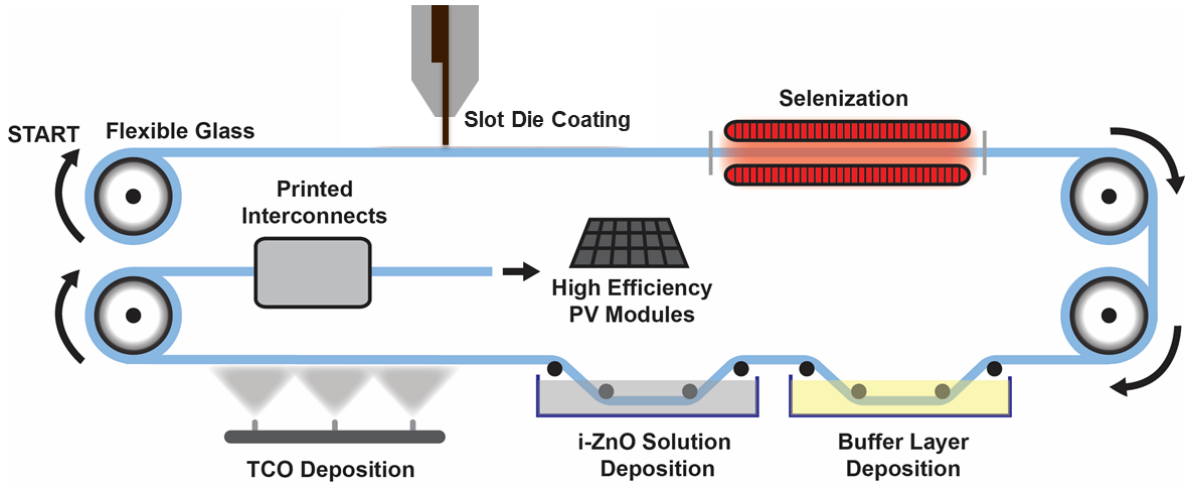

Figure 2.1. Envisioned continuous roll-to-roll deposition of CIGSSe thin films using a variety of solution processing methods.

Solution processing offers the potential to solve many manufacturing challenges associated with vacuum processing, thereby reducing manufacturing costs substantially. Both dominant thin film materials, CdTe and CIGSSe, have been fabricated through solution processing routes with champion efficiencies of 12.2 and 18.1% (17.2% certified average cell) respectively.[3,4] Due to the relatively higher efficiency of CIGSSe solution processed photovoltaics, this section will focus on this material system.

CIGSSe is an alloyed material based on $CuInSe_2$, where Ga can replace In, Se can replace S, and further substitutions, such as Ag with Cu, are possible. The bandgap is highly tunable, where various compositions can widely vary the bandgap. For instance, $CuInSe_2$ (CISe) and $CuInS_2$ (CIS) have bandgaps of 1.0 and 1.5 eV. $CuGaSe_2$ and $CuGaS_2$ have bandgaps of 1.7 and 2.4 eV respectively.[5] Combinations of these materials can be prepared as alloys to tune the bandgap, even across the absorber thickness to facilitate a gallium grading.[6] Typically, gallium content is retained below a Ga/(In+Ga) of 0.7 due to the high defect density of high gallium CIGSSe alloys.[7] CIGSSe is typically prepared with a final copper deficient stoichiometry that allows copper vacancies to impart p-type conductivity and prevents the segregation of $Cu_{2-x}Se$, a highly conductive secondary phase which can shunt devices.[5] The conventional vacuum deposition of CIGSSe is performed using either three-stage coevaporation or sputtering of metallic precursors followed with subsequent chalcogenization.[8,9] In both methods, complex reactions take place to form the final absorber layer and must carefully be tuned with deposition or chalcogenization temperature,

heating rates, and chalcogen content. For uniform reactions to take place over the area of a module, very uniform and carefully tuned flux of metals and selenium or controlled thickness of precursor layers must be deposited, which presents difficulty for vacuum processing over large areas.

Another limitation of vacuum processing is manifested in the deposition of the n-type layer deposited on the absorber layer, which in state of the art CIGSSe photovoltaics is performed using a solution-based process known as chemical bath deposition (CBD). Both CdS and Zn(S,O,OH) are used as n-type layers and deposited by CBD in the highest efficiency CIGSSe devices[8,9] This presents an additional challenge to vacuum processing, necessitating the removal of the absorber layer from the vacuum chamber post deposition in order to deposit CdS or Zn(S,O,OH) via a solution process under ambient conditions. As such, there has been considerable effort to adapt various vacuum processes such as sputtering or ALD to deposit CdS, Zn(S,O), or alternative materials such as $Zn_xMg_{1-x}O$ such that all vacuum processed absorbers could be realized allowing for continuous processing between active layers.[10–12] Solution processing of the absorber would remove the successive pump down cycles needed when switching between process equipment, thereby increasing throughput even if the batch CBD processes are retained.

Several solution processing routes have emerged for CIGSSe photovoltaics. The highest efficiencies have been obtained using a molecular precursor approach making use of hydrazine to solubilize metal chalcogenides, metals, and chalcogens. Initially developed by IBM, the hydrazine processing route directly dissolves Cu_2S with S, In_2Se_3 with Se, and Ga with Se.[13–17] Homogenous solutions are formed containing hydrazinium complexes of metals and chalcogen. Additional Se or S can be added to tune the bandgap and assist with crystallization. Through spin coating of the molecular precursor solutions followed by thermal decomposition, high quality films free of any contaminant species can be obtained. Through a simple thermal annealing, which can be done without an excess chalcogen containing atmosphere, uniform large films are obtained. In work by Zhang et a., a double gallium grading and the implementation of a solution processed ZnO nanoparticle buffer layer yielded efficiencies up to 18.1% (17.2% average device certified) as shown in Figure 2.2.[4]

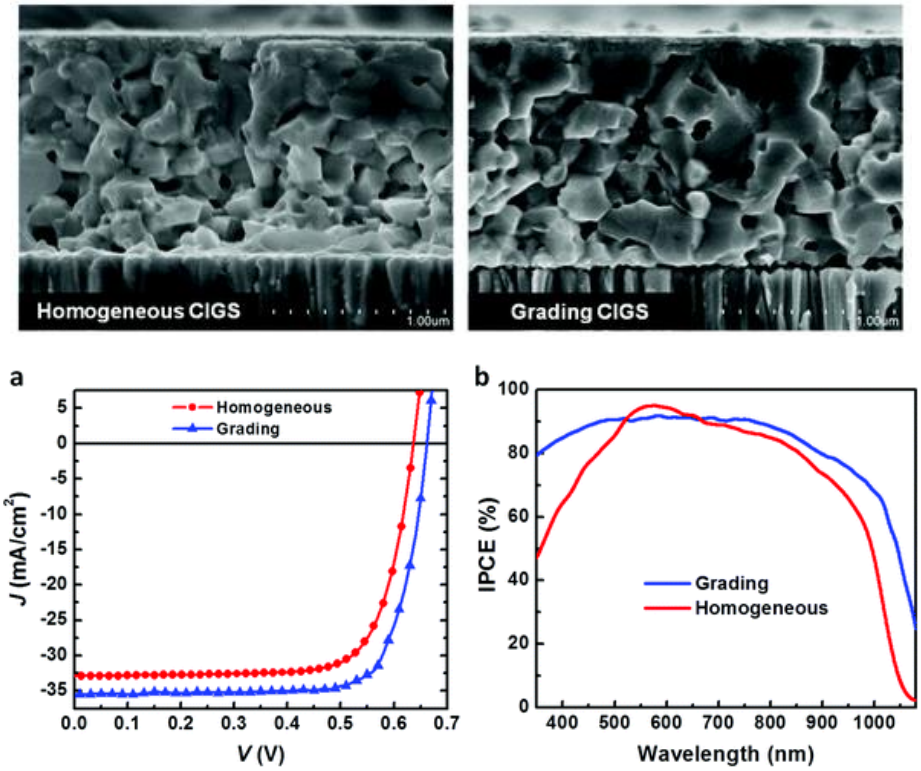

Figure 2.2. Hydrazine based CIGSSe, with and without a gallium double grading. Power conversion efficiencies up to 18.1% were achieved.[4]

While high quality films are possible, hydrazine-based solution processing is inherently limited by the high toxicity of hydrazine. Hydrazine's highly carcinogenic and explosive properties would potentially introduce numerous challenges associated with safe scale up of the technology, likely introducing additional cost burdens and lessening solution processing's cost advantage.[18]

As such, a wide variety of hydrazine-free solution processing routes have been developed over the last two decades, largely falling within two classes: molecular precursor and colloidal nanoparticles. Like the hydrazine system, various molecular precursors can solubilize metal salts,[19–24] organometallic complexes,[20,25] metals,[26–28] metal chalcogenides,[27,29] chalcogen salts,[30] or chalcogen[31] in a variety of solvent systems with substantially safer chemistries. Metal chlorides with thiourea in dimethyl formamide (DMF) or dimethyl sulfoxide (DMSO) have emerged as an attractive method of absorber fabrication due to their simplicity and ease of preparation.[21,22] Sulfide precursor films can converted to selenide absorber layers for use in high efficiency devices through selenization with elemental selenium vapor. Another metal salt containing approach is the use of metal nitrates to prepare oxide precursor films.[32] Low toxicity solvents such as methanol

have been used in this approach. However, due to stability of oxides, especially in the case of gallium oxide, reduction steps using hydrogen or H_2S are generally needed prior to selenization to avoid excessive oxygen content in the film. Any residual oxide can substantially detriment device performance via an increase series resistance. Metal dithiocarbamates have also been used to deposit high quality absorber layers.[25] These species can be prepared relatively easily, for example, by using a metal oxide, carbon disulfide and an alkylamine, to directly form a metal dithiocarbamate. Upon thermal annealing, these species decompose to metal sulfides. Another popular molecular precursor route is the use of co-solvent mixture of alkylamines and alkylthiols. This mixture has emerged as an alternative to hydrazine solution processing due to its "universal solvent" like ability, dissolving a wide variety of metal salts, metals, metal chalcogenides, and chalcogens. Metal thiolate species are formed in solution and can be thermally decomposed to form metal sulfides, selenides and tellurides.[19,20,23,24,26–29,31] Solution processed CIGSSe efficiencies exceeding 15% (active area) have been demonstrated using this method.[33,34]

The second method to solution process CIGSSe photovoltaics is the use of colloidal nanoparticles. In this method, precursor nanoparticles are first synthesized and can consist of oxides, metal-alloys, selenides, or sulfides. Following purification, the nanoparticles are dispersed in a suitable solvent, sometimes with added dispersants or coating modifiers, and coated onto a substrate. While generally containing more processing steps than its molecular precursor counterpart, the nanoparticle approach retains several advantages. Higher mass concentration inks can be prepared allowing for thick absorber layers via drop casting or blade coating.[35–39] Thicker coatings can also help increase throughput and reduce the capital costs needed for a solution processing line. These high mass concentration inks can be prepared in a wide variety of solvents through careful tuning of the nanoparticle ligand chemistry. Another advantage is the potential for air stable coating due to the decoupling of material formation and coating in colloidal nanoparticles. Many molecular precursors contain oxygen and moisture sensitive complexes, necessitating coating under an inert atmosphere,[19,20,26–29,39] driving up costs for a solution processing line and reducing cost advantage. While the champion efficiencies between the two approaches are constantly evolving, currently, a colloidal nanoparticle approach holds the highest non-hydrazine total area efficiency of 15% (16.4% active area).[39] While both approaches have demonstrated significant promise, the focus of this chapter will be on the development of colloidal nanoparticles-based routes to CIGSSe photovoltaics, addressing the various stages of development, wide variety

of approaches, challenges, and future directions. While numerous reports detail synthesis of various nanoparticles at length,[40,41] this section will focus on methods that were used to complete photovoltaic devices.

2.2 Use of Colloidal Metal Oxide Nanoparticles for CIGSSe Photovoltaics

The solution processing of CIGSSe photovoltaics using metal oxide colloids became an attractive option due to relative ease of preparation and air stability of resultant colloids and was explored by a number of startup companies. Additionally, substantial literature on dispersing oxide powders had already been established, allowing for easy translation to photovoltaic applications. As early as 2001, researchers at the International Solar Electric Technology (ISET) company were producing photovoltaics based on oxide precursors, reporting efficiencies over 13%.[42] Their synthesis method consisted of several steps, first dissolution of Cu, In, and Ga precursor salts followed by the addition of NaOH formed a gelatinous precipitate of metal hydroxides. The precipitate was then washed, dried, and fired at 450℃ to form mixed oxide powders. In order to disperse the oxide powders, an aqueous dispersing agent was added, and mechanical milling was performed. Blade coating was used to coat a 2.5-3.0 μm precursor films. However, due to the high stability of the precursor oxides, notably In and Ga oxides, a reduction step is needed prior to selenization. Generally, annealing between 475 and 525℃ under a hydrogen containing, forming gas atmosphere was sufficient to convert the oxide precursors to metallic precursors. The reduction step can also help volatilize organic species while the hydrogen atmosphere prevents the formation of coke like pyrolysis degradation products which can leave significant carbon residues in the film. The reaction kinetics are enhanced due to the porosity and high surface area of the nanoparticle film. After reduction, selenization was performed using a H_2Se gas containing atmosphere. A schematic of the experimental procedure is shown in Figure 2.3.

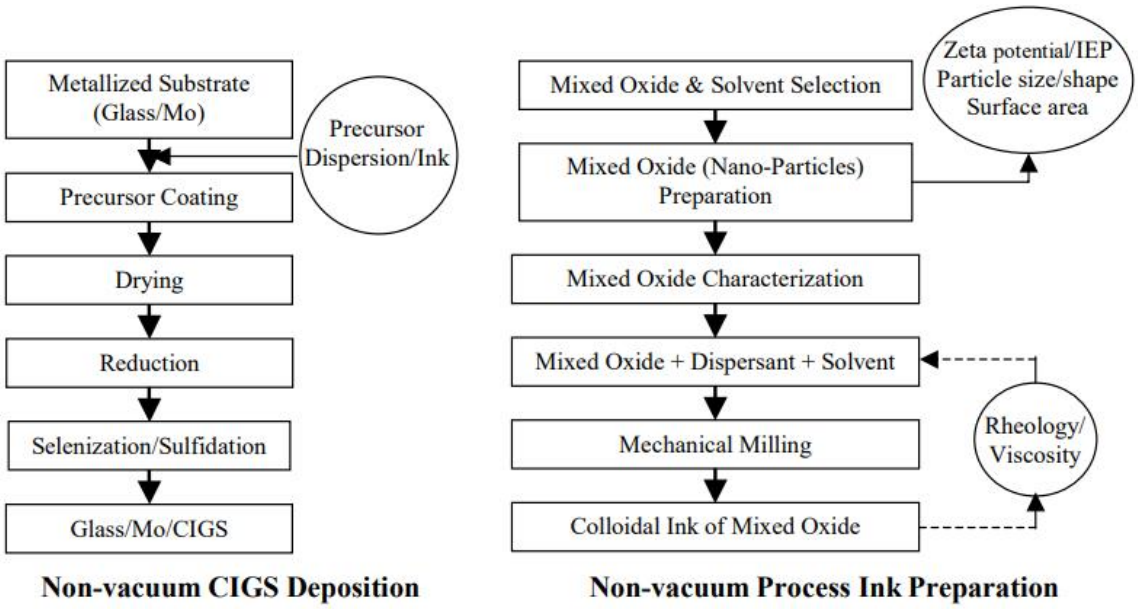

Figure 2.3. Ink preparation and CIGS process by ISET's non-vacuum process.[42]

In a similar process, Unisun used an aerosol pyrolysis processes followed by mixing the precursor powder with adequate solvents, dispersants, and surfactants. After reactive sintering with H_2Se, they achieved a champion power conversion efficiency of 11.7%.[43] No explicitly described reduction step was used, potentially retaining oxide secondary phases and explaining the difference in efficiency compared to ISET's work. While ISET showed device performance over 13%, the use of highly toxic H_2Se gas requires the need for rigorous engineering controls to ensure process safety, potentially driving up manufacturing costs.[44] Elemental selenium vapor is a significantly less toxic alternative, which is easily generated from solid selenium's relatively high vapor pressure at elevated temperatures.[45] However, work using elemental selenium and oxide precursors has been met with significant challenges, namely the presence of impurity oxide phases post selenization. In work from Kaelin et al., selenization of oxide nanoparticle precursor layers was performed with elemental selenium vapor. They observed remaining In_2O_3 impurity phases via XRD, as well as significant cracking of the nanoparticle film.

Later exploration of a pseudo-oxide system for $CuInSe_2$ absorber formation, by Uhl et al. in 2014, aimed to sidestep the reduction process needed for high efficiency device fabrication while simultaneously avoiding H_2Se for selenization.[46] In this approach colloids of $Cu_2(OH)_3(NO_3)$ and mixed $In(OH)_3$, InOOH, and $InCl_3$ were used. The solids were dispersed in butyl glycol acetate

along with polymeric dispersant. Thermogravimetric analysis of these colloids revealed the copper precursor decomposed to copper oxide at approximately 250°C whereas the indium precursor decomposed to indium oxide between 200 and 400°C. In both cases, organic content from polymeric dispersant and solvent appeared to have been removed by 400°C. However, the precursor film was never annealed over 200°C prior to selenization preventing complete decomposition to oxides. Selenization was uniquely performed by first evaporating several microns of elemental selenium on the surface of the nanoparticle precursor film followed by rapid thermal annealing to 500°C. In-situ XRD analysis showed the formation of an In_2O_3 phase at 330°C, however, by 500°C, this phases' XRD peaks were removed as shown in Figure 2.4.

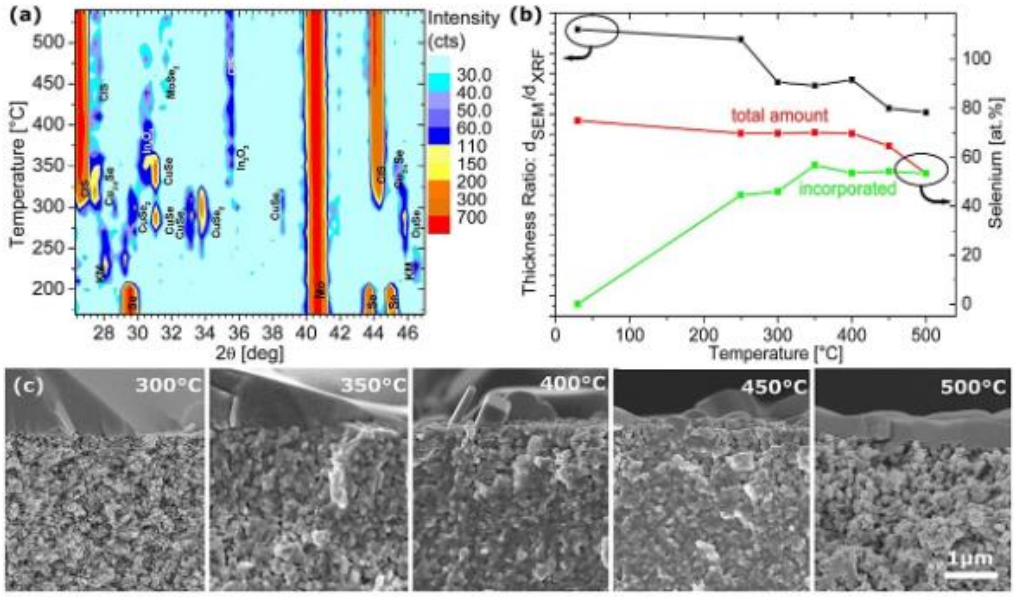

Figure 2.4. (a) *In situ* XRD patterns of precursor film during heating up to to 550 °C. (b) Thickness ratio between the thickness of the selenized precursor layer normalized by the precursor thickness. (c) SEM cross sections of films during the heat up process at various temperatures.[46]

The removal of the reduction step represented a step forward in the simplification of oxide (or pseudo-oxide in this case) precursors for absorber formation. Champion power conversion efficiencies up to 8.0% were obtained.[46] Though this represents a promising initial result, inclusion of gallium using this method remains a significant challenge. While the employed selenization was

able to remove In_2O_3 crystalline phases that formed during heat up, the higher stability of Ga_2O_3 is likely to present additional challenge without the use of a reduction step.

2.3 Use of Colloidal Metallic Alloy Nanoparticles for Solution Processed CIGSSe

Due to the limitations associated with removing highly stable oxide phases, an alternative approach was investigated to bypass the need for a reduction step to form a metallic precursor layer. Synthesis and casting of metal and metal alloy nanoparticles was developed to directly form metallic precursor layers that can be subjected to selenization. Some of the first device quality films prepared from metallic nanoparticles were again prepared by ISET starting in 1998, around the same time they were exploring oxide nanoparticles.[47] Cu-In alloys were prepared by heating metallic Cu and In in a crucible under a hydrogen atmosphere to 900°C. The molten alloys were then turned in powder using a gas atomizer, forming ~625 mesh materials. The product material was identified as a mixture of metallic In, Cu_9In_4, and potential Cu_2In and $Cu_{16}In_9$ phases. The powder could be added to water along with wetting agents and dispersants followed by ball milling for 42 hours. After casting the resulting ink, selenization in an $H_2Se + N_2$ atmosphere converted the metal alloys to $CuInSe_2$. Efficiencies in the range of 10-11% were obtained using this technique. The use of highly toxic H_2Se was again necessitated in these methods. Coating quality and a porous starting film were significant concerns which could potentially have lowered efficiencies. Attempts to densify the porous precursor film were partially successful, making use of a mechanical press with approximately $7x10^4$ kN/m^2 of force. Absorber layers from compacted films had significantly improved grain growth, however, devices were not prepared from this method.[48] A major limitation of these methods was the need for a high temperature, low throughput, and relatively complex synthesis method for the metal alloy nanomaterials.[49]

To bypass these complex synthesis methods, wet chemical colloidal syntheses were investigated for metal and metal alloy nanoparticles. An early synthesis made use of polyol/borhydride reduction in work by Chen et al.[50] In this approach, chlorides of copper and indium along with poly(vinyl pyrrolidone) (PVP) were dissolved in diethylene glycol (DEG). Then, a mixture of $NaBH_4$ and tetraethylene glycol (TEG) were added to the previous solution, initiating nucleation of metallic nanoparticles. Cu, In, or Cu-In nanoparticles could be synthesized by changing the metal salts present in the initial solution. The PVP in the reaction mixture was used as a ligand to stabilize the nanoparticles in polar media. After separation and purification via

washing and centrifugation several times, the particles could be redispersed in ethanol through ultrasonication or grinding. Highly polydisperse particles were obtained, with sizes between 10 and 200 nm, where the dominant phases were $Cu_{11}In_9$ and In. After coating, the precursor films were sulfurized to form $CuInS_2$ absorbers, however, poor device efficiencies of 0.7 and later 1.48% were obtained.[50,51] Similar work was performed by Shih-Hsien et al., making use of chemical reduction in ethylene glycol, forming CuIn and $Cu_{11}In_9$ nanoparticles with sizes between 40 and 60 nm. While selenization was performed, no devices were fabricated in this report.[52]

In another report on wet chemical synthesis of metal alloy nanoparticles, Kud et al. made use of citrate as a ligand in the synthesis of $Cu_{11}In_9$ nanoparticles.[53] Synthesis was performed by dissolving $CuCl_2{\cdot}2H_2O$ and $InCl_3{\cdot}4H_2O$ along with disodium citrate hydrate in diethylene glycol. After heating to 100°C, $NaBH_4$ dissolved in water was injected nucleating nanoparticles, which were held at 100°C for 15 minutes. After precipitating, washing, and drying the nanoparticles, they could be dispersed in ethanol at high mass concentrations of 200-250 mg/mL and coated via blade coating. Selenization was performed with the sample held at 550°C while elemental selenium was heated to 400-500°C in a separate zone of the furnace. The advantage of using citrate as a ligand versus polymeric species such as PVP are the ease of thermal decomposition of citrate, significantly reducing carbon contamination in the film. A champion power conversion efficiency of 7.0% was obtained.[53] However, the film morphology after selenization was marred by a porous and small grained layer towards the back contact, possibly due to the initial precursor film also having significant porosity. A cross section of the absorber layer is shown in Figure 2.5 along with J-V characteristics.

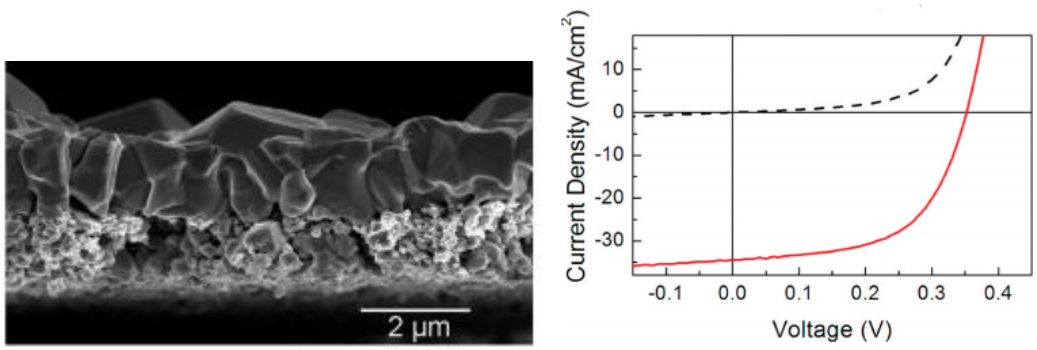

Figure 2.5. SEM cross section of selenized absorber layer and J-V curve of completed devices. Champion efficiency of 7.0% with a J_{sc} of 34.3 mA, V_{oc} of 0.352V, and fill factor of 57% were obtained.[53]

An ongoing limitation with these methods is the incorporation of gallium. To the best of our knowledge, no CIGSSe photovoltaics have been prepared from metal alloy nanoparticles obtained from wet chemical methods.

2.4 Use of Colloidal Selenide Nanoparticles for Solution Processed CIGSSe

All previous methods have relied on the synthesis of a precursor nanoparticle which must undergo a reactive annealing process in order to form CIGSSe. An alternative method is to use wet chemical methods to synthesis colloidal CIGSSe, thereby removing the need for complex reactions of non-selenide precursors. Early syntheses dating back to 1997 in work by Schulz et al. relied on low temperature metathesis type reactions between CuI, InI_3, and GaI_3 in pyridine with Na_2Se in methanol.[54] In the metathesis reaction, NaI is formed, which is soluble in methanol, while Cu-In-Ga-Se amorphous material precipitates as a colloid. The exact phase composition could not be determined, but individual reaction of CuI, InI_3, and GaI_3 with Na_2Se yielded the amorphous binary species $Cu_2Se/Cu_{2-x}Se$, β-In_2Se_3, and α-Ga_2Se_3 along with NaI. A composition of $Cu_{1.10}In_{0.68}Ga_{0.23}Se_x$ was obtained. These colloids were spray coated onto a molybdenum substrate. To compensate for the deficiency of In/Ga, additional In/Ga was evaporated on the surface using physical vapor deposition (PVD) methods. Selenization was performed under controlled Se flux, yielding growth of the top In/Ga layer into dense $Cu(In,Ga)Se_2$ (CIGSe) while the deposited nanoparticle layer did not grow to any appreciable extent. A cross section of the selenized film is shown in Figure 2.6.

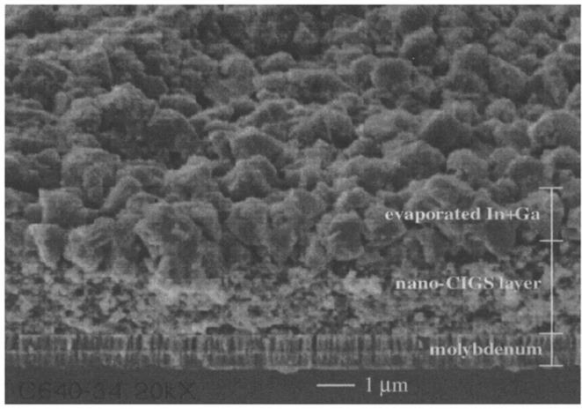

Figure 2.6. SEM cross section of a selenized Cu-In-Ga-Se nanoparticle precursor film with evaporated In/Ga capping layer.[54]

Efficiencies of 4.6% were obtained using this method.[54,55] Numerous following reports expanded on this work through optimization of the reaction conditions.[56–58] However, for a pure solution processed route (without physical vapor deposited In/Ga as was used in the previous 4.6% champion device), an efficiency of only 0.5% has been achieved.[47] Unlike metal-alloy films, which undergo volume expansion during selenization due to the addition of selenium to the crystal lattice, CIGSe nanoparticles do not have volume expansion upon selenization, and may rely on sintering like mechanisms alone. The high porosity of the nanoparticle film is largely retained post selenization, potentially contributing to the poor performance observed.

Colloidal syntheses making use of bulkier organic ligands as both reactants and solvents are an alternative synthesis method where significantly improved colloidal stability as compared to metathesis methods can help prepare higher quality precursor films. The high colloidal stability is owed to the bulky organic species that bind to and passivate dangling bonds on the nanoparticle surface and are known as ligands. These bulky groups prevent aggregation of the high surface energy nanoparticles through steric hinderance. In non-polar media, excellent colloidal stability can be observed due to favorable solvent-ligand interactions between long alkyl chains. As early as 1998, $CuInSe_2$ quantum dots were being synthesized using metal salts along with trioctyl phosphine (TOP) to solubilize elemental selenium while also acting as a surface ligand.[59,60] Alternative syntheses made use of selenium powder dispersed in oleylamine.[35,36] While selenium is insoluble in oleylamine at room temperature, oleylamine can form amine-selenide complexes at higher temperatures, facilitating selenide nanoparticle synthesis. The reaction mechanism of metal salts with elemental selenium in oleylamine has been studied in detail by Kar et al., where a binary

mediated synthesis was observed. First the formation of CuSe and InSe binary species were observed, followed by the reaction of the two solid species to form ternary $CuInSe_2$.[61] Due to the bulky organic ligands, either TOP or oleylamine, excellent colloidal stability in non-polar solvents was observed. In work by Guo et al., both oleylamine and TOP were used with metal salts to synthesize $CuInSe_2$ nanoparticles and nanorings as shown in Figure 2.7.

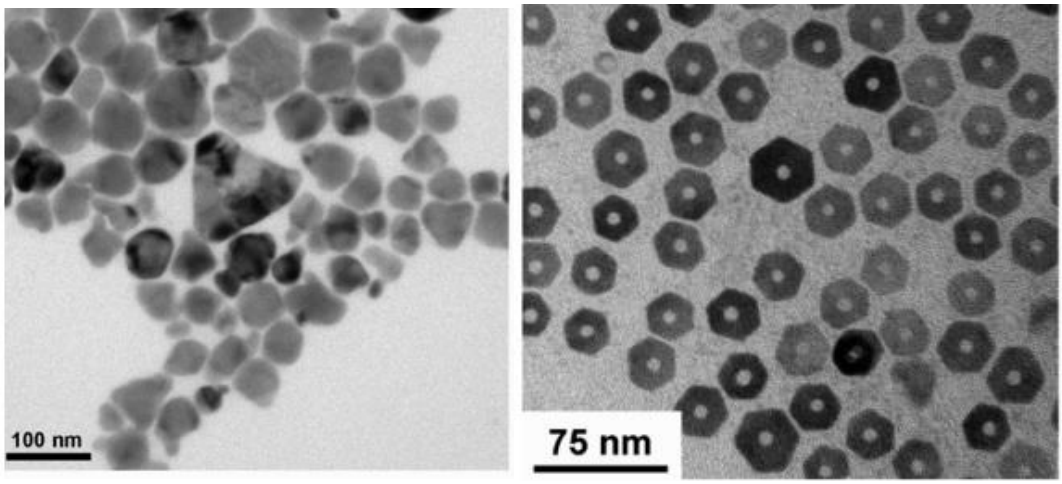

Figure 2.7. TEM images of CuInSe2 nanoparticles synthesized using oleylamine and TOP respectively.[35]

Inks of these nanoparticles in toluene were used to prepare devices via drop casting. In order to remove the insulating organic ligands, a one hour anneal under flowing argon at 500℃ was employed. Selenization was then performed between 450-550℃ using elemental selenium under an argon atmosphere. A bilayer morphology was observed, where a layer of fine grain material was observed capped by larger dense grains. Approximately micron sized grains were achieved in the upper layer as shown in Figure 2.8.[35]

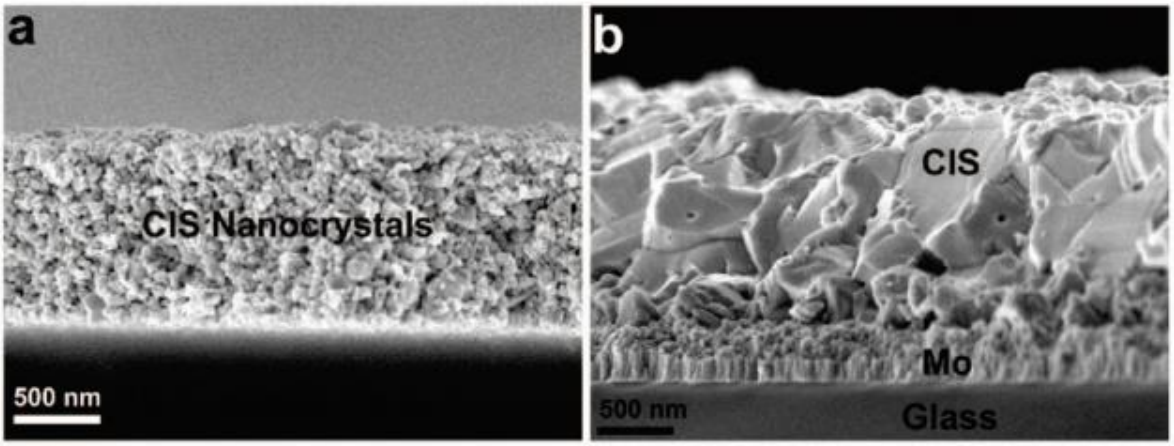

Figure 2.8. SEM cross sections of $CuInSe_2$ nanoparticle precursor film before and after selenization respectively.[35]

While the inert anneal provided some removal of organic species allowing for grain growth to some extent, later research would show that species such as oleylamine do not cleanly volatilize under inert annealing, leaving behind substantial amounts of carbonaceous residues.[62] Without selenization or removal of bulky organic ligands, researchers initially achieved low power conversion efficiencies between 0.01 and 0.24%, likely due to the insulating effect of the organic ligands between each nanoparticle.[36]

Various attempts have been made to improve grain growth during selenization via colloidal selenide nanoparticles. In work by Walker et al., Cu_2Se and CuSe nanoparticles were added to the CIGSe nanoparticle inks to help flux the selenization process with copper selenide liquid phases.[63] The coated films were not subjected to a high temperature inert annealing prior to selenization. At a selenization temperature of 550°C, efficiencies of 0.2%, 2.6%, and 4.3% were obtained for pure CIGSe nanoparticles, mixed CIGSe and Cu_2Se nanoparticles, and mixed CIGSe and CuSe nanoparticles respectively.[63] Cross sectional SEM and J-V curves are shown in Figure 2.9.

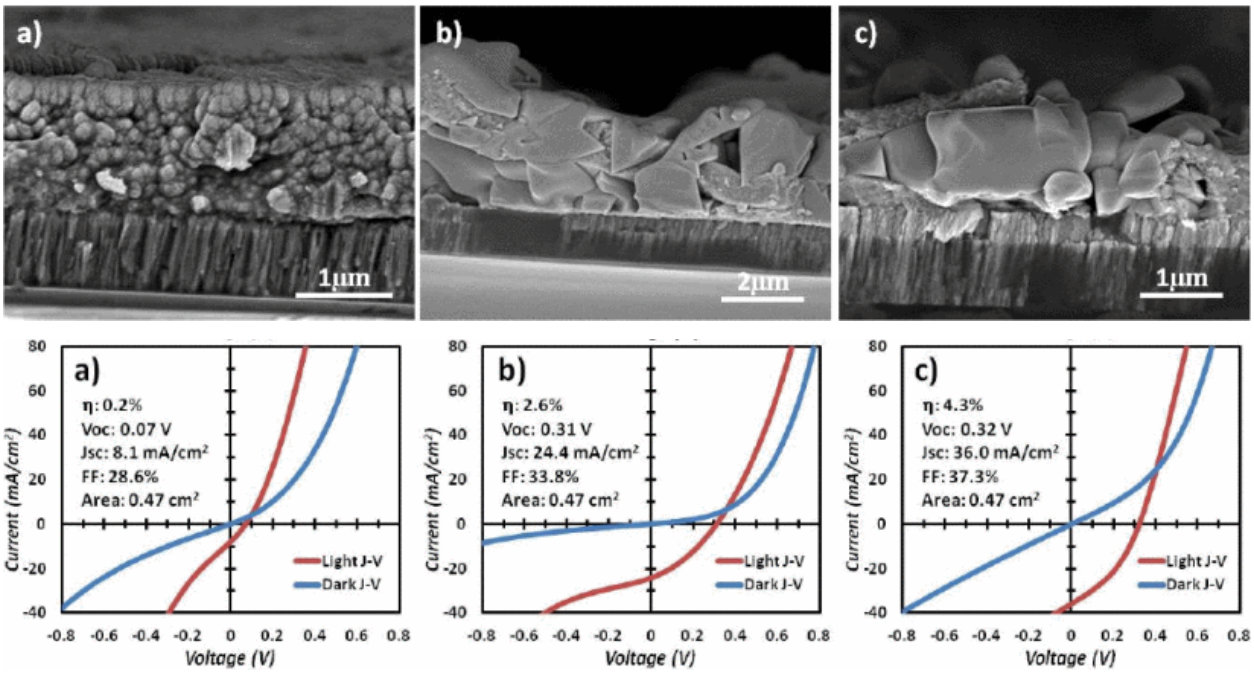

Figure 2.9. SEM cross sections and JV curves of films made from a) CISe nanoparticles, b) CISe and $Cu_{2-x}Se$ nanoparticles, and c) CISe and CuSe nanoparticles.[63]

However, a major limitation for all devices was severe shunting, likely due to incomplete consumption of highly conductive copper selenide species and/or formation of conductive graphitic carbon residing between grains forming shunt pathways. Other work by Jeong et al. using multiphase nanoparticles prepared using microwave-assisted polyol synthesis with metal salts and selenium in polyethelene glycol at 280°C.[64] Multiphase nanomaterials were formed, identified as $CuInSe_2$, CuSe, $Cu_{2-x}Se$, and In_2O_3. After purification, PVP was added to ethylene glycol and ethanol-based inks to prevent film cracking. Selenization was performed using selenium vapor in a vacuum chamber at a substrate temperature of 530°C, yielding a device with an efficiency of 8.2%.[64] A bilayer morphology was again observed likely due to segregation of the high carbon content from PVP in the film to the back contact as shown in Figure 2.10 along with the champion device JV curve.

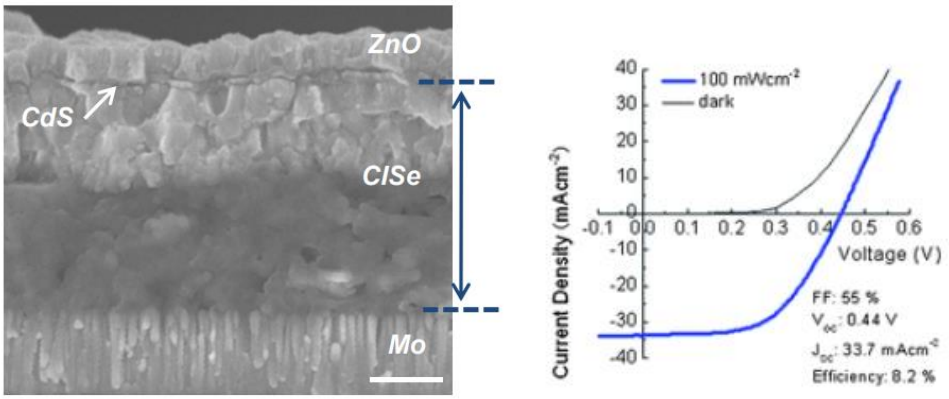

Figure 2.10. SEM cross section of selenized film prepared from multiphase nanoparticles synthesized from a polyol method.[64]

A further limitation of this work was the use of vacuum for selenization, which hinders the goals of continuous processing that solution processing aims to achieve.

2.5 Use of Colloidal Sulfide Nanoparticles for Solution Processed CIGSSe

The use of sulfide nanoparticles emerged as a method to revisit the reactive selenization similar to those used for metal alloys, where volume expansion can assist in densification through a breakdown and reformation of the nanoparticle, replacing sulfur with selenium. Further, a unique feature of sulfide nanoparticles was observed – approximately micron size grain growth at relatively low temperatures of 500℃, with or without removal of organic species. Another advantage of using sulfide precursors in that unlike oxides, residual sulfide material in the film does not substantially detriment device performance and can be used to increase the bandgap of the material. Shortly after the work developing colloidal nanoparticle methods for CISe photovoltaics, Guo et al. began using $CuInS_2$ (CIS) and CIGS nanoparticles for fabrication of $CuIn(S,Se)_2$ and CIGSSe photovoltaics.[37] Similar synthetic methods were used, where CuCl, $InCl_3$, and $GaCl_3$ salts were heated in oleylamine to 225℃ followed by hot injection of sulfur dissolved in oleylamine. After holding at reaction temperature for 30 minutes, the mixture was cooled, and nanoparticles were separated and purified. The purified nanoparticles were dispersed in toluene and coated by dropcasting. An inert anneal at 400℃ was performed to reduce organic content, followed by selenization with elemental selenium in an argon atmosphere to form densified grains.

Greater than micron sized grains were obtained and device efficiencies of 5.1% and 5.5% were achieved for CISSe and CIGSSe respectively as shown in Figure 2.11.[37]

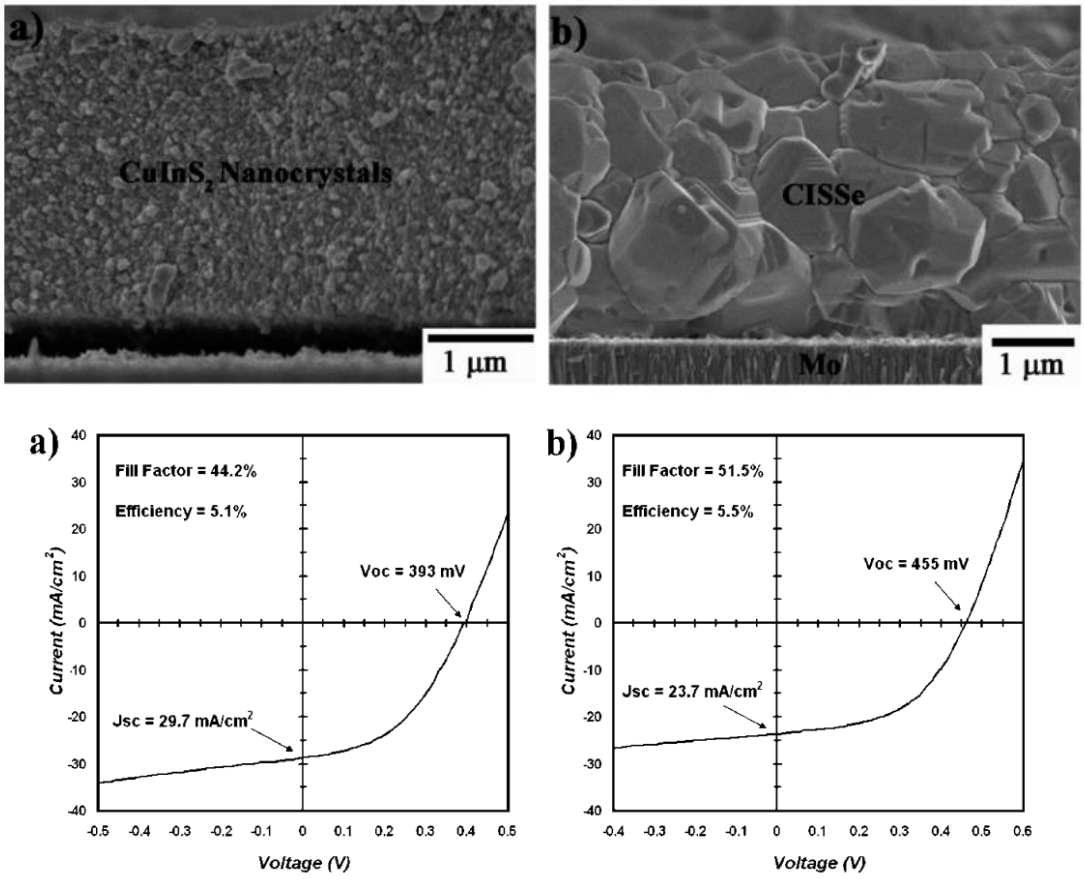

Figure 2.11. SEM cross-sections from a $CuInS_2$ nanoparticle film before and after selenization respectively. JV curves for a completed CISSe and CIGSSe photovoltaics are also shown.[37]

Notable shunting is observed in the J-V curves, potentially from conductive inter-grain graphitic carbon formed during the inert anneal at 400°C.

Additional process improvement by Guo et al. was able to drive up efficiencies to 12.0% using $Cu(In,Ga)S_2$ nanoparticles.[38] Toluene was replaced with hexanethiol as a solvent, and blade coating was used instead of dropcasting. Additionally, no high temperature annealing under an inert atmosphere was performed, replaced by a 300°C anneal in ambient atmosphere for 1 minute between each coating. Two coatings were used to form an approximately 1 μm absorber layer. An aqueous potassium cyanide (KCN) etch was used in between coatings and an aqueous soak in 1M NaCl solution was employed prior to selenization. Notably, the addition of sodium was shown to improve efficiencies from 7.7% to 12.0%, both without the use of an antireflection coating.[38] The

absorber morphology was characterized by a dense large grain upper layer followed by a fine grain layer at the back contact. Further process optimizations such as use of air free techniques for precursor storage, adjustment of ink concentration and annealing conditions as well as application of an antireflection coating were able to push total area efficiencies to 15.0% (16.4 active area) in work by McLeod et al.[39] To the best of our knowledge, this remains the highest non-hydrazine total area efficiency achieved by a solution process. A potential limitation of the work by McLeod et al. was the low thickness of the prepared absorber at approximately 800 nm. Compared the state-of-the-art vacuum processed absorbers with thicknesses ranging from 2-3 microns, the absorber by McLeod et al remains substantially thinner potentially reducing light absorption and decreasing J_{sc}. The SEM cross section and JV curve of the champion device are shown in Figure 2.12.

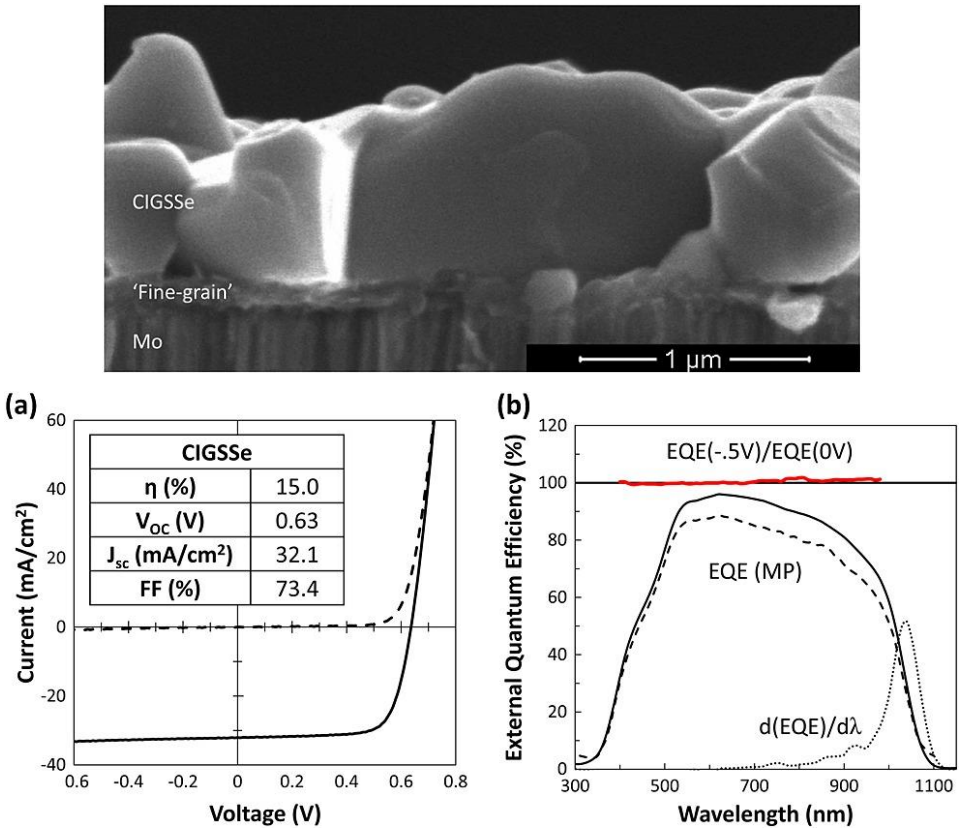

Figure 2.12. SEM cross section of champion absorber layer, showing a distinct densified large grain layer with an underlying fine grain layer. JV and EQE data for the champion devices is also shown.[39]

Thicker films have been deposited by similar methods in a later report by McLeod et al. where the KCN etch was also dropped.[65] Rapid thermal processing was adopted as opposed to selenization

in a tubular furnace. A grain growth model was established for selenization of oleylamine capped nanoparticles. While grains exceeding the 800 nm of the previous report were obtained, no devices were reported.[65] Further exploration of the system was performed by Alruqobah et al. where the influence of sodium and potassium was investigated on oleylamine capped sulfide nanoparticles.[66] Introduction of NaF and KF were shown to improve device through both improved grain growth as well as potential defect passivation. Additionally, evidence of the presence of a $KInSe_2$ surface layer was presented, which has been shown to form during potassium post deposition treatments in vacuum processed absorbers.[67] This thin surface layer improves junction properties and allows for thinning of the CdS buffer layer, thereby decreasing the parasitic absorption of CdS.[8] The toxic KCN etching step was not used in this work. Efficiencies up to 12.0% were obtained when both sodium and potassium fluorides were used.[66] While scalable blade coating was used in the previous examples, further improvements to scalability through techniques such as inkjet printing have also been investigated by Barbé et al.[68] A hexanthiol based ink was used again, however, the high boiling point molecule dodecanethiol was also added to help prevent cracking, tears-of-wine, and coffee ring effects.[69] Efficiencies up to 6.5% were obtained.[68] However, due to existing oleylamine ligands and the high boiling dodecanethiol additive, a carbon rich layer at the back contact was observed and may contribute to the low observed efficiencies. Other unique solution processing methods have been explored with sulfide nanoparticles. In work by Kar et al. a solution phase selenization was investigated using a precursor film of either $Cu_{2-x}Se$ or Cu_yS that were submerged in a solution of oleylamine, selenium, and $InCl_3$.[70] Through solution mediated reaction, the nanocrystalline layers were converted into densified large grain absorbers of $CuInSe_2$, although in the case of $Cu_{2-x}Se$ nanoparticle layers, little growth was observed. Efficiencies of 1.97% and 2.02% were obtained for $Cu_{2-x}Se$ and Cu_yS based CISSe absorbers respectively.[70] A major limitation observed with this method is the contamination of oleylamine in the final absorber. A 1M hydrazine solution in ethanol was employed to help remove some of the contaminant organic species, however, due to the previously discussed high toxicity of hydrazine, such processing is not ideal for large scale processing.

In all previous work from this section, an ongoing limitation of these processing methods is residual carbon impurities from oleylamine ligands on the nanoparticle surface. As previously mentioned, annealing under an inert environment results in decomposition of some of the oleylamine ligand to graphitic carbon.[62] As such residual carbon in the film brought into the

selenization process decomposes to graphitic carbon species. Further, it is pushed towards the back contact by a front of liquid selenium that condenses on the film during selenization.[65,71] Annealing in air prior to selenization can help avoid this issue through combustion of the oleylamine molecule,[62] however, air annealing can readily oxidize the sulfide nanoparticles. As discussed in a previous section on oxides, removal of indium and gallium oxides via selenization with elemental selenium presents significant challenges. The use of KCN in the work by Guo et al. and McLeod et al. between each coating may have been able to etch some of the surface oxide formed by annealing in air at or above 300℃. However, if the use of highly toxic KCN is to be avoided, air annealing to remove oleylamine may prove to be an unideal method.

Other approaches making use of sulfide nanoparticles with less carbon contamination have been explored to bypass the limitations of the previously described systems. In work by Eeles et al. CIGS nanoparticles were synthesized using Nanoco's patented approach which makes use of octanethiol as a ligand.[72] Thermal decomposition of this ligand during annealing prior to selenization provides opportunity to prevent substantial carbon contamination. However, a distinct fine grain layer was still observed in this method, implying either reactivity limitations during the conversion of nanoparticles to large grains, or residual carbon content was segregated to the back contact. The low temperature metathesis approaches used to form CIGSe nanomaterials has also successfully been implemented for formation of CIS and CIGS nanoparticles. With respect to carbon contamination, this method is advantageous in that pyridine and methanol are the only two organic species used during synthesis. Both have low boiling points and should be easily removed by moderate temperature annealing, even under an inert atmosphere. In work by Rehan et al, the metathesis reaction of CuI, InI_3 in pyridine with Na_2S in methanol was performed at 0℃ for 1 minute under a nitrogen atmosphere. Uniquely, the researchers mixed the resultant colloid with a molecular precursor of metal salts to improve film density and subsequent selenization. The films were coated by spincoating the hybrid ink and selenization was performed using elemental selenium in a vacuum chamber at 40 torr. Efficiencies up to 12.8% were obtained with the use of sodium to help suppress fine grain formation.[72] While a traditional carbonaceous fine grain layer was not observed, a bilayer morphology where dense large grains were on the surface and smaller porous grains towards the back contact was observed.

2.6 Shortcoming of Existing Methods to be Addressed

While each of the discussed methods have merits, a number of common process improvements are needed across the board in order to further close the vacuum – solution processed efficiency gap. While wet chemical syntheses of colloidal nanoparticles have emerged as a simple and potentially commercially viable method of forming CIGSSe precursors, the use of metal salts in nearly every report brings about an inherent problem.[40,41] Common metal salts have impurity anions such as halides, acetates, acetylacetaonates, sulfates, nitrates, etc. These impurity anions can bind to nanoparticle surfaces during synthesis or directly incorporate into the crystal lattice of the nanomaterial.[73] In the case of halides, an n-type dopant, degradation of electrical properties can be observed. In the case of acetylacetonates or nitrates, thermal decomposition in the absence or in chalcogen deficient conditions can form oxide phases,[74] thereby introducing high resistivity secondary phases that can detriment solar cell performance. Naturally the use of pure metals as colloidal synthesis precursors could avoid anionic impurities, limited success has been observed in the literature for pure metal methods, such as poor colloidal stability.[74] To address this shortcoming, in Chapter 3, the novel synthesis of metal chalcogenide nanoparticles from pure metals using amine thiol chemistry is investigated.

Another major limitation is the incorporation of carbonaceous impurities, forming impurity fine grain layers. While these layers can certainly increase recombination due to many grain boundaries, they are also several orders of magnitude higher resistivity than the molybdenum back contact and can even effect elemental redistribution in the materials.[75,76] As such, removal of impurity carbon is essential in order to reach high efficiencies. The removal of impurity carbon is addressed in Chapter 4 and 5 for the fabrication of carbon impurity free solution processed photovoltaics.

Finally, while initial investigations into scalable coating methods such as blade coating,[38,39,65,66] inkjet printing,[68] or spray coating[48] have been performed, some of the highest quality coating methods, such as slot-die coating, have not been investigated for colloidal CIGSSe nanoparticles. We address the challenge of developing scalable coating methods, namely slot-die coating, for solution processed photovoltaics in Chapter 6.

2.7 References

(1) Bermudez, V.; Perez-Rodriguez, A. Understanding the Cell-to-Module Efficiency Gap in Cu(In,Ga)(S,Se)$_2$ Photovoltaics Scale-Up. **2018**. https://doi.org/10.1038/s41560-018-0177-1.

(2) Patidar, R.; Burkitt, D.; Hooper, K.; Richards, D.; Watson, T. Slot-Die Coating of Perovskite Solar Cells: An Overview. *Mater. Today Commun.* **2020**, *22*, 100808. https://doi.org/10.1016/j.mtcomm.2019.100808.

(3) Panthani, M. G.; Kurley, J. M.; Crisp, R. W.; Dietz, T. C.; Ezzyat, T.; Luther, J. M.; Talapin, D. V. High Efficiency Solution Processed Sintered CdTe Nanocrystal Solar Cells: The Role of Interfaces. *Nano Lett.* **2014**, *14* (2), 670–675. https://doi.org/10.1021/nl403912w.

(4) Zhang, T.; Yang, Y.; Liu, D.; Tse, S. C.; Cao, W.; Feng, Z.; Chen, S.; Qian, L. High Efficiency Solution-Processed Thin-Film Cu(In,Ga)(Se,S)$_2$ Solar Cells. *Energy Environ. Sci.* **2016**, *9* (12), 3674–3681. https://doi.org/10.1039/c6ee02352e.

(5) Rau, U.; Schock, H. W. Cu(In,Ga)Se2 Thin-Film Solar Cells. In *Solar Cells*; Elsevier, 2013; pp 261–304. https://doi.org/10.1016/B978-0-12-386964-7.00009-3.

(6) Dullweber, T.; Hanna, G.; Shams-Kolahi, W.; Schwartzlander, A.; Contreras, M. A.; Noufi, R.; Schock, H. W. Study of the Effect of Gallium Grading in Cu(In,Ga)Se$_2$. *Thin Solid Films* **2000**, *361*, 478–481. https://doi.org/10.1016/S0040-6090(99)00845-7.

(7) Eisenbarth, T.; Unold, T.; Caballero, R.; Kaufmann, C. A.; Abou-Ras, D.; Schock, H. W. Origin of Defects in $CuIn_{1-x}Ga_xSe_2$ Solar Cells with Varied Ga Content. *Thin Solid Films* **2009**, *517* (7), 2244–2247. https://doi.org/10.1016/j.tsf.2008.10.142.

(8) Jackson, P.; Wuerz, R.; Hariskos, D.; Lotter, E.; Witte, W.; Powalla, M. Effects of Heavy Alkali Elements in Cu(In,Ga)Se$_2$ Solar Cells with Efficiencies up to 22.6%. *Phys. Status Solidi - Rapid Res. Lett.* **2016**, *10* (8), 583–586. https://doi.org/10.1002/pssr.201600199.

(9) Nakamura, M.; Yamaguchi, K.; Kimoto, Y.; Yasaki, Y.; Kato, T.; Sugimoto, H. Cd-Free Cu(In,Ga)(Se,S)2 Thin-Film Solar Cell with Record Efficiency of 23.35%. *IEEE J. Photovoltaics* **2019**, *9* (6), 1863–1867. https://doi.org/10.1109/JPHOTOV.2019.2937218.

(10) Törndahl, T.; Platzer-Björkman, C.; Kessler, J.; Edoff, M. Atomic Layer Deposition of Zn1−xMgxO Buffer Layers for Cu(In,Ga)Se$_2$ Solar Cells. *Prog. Photovoltaics Res. Appl.* **2007**, *15* (3), 225–235. https://doi.org/10.1002/pip.733.

(11) Kim, H.-S.; Kim, G.; Kim, E.; Cho, S. J.; Lee, D. J.; Choi, S. G.; Shan, F.; Kim, S.-J. Improvement of the Electrical Properties of a Cu(In,Ga)Se 2 Solar Cell Based on a ZnS Buffer Layer from Radio Frequency Magnetron Sputtering . *J. Nanosci. Nanotechnol.* **2018**, *19* (3), 1799–1803. https://doi.org/10.1166/jnn.2019.16255.

(12) Choi, W.-J.; Park, W. W.; Kim, Y.; Son, C. S.; Hwang, D. The Effect of ALD-Zn(O,S) Buffer Layer on the Performance of CIGSSe Thin Film Solar Cells. *Energies* **2020**, *13* (2), 412. https://doi.org/10.3390/en13020412.

(13) Mitzi, D. B.; Min Yuan; Wei Liu; Kellock, A.; Chey, S. J.; Schrott, A.; Deline, V. Solution Processing of CIGS Absorber Layers Using a Hydrazine-Based Approach. In *Conference Record of the IEEE Photovoltaic Specialists Conference*; 2008. https://doi.org/10.1109/PVSC.2008.4922730.

(14) Mitzi, D. B. Solution Processing of Chalcogenide Semiconductors via Dimensional Reduction. *Advanced Materials*. John Wiley & Sons, Ltd August 21, 2009, pp 3141–3158. https://doi.org/10.1002/adma.200802027.

(15) Mitzi, D. B.; Yuan, M.; Liu, W.; Kellock, A. J.; Chey, S. J.; Gignac, L.; Schrott, A. G. Hydrazine-Based Deposition Route for Device-Quality CIGS Films. *Thin Solid Films* **2009**, *517* (7), 2158–2162. https://doi.org/10.1016/j.tsf.2008.10.079.
(16) Liu, W.; Mitzi, D. B.; Yuan, M.; Kellock, A. J.; Jay Chey, S.; Gunawan, O. 12% Efficiency $CuIn(Se,S)_2$ Photovoltaic Device Prepared Using a Hydrazine Solution Process. *Chem. Mater.* **2010**, *22* (3), 1010–1014. https://doi.org/10.1021/cm901950q.
(17) Todorov, T. K.; Gunawan, O.; Gokmen, T.; Mitzi, D. B. Solution-Processed $Cu(In,Ga)(S,Se)_2$ Absorber Yielding a 15.2% Efficient Solar Cell. *Prog. Photovoltaics Res. Appl.* **2013**, *21* (1), 82–87. https://doi.org/10.1002/pip.1253.
(18) Bob, B.; Lei, B.; Chung, C.-H.; Yang, W.; Hsu, W.-C.; Duan, H.-S.; Hou, W. W.-J.; Li, S.-H.; Yang, Y. The Development of Hydrazine-Processed $Cu(In,Ga)(Se,S)_2$ Solar Cells. *Adv. Energy Mater.* **2012**, *2* (5), 504–522. https://doi.org/10.1002/aenm.201100578.
(19) Zhang, R.; Szczepaniak, S. M.; Carter, N. J.; Handwerker, C. A.; Agrawal, R. A Versatile Solution Route to Efficient $Cu_2ZnSn(S,Se)_4$ Thin-Film Solar Cells. *Chem. Mater.* **2015**, *27* (6), 2114–2120. https://doi.org/10.1021/cm504654t.
(20) Zhao, X.; Lu, M.; Koeper, M. J.; Agrawal, R. Solution-Processed Sulfur Depleted $Cu(In, Ga)Se_2$ Solar Cells Synthesized from a Monoamine-Dithiol Solvent Mixture. *J. Mater. Chem. A* **2016**, *4* (19), 7390–7397. https://doi.org/10.1039/c6ta00533k.
(21) Uhl, A. R.; Katahara, J. K.; Hillhouse, H. W. Molecular-Ink Route to 13.0% Efficient Low-Bandgap $CuIn(S,Se)_2$ and 14.7% Efficient $Cu(In,Ga)(S,Se)_2$ Solar Cells. *Energy Environ. Sci.* **2016**, *9* (1), 130–134. https://doi.org/10.1039/c5ee02870a.
(22) Jiang, J.; Giridharagopal, R.; Jedlicka, E.; Sun, K.; Yu, S.; Wu, S.; Gong, Y.; Yan, W.; Ginger, D. S.; Green, M. A.; Hao, X.; Huang, W.; Xin, H. Highly Efficient Copper-Rich Chalcopyrite Solar Cells from DMF Molecular Solution. *Nano Energy* **2020**, *69*, 104438. https://doi.org/10.1016/j.nanoen.2019.104438.
(23) Miskin, C. K.; Dubois-Camacho, A.; Reese, M. O.; Agrawal, R. A Direct Solution Deposition Approach to CdTe Thin Films. *J. Mater. Chem. C* **2016**, *4*, 9167–9171. https://doi.org/10.1039/C6TC02986H.
(24) Murria, P.; Miskin, C. K.; Boyne, R.; Cain, L. T.; Yerabolu, R.; Zhang, R.; Wegener, E. C.; Miller, J. T.; Kenttämaa, H. I.; Agrawal, R. Speciation of CuCl and $CuCl_2$ Thiol-Amine Solutions and Characterization of Resulting Films: Implications for Semiconductor Device Fabrication. *Inorg. Chem.* **2017**, *56* (23), 14396–14407. https://doi.org/10.1021/acs.inorgchem.7b01359.
(25) Zhao, W.; Cui, Y.; Pan, D. Air-Stable, Low-Toxicity Precursors for $CuIn(SeS)_2$ Solar Cells with 10.1 % Efficiency. *Energy Technol.* **2013**, *1* (2–3), 131–134. https://doi.org/10.1002/ente.201200044.
(26) Zhao, D.; Tian, Q.; Zhou, Z.; Wang, G.; Meng, Y.; Kou, D.; Zhou, W.; Pan, D.; Wu, S. Solution-Deposited Pure Selenide CIGSe Solar Cells from Elemental Cu, In, Ga, and Se. *J. Mater. Chem. A* **2015**, *3* (38), 19263–19267. https://doi.org/10.1039/c5ta05300e.
(27) Zhang, R.; Cho, S.; Lim, D. G.; Hu, X.; Stach, E. A.; Handwerker, C. A.; Agrawal, R. Metal-Metal Chalcogenide Molecular Precursors to Binary, Ternary, and Quaternary Metal Chalcogenide Thin Films for Electronic Devices. *Chem. Commun.* **2016**, *52* (28), 5007–5010. https://doi.org/10.1039/c5cc09915c.

(28) Zhao, X.; Deshmukh, S. D.; Rokke, D. J.; Zhang, G.; Wu, Z.; Miller, J. T.; Agrawal, R. Investigating Chemistry of Metal Dissolution in Amine-Thiol Mixtures and Exploiting It toward Benign Ink Formulation for Metal Chalcogenide Thin Films. *Chem. Mater.* **2019**, *31* (15), 5674–5682. https://doi.org/10.1021/acs.chemmater.9b01566.

(29) Fan, Q.; Tian, Q.; Wang, H.; Zhao, F.; Kong, J.; Wu, S. Regulating the Starting Location of Front-Gradient Enabled Highly Efficient Cu(In,Ga)Se_2 Solar Cells: Via a Facile Thiol-Amine Solution Approach. *J. Mater. Chem. A* **2018**, *6* (9), 4095–4101. https://doi.org/10.1039/c7ta10889c.

(30) Clark, J. A.; Murray, A.; Lee, J. M.; Autrey, T. S.; Collord, A. D.; Hillhouse, H. W. Complexation Chemistry in N,N-Dimethylformamide-Based Molecular Inks for Chalcogenide Semiconductors and Photovoltaic Devices. *J. Am. Chem. Soc.* **2019**, *141* (1), 298–308. https://doi.org/10.1021/jacs.8b09966.

(31) Webber, D. H.; Buckley, J. J.; Antunez, P. D.; Brutchey, R. L. Facile Dissolution of Selenium and Tellurium in a Thiol-Amine Solvent Mixture under Ambient Conditions. *Chem. Sci.* **2014**, *5* (6), 2498–2502. https://doi.org/10.1039/c4sc00749b.

(32) Park, G. S.; Chu, V. Ben; Kim, B. W.; Kim, D. W.; Oh, H. S.; Hwang, Y. J.; Min, B. K. Achieving 14.4% Alcohol-Based Solution-Processed Cu(In,Ga)$(S,Se)_2$ Thin Film Solar Cell through Interface Engineering. *ACS Appl. Mater. Interfaces* **2018**, *10* (12), 9894–9899. https://doi.org/10.1021/acsami.8b00526.

(33) Zhao, Y.; Yuan, S.; Kou, D.; Zhou, Z.; Wang, X.; Xiao, H.; Deng, Y.; Cui, C.; Chang, Q.; Wu, S. High Efficiency CIGS Solar Cells by Bulk Defect Passivation through Ag Substituting Strategy. *ACS Appl. Mater. Interfaces* **2020**, *12* (11), 12717–12726. https://doi.org/10.1021/acsami.9b21354.

(34) Yuan, S.; Wang, X.; Zhao, Y.; Chang, Q.; Xu, Z.; Kong, J.; Wu, S. Solution Processed CIGSSe Solar Cells with 15.25% Efficiency by Surface Sulfurization. *ACS Appl. Energy Mater.* **2020**. https://doi.org/10.1021/acsaem.0c00917.

(35) Guo, Q.; Kim, S. J.; Kar, M.; Shafarman, W. N.; Birkmire, R. W.; Stach, E. A.; Agrawal, R.; Hillhouse, H. W. Development of $CuInSe_2$ Nanocrystal and Nanoring Inks for Low-Cost Solar Cells. *Nano Lett.* **2008**, *8* (9), 2982–2987. https://doi.org/10.1021/nl802042g.

(36) Panthani, M. G.; Akhavan, V.; Goodfellow, B.; Schmidtke, J. P.; Dunn, L.; Dodabalapur, A.; Barbara, P. F.; Korgel, B. A. Synthesis of $CuInS_2$, $CuInSe_2$, and $Cu(In_xGa_{1-x})Se_2$ (CIGS) Nanocrystal "Inks" for Printable Photovoltaics. *J. Am. Chem. Soc.* **2008**, *130* (49), 16770–16777. https://doi.org/10.1021/ja805845q.

(37) Guo, Q.; Ford, G. M.; Hillhouse, H. W.; Agrawal, R. Sulfide Nanocrystal Inks for Dense $Cu(In_{1-x}Ga_x)(S_{1-y}Se_y)_2$ Absorber Films and Their Photovoltaic Performance. *Nano Lett.* **2009**, *9* (8), 3060–3065. https://doi.org/10.1021/nl901538w.

(38) Guo, Q.; Ford, G. M.; Agrawal, R.; Hillhouse, H. W. Ink Formulation and Low-Temperature Incorporation of Sodium to Yield 12% Efficient Cu(In,Ga)$(S,Se)_2$ Solar Cells from Sulfide Nanocrystal Inks. *Prog. Photovoltaics Res. Appl.* **2013**, *21* (1), 64–71. https://doi.org/10.1002/pip.2200.

(39) McLeod, S. M.; Hages, C. J.; Carter, N. J.; Agrawal, R. Synthesis and Characterization of 15% Efficient CIGSSe Solar Cells from Nanoparticle Inks. *Prog. Photovoltaics Res. Appl.* **2015**, *23* (11), 1550–1556. https://doi.org/10.1002/pip.2588.

(40) Van Embden, J.; Chesman, A. S. R.; Jasieniak, J. J. The Heat-up Synthesis of Colloidal Nanocrystals. *Chemistry of Materials*. American Chemical Society April 14, 2015, pp 2246–2285. https://doi.org/10.1021/cm5028964.

(41) Coughlan, C.; Ibáñez, M.; Dobrozhan, O.; Singh, A.; Cabot, A.; Ryan, K. M. Compound Copper Chalcogenide Nanocrystals. *Chem. Rev.* **2017**, *117* (9), 5865–6109. https://doi.org/10.1021/acs.chemrev.6b00376.
(42) Kapur, V. K.; Fisher, M.; Roe, R. Nanoparticle Oxides Precursor Inks for Thin Film Copper Indium Gallium Selenide (CIGS) Solar Cells. In *Materials Research Society Symposium - Proceedings*; 2001; Vol. 668, pp H261–H267. https://doi.org/10.1557/proc-668-h2.6.
(43) Eberspacher, C.; Pauls, K.; Serra, J. Non-Vacuum Processing of CIGS Solar Cells. In *Conference Record of the IEEE Photovoltaic Specialists Conference*; 2002; pp 684–687. https://doi.org/10.1109/PVSC.2002.1190657.
(44) Kaelin, M.; Rudmann, D.; Tiwari, A. N. Low Cost Processing of CIGS Thin Film Solar Cells. *Sol. Energy* **2004**, *77* (6), 749–756. https://doi.org/10.1016/j.solener.2004.08.015.
(45) Brooks, L. S. Vapor Pressures of Tellurium and Selenium. *J. Am. Ceram. Soc.* **1952**, *74*, 227–229.
(46) Uhl, A. R.; Fuchs, P.; Rieger, A.; Pianezzi, F.; Sutter-Fella, C. M.; Kranz, L.; Keller, D.; Hagendorfer, H.; Romanyuk, Y. E.; LaMattina, F.; Yoon, S.; Karvonen, L.; Magorian-Friedlmeier, T.; Ahlswede, E.; VanGenechten, D.; Stassin, F.; Tiwari, A. N. Liquid-Selenium-Enhanced Grain Growth of Nanoparticle Precursor Layers for $CuInSe_2$ Solar Cell Absorbers. *Prog. Photovoltaics Res. Appl.* **2015**, *23* (9), 1110–1119. https://doi.org/10.1002/pip.2529.
(47) Ahn, S. J.; Kim, K. H.; Yoon, K. H. $Cu(In,Ga)Se_2$ Thin Film Solar Cells from Nanoparticle Precursors. *Curr. Appl. Phys.* **2008**, *8* (6), 766–769. https://doi.org/10.1016/j.cap.2007.04.037.
(48) Norsworthy, G.; Leidholm, C. R.; Halani, A.; Kapur, V. K.; Roe, R.; Basol, B. M.; Matson, R. CIS Film Growth by Metallic Ink Coating and Selenization. *Sol. Energy Mater. Sol. Cells* **2000**, *60* (2), 127–134. https://doi.org/10.1016/S0927-0248(99)00075-6.
(49) Başol, B. M. Low Cost Techniques for the Preparation of $Cu(In,Ga)(Se,S)_2$ Absorber Layers. *Thin Solid Films* **2000**, *361*, 514–519. https://doi.org/10.1016/S0040-6090(99)00823-8.
(50) Chen, G.; Wang, L.; Sheng, X.; Liu, H.; Pi, X.; Yang, D. Chemical Synthesis of Cu(In) Metal Inks to Prepare $CuInS_2$ Thin Films and Solar Cells. *J. Alloys Compd.* **2010**, *507* (1), 317–321. https://doi.org/10.1016/j.jallcom.2010.07.190.
(51) Chen, G.; Wang, L.; Sheng, X.; Yang, D. Cu-In Intermetallic Compound Inks for $CuInS_2$ Solar Cells. *J. Mater. Sci. Mater. Electron.* **2011**, *22* (8), 1124–1129. https://doi.org/10.1007/s10854-010-0271-z.
(52) Liu, S. H.; Chen, F. S.; Lu, C. H. Preparation of Thin $CuInSe_2$ Films Using Cu-In Alloy Nanoparticles. *Chem. Lett.* **2010**, *39* (12), 1333–1335. https://doi.org/10.1246/cl.2010.1333.
(53) Kind, C.; Feldmann, C.; Quintilla, A.; Ahlswede, E. Citrate-Capped $Cu_{11}In_9$ Nanoparticles and Its Use for Thin-Film Manufacturing of CIS Solar Cells. *Chem. Mater.* **2011**, *23* (23), 5269–5274. https://doi.org/10.1021/cm2024668.
(54) Schulz, D. L.; Curtis, C. J.; Flitton, R. A.; Wiesner, H.; Keane, J.; Matson, R. J.; Parilla, P. A.; Noufi, R.; Ginley, D. S. Nanoparticle Colloids as Spray Deposition Precursors to CIGS Photovoltaic Materials. In *AIP Conference Proceedings*; 1997; Vol. 394, p 683. https://doi.org/10.1063/1.52915.
(55) Schulz, D. L.; Curtis, C. J.; Flitton, R. A.; Wiesner, H.; Keane, J.; Matson, R. J.; Jones, K. M.; Parilla, P. A.; Noufi, R.; Ginley, D. S. Cu-In-Ga-Se Nanoparticle Colloids as Spray Deposition Precursors for $Cu(In,Ga)Se_2$ Solar Cell Materials. *J. Electron. Mater.* **1998**, *27* (5), 433–437. https://doi.org/10.1007/s11664-998-0173-5.

(56) Kim, K.-H.; Chun, Y.-G.; Park, B.-O.; Yoon, K.-H. Preparation of $CuInGaSe_2$ Absorber Layer by Nanoparticles-Based Spray Deposition. In *MRS Proceedings*; Cambridge University Press, 2004; Vol. 836, p L5.10. https://doi.org/10.1557/PROC-836-L5.10.

(57) Kim, K.-H.; Chun, Y.-G.; Park, B.-O.; Yoon, K.-H. Synthesis and Characterization of $Cu_x(In,Ga)_ySe_z$ Nanoparticles by Colloidal Route. In *MRS Proceedings*; Cambridge University Press, 2004; Vol. 836, p L5.9. https://doi.org/10.1557/PROC-836-L5.9.

(58) Ahn, S. J.; Kim, K. H.; Chun, Y. G.; Yoon, K. H. Nucleation and Growth of $Cu(In,Ga)Se_2$ Nanoparticles in Low Temperature Colloidal Process. *Thin Solid Films* **2007**, *515* (7–8), 4036–4040. https://doi.org/10.1016/j.tsf.2006.10.102.

(59) Malik, M. A.; O'brien, P.; Revaprasadu, N.; Wakefield, G. Novel Route for the Preparation of CuSe and $CuInSe_2$ Nanoparticles. *MRS Proc.* **1998**, *536*, 371. https://doi.org/10.1557/PROC-536-371.

(60) Malik, M. A.; O'Brien, P.; Revaprasadu, N. A Novel Route for the Preparation of CuSe and $CuInSe_2$ Nanoparticles. *Adv. Mater.* **1999**, *11* (17), 1441–1444. https://doi.org/10.1002/(SICI)1521-4095(199912)11:17<1441::AID-ADMA1441>3.0.CO;2-Z.

(61) Kar, M.; Agrawal, R.; Hillhouse, H. W. Formation Pathway of $CuInSe_2$ Nanocrystals for Solar Cells. *J. Am. Chem. Soc.* **2011**, *133* (43), 17239–17247. https://doi.org/10.1021/ja204230d.

(62) Martin, T. R.; Katahara, J. K.; Bucherl, C. N.; Krueger, B. W.; Hillhouse, H. W.; Luscombe, C. K. Nanoparticle Ligands and Pyrolized Graphitic Carbon in CZTSSe Photovoltaic Devices. *Chem. Mater.* **2016**, *28* (1), 135–145. https://doi.org/10.1021/acs.chemmater.5b03426.

(63) Walker, B.; Agrawal, R. Grain Growth Enhancement of Selenide CIGSe Nanoparticles to Densified Films Using Copper Selenides. In *Conference Record of the IEEE Photovoltaic Specialists Conference*; 2012; pp 2654–2657. https://doi.org/10.1109/PVSC.2012.6318141.

(64) Jeong, S.; Lee, B. S.; Ahn, S.; Yoon, K.; Seo, Y. H.; Choi, Y.; Ryu, B. H. An 8.2% Efficient Solution-Processed $CuInSe_2$ Solar Cell Based on Multiphase $CuInSe_2$ Nanoparticles. *Energy Environ. Sci.* **2012**, *5* (6), 7539–7542. https://doi.org/10.1039/c2ee21269b.

(65) McLeod, S.; Alruqobah, E.; Agrawal, R. Liquid Assisted Grain Growth in Solution Processed $Cu(In,Ga)(S,Se)_2$. *Sol. Energy Mater. Sol. Cells* **2019**, *195*, 12–23. https://doi.org/10.1016/j.solmat.2019.02.020.

(66) Alruqobah, E. H.; Agrawal, R. Potassium Treatments for Solution-Processed $Cu(In,Ga)(S,Se)_2$ Solar Cells. *ACS Appl. Energy Mater.* **2020**, *3* (5), 4821–4830. https://doi.org/10.1021/acsaem.0c00422.

(67) Lepetit, T.; Harel, S.; Arzel, L.; Ouvrard, G.; Barreau, N. Coevaporated $KInSe_2$: A Fast Alternative to KF Postdeposition Treatment in High-Efficiency $Cu(In,Ga)Se_2$ Thin Film Solar Cells. *IEEE J. Photovoltaics* **2016**, *6* (5), 1316–1320. https://doi.org/10.1109/JPHOTOV.2016.2589365.

(68) Barbé, J.; Eid, J.; Ahlswede, E.; Spiering, S.; Powalla, M.; Agrawal, R.; Del Gobbo, S. Inkjet Printed $Cu(In,Ga)S_2$ Nanoparticles for Low-Cost Solar Cells. *J. Nanoparticle Res.* **2016**, *18* (12). https://doi.org/10.1007/s11051-016-3686-5.

(69) Lim, T. O.; Yang, J.; Lee, S.; Chung, J.; Hong, D. Deposit Pattern of Inkjet Printed Pico-Liter Droplet. *Int. J. Precis. Eng. Manuf.* **2012**, *13* (6), 827–833. https://doi.org/10.1007/s12541-012-0108-1.

(70) Kar, M.; Hillhouse, H. W.; Agrawal, R. Chemical Liquid Deposition of $CuInSe_2$ and $CuIn(S,Se)_2$ Films for Solar Cells. *Thin Solid Films* **2012**, *520* (16), 5431–5437. https://doi.org/10.1016/j.tsf.2012.04.012.
(71) Hages, C. J.; Koeper, M. J.; Miskin, C. K.; Brew, K. W.; Agrawal, R. Controlled Grain Growth for High Performance Nanoparticle-Based Kesterite Solar Cells. *Chem. Mater.* **2016**, *28* (21), 7703–7714. https://doi.org/10.1021/acs.chemmater.6b02733.
(72) Eeles, A.; Arnou, P.; Bowers, J. W.; Walls, J. M.; Whitelegg, S.; Kirkham, P.; Allen, C.; Stubbs, S.; Liu, Z.; Masala, O.; Newman, C.; Pickett, N. High-Efficiency Nanoparticle Solution-Processed $Cu(In,Ga)(S,Se)_2$ Solar Cells. *IEEE J. Photovoltaics* **2018**, *8* (1), 288–292. https://doi.org/10.1109/JPHOTOV.2017.2762581.
(73) Marin, R.; Skripka, A.; Huang, Y. C.; Loh, T. A. J.; Mazeika, V.; Karabanovas, V.; Chua, D. H. C.; Dong, C. L.; Canton, P.; Vetrone, F. Influence of Halide Ions on the Structure and Properties of Copper Indium Sulphide Quantum Dots. *Chem. Commun.* **2020**, *56* (22), 3341–3344. https://doi.org/10.1039/c9cc08291c.
(74) Niederberger, M.; Garnweitner, G.; Buha, J.; Polleux, J.; Ba, J.; Pinna, N.; Niederberger, M.; Garnweitner, G.; Buha, J.; Polleux, J.; Ba, J.; Pinna Martin-Luther-, N. Nonaqueous Synthesis of Metal Oxide Nanoparticles: Review and Indium Oxide as Case Study for the Dependence of Particle Morphology on Precursors and Solvents. *J Sol-Gel Sci Techn* **2006**, *40*, 259–266. https://doi.org/10.1007/s10971-006-6668-8.
(75) Eberspacher, C.; Fredric, C.; Pauls, K.; Serra, J. Thin-Film CIS Alloy PV Materials Fabricated Using Non-Vacuum, Particles-Based Techniques. *Thin Solid Films* **2001**, *387* (1–2), 18–22. https://doi.org/10.1016/S0040-6090(00)01729-6.
(76) Rehan, S.; Kim, K. Y.; Han, J.; Eo, Y. J.; Gwak, J.; Ahn, S. K.; Yun, J. H.; Yoon, K. H.; Cho, A.; Ahn, S. J. Carbon-Impurity Affected Depth Elemental Distribution in Solution-Processed Inorganic Thin Films for Solar Cell Application. *ACS Appl. Mater. Interfaces* **2016**, *8* (8), 5261–5272. https://doi.org/10.1021/acsami.5b10789.

3. VERSATILE COLLOIDAL SYNTHESES OF METAL CHALCOGENIDE NANOPARTICLES FROM ELEMENTAL PRECURSORS USING AMINE-THIOL CHEMISTRY

Reprinted with permission from Deshmukh, S. D.; Ellis, R. G.; Sutandar, D. S.; Rokke, D. J.; Agrawal, R. Versatile Colloidal Syntheses of Metal Chalcogenide Nanoparticles from Elemental Precursors Using Amine-Thiol Chemistry. *Chem. Mater.* **2019**, *31* (21), 9087–9097. https://doi.org/10.1021/acs.chemmater.9b03401. The journal article and supporting information have been merged and text and figures have been modified where appropriate.

3.1 Introduction

The synthesis of CIGS, CZTS and other metal chalcogenide nanoparticles typically relies on the use of non-chalcogenide metal salts such as metal acetylacetonates, chlorides, iodides, acetates, nitrates, sulfates, oxides, hybrid salts such as $Sn(acac)_2Br_2$, and various hydrate derivatives.[1–7] While careful selection of the salt can tune the reactivity in colloidal synthesis, a drawback to this approach is the presence of anionic impurities which can potentially introduce contaminant elements. In the case of chlorides, Kar et al. observed a distinct C-Cl bond stretch in FTIR, a result of the oleylamine solvent/ligand interaction with chlorine in solution.[8] Such chlorine impurity in CIGSSe photovoltaic device can act as an n-type dopant, influencing the device performance.[9] Similar impurities have been observed in molecular precursors making use of metal halide salts where Murria et al. observed presence of chlorine in organometallic complexes in the solution as well as in the resultant thin films.[10] The highest efficiency CIGSSe photovoltaics fabricated from nanoparticles have made use of acetylacetonates salts in place of chloride salts.[11] However, in the case of indium acetylacetonate and acetate, it has been shown that the heat up in the absence of a sulfur source in oleylamine yields indium oxide.[12] The formation of an oxide phase, especially in the case of the extremely stable, high bandgap gallium oxide, can significantly hinder photovoltaic performance.[13] Along with direct reactions with metals or metal chalcogenides, these anionic impurities can also bind to the nanocrystal surface as a covalently bonded X-type ligand to passivate cationic dangling bonds, which necessitates their removal by post synthesis meta-thesis type ligand exchange processes.[14]

The development of single source organometallic precursors has been explored in colloidal nanoparticle synthesis which can avoid the presence of anionic impurities described in the latter

case. Metal dithiocarbamates and xanthates have been explored for the synthesis of $CuInS_2$ (CIS),[15] CIGS,[16] and CZTS[17] molecular precursors and nanoparticles. However, most of these syntheses involve either the use or the formation of water molecules which requires its complete removal from the product to avoid the formation of metal oxides at higher reaction temperatures during nanoparticle syntheses. Another limitation of this system is the difficulty in forming the selenium containing analogs of xanthates and thiocarbamates for selenide nanoparticle synthesis which requires the use of highly toxic carbon diselenide.[18] Along with these, various other complex organometallic single source precursors have also been explored, which include $(PPh_3)_2CuIn(SPh)_4$, $(TOP)_3CuIn(S(n\text{-}Pr,t\text{-}Bu)_4$, $(Ph_3P)_2Cu(\mu\text{-}Set)_2In(SEt)_2$, $(Ph_3P)_2Cu(\mu\text{-}SEt)_2Ga(SEt)_2$ etc.[4] However, these precursors suffer from more complex synthetic pathways and cannot be synthesized in-situ for large-scale synthesis. There has been a limited exploration into the synthesis of CIGS and CIGSe nanoparticles using pure metals and chalcogens in ethylenediamine via solvothermal synthesis routes. The mechanism for these syntheses relies on the reaction of the immiscible liquid metals (In and Ga) with dissolved copper and selenium, resulting in polydispersed (30-80 nm) and colloidally unstable nanoparticles[19,20] which severely limit the prospects of this synthetic method being employed for solution processed device fabrication.

Recently, amine-thiol chemistry has emerged as a versatile system with the unprecedented ability to dissolve various metal precursors including metal salts,[21,22] pure metals,[23–25] chalcogens,[26–28] and metal chalcogenides[24,25] at relatively high concentrations. These systems have been used to deposit thin films of various metal chalcogenide materials. Although these systems have demonstrated promising performances for CIGSSe and CZTSSe thin film photovoltaic devices, deposition of thin films using this solvent mixture has various issues due to high reactivity, air sensitivity, and highly corrosive nature. Amine-thiol chemistry has largely focused on molecular precursor formation with extremely limited reports of nanoparticle synthesis making use of the chemistry. Amine-thiol chemistry has been used for the synthesis of limited chalcogenide nanoparticles such as lead chalcogenides, $Cu_2ZnSnSe_4$, and $CuInSe_2$, however, non-chalcogenide metal salts were still used as cation precursors.[27,29] To date, there is only one report of elemental metals in amine-thiol solutions used for colloidal chalcogenide nanoparticle synthesis, applied by our group to synthesize binary ZnSe nanoparticles.[30]

In this report, the benefits from the amine-thiol based molecular precursor approach and colloidal nanoparticle-based approach are combined, yielding an extremely versatile synthetic pathway for colloidal metal chalcogenide nanoparticle synthesis. Amine-thiol chemistry is employed to solubilize elemental metals, chalcogens, and metal chalcogenides to create reactive metal thiolate precursors. These metal thiolate precursors are free of any of the aforementioned anionic (halide, acetylacetonate, acetate, etc.), oxide, and moisture impurities, and can be used directly without the need for additional separation or purification of the precursor solutions. In this report, the versatility of the system is demonstrated through the synthesis of a variety of binary, ternary, and quaternary photovoltaic relevant nanoparticles including In_2S_3, $(In_xGa_{1-x})S_3$, $CuInS_2$, $CuIn(S_xSe_{1-x})_2$ (CISSe), $Cu(In_xGa_{1-x})S_2$, Cu_2ZnSnS_4, and $AgInS_2$. The reactive metal thiolates were thermally decomposed in the coordinating solvent oleylamine to form colloidally stable, phase pure nanoparticles. The flexibility in the experimental synthetic method was also demonstrated by the synthesis of phase pure nanoparticle via hot injection, heat up, and microwave assisted solvothermal reactions. Additionally, in the case of sulfide nanoparticles, no additional sulfur source was used due to the presence of covalent bonds between the metal center and sulfurs in the metal thiolate precursors, eliminating rapid sulfur-metal intermixing concerns present in other synthetic methods.[31] Phase purity, compositional uniformity, morphology, size and ligand moiety for these particles were investigated by a wide variety of analytical techniques such as XRD, Raman, XRF, TEM, STEM-EDS, ^{1}H-NMR, and FTIR. The decomposition pathway of these precursors is further investigated via GC-MS and XRD analysis which demonstrates the decomposition of metal thiolates into metal sulfides along with few non-contaminating volatile byproducts. Additionally, the control over size and phase of the particles was demonstrated through variation of reaction conditions, allowing for tailoring of nanoparticles for specific applications.

3.2 Experimental Section

3.2.1 Materials

Ga pellets (6 mm dia, 99.99999% metals basis) were purchased from Alfa Aesar. Cu (40-60 nm, >99.5% metal basis with 2% oxygen), In (100 mesh, 99.99% metal basis), Zn (<50 nm, >99% metal basis), Sn (<150 nm, >99% metal basis), Se (100 mesh, 99.99% metal basis), Cu_2S (powder, 99.99%), Ag_2S (powder, 99.9%), n-propylamine (PA, 99%), n-octylamine (OA, 99%),

1,2-ethanedithiol (EDT, >98%) and oleylamine (OLA, 70%, primary amines >98%) were purchased from Sigma-Aldrich. All chemicals were used as received except for Ga pellets and oleylamine. The Surface oxide was removed from as-received gallium pellets using a blade and oleylamine was degassed via successive freeze pump thaw cycles prior to use.

3.2.2 Precursor Solution Preparation

All precursor inks for hot injection and heat up nanoparticle syntheses were prepared by dissolving pure metals in PA and EDT solution at a mole ratio of PA:EDT=2:1. Metal precursor weighing and solution preparations were performed in a glovebox under an inert atmosphere of nitrogen (oxygen and moisture concentration maintained below 1 ppm). For binary nanoparticle synthesis of indium sulfide, 0.4 M ink was prepared by dissolving indium powder in a PA-EDT solution at room temperature. For In-Ga alloyed binary sulfide nanoparticles, inks were prepared with various mole ratios of In to Ga such that the total concentration of In+Ga was maintained at 0.4 M. Metal dissolutions for CIS, CIGS and CZTS nanoparticle synthesis were performed on a Schlenk line under argon atmosphere at 45°C with constant refluxing for faster dissolution to obtain 0.4 M (Cu based) inks. A Cu:In mole ratio of 0.9 was used for CIS nanoparticles while Cu/(In+Ga) and Ga/(In+Ga) mole ratios of 0.9 and 0.3 were used for CIGS nanoparticle synthesis respectively. In the case of CZTS nanoparticle synthesis, Cu/Sn and Zn/Sn precursor mole ratios were maintained at 1.92 and 1.2 respectively. Inks used for time study aliquot experiments for CIGS nanoparticle syntheses were prepared with Cu concentrations of 0.8 M, keeping the metal ratios constant. Inks prepared for CIS nanoparticle syntheses were further used as a solvent for Se powder dissolution to prepare inks for CISSe nanoparticle syntheses. Precursor inks for microwave assisted solvothermal syntheses of CIS nanoparticles were prepared on a Schlenk line under an argon atmosphere at 65°C in OLA-EDT solution instead of PA-EDT solution with an OLA:EDT mole ratio of 2:1, Cu concentration of 0.2 M, and a Cu:In mole ratio of 0.9. An indium precursor ink for GC-MS analysis was also prepared under Schlenk line using OA-EDT solution with an indium concentration of 0.4 M. For experiments involving metal chalcogenides as starting precursors, inks for CIGS and $AgInS_2$ nanoparticle synthesis were prepared by mixing two solutions prior to reaction; i. Metal chalcogenide ink (Cu_2S or Ag_2S) in 2:1 mole ratio of PA:EDT with a metal concentration of 0.8 M, ii. Pure metal inks (In+Ga or In) in 2:1 mole ratio of PA:EDT with a metal concentration of 0.88 M.

3.2.3 Nanoparticle Synthesis

For standard heat up reactions, 1 mL of the metal precursor ink in PA-EDT solution was mixed with 8 mL of OLA in a 3 neck flask assembly and then heated to desired reaction temperature (285°C for In_2S_3, $(In_xGa_{1-x})_2S_3$, CIGS and 250°C for CIS, CISSe, CZTS) under a flowing argon atmosphere on a Schlenk line. A condenser with cooling water was used to reflux the reaction mixture until ~150°C, above which, the cooling water was disconnected for the duration of the reaction to reduce reflux and remove excess PA-EDT from the reaction mixture. Without removal of cooling water, the heating mantles were unable to reach the reaction temperature setpoint. The duration of the reaction was measured once the reaction mixture reached the setpoint temperature. CIGS aliquot experiments were performed through this heat up procedure using 30 mL of OLA and 3 mL of 0.8 M (Cu based) ink. For this experiment, once the reaction mixture reached 285°C, samples were collected over the course of the reaction (0 hr, 0.5 hr, 1 hr, 3 hr, 6 hr, 12 hr, and 24 hr) by removing 2 mL of reaction mixture at 285°C using a glass syringe with a stainless steel needle and then quenching it in 5 mL OLA maintained at room temperature.

The standard hot injection reaction for nanoparticle synthesis was performed by heating up 2 solvents separately. Reaction solvent i.e. OLA (8 mL) was heated to desired reaction temperature in 3 neck flask assembly while the metal precursor ink in PA-EDT (1.5 mL) diluted with an equal volume of OLA (1.5 mL) was heated to 45°C in a one-neck flask sealed with a rubber septum. Once both the mixtures reached the set temperature, 2 mL of metal precursor ink was quickly injected in hot OLA and then the reaction was continued for the desired duration. Similar to heat up process, the cooling water used for reaction reflux was removed after injection to remove the excess quantities of PA-EDT solvents. The time study on In_2S_3 nanoparticle synthesis was performed using hot injection approach with aliquots at t = 5 min, 1 hr, 6 hr, and 18 hr collected in the manner similar to the CIGS heat up experiment.

For the microwave assisted solvothermal reaction route, 1 mL of 0.2 M (Cu based) CIS-OLA-EDT ink was diluted to 5 mL with OLA and sealed with a crimped PTFE coated silicone septa cap on a 5 mL borosilicate glass microwave reactor with magnetic PTFE stir bar. The reaction was carried out for 15 min at 225°C with a stirring rate of 600 rpm using a Biotage Initiator EXP 400W microwave reactor in “Normal” absorption mode.

All particles formed through heat up, hot injection, or microwave assisted solvothermal route were washed using the same procedure. The cooled reaction mixture was transferred to a

centrifuge tube and was centrifuged at 14000 rpm for 5 min using isopropanol as an antisolvent. The supernatant from this process was discarded and the precipitated particles were re-dispersed in hexanes. This process was repeated 3 times to remove excess OLA from the nanoparticles. Finally, the nanoparticles were dried under argon flow to remove residual washing solvents and then stored in an inert atmosphere for further analysis.

3.2.4 Material Characterization

X-ray diffractograms (XRD) were obtained using a Rigaku Smart Lab diffractometer in Parallel-Beam mode, using a Cu Kα (λ = 1.5406 Å) source operating at 40 kV/44 mA. Transmission electron microscopy (TEM) images were collected using Tecnai G2 20 TEM with an accelerating voltage of 200 kV. STEM-EDS data were collected on Talos 200X TEM containing four silicon drift detectors using SiN grid. Atomic force microscopy was performed using digital instruments multimode atomic force microscope with a IIIa controller under contact mode. Absorption data for particles were collected using the Agilent Cary 60 UV-Vis Spectrophotometer in transmission mode on soda lime glass substrate. Raman spectra were collected on a Horiba/Jobin-Yvon HR800 microscope with an excitation laser wavelength of 632.8 nm. FTIR spectra were collected on Thermo-Nicolet Nexus 670 FTIR unit in transmission mode using NaCl crystal substrates. ^{1}H-NMR spectra were collected using a Bruker AV-III-400-HD instrument and deuterated chloroform as a nanoparticle dispersing solvent along with ethylene carbonate as a NMR standard. Bulk nanoparticle composition was analyzed using a Fisher XAN 250 X-ray fluorescence (XRF) instrument at 50 kV voltage with primary Ni filter containing silicon drift detector. Gas chromatography mass spectrometry was performed using Agilent 5975C MSD (mass selective detector) equipped with a 7890A gas chromatograph. The column used during this analysis was a DB-5MS 30m x 0.25mm x 0.25um film. The full scan EI spectra were obtained from 30-400 amu.

3.3 Result and Discussion

3.3.1 Synthesis of CIS Nanoparticles

The synthesis of nanoparticles from elemental metals using amine-thiol chemistry proceed under two regimes, metal thiolate formation and their thermal decomposition to metal

chalcogenides. The formation of metal thiolate species takes place via the reaction of a metal with an amine-thiol solution. Our group has reported elsewhere the solution chemistry of elemental indium and copper after reactive dissolution with a monoamine and dithiol solution.[32] The species formed from these dissolutions were identified as an alkylammonium bis(1,2-ethanedithiolate) indium (III) complex and alkylammonium high nuclearity copper (I) thiolate clusters in the case of indium and copper dissolutions respectively. These species have shown high solubility in the bulk amine-thiol solution, making a homogenous precursor that does not require any additional purification. Traditionally, a mixture of ethylenediamine and ethanedithiol is used for the dissolution of pure metals and subsequent fabrication of thin film metal chalcogenides. However, in this work a mixture of propylamine and ethanedithiol is used for pure metal dissolution due to propylamine's higher volatility as compared to ethylenediamine (ethylenediamine b.p. 116°C, propylamine b.p. 47.8°C), allowing for better removal through volatilization during high temperature nanoparticle synthesis. This prevents short chain ligands from binding, which may compromise colloidal stability. For CIS nanoparticle synthesis, copper and indium were dissolved together in PA-EDT solution as described in the experimental section. The completion of metal thiolate formation was indicated by disappearance of metal powders and a color change to a clear pale yellow/orange solution. In the second regime, the dissolved metal thiolates were thermally decomposed in the presence of a coordinating solvent to create a colloidally stable nanoparticle suspension. Oleylamine was selected as the coordinating solvent for reaction due to its wide use in colloidal syntheses of copper based metal chalcogenide nanoparticles.[4] Oleylamine's high boiling point of ~350°C and excellent thermal stability allow for high temperature synthesis. Additionally, its long carbon chain length affords excellent colloidal stability through steric hindrance between nanoparticles while strongly coordinating to the nanoparticle surface via the nitrogen lone pair on the amine.[33]

Hot injection is a commonly used approach for the synthesis of CIS nanoparticles.[1,4] The hot injection approach was explored using the procedure described in the experimental section whereby the metal thiolate precursor diluted with OLA was injected into preheated OLA. After a swift injection, the reaction was held at 250°C for a duration of one hour followed by natural cooling. Purified particles were obtained from this reaction mixture following a particle washing process as explained in the experimental section. The XRD spectrum for synthesized particles is shown in Figure 3.1a, confirming the formation of CIS material. The absence of any binaries was

further confirmed via Raman analysis (Figure 3.1c), and an average particle size of around 6-8 nm was observed from the TEM image of these particles (Figure 3.1b). The traditional hot injection method is generally considered to suffer from poor scalability due to mixing concerns in high volume reactions, and irreproducibility concerns from the injection itself. These concerns are largely mitigated while using the developed amine-thiol approach. Especially, the intermixing of separate metal cation and sulfur solutions is eliminated due to the covalently bonded metal centers with sulfur atoms in the metal thiolate precursors.

Despite the success with this improved hot injection route, the reaction conditions like the local concentration at the point of injection and the impact it has on ligand coordination may affect the reaction kinetics as the result of mixing dynamics. An alternative experimental technique that is widely considered more scalable than the hot injection method is a one pot heat up method, which has demonstrated easily scaled reactions with greater than gram scale syntheses of metal chalcogenide nanoparticles. To study the one pot heat up synthesis of CIS nanoparticles using amine-thiol precursors, reaction parameters were chosen as described in the experimental section. Unlike hot injection experiments for CIS nanoparticles where the CIS precursor is exposed to high temperature (250°C) very rapidly resulting in immediate nucleation of nanoparticles, the heat up process exposes the precursor solution to various increasing temperatures over a much longer time scale. During this heat up process, the initially clear pale yellow/orange reaction mixture turned transparent dark yellow at around 120°C and at approximately 140°C, the reaction mixture turned dark brown/black suggesting the nucleation of nanoparticles. The reaction was ramped to 250^{o}C and maintained at this temperature for 1 hour. Although this approach is suitable for large scale batch reactions, it tends to form slow-to-consume binary phases at temperatures below the reaction dwell temperature and affect the properties of synthesized particles.[18] However, the resultant XRD spectrum (Figure 3.1a) and Raman spectrum (Figure 3.1c) for synthesized particles confirm formation of CIS material without any binary phases with average particle size in the range of 6-8 nm, similar to that of hot injection method (Figure 3.1b).

Another scalable synthetic method based on heat up principles is microwave assisted solvothermal reaction which was utilized to demonstrate flexibility in nanoparticle synthesis routes from amine-thiol precursor solutions. To avoid the over pressurization of the reaction vessel, a metal precursor ink for this reaction was formulated using OLA-EDT instead of PA-EDT as described in the experimental section. Due to the equipment limitation, the reaction was carried

out at slightly lower temperature (i.e. 225°C instead of 250°C) for 15 min, resulting in smaller particle sizes (< 5nm) as can be seen from Figure 3.1 b. The XRD for these particles (Figure 3.1a) show a broader peak at 27.9° with the absence of a peak near 32.3° when compared to heat up and hot injection particles. This variation in XRD spectrum could result from increased FWHM due to smaller particle size or formation of wurtzite phase CIS, possibly due to the different reaction conditions such as lower initial thiol volume, high pressure, rapid heating, retention of volatile species (notably thiols), etc. The Raman spectrum of these particles also supports formation of CIS but with reduced crystallinity observed from peak broadening for A1 mode of CIS particles at 294 cm^{-1} (Figure 3.1c).

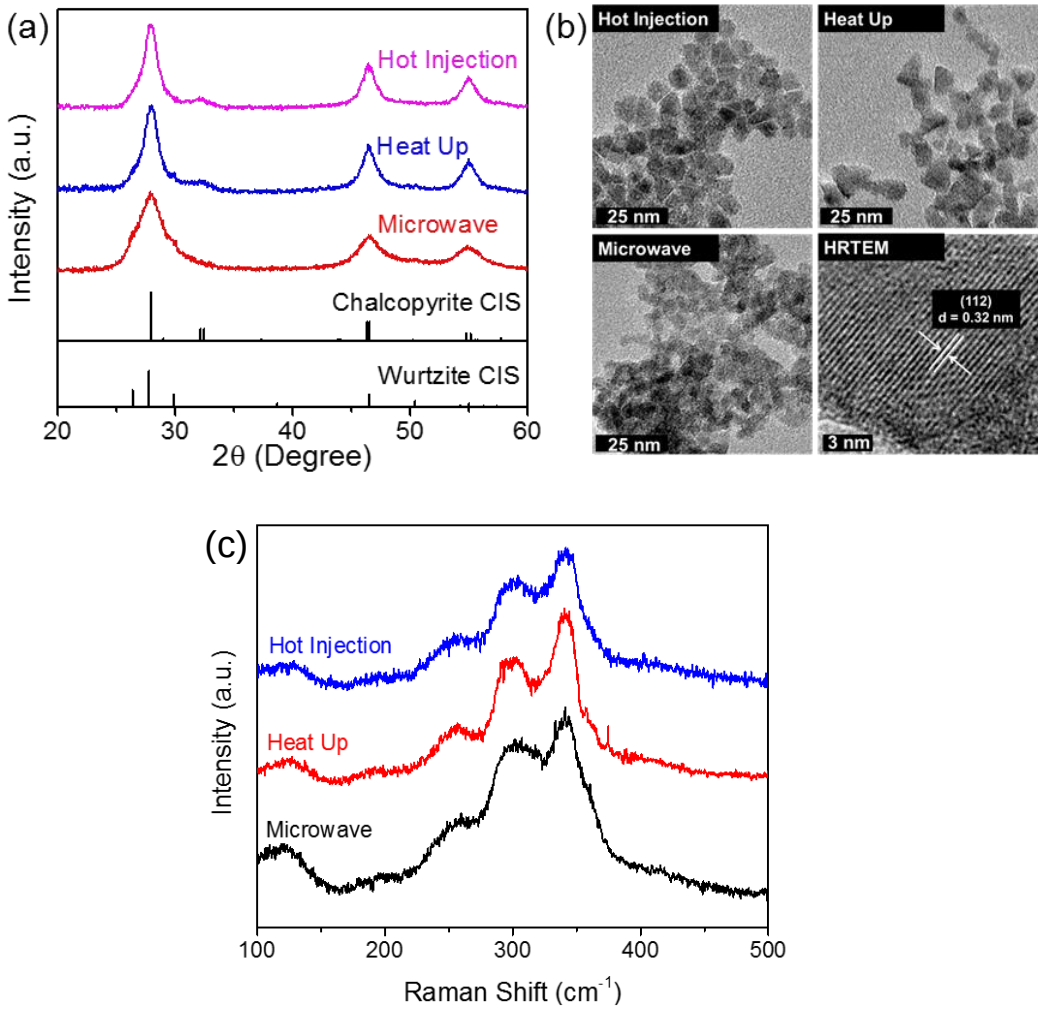

Figure 3.1. (a) XRD analysis, (b) TEM images (HRTEM image on bottom right corresponds to heat up synthesized CIS nanoparticles, chalcopyrite and wurtzite phase CIS standards with ICSD

collection code 186714 and 163489 respectively), and (c) Raman spectra of CIS nanoparticles synthesized using hot injection, heat up and microwave assisted solvothermal reactions.

3.3.2 Metal Thiolate Decomposition Mechanism to Metal Chalcogenide Nanoparticles

The dissolution of metals in amine-thiol solutions have shown to form metal thiolate species which break upon heating to metal chalcogenide materials. Unlike CIS which has little to no solubility in amine-thiol solutions, binary chalcogenides including In_2S_3, Cu_2S, and CuS have reasonable solubility in amine-thiol solutions. This may suppress the nucleation of binary chalcogenides in the presence of ethanedithiol and oleylamine at temperatures below ethanedithiol's boiling point of 146°C, resulting in phase pure CIS nanoparticle synthesis. To understand the thermal decomposition mechanism of metal thiolates into metal chalcogenides, the exposure of an individual metal thiolate species to higher temperatures was investigated. This can be done by performing a reaction of either Cu or In thiolate at higher temperatures to form copper sulfide or indium sulfide respectively. As the indium thiolate complex in an amine-thiol solution is well defined, it was chosen to study the reaction mechanism and the effect of amine-thiol solvents on nucleation of binary metal chalcogenides.

The synthesis of binary indium sulfide was carried out at 285°C via the hot injection route as described in the experimental section. Immediate injection of the In-PA-EDT (diluted in OLA) ink in preheated OLA resulted in a vibrant yellow color suspension suggesting the formation of indium sulfide particles. Aliquots at different time intervals (5 min, 1 hr, 6 hr, and 18 hr) were collected for analysis after injection of the precursor ink. The XRD spectra collected on the particles obtained after purification are shown in Figure 3.2.

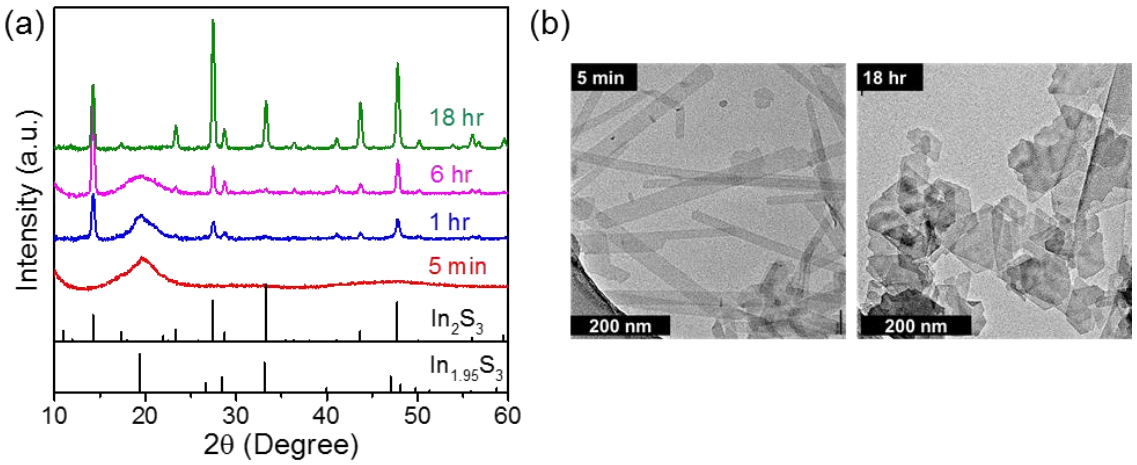

Figure 3.2. (a) XRD analysis and (b) TEM images of indium sulfide particles synthesized using hot injection route with different time aliquots showing amorphous to crystalline transition with time. (Tetragonal phase In_2S_3 and trigonal phase $In_{1.95}S_3$ standards with ICSD collection code 151645 and 244280 respectively)

The first aliquot taken 5 minutes after injection shows broad XRD peaks, indicative of the low crystallinity of the formed material. The peak centered at a 2θ of 19.5° matches closely to the trigonal crystal structure of $In_{1.95}S_3$. Subsequent aliquots show the conversion of trigonal crystal structure to tetragonal In_2S_3 crystal structure with complete phase purity achieved after maintaining the mixture at the reaction temperature for 18 hours. Compared to the ICSD standard for In_2S_3, the XRD spectrum of synthesized material shows different relative peak intensities which suggest a relatively different crystal orientation in the synthesized material.

Along with phase evolution with time, the indium sulfide nanoparticles formed via this route also show structural evolution from amorphous nano-wire-like structures (5 min reaction) to crystalline faceted 2D nano-sheet-like structures (18 hr reaction) as shown in Figure 3.2b. The conversion of $In_{1.95}S_3$ to In_2S_3 over 18 hours is suspected to be an effect of ethanedithiol quantity in the solution, while the increasing crystallinity could be attributed to the longer annealing times at the reaction temperature. It is hypothesized that the removal of ethanedithiol (which can act as a sulfur source during the reaction), due to boiling off from continuous heating at 285°C, could drive the sulfur reduction in the trigonal crystal structure resulting in tetragonal In_2S_3. This hypothesis was verified by injecting an indium ink with a reduced EDT quantity, prepared using PA:EDT mole ratio of 11:1 instead of 2:1, into OLA at 285°C. This injection resulted in a mixture of $In_{1.95}S_3$ and In_2S_3 after one hour of reaction with a relatively higher quantity of In_2S_3 as compared to the previous indium sulfide synthesis (Figure 3.3), specifying the role of thiol quantity on the phase of indium sulfide particles.

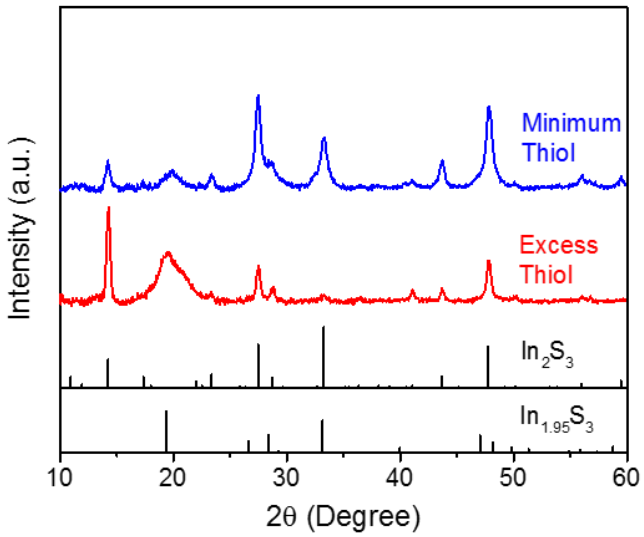

Figure 3.3. XRD analysis of indium sulfide particles synthesized using hot injection route for 60 min reactions with different thiol quantities. (Tetragonal phase In_2S_3 and trigonal phase $In_{1.95}S_3$ standards with ICSD collection code 151645 and 244280 respectively)

The effect of thiol quantity and its role in the formation of phase pure In_2S_3 was further exploited to understand the complete reaction pathway for converting metal thiolate species to metal chalcogenides. For this purpose, a microwave assisted solvothermal route, which has the ability to contain all the reaction products and byproducts in one sealed vessel, was used. The indium ink used for this reaction was prepared in OA-EDT mixture instead of PA-EDT mixture to maintain comparatively low pressure in the sealed reaction vessel when heating to 200°C. The amount of ethanedithiol used for the indium precursor preparation was the minimum required amount for dissolution according to the stoichiometry discussed by Zhao et al. to form phase pure In_2S_3 and to avoid binary redissolution after reaction completion.[32] This reaction was carried out for 15 min at 200°C via microwave heating followed by natural cooling to room temperature. The reaction mixture was then centrifuged in an inert atmosphere without the addition of an antisolvent to precipitate indium sulfide nanoparticles from solution. The supernatant obtained from this separation was analyzed using GC-MS to identify liquid and dissolved gas byproducts formed during the metal thiolate thermal decomposition. Octylamine, with an elution time of 11 minutes in the GC column, was a major component in the reaction mixture. To avoid its domination in GC spectra, the sample was analyzed up to a 10 min elution time. Results obtained from this analysis

are presented in Figure 3.4, showing three peaks in the GC spectrum at elution times of around 1.35 min, 2.1 min and 6.1 min.

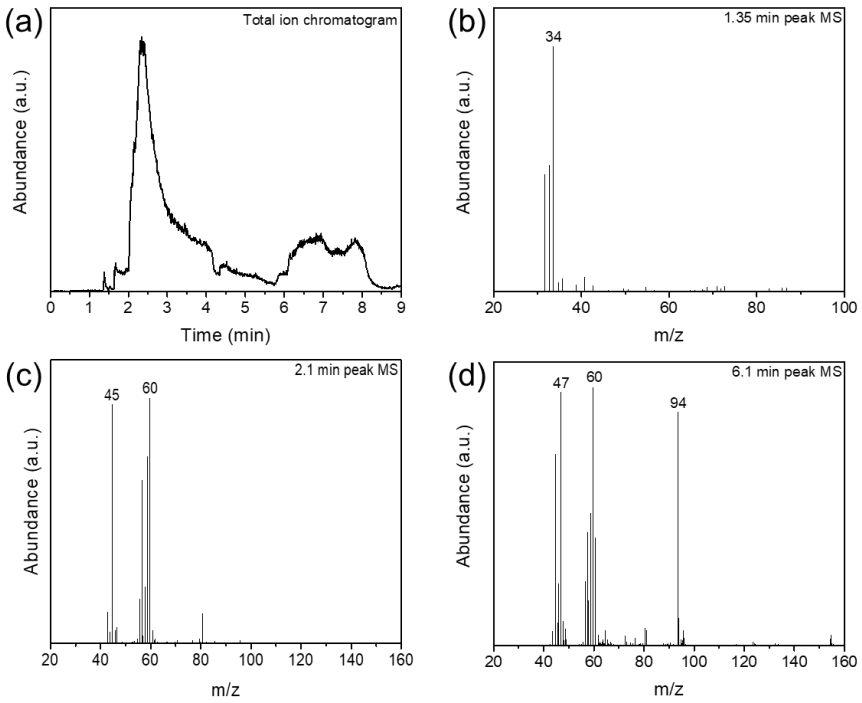

Figure 3.4. (a) Total ion chromatogram collected for indium-octylamine-ethanedithiol solution. Analyzed mass spectrum of isolated peak at elution time of (b) 1.35 min, (c) 2.1 min and (d) 6.1 min.

After analysis in the mass spectrometer, the peaks were assigned to H_2S, thiirane, and 1,2-ethanedithiol respectively. Based on the indium thiolate structure proposed by our group for an indium-hexylamine-ethanedithiol solution[32] in conjunction with the GC-MS analysis of reaction products, a balanced chemical reaction is proposed in Figure 3.5. This reaction demonstrates the clean decomposition of metal thiolate to metal chalcogenide and volatile byproducts that will quickly evaporate from the reaction mixture at high temperature, supporting the use of amine-thiol chemistry for impurity-free metal chalcogenide nanoparticles synthesis.

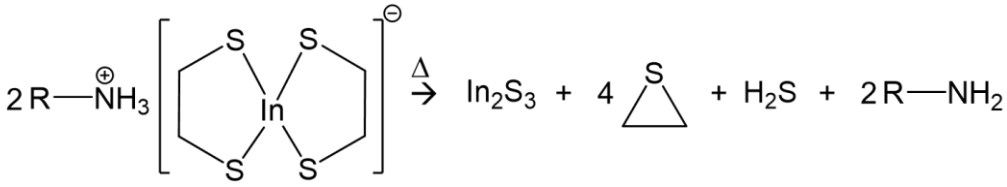

Figure 3.5. Proposed reaction mechanism for indium sulfide synthesis from an alkylammonium indium thiolate species.

In the case of ternary CIS nanoparticle synthesis, the copper complex is present alongside the indium complex. The decomposition of the copper-thiolate complex alone in OLA is found to form mixed phase copper sulfide material as verified by XRD (Figure 3.6).

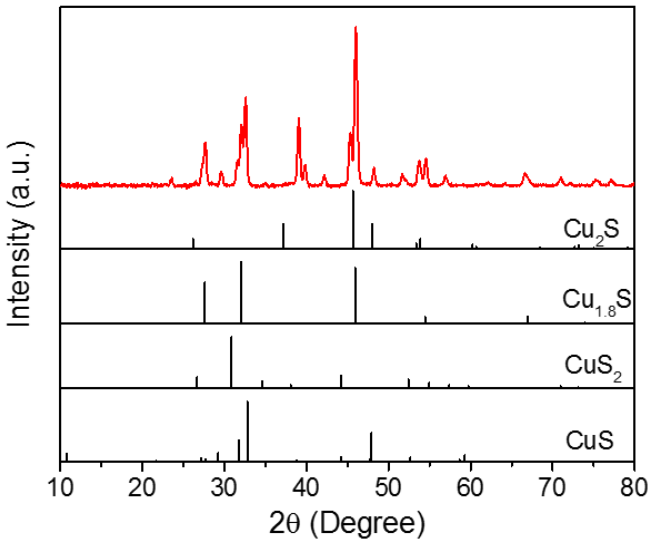

Figure 3.6. XRD analysis of nanoparticles synthesized via hot injection of Cu-PA-EDT ink in OLA showing formation of different phases of copper sulfides. (Cu_2S, $Cu_{1.8}S$, CuS_2 and CuS standards with ICSD collection code 200988, 95395, 100510 and 61793 respectively)

This multiphase copper sulfide formation could be attributed to the presence of variety of copper complexes in Cu-amine-thiol solution as opposed to well-defined single indium complex in In-amine-thiol solution as studied by Zhao et al.[32] Although multiple complexes were proposed for copper (I) thiolates, the structural motif for these structures is similar to the indium thiolate complex. So, it is expected that the copper species also undergo a similar decomposition pathway as indium species giving similar volatile byproducts. It is believed that the co-existence of copper and indium thiolate species in the solution directly nucleates the ternary phase CIS at relatively low temperatures of ~120-140°C, while keeping the binaries dissolved under the boiling point of ethanedithiol, demonstrating a viable reaction pathway to avoid deleterious binary formation.

Alloying:

In/Ga alloying:

Along with pure metal chalcogenides, alloyed materials formed via metal or chalcogen alloying provide tunability of various optoelectronic properties. In the case of CIS photovoltaics, alloying of indium/gallium, and selenium/sulfur has led to substantial improvements in photovoltaic power conversion efficiencies through bandgap tunability and grading. As such, metal alloying was investigated for the amine-thiol based synthetic methods developed in this report. Alloying was first tested with the incorporation of Ga into indium sulfide nanoparticles. From the available literature, the dissolution of gallium by the amine-thiol route has been possible only in the presence of selenium using diamine-dithiol mixtures, limiting the possibility of gallium containing pure sulfide materials.[34] However, in our group's work, it was discovered that gallium could be co-dissolved with indium in a monoamine-dithiol solution without selenium.[35] This enabled the novel preparation of indium gallium sulfide nanoparticles in this work. For these experiments, In+Ga solutions were prepared in PA-EDT mixtures at Ga/(In+Ga) mole ratios of 0.5 (50% Ga) and 0.9 (90% Ga) with a total In+Ga concentration of 0.4 M. A hot injection reaction (as described in the experimental section) was performed using these solutions for a duration of 1 hour at 285°C. XRD analysis of the resulting nanoparticles is presented in Figure 3.7, showing a shift in trigonal In_2S_3 peak and the presence of a new broad peak at around 30° suggesting the incorporation of gallium.

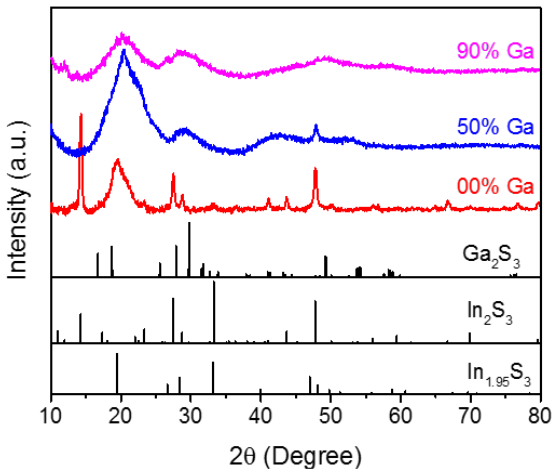

Figure 3.7. XRD analysis of indium-gallium sulfide particles synthesized using hot injection route with different gallium fractions. (Tetragonal phase In_2S_3, trigonal phase $In_{1.95}S_3$ and Ga_2S_3 standards with ICSD collection code 151645, 244280 and 409550 respectively)

The XRD obtained with Ga incorporation also shows the reduced crystallinity of the nanoparticles as compared to the pure indium sulfide. This variation is also observed in the particle morphology, where faceted 2D nano-sheet-like structures break down to nano-wire-like structures (Figure 3.8) with increasing Ga content.

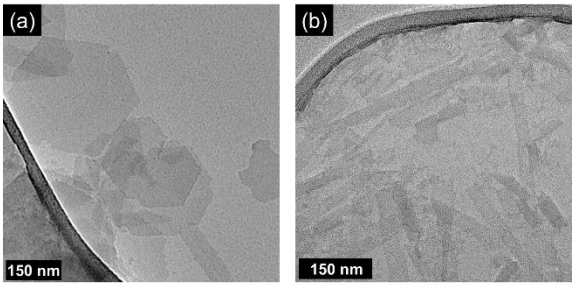

Figure 3.8. TEM images of indium-gallium sulfide nanostructures synthesized using hot injection with (a) 50% Ga and (b) 90% Ga fraction.

The lower crystallinity observed in Ga rich material is in agreement with the literature, as gallium sulfide materials are known to exhibit poor crystallinity, even up to synthesis temperatures of 400°C.[36] The incorporation of Ga in the bulk material was also analyzed using X-ray fluorescence, which confirmed the Ga/(Ga+In) ratio of 0.42 and 0.85 in final material for reactions with starting Ga/(Ga+In) ratio of 0.5 and 0.9 respectively. Although the bulk material showed incorporation of Ga, the amorphous nature of XRD makes it difficult to verify the presence of alloying in the material. The possibility of the formation of two different phases in the reaction, one with amorphous Ga_2S_3 and other with small In_2S_3 particles, cannot be completely ruled out based on the XRD pattern. So, to confirm the indium-gallium alloying, UV-Vis absorption spectroscopy was performed on thin films cast from suspensions of the purified nanoparticles as shown in Figure 3.9a. As the direct bandgap of pure In_2S_3 is ~2.1 eV and that of Ga_2S_3 is ~3.45 eV, the gradual increase observed in optical bandgap of $(In,Ga)_2S_3$ with increasing Ga content supports the formation of gallium alloyed indium sulfide nanoparticles and eliminates the possibility for discrete In_2S_3 and Ga_2S_3 formation. The homogeneity of Ga incorporation within single nanoparticle was further verified via STEM-EDS mapping of the material containing 50% starting Ga content and is shown in Figure 3.9b.

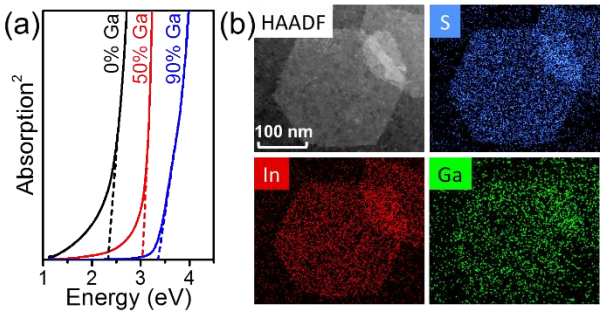

Figure 3.9 (a) Tauc plot for the data obtained through UV-vis absorption spectroscopy on indium-gallium sulfide nanoparticles with different gallium content. (b) STEM-EDS elemental mapping of indium-gallium sulfide nanoparticles containing 50% Ga.

To verify the observed uniformity is consistent among multiple nanoparticles, larger scale STEM-EDS was performed across multiple nanosheets as showin in Figure 3.10. Seemingly uniform distributions of In and Ga were observed.

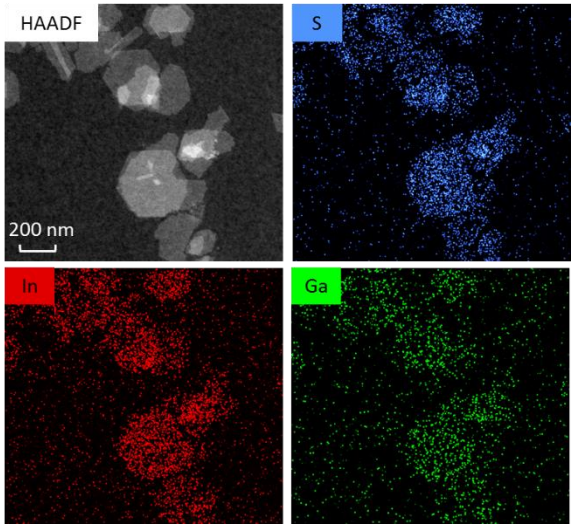

Figure 3.10. STEM-EDS elemental mapping of indium-gallium sulfide nanostructure containing 50% Ga showing uniformity of alloying within single particles as well as between multiple particles.

The thickness of one of these particles was observed in the range of 4-6 nm when measured using atomic force microscopy, which confirms the nano-sheet-like nature of this material (Figure 3.11).

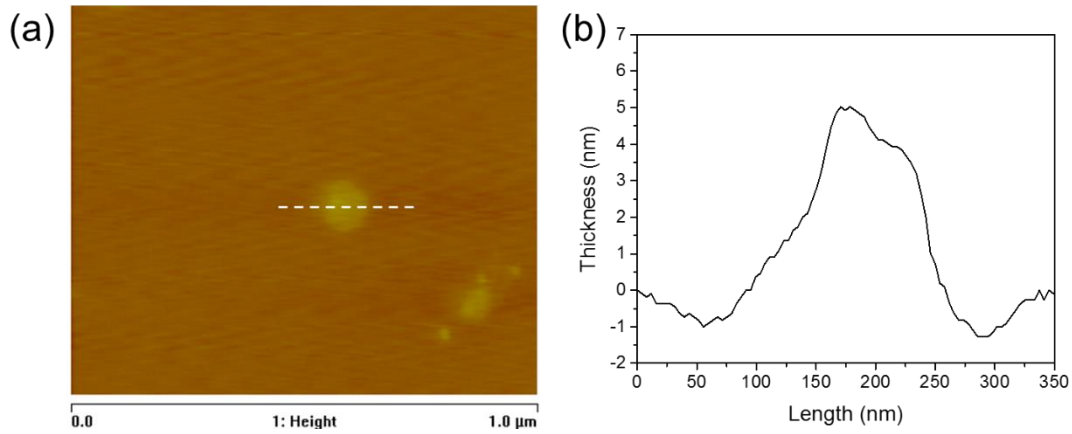

Figure 3.11. Atomic force microscopy on indium gallium sulfide nanostructure containing 50% Ga. (a) AFM image of the nanostructure (b) Plot showing thickness measurement of the nanostructure along the white dash line.

The successful alloying of gallium into indium sulfide was further applied to the ternary alloy system of CIGS using a one-pot heat up process similar to the aforementioned CIS nanoparticle synthesis. To study the incorporation of gallium and phase purity as a function of temperature, aliquots were collected at temperature intervals of around 25°C starting at 175°C to the final reaction temperature of 285°C. The Raman spectrum of the first aliquot collected at 175°C shows the absence of any binary metal chalcogenides and confirms the formation of CIS (Figure 3.12, black spectrum).

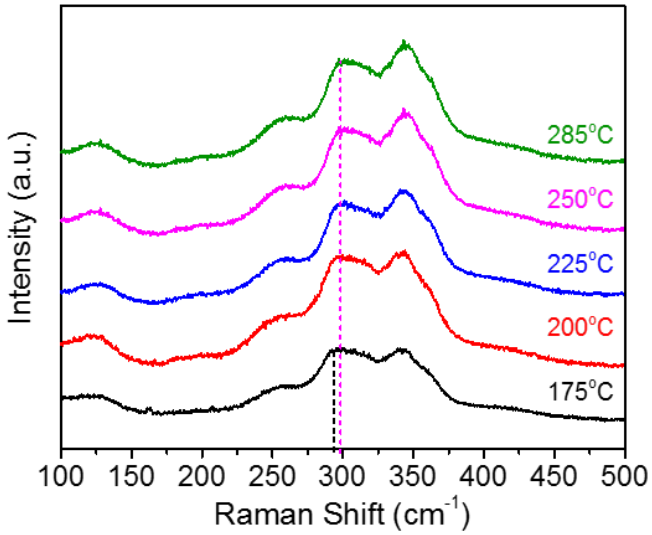

Figure 3.12. Raman analysis of CIGS nanoparticles during heat up process, showing incorporation of gallium in CIS structure as a function of temperature.

The XRD peak near 2θ of 46.5° shows a gradual shift towards higher angle demonstrating the incorporation of Ga into the CIS crystal structure as a function of temperature (Figure 3.13a). This Ga incorporation was further confirmed by analyzing the bulk composition of purified particles using X-ray fluorescence technique (Figure 3.13b). While at 175°C, very little gallium had incorporated into the nanoparticles, by 285°C, XRF analysis confirmed that the CIGS nanoparticles achieved the target composition of Ga/(Ga+In) = 0.3. As is consistent in other CIGS synthetic pathways, gallium incorporation indeed requires higher temperatures than CIS nanoparticle formation.[4] However, for this study, aliquots were taken during heat up process with no dwell time at each temperature. Additional dwell time at lower temperatures may provide a route to form the targeted CIGS composition without heating to higher temperatures.

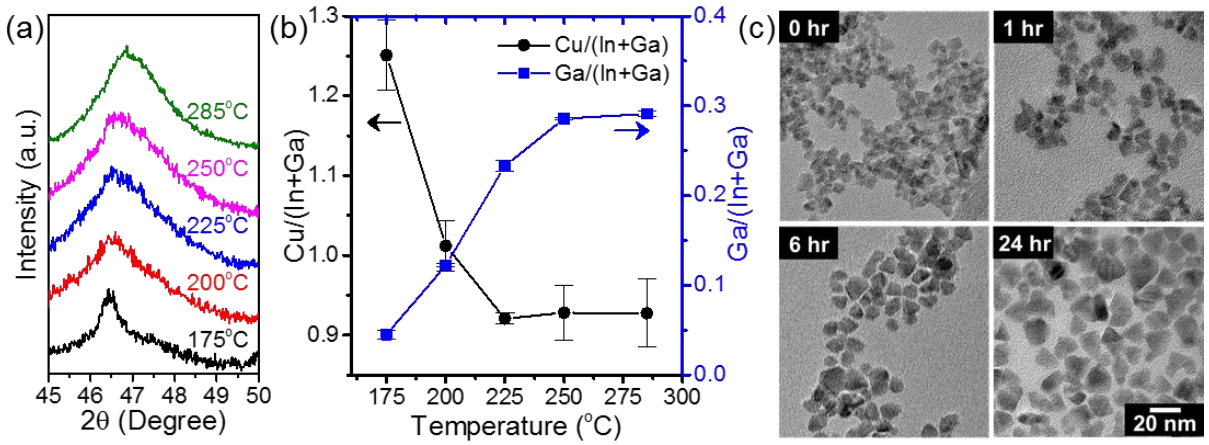

Figure 3.13. (a) XRD analysis focused on a peak near 2θ of 46.5° and (b) Plot summarizing X-ray fluorescence analysis on CIGS nanoparticles showing gallium incorporation as a function of temperature. (c) TEM images of CIGS nanoparticles showing size variation as a function of time.

Along with the effects of the gradual increase in reaction temperature on particle composition, the size of the particles was also studied with respect to time. After reaching the reaction temperature of 285°C, aliquots were collected at t = 0 hr, 0.5 hr, 1 hr, 3 hr, 6 hr, 12 hr, and 24 hr. The average nanoparticle size analyzed via transmission electron microscopy (Figure 3.13c) and XRD (Figure 3.14) shows a gradual increase in particle size with respect to time, reaching an average particle size of >15nm for the 24 hr reaction.

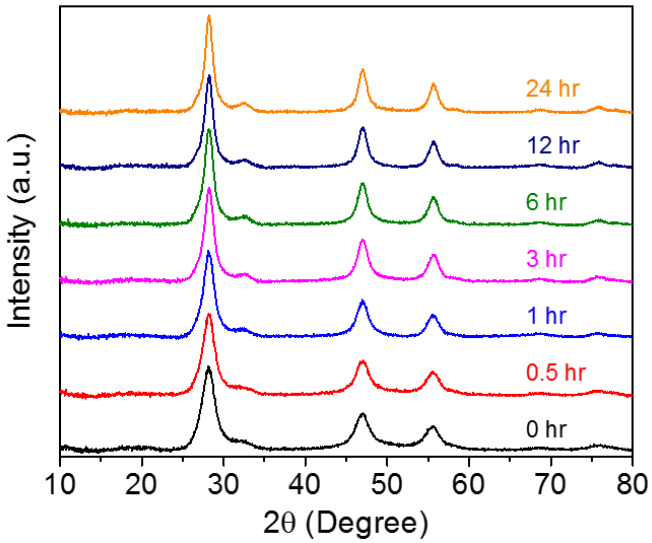

Figure 3.14. XRD analysis of CIGS nanoparticles synthesized using heat up route with different time aliquots showing reduced FWHM of peaks corresponding to increased particle size.

The CIGS particles formed via this amine-thiol route have shapes and size distributions similar to the previously discussed CIS syntheses. While the bulk composition of the synthesized nanoparticles measured by XRF shows that the targeted composition was reached, the elemental uniformity within single particles was analyzed using STEM-EDS. The elemental mapping obtained for 3 hr reaction particles from STEM-EDS analysis of two adjacent particles is shown in Figure 3.15, which confirms elemental uniformity between two particles as well as within a single particle.

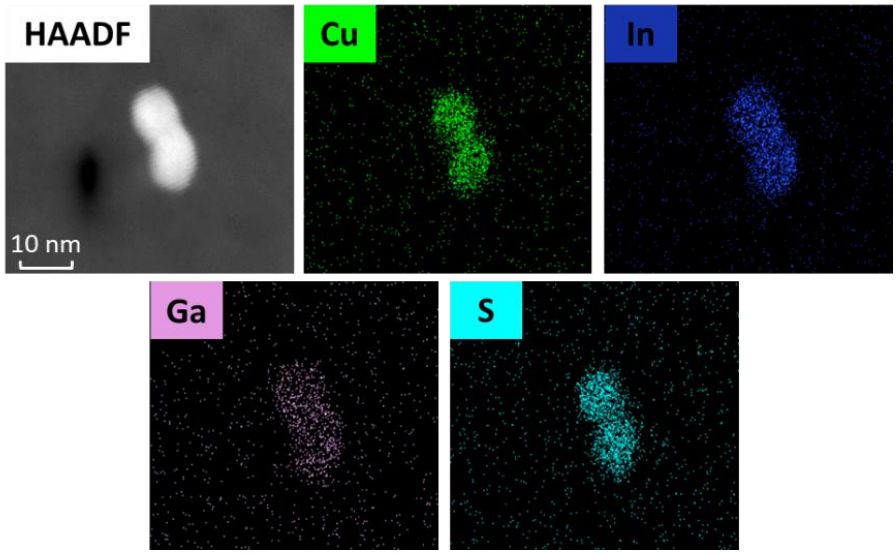

Figure 3.15. STEM-EDS elemental mapping of CIGS nanoparticles containing Ga/(Ga+In) of 0.3, showing elemental uniformity within single particles as well as between multiple particles.

The particles were also analyzed via FTIR and ^{1}H-NMR techniques, confirming the presence of oleylamine on the particle surface acting as a ligand (Figure 3.16).

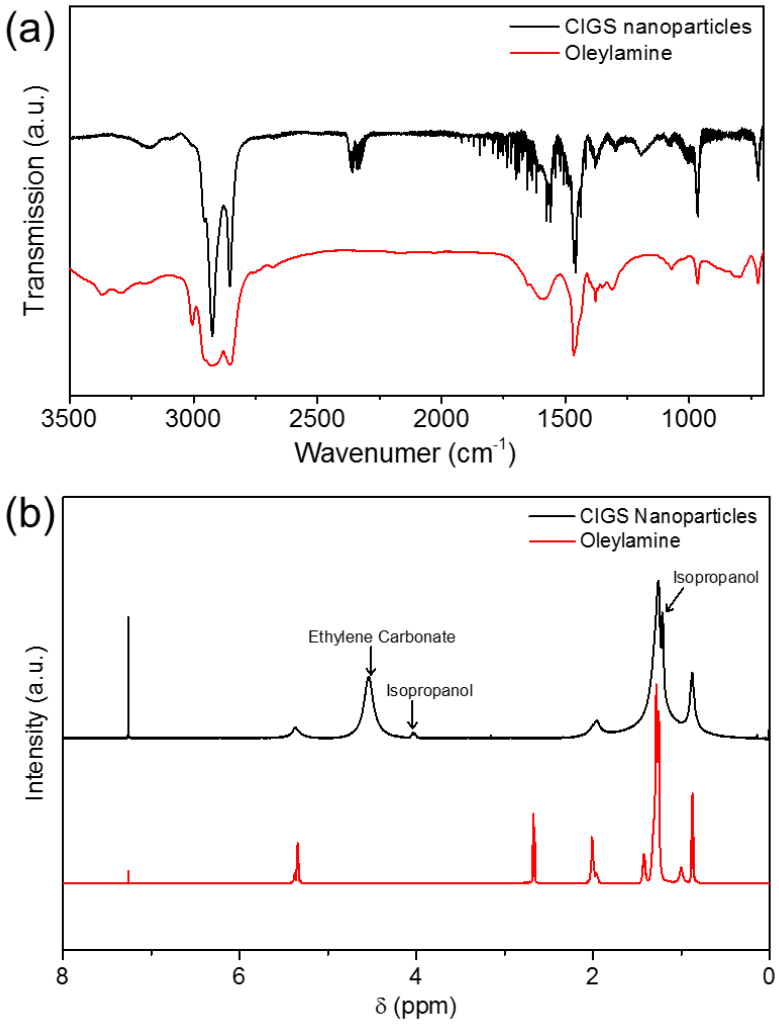

Figure 3.16. (a) FTIR analysis and (b) ^{1}H-NMR analysis of CIGS nanoparticles synthesized using heat up route confirming the presence of oleylamine on particle surface.

This provided a stable particle suspension in nonpolar (or very low polarity) solvents like toluene under an inert atmosphere for well over 6 months with no visible settling, exemplifying the excellent colloidal stability of the nanoparticles.

S/Se alloying:

Similar to metal alloying, chalcogen alloying of various semiconducting materials also provide tunability in material properties. In the case of CIS, incorporation of Se into the CIS crystal structure reduces the bandgap of the material from 1.5 eV for the pure sulfide to 1.0 eV for the pure selenide.[37] As the amine-thiol solvent system also dissolves pure chalcogens, it provides additional benefits over traditional synthesis routes for metal selenide nanoparticles,[27] which often rely on alkyl-phosphines for dissolution.[1,4] Utilizing the elemental Se dissolution ability of the amine-thiol system, CISSe nanoparticles were synthesized through a one pot heat up process. The formation of sulfur-free selenides through the pure metal amine-thiol route is challenging and relies on excess selenium in the reaction mixture due to the covalent bonding between the metal atom and the sulfur in the metal thiolate complex. To study the incorporation of Se in the metal chalcogenide structure, various quantities of Se powder were dissolved in the CIS solution prepared in PA-EDT solvent to obtain Se/(Cu+In) ratios of 0, 0.5, 1, and 2 in the precursor ink. The XRD analysis of synthesized particles is presented in Figure 3.17.

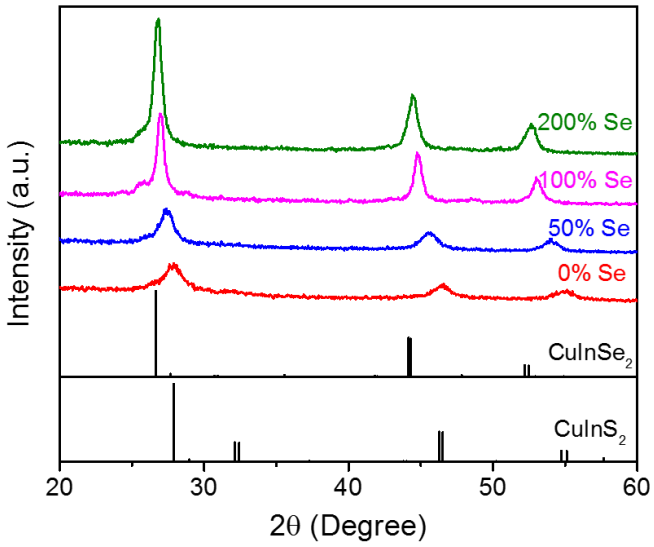

Figure 3.17. XRD analysis on CISSe nanoparticles as a function of Se quantity. (Chalcopyrite phase CIS and CISe standards with ICSD collection code 186714 and 73351 respectively)

A zoom in of the XRD region near a 2θ of 27° (112 plane) demonstrates a distinct shift as the material transitions from sulfide to selenide with increasing selenium quantities while a simultaneous transition from sulfide to selenide peaks in Raman is shown in Figure 3.18.

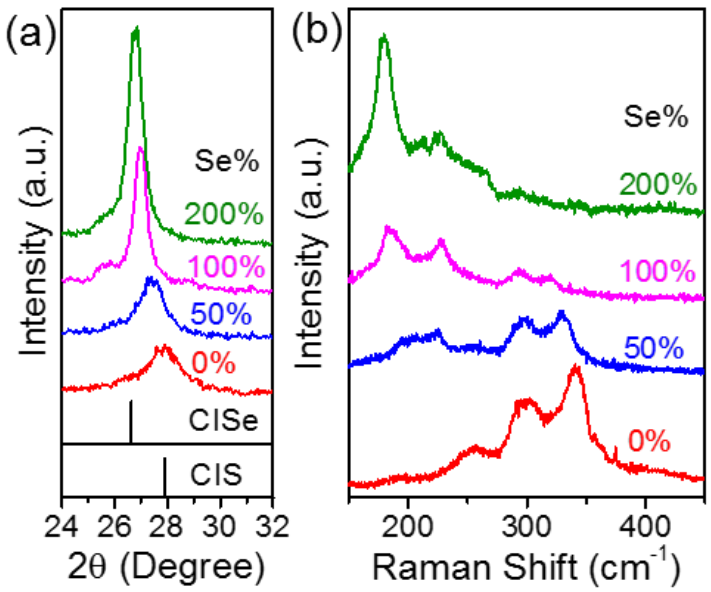

Figure 3.18. (a) XRD analysis, focused on a peak near 2θ of 27º (Chalcopyrite phase CIS and CISe standards with ICSD collection code 186714 and 73351 respectively) and (b) Raman spectroscopy analysis on CISSe nanoparticles as a function of Se quantity.

The disappearance of CIS Raman peaks at around 294 cm^{-1} and 340 cm^{-1} with increasing Se content in the reaction mixture and the simultaneously increasing intensity of CISe peaks at 180 cm^{-1} and 228 cm^{-1}, confirms the transition of pure CIS to a sulfur poor CISSe nanoparticles. XRF analysis performed on these particles also supports this trend with Se/(Cu+In) ratios of 0, 0.44, 0.75, and 0.92 obtained for starting Se/(Cu+In) ratios of 0, 0.5, 1, and 2 respectively. The elemental mapping of CISSe nanoparticles with Se/(Cu+In) ratio of 0.92 is shown in Figure 3.19, which confirms uniform incorporation of Se and the presence of residual S in the particles.

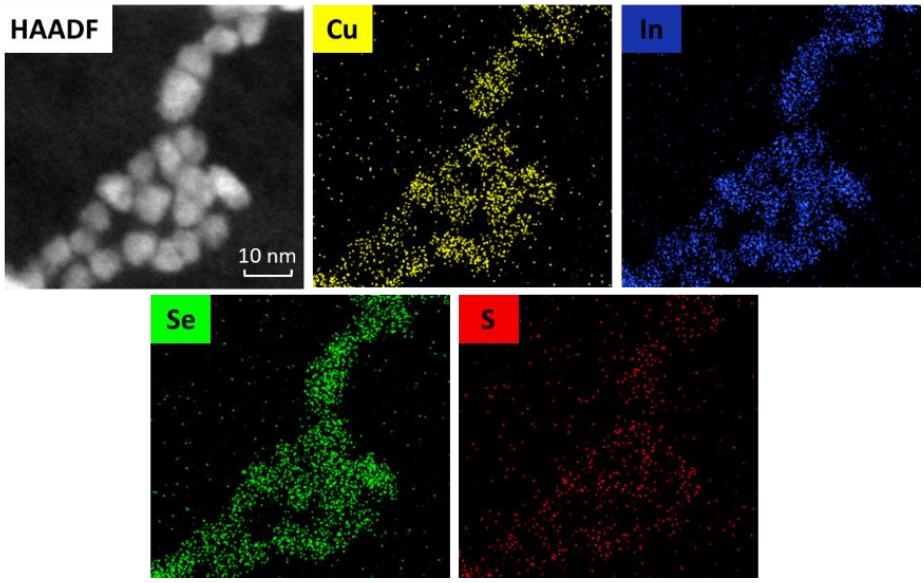

Figure 3.19. STEM-EDS elemental mapping of CISSe nanoparticles synthesized with reaction containing Se/(Cu+In) ratio of 2, showing elemental uniformity within single particles as well as between multiple particles.

It is expected that additional increases in the Se/(Cu+In) ratio in starting precursor will drive the reaction to increasingly pure selenide material. While reaction time was not extensively studied for selenium alloying, longer reaction times may also allow for more complete incorporation of selenium into the synthesized material.

3.3.3 Versatility of Synthesis Route

Synthesis of CZTS nanoparticles

Due to the high demand and scarcity of indium, the search for earth-abundant metal chalcogenide photovoltaic materials led to the development of the CZTS material system which is analogous to the CIGS system. The chemistry explored for the synthesis of binary indium sulfide, indium gallium sulfide and ternary CIS, CIGS, CISSe was applied to the quaternary system of CZTS as the pure Zn and Sn metals are soluble in the amine-dithiol mixture. A CZTS nanoparticle synthesis was performed via a heat up process as explained in the experimental section. As many traditional syntheses of CZTS material in OLA are carried out at 250°C, the same temperature was chosen for this reaction. The reaction was carried out for a total of 3 hours after the reaction mixture had reached 250°C. After purification, the nanoparticles were analyzed via XRD, Raman, and

STEM-EDS analysis. The XRD spectrum collected on these particles confirms the formation of kesterite phase CZTS nanoparticles (Figure 3.21a). These particles are smaller in size when compared to previously synthesized CIS particles synthesized under similar reaction conditions. TEM of the CZTS nanoparticles is shown in Figure 3.21b. Traditionally, syntheses of CZTS nanoparticles are known to form compositional inhomogeneities with particle size distribution. Various approaches including longer reaction time, size selective particle separation, change in precursor injection sequence etc. were adopted to reduce this inhomogeneity.[31,38,39] Unlike these syntheses, the nanoparticles obtained for the CZTS system using the chemistry in this work show reduced polydispersity suggesting better homogeneity in particle composition, possibly due to metal-sulfur covalent bond in the precursor solution. This uniformity is also supported by elemental mapping of CZTS particles obtained via STEM-EDS analysis 3.20b.

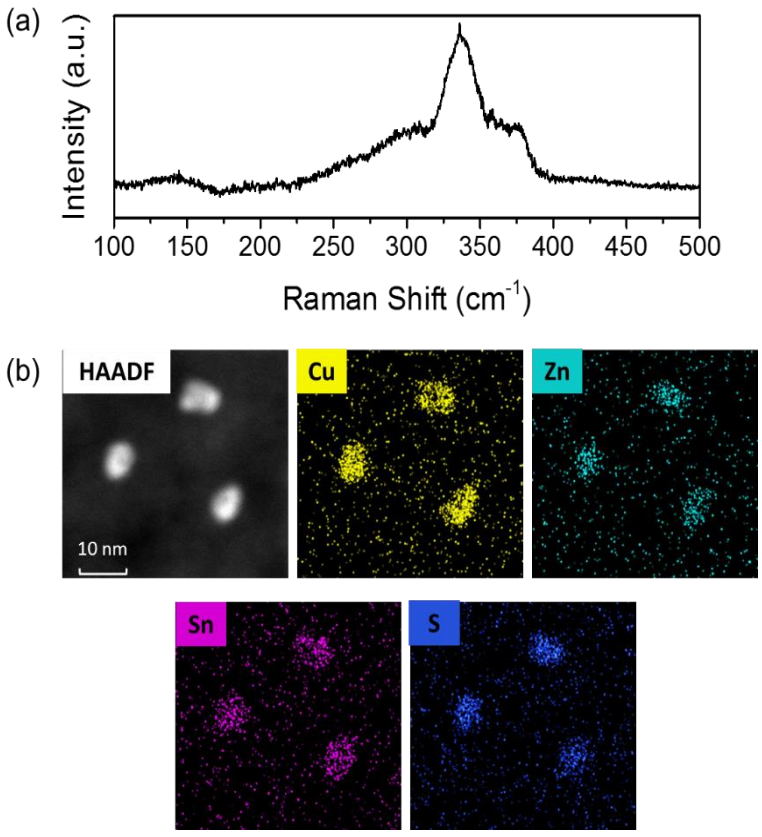

Figure 3.20. (a) Raman Spectroscopy analysis and (b) STEM-EDS elemental mapping of CZTS nanoparticles.

The Raman analysis showin in Figure 3.20a also confirm the formation of CZTS material with characteristic peaks observed at 289 cm^{-1}, 339 cm^{-1} and 374 cm^{-1} dominating the spectrum. Due to the very similar Raman spectra of Cu_2SnS_3 (CTS) and CZTS, and also the presence of a possible minor peak at 356 cm^{-1}, the coexistence of a secondary CTS phase in the nanoparticles cannot be ruled out. This secondary phase, if present, is commonly observed for CZTS nanoparticle synthesis.[31]

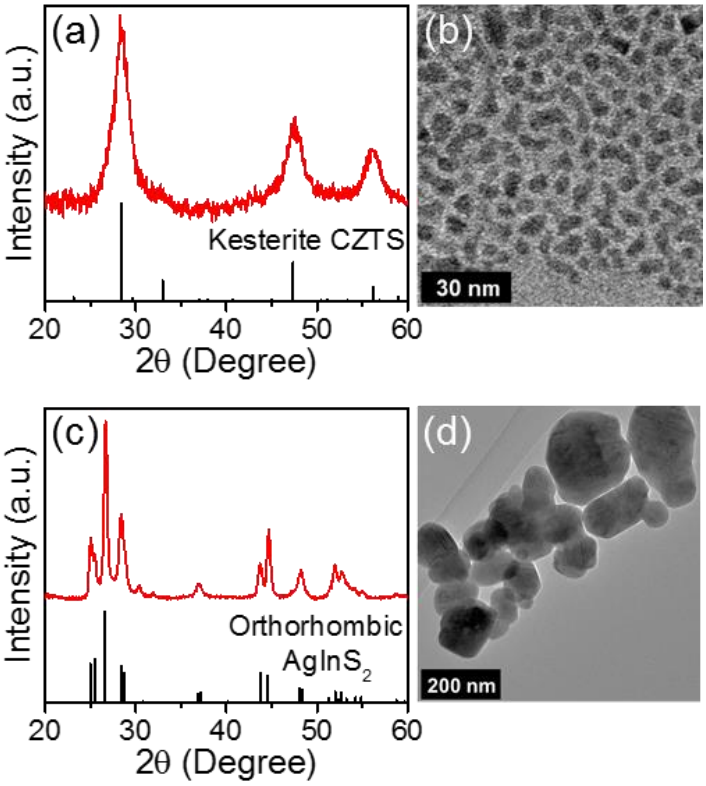

Figure 3.21. (a) XRD analysis (simulated kesterite phase CZTS standard obtained from JCPDS 26-0575) and (b) TEM image of CZTS nanoparticles. (c) XRD analysis (Orthorhombic phase $AgInS_2$ standard with ICSD collection code 51618) and (d) TEM image of $AgInS_2$ nanoparticles.

Using Metal Chalcogenide Precursors

Interestingly, it was found that high purity copper (>3N) was extremely difficult to dissolve, and its dissolution only marginally took place over several weeks in PA-EDT solutions. Typically, nanopowders of copper were used as a feedstock to ensure dissolutions over the course of days as opposed to weeks. However, these as received nanopowders of copper typically contained a small fraction of surface oxide, which is not ideal in the pursuit of impurity-free feedstocks (Figure

3.22a). It is unclear whether the higher reaction/dissolution rate was purely a function of nanoparticle size or if the small oxide content catalyzed the reaction and is currently the topic of further study. Because metal sulfides are known to be readily soluble in amine-thiol solutions, the copper nanopowder was easily replaced with high purity (4N) copper (I) sulfide, which did not contain any appreciable oxide content (Figure 3.22b).

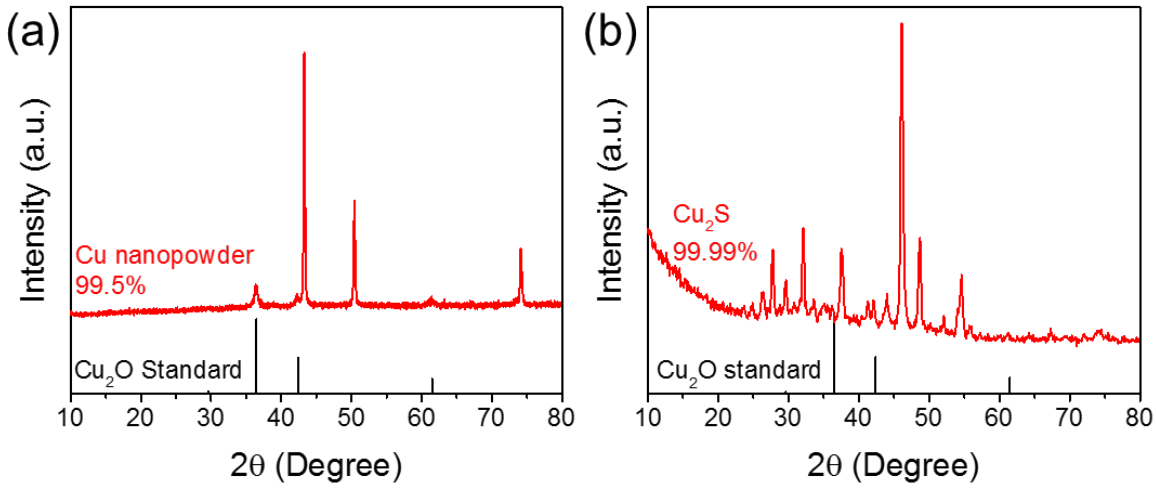

Figure 3.22. XRD analysis on as received (a) 99.5% pure Cu nanopowder showing presence of Cu_2O material and (b) 99.99% pure Cu_2S powder showing absence of Cu_2O materials.

It was found that copper sulfide was rapidly soluble in propylamine-dithiol mixtures. Higher solubility and higher dissolution rates were observed when Cu_2S was dissolved separately from In/Ga. The Cu_2S and In/Ga precursor solutions were mixed after complete dissolution yielding a 0.8M (Cu based) solution of Cu_2S, In, and Ga complexes. The mixed metal sulfide/pure metal precursor solution was used under identical reaction conditions as the previous CIGS heat up reactions from pure metal precursor solutions. Slightly different reactivity was observed when using copper sulfide as a precursor, with the initial color change from a transparent yellowish solution to a dark blackish brown suspension observed between 90-110°C as opposed to 120-140°C for the pure metal precursor case. It is hypothesized that the additional sulfur in solution from the Cu_2S precursor as compared to the pure metal case may enhance the net reactivity and may initially form CIS at a lower temperature. XRD and Raman spectra, collected on purified nanoparticles obtained after 3 hr of reaction, as shown in Figure 3.23, confirm the presence of

phase pure chalcopyrite CIGS nanoparticles and the TEM image of these particles also show similar average size compared to nanoparticles synthesized from pure metal precursor inks.

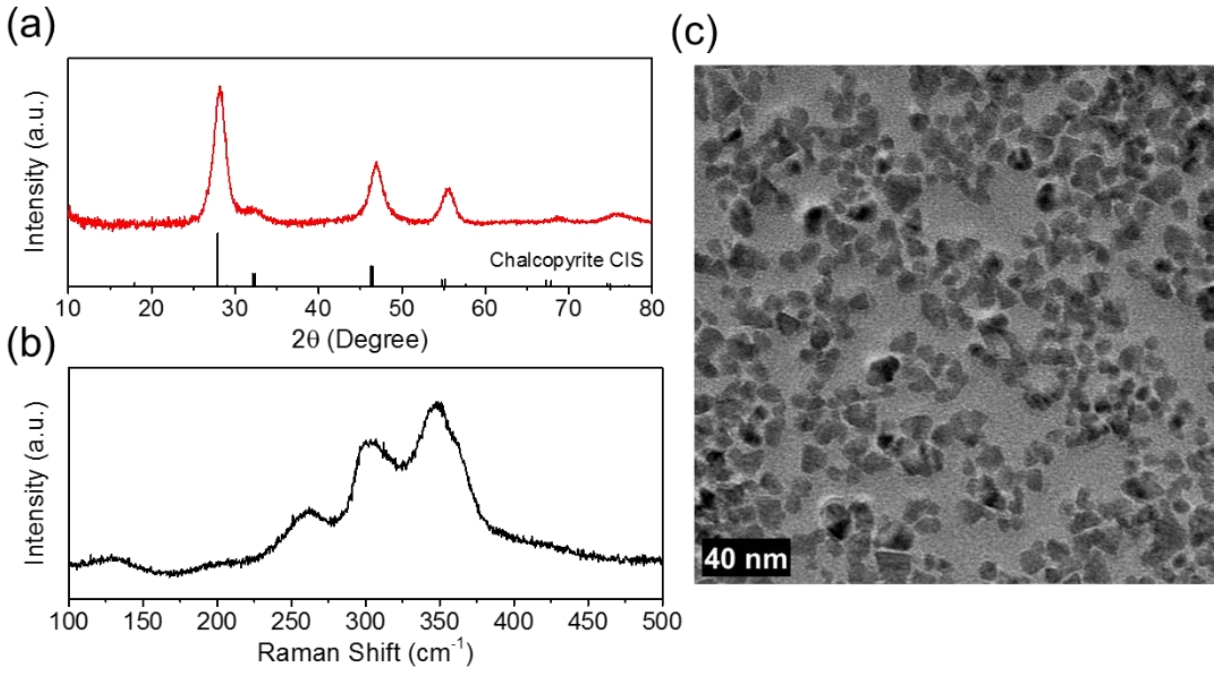

Figure 3.23. (a) XRD analysis, (b) Raman analysis and (c) TEM image of CIGS nanoparticles synthesized via heat up route using Cu_2S precursor instead of elemental Cu. (Chalcopyrite phase CIS standards with ICSD collection code 186714)

Like previously observed, the size of the nanoparticles would be modified through changing the duration of the reaction time. By varying the reaction time from 0 hours (counted from when the reaction mixture reached the 285℃ setpoint after heatup) to 4 hours, the nanoparticle size could also be varied. As shown in Figure 3.24, a clear increase in nanoparticle size is observed as a function of dwell time at reaction temperature.

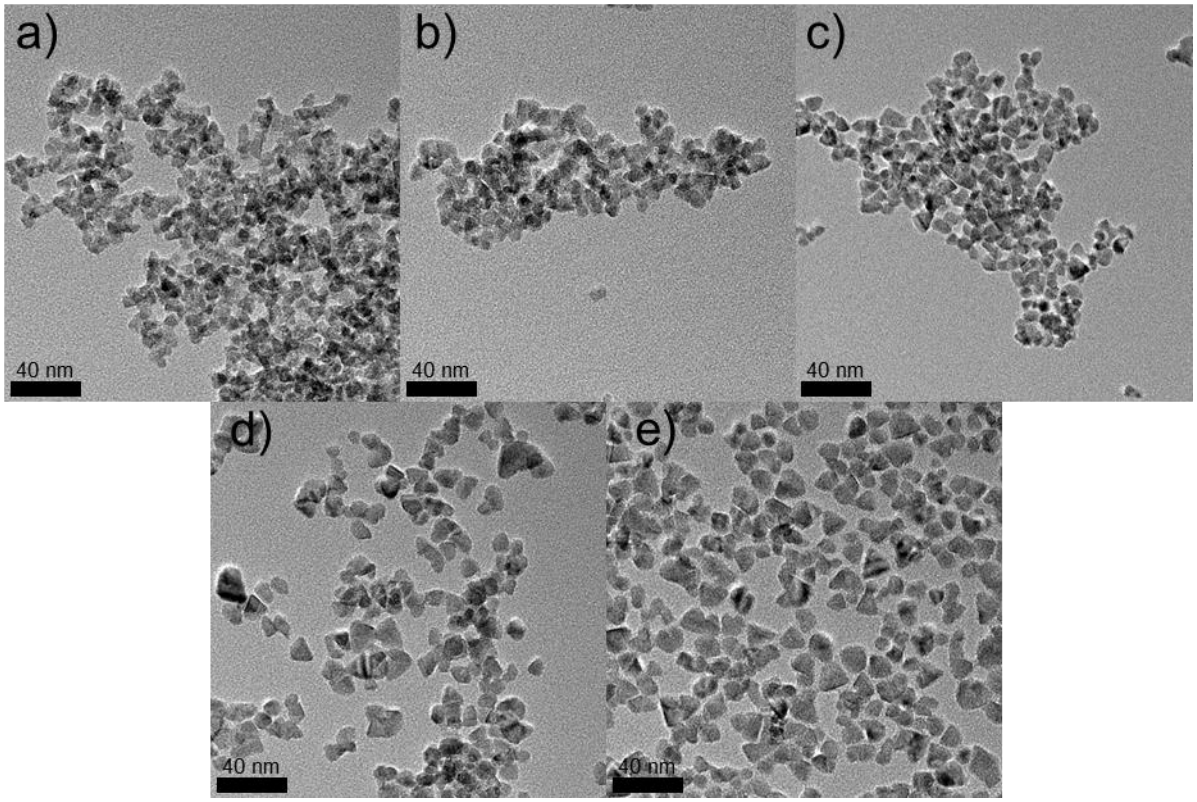

Figure 3.24. Heat up Cu(In,Ga)S_2 nanoparticle synthesis using Cu_2S, In, and Ga at 285°C, aliquots withdrawn at a) 0 hr, b) 1 hr, c) 2hr, d) 3hr, and e) 4 hr.

Further, it was observed that the colloidal stability and degree of aggregation was higher for short reaction times, the 0 and 1 hr cases, which can be seen by the small interparticle separation. Typically, smaller nanoparticles have higher surface area, and therefore a higher mass percentage of ligand. This should allow for increased resistance to settling by gravity, however, the observed aggregation caused the 0 hr ink to be prone to settling over the course of a week. The mechanism behind the poor colloidal stability of the 0 hr reaction is not fully known, but has been observed consistently using this synthetic method.

The use of metal sulfides in place of pure metals is also advantageous in the case where the pure metal is insoluble in amine-thiol solutions. This was demonstrated for the synthesis of $AgInS_2$ nanoparticles. Although there have been reports on co-dissolution of silver with copper, zinc and tin precursors in diamine-dithiol solution, [40] we observed no solubility of pure silver with or without indium in amine-thiol solution. In its place, we find that Ag_2S can be solubilized in under a minute at room temperature using PA-EDT solutions at a concentration of 0.8M (Ag based). Synthesis of $AgInS_2$ was performed by mixing precursor inks of Ag_2S-PA-EDT and In-PA-EDT.

These precursor inks were diluted with OLA and used for a hot injection reaction at 250°C for one hour. The XRD obtained for these particles supports the formation of orthorhombic $AgInS_2$ system as can be seen from Figure 3.21c. A very weak diffraction signal observed at 30.3° does not correspond to orthorhombic $AgInS_2$, rather it represents a marginal presence of tetragonal phase $AgInS_2$. Unlike CIS nanoparticles, the particles obtained for $AgInS_2$ system are bigger and polydisperse with sizes in the range of 50-200nm (Figure 3.21d). The effect of various Ag precursors and their corresponding reactivity resulting in diverse as well as larger particle morphology has been studied in a literature[41] which suggests the possibility of greater reactivity of Ag-amine-thiol precursor as compared to traditional Ag salt precursors. Further optimization of reaction conditions such as temperature, time, solvent etc., is required for better control over the size of the particles.

Synthesis of Wurtzite Phase CIGS nanoparticles

While demonstrating the versatility of nanoparticle synthesis through the dissolution of variety metal precursors, this chemistry also provided a route to control the phase of a material via a change in the reaction conditions. As mentioned earlier, microwave assisted route for CIS nanoparticles suggested a possible formation of wurtzite phase which was suspected to be a result of different reaction conditions obtained in microwave assisted synthesis compared to normal heat up or hot injection route. The microwave assisted solvothermal route is in principle similar to heat up route except it has a faster heating rate, higher reaction pressure, and volatile byproducts are retained in the sealed vessel. To identify the role of heating rate in the formation of wurtzite phase material, another heat-up synthesis was carried out for CIGS nanoparticles with a faster heating rate under ambient pressure. The heating rate used during the aliquot experiment in the previous section for chalcopyrite CIGS nanoparticles was on average 4.4°C/min. This rate was changed to an average value of 8.8°C /min and a similar aliquot time study was performed. The XRD analysis (Figure 3.24) of initial aliquots show similar spectrum to that of microwave assisted CIS nanoparticles with peak broadening at 2θ of 28.2° and absence of the peak at 2θ of 32.5° (note that these positions are different from CIS peak positions due to the incorporation Ga).

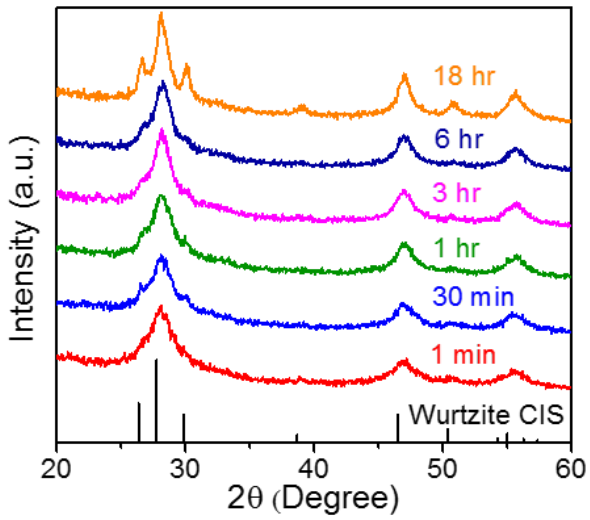

Figure 3.25. X-ray diffraction analysis on CIGS nanoparticles as a function of time synthesized via heat up synthesis with 8.8°C /min heating rate showing the formation of wurtzite phase. (Wurtzite phase CIS standard with ICSD collection code 163489)

Particles obtained after 18 hours of reaction showed 3 unique sharp peaks near 2θ of 28.2° and a new peak at around 2θ of 50.7°, confirming the formation of wurtzite phase CIGS. TEM image of the 3 hr reaction particles (Figure 3.25) shows a similar particle size of around 10 nm as compared to 3 hr chalcopyrite CIGS.

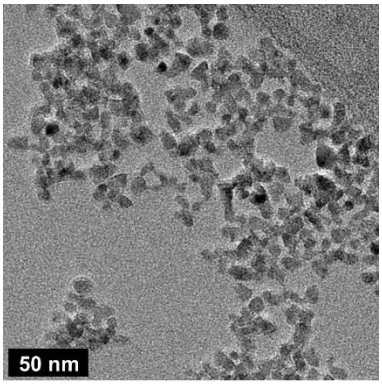

Figure 3.26. TEM images of wurtzite phase CIGS nanoparticles synthesized via heat up route with faster heating rate and 3 hours of reaction time.

3.4 Conclusions

In summary, the metal dissolution ability of the reactive amine-thiol solvent system was utilized for anion impurity-free colloidal syntheses of semiconducting metal chalcogenide nanoparticles, an alternative to traditional metal salt-based nanoparticle syntheses. Metals like Cu, In, Ga, Zn, Sn, Se were used in their elemental form to synthesize alkylammonium metal thiolate species using a propylamine and ethanedithiol solution. The thermal decomposition of these precursors was then studied using XRD and GC-MS analysis revealing a clean conversion of metal thiolates to metal chalcogenides along with volatile byproducts. Using this route, anion impurity-free, phase pure syntheses for binary In_2S_3, ternary $CuInS_2$ and quaternary Cu_2ZnSnS_4 systems were demonstrated. Uniform metal alloying between In and Ga was also successfully achieved for the binary alloy $(In_xGa_{1-x})_2S_3$ and the ternary alloy CIGS system, while chalcogen alloying with Se was demonstrated for the CISSe system. The success of heat-up, hot injection and microwave assisted solvothermal route for synthesizing phase pure material provided flexibility in experimental methods while the formation of different size, shape, and phase of nanoparticles via selective reaction parameters provided control over reaction products from these new precursor solutions. The applicability of this route was further explored by preparing precursor inks using metal chalcogenides instead of pure metals, which still avoid the use of any foreign impurity, to synthesize ternary metal chalcogenide nanoparticles of CIGS and $AgInS_2$.

3.5 Acknowledgements

This work was supported by funding from the National Science Foundation under grant #1534691-DMR (DMREF) and grant #1735282-NRT (SFEWS). The authors would also like to acknowledge Jonathan Turnley and Aashish Rai for their help with nanoparticle synthesis experiments, Joseph Andler for his help with atomic force microscopy measurements, Prof. Daniel Flaherty from Department of Medicinal Chemistry and Molecular Pharmacology at Purdue University for allowing use of their microwave reactor and Prof. John Blendell from Department of Materials Engineering at Purdue University for allowing use of the atomic force microscope.

3.6 References

(1) Guo, Q.; Kim, S. J.; Kar, M.; Shafarman, W. N.; Birkmire, R. W.; Stach, E. A.; Agrawal, R.; Hillhouse, H. W. Development of CulnSe$_2$ Nanocrystal and Nanoring Inks for Low-Cost Solar Cells. *Nano Lett.* **2008**, *8* (9), 2982–2987. https://doi.org/10.1021/nl802042g.

(2) Guo, Q.; Hillhouse, H. W.; Agrawal, R. Synthesis of Cu2ZnSnS$_4$ Nanocrystal Ink and Its Use for Solar Cells. *J. Am. Chem. Soc.* **2009**, *131* (33), 11672–11673. https://doi.org/10.1021/ja904981r.

(3) Hages, C. J.; Agrawal, R. Synthesis of CZTSSe Thin Films from Nanocrystal Inks. In *Copper Zinc Tin Sulfide-Based Thin-Film Solar Cells*; Ito, K., Ed.; John Wiley & Sons Ltd: Chichester, UK, 2015; pp 239–270. https://doi.org/10.1002/9781118437865.ch11.

(4) Coughlan, C.; Ibáñez, M.; Dobrozhan, O.; Singh, A.; Cabot, A.; Ryan, K. M. Compound Copper Chalcogenide Nanocrystals. *Chem. Rev.* **2017**, *117* (9), 5865–6109. https://doi.org/10.1021/acs.chemrev.6b00376.

(5) Liu, Y.; Liu, M.; Yin, D.; Qiao, L.; Fu, Z.; Swihart, M. T. Selective Cation Incorporation into Copper Sulfide Based Nanoheterostructures. *ACS Nano* **2018**, *12* (8), 7803–7811. https://doi.org/10.1021/acsnano.8b01871.

(6) Liu, Y.; Liu, M.; Yin, D.; Wei, W.; Prasad, P. N.; Swihart, M. T. Kuramite Cu$_3$ SnS$_4$ and Mohite Cu$_2$ SnS$_3$ Nanoplatelet Synthesis Using Covellite CuS Templates with Sn(II) and Sn(IV) Sources. *Chem. Mater.* **2017**, *29* (8), 3555–3562. https://doi.org/10.1021/acs.chemmater.6b05428.

(7) Houck, D. W.; Nandu, S. V.; Siegler, T. D.; Korgel, B. A. CuGaSe$_2$ and CuIn$_x$Ga$_{1-x}$Se$_2$ Nanocrystals with Sphalerite or Wurtzite Phase for Optoelectronic Applications. *ACS Appl. Nano Mater.* **2019**, *2* (7), 4673–4680. https://doi.org/10.1021/acsanm.9b01237.

(8) Kar, M.; Agrawal, R.; Hillhouse, H. W. Formation Pathway of CuInSe$_2$ Nanocrystals for Solar Cells. *J. Am. Chem. Soc.* **2011**, *133* (43), 17239–17247. https://doi.org/10.1021/ja204230d.

(9) Lany, S.; Yu-Jun Zhao; Persson, C.; Zunger, A. N-Type Doping Principles for Doping CuInSe$_2$ and CuGaSe$_2$ with Cl, Br, I, Mg, Zn, and Cd. In *Conference Record of the Thirty-first IEEE Photovoltaic Specialists Conference, 2005.*; IEEE; pp 343–346. https://doi.org/10.1109/PVSC.2005.1488139.

(10) Murria, P.; Miskin, C. K.; Boyne, R.; Cain, L. T.; Yerabolu, R.; Zhang, R.; Wegener, E. C.; Miller, J. T.; Kenttämaa, H. I.; Agrawal, R. Speciation of CuCl and CuCl$_2$ Thiol-Amine Solutions and Characterization of Resulting Films: Implications for Semiconductor Device Fabrication. *Inorg. Chem.* **2017**, *56* (23), 14396–14407. https://doi.org/10.1021/acs.inorgchem.7b01359.

(11) McLeod, S. M.; Hages, C. J.; Carter, N. J.; Agrawal, R. Synthesis and Characterization of 15% Efficient CIGSSe Solar Cells from Nanoparticle Inks. *Prog. Photovoltaics Res. Appl.* **2015**, *23* (11), 1550–1556. https://doi.org/10.1002/pip.2588.

(12) Selishcheva, E.; Parisi, J.; Kolny-Olesiak, J. Copper-Assisted Shape Control in Colloidal Synthesis of Indium Oxide Nanoparticles. *J. Nanoparticle Res.* **2012**, *14* (2), 711. https://doi.org/10.1007/s11051-011-0711-6.

(13) Cavallari, N.; Pattini, F.; Rampino, S.; Annoni, F.; Barozzi, M.; Bronzoni, M.; Gilioli, E.; Gombia, E.; Maragliano, C.; Mazzer, M.; Pepponi, G.; Spaggiari, G.; Fornari, R. Low Temperature Deposition of Bifacial CIGS Solar Cells on Al-Doped Zinc Oxide Back Contacts. *Appl. Surf. Sci.* **2017**, *412*, 52–57. https://doi.org/10.1016/J.APSUSC.2017.03.242.

(14) Boles, M. A.; Ling, D.; Hyeon, T.; Talapin, D. V. The Surface Science of Nanocrystals. *Nature Materials*. Nature Publishing Group February 1, 2016, pp 141–153. https://doi.org/10.1038/nmat4526.

(15) Rath, T.; Edler, M.; Haas, W.; Fischereder, A.; Moscher, S.; Schenk, A.; Trattnig, R.; Sezen, M.; Mauthner, G.; Pein, A.; Meischler, D.; Bartl, K.; Saf, R.; Bansal, N.; Haque, S. A.; Hofer, F.; List, E. J. W.; Trimmel, G. A Direct Route towards Polymer/Copper Indium Sulfide Nanocomposite Solar Cells. *Adv. Energy Mater.* **2011**, *1* (6), 1046–1050. https://doi.org/10.1002/aenm.201100442.

(16) Wang, G.; Wang, S.; Cui, Y.; Pan, D. A Novel and Versatile Strategy to Prepare Metal-Organic Molecular Precursor Solutions and Its Application in Cu(In,Ga)$(S,Se)_2$ Solar Cells. *Chem. Mater.* **2012**, *24* (20), 3993–3997. https://doi.org/10.1021/cm3027303.

(17) Chesman, A. S. R.; Van Embden, J.; Duffy, N. W.; Webster, N. A. S.; Jasieniak, J. J. In Situ Formation of Reactive Sulfide Precursors in the One-Pot, Multigram Synthesis of Cu_2ZnSnS_4 Nanocrystals. *Cryst. Growth Des.* **2013**, *13* (4), 1712–1720. https://doi.org/10.1021/cg4000268.

(18) van Embden, J.; Chesman, A. S. R.; Jasieniak, J. J. The Heat-Up Synthesis of Colloidal Nanocrystals. *Chem. Mater.* **2015**, *27* (7), 2246–2285. https://doi.org/10.1021/cm5028964.

(19) Jiang, Y.; Wu, Y.; Mo, X.; Yu, W.; Xie, Y.; Qian, Y. Elemental Solvothermal Reaction to Produce Ternary Semiconductor $CuInE_2$ (E = S, Se) Nanorods. *Inorg. Chem.* **2000**, *39* (14), 2964–2965. https://doi.org/10.1021/ic000126x.

(20) Chun, Y.-G.; Kim, K.-H.; Yoon, K.-H. Synthesis of $CuInGaSe_2$ Nanoparticles by Solvothermal Route. *Thin Solid Films* **2005**, *480–481*, 46–49. https://doi.org/10.1016/j.tsf.2004.11.078.

(21) Zhao, X.; Lu, M.; Koeper, M. J.; Agrawal, R. Solution-Processed Sulfur Depleted Cu(In, Ga)Se_2 Solar Cells Synthesized from a Monoamine–Dithiol Solvent Mixture. *J. Mater. Chem. A* **2016**, *4* (19), 7390–7397. https://doi.org/10.1039/C6TA00533K.

(22) Zhang, R.; Szczepaniak, S. M.; Carter, N. J.; Handwerker, C. A.; Agrawal, R. A Versatile Solution Route to Efficient Cu2ZnSn(S,Se)$_4$ Thin-Film Solar Cells. *Chem. Mater.* **2015**, *27* (6), 2114–2120. https://doi.org/10.1021/cm504654t.

(23) Zhao, D.; Tian, Q.; Zhou, Z.; Wang, G.; Meng, Y.; Kou, D.; Zhou, W.; Pan, D.; Wu, S. Solution-Deposited Pure Selenide CIGSe Solar Cells from Elemental Cu, In, Ga, and Se. *J. Mater. Chem. A* **2015**, *3* (38), 19263–19267. https://doi.org/10.1039/c5ta05300e.

(24) Zhang, R.; Cho, S.; Lim, D. G.; Hu, X.; Stach, E. A.; Handwerker, C. A.; Agrawal, R. Metal–Metal Chalcogenide Molecular Precursors to Binary, Ternary, and Quaternary Metal Chalcogenide Thin Films for Electronic Devices. *Chem. Commun.* **2016**, *52* (28), 5007–5010. https://doi.org/10.1039/C5CC09915C.

(25) Fan, Q.; Tian, Q.; Wang, H.; Zhao, F.; Kong, J.; Wu, S. Regulating the Starting Location of Front-Gradient Enabled Highly Efficient Cu(In,Ga)Se_2 Solar Cells via a Facile Thiol–Amine Solution Approach. *J. Mater. Chem. A* **2018**, *6* (9), 4095–4101. https://doi.org/10.1039/C7TA10889C.

(26) Webber, D. H.; Buckley, J. J.; Antunez, P. D.; Brutchey, R. L. Facile Dissolution of Selenium and Tellurium in a Thiol–Amine Solvent Mixture under Ambient Conditions. *Chem. Sci.* **2014**, *5* (6), 2498. https://doi.org/10.1039/c4sc00749b.

(27) Walker, B. C.; Agrawal, R. Contamination-Free Solutions of Selenium in Amines for Nanoparticle Synthesis. *Chem. Commun.* **2014**, *50* (61), 8331–8334. https://doi.org/10.1039/C4CC02379J.

(28) Liu, Y.; Yao, D.; Shen, L.; Zhang, H.; Zhang, X.; Yang, B. Alkylthiol-Enabled Se Powder Dissolution in Oleylamine at Room Temperature for the Phosphine-Free Synthesis of Copper-Based Quaternary Selenide Nanocrystals. *J. Am. Chem. Soc.* **2012**, *134* (17), 7207–7210. https://doi.org/10.1021/ja300064t.

(29) Miskin, C. K.; Deshmukh, S. D.; Vasiraju, V.; Bock, K.; Mittal, G.; Dubois-Camacho, A.; Vaddiraju, S.; Agrawal, R. Lead Chalcogenide Nanoparticles and Their Size-Controlled Self-Assemblies for Thermoelectric and Photovoltaic Applications. *ACS Appl. Nano Mater.* **2019**, *2* (3), 1242–1252. https://doi.org/10.1021/acsanm.8b02125.

(30) Agrawal, R.; Zhang, R.; Walker, B. C.; Handwerker, C. Homogeneous Precursor Formation Method and Device Thereof. US 9,738,799 B2, August 12, 2015.

(31) Miskin, C. K.; Yang, W.-C.; Hages, C. J.; Carter, N. J.; Joglekar, C. S.; Stach, E. A.; Agrawal, R. 9.0% Efficient $Cu_2ZnSn(S,Se)_4$ Solar Cells from Selenized Nanoparticle Inks. *Prog. Photovoltaics Res. Appl.* **2015**, *23* (5), 654–659. https://doi.org/10.1002/pip.2472.

(32) Zhao, X.; Deshmukh, S. D.; Rokke, D. J.; Zhang, G.; Wu, Z.; Miller, J. T.; Agrawal, R. Investigating Chemistry of Metal Dissolution in Amine–Thiol Mixtures and Exploiting It toward Benign Ink Formulation for Metal Chalcogenide Thin Films. *Chem. Mater.* **2019**, *31* (15), 5674–5682. https://doi.org/10.1021/acs.chemmater.9b01566.

(33) Dierick, R.; Van den Broeck, F.; De Nolf, K.; Zhao, Q.; Vantomme, A.; Martins, J. C.; Hens, Z. Surface Chemistry of $CuInS_2$ Colloidal Nanocrystals, Tight Binding of L-Type Ligands. *Chem. Mater.* **2014**, *26* (20), 5950–5957. https://doi.org/10.1021/cm502687p.

(34) Fan, Q.; Tian, Q.; Wang, H.; Zhao, F.; Kong, J.; Wu, S. Regulating the Starting Location of Front-Gradient Enabled Highly Efficient $Cu(In,Ga)Se_2$ Solar Cells *via* a Facile Thiol–Amine Solution Approach. *J. Mater. Chem. A* **2018**, *6* (9), 4095–4101. https://doi.org/10.1039/C7TA10889C.

(35) Rokke, D.; Deshmukh, S. D.; Agrawal, R. A Novel Approach to Amine-Thiol Molecular Precursors for Fabrication of High Efficiency Thin Film CISSe/CIGSSe Devices. In *46th IEEE PVSC*; 2019.

(36) Dutta, D. P.; Sharma, G.; Tyagi, A. K.; Kulshreshtha, S. K. Gallium Sulfide and Indium Sulfide Nanoparticles from Complex Precursors: Synthesis and Characterization. *Mater. Sci. Eng. B* **2007**, *138* (1), 60–64. https://doi.org/10.1016/J.MSEB.2007.01.017.

(37) Rau, U.; Schock, H. W. $Cu(In,Ga)Se_2$ Thin-Film Solar Cells. In *Solar Cells*; Elsevier, 2013; pp 261–304. https://doi.org/10.1016/B978-0-12-386964-7.00009-3.

(38) Carter, N. J.; Yang, W. C.; Miskin, C. K.; Hages, C. J.; Stach, E. A.; Agrawal, R. Cu2ZnSn(S,Se)4 Solar Cells from Inks of Heterogeneous Cu-Zn-Sn-S Nanocrystals. *Sol. Energy Mater. Sol. Cells* **2014**, *123*, 189–196. https://doi.org/10.1016/j.solmat.2014.01.016.

(39) Yang, W.-C.; Miskin, C. K.; Carter, N. J.; Agrawal, R.; Stach, E. A. Compositional Inhomogeneity of Multinary Semiconductor Nanoparticles: A Case Study of Cu_2ZnSnS_4. **2014**. https://doi.org/10.1021/cm502930d.

(40) Yu, X.; Cheng, S.; Yan, Q.; Yu, J.; Qiu, W.; Zhou, Z.; Zheng, Q.; Wu, S. Efficient $(Cu_{1-x}Ag_x)_2ZnSn(S,Se)_4$ Solar Cells on Flexible Mo Foils. *RSC Adv.* **2018**, *8* (49), 27686–27694. https://doi.org/10.1039/C8RA04958K.

(41) Liu, Z.; Tang, K.; Wang, D.; Wang, L.; Hao, Q. Facile Synthesis of $AgInS_2$ Hierarchical Flowerlike Nanoarchitectures Composed of Ultrathin Nanowires. *Nanoscale* **2013**, *5* (4), 1570–1575. https://doi.org/10.1039/c2nr33219a.

4. HYBRID LIGAND EXCHANGE OF CU(IN,GA)S_2 NANOPARTICLES FOR CARBON IMPURITY REMOVAL IN SOLUTION PROCESSED PHOTOVOLTAICS

Reprinted with permission Ellis, R. G.; Turnley, J. W.; Rokke, D. J.; Fields, J. P.; Alruqobah, E. H.; Deshmukh, S. D.; Kisslinger, K.; Agrawal, R. Hybrid Ligand Exchange of Cu(In,Ga)S_2 Nanoparticles for Carbon Impurity Removal in Solution-Processed Photovoltaics. Chem. Mater. 2020, 32, 5091–5103. https://doi.org/10.1021/acs.chemmater.0c00966. The journal article and supporting information have been merged and text and figures have been modified where appropriate.

4.1 Introduction

Colloidal nanoparticle-based photovoltaics have continually suffered from carbonaceous impurity residues that could increase series resistance and recombination, potentially limiting efficiency. These carbonaceous residues originate from long chain organic ligands bound to the surface of the nanoparticles.[1,2] Virtually all common synthetic pathways for chalcogenide nanocrystals make use of low-volatility coordinating ligands that consist of a polar head group to coordinate with the nanocrystal surface, and a long alkyl chain tail to afford colloidal stability via steric repulsion between nanoparticles. Commonly used ligands during colloidal synthesis include oleylamine (OLA, b.p 348-350°C), dodecanethiol (DDT, b.p 266-283°C), trioctylphosphine (TOP, b.p. 284-291°C), and oleic acid (OA, b.p. 360°C).[3,4] These long chain surfactant-like molecules are used during synthesis for their high boiling point, ability to solubilize precursors, and ability to control reaction kinetics and nanoparticle morphology. However, due to the high boiling point of these molecules, they are difficult to remove via thermal treatment and can leave coke residues in the nanoparticle film when annealed under an inert atmosphere.[1] In the case of solution processed CIGSSe and $Cu_2ZnSn(S,Se)_4$ (CZTSSe) photovoltaics from colloidal nanoparticle inks, these ligands decompose and react with a liquid front of selenium during the selenization process. The liquid selenium front segregates a polymeric carbon/selenium fine grain layer to the back contact.[5,6] While this layer is fairly conductive, it still has several orders of magnitude higher resistance than the molybdenum back contact and thereby may increase series resistance.[7,8] Additionally, it has been suggested that the presence of carbon can detrimentally impact the elemental redistribution process that occurs during selenization.[2]

Naturally, removal of these bulky ligands would prevent carbon residues from contaminating nanoparticle thin films. However, due to the benefits of these ligands during nanoparticle synthesis, their removal is preferred post nanoparticle synthesis via ligand exchange reactions. A significant body of literature has explored ligand exchange for metal and metal chalcogenide nanomaterials. Binary materials such as CdSe, CdTe, and PbS have been studied extensively due to their well-defined surface chemistry and application in quantum dot based devices.[9] Their native ligands have been replaced using a wide variety of organics such as pyridine,[10–12] butylamine,[13] ethylenediamine,[14] ethanedithiol,[15] tert-butylthiol,[16] benzenedithiol, 3-mercaptopropionic acid, benzenthiol,[9] and many others. Additionally, inorganic ligands such as hydrazine,[17] diammonium sulfide (DAS), sodium sulfide, sodium azide,[18] ammonium thiocyanate,[17] as well as molecular metal chalcogenide complexes (MCCs) have emerged as promising ligands.[17] These inorganic ligands can be advantageous in that ligands can be selected without impurity elements such as carbon while simultaneously retaining colloidal stability via electrostatic repulsion between nanoparticles. Of these various ligands, several binding motifs have been observed and classified. Depending on the chemistry of the ligand, different binding modes are classified as L, X, or Z-type ligands. In the case of L-type ligands, a neutral molecule donates a lone electron pair to a cationic nanoparticle surface atom. For an X-type ligand, a negatively charged molecule donates a single electron to a cationic nanoparticle surface atom forming a covalent bond. For Z-type ligands, a nanoparticle anchored metal donates two electrons to a neutral ligand.[9]

Despite the large body of literature on ligand exchange, very few reports have explored ligand exchange on more complex ternary, quaternary, and quinary materials such as $Cu(In_xGa_{1-x})(S_ySe_{1-y})_2$ or $Cu_2ZnSn(S_ySe_{1-y})_4$, with even less focusing on applications for photovoltaic devices. Due to the presence of many cationic species, the surface chemistry of these nanomaterials is less defined and subject to more variability, complicating ligand exchange pathways. Further complicating matters, the various cations can have significantly different reactivities as defined by Pearson hard-soft acid-base (HSAB) theory.[17] For example, in $CuInS_2$ (CIS) nanoparticles, indium is a hard acid while copper is a soft acid, thereby necessitating special consideration in pairing base ligands for ligand exchange. Multi-ligand, multi-step strategies have often been necessary due to the variety of surface sites on these ternary and quaternary chalcogenide nanomaterials.[19] Several reports have attempted to adapt ligand exchange methods for derivatives of CIGSSe and CZTSSe

nanoparticles with varying degrees of success, with few making use of quantitative measures of native ligand removal. In a comprehensive study of alkylamine and thiol ligand binding on CIS, Diereck et al. explored ligand chemistry through proton nuclear magnetic resonance (^{1}H-NMR) studies, observing that L-type alkylamine ligands (OLA and octadecylamine) exhibit very tight binding, uncharacteristic of L-type ligands for other materials systems. This tight binding of alkylamine ligands generally necessitated temperatures greater than 100 °C for organic-organic ligand exchange facilitated by alkylamine desorption, further complicating ligand exchange pathways.[20] The lack of oleylamine desorption below 100°C and further difficulty of direct exchange with other species has been observed in other reports, where molecular iodine was needed to facilitate exchange to other bulky carbonaceous ligands.[21] Other attempts in the literature using room temperature phase transfer exchanges with DAS have yielded poor removal of native OLA ligands (~50% removal) as determined by ^{1}H-NMR.[22]

In this report, various ligand exchange pathways were explored to yield exhaustive native ligand removal via a rapid process. Several criteria were identified for successful ligand exchange and subsequent utility of exchanged nanoparticles. First, the ligand exchange should remove the majority of native ligands to minimize carbonaceous residues. Second, the ligand exchange should not change the nanoparticle stoichiometry through etching of the nanoparticle surface, especially for low earth abundance elements such as indium. Third, the ligand exchanged nanoparticles should be dispersible at high mass concentrations exceeding 200 mg/mL for compatibility with scalable coating techniques such as blade coating and slot-die printing. Each of these criteria were systematically investigated and a sequential hybrid solvothermal organic and room temperature inorganic exchange was developed using pyridine and DAS. Native ligand removal of >98% was achieved and did not appreciably alter the stoichiometry of the as-synthesized nanoparticle. Finally, inks with mass concentrations exceeding 200 mg/mL were successfully prepared with colloidal stability on the order of months in low toxicity solvents such as DMSO. Blade coating and initial device fabrication was demonstrated with promising total-area power conversion efficiencies reaching 12.0%.

4.2 Experimental Section

4.2.1 Materials

Copper (I) sulfide (99.99%), Ga (99.9999%), 1,2-ethanedithiol (98%), propylamine (99%), oleylamine (OLA, Technical grade, 70%), pyridine (anhydrous, 99.9%), acetonitrile (anhydrous, 99.9%), diammonium sulfide solution (DAS, 40-48 wt% aqueous solution), toluene (anhydrous, 99.8%), N-methyl formamide (NMF, 99%), dimethyl sulfoxide (DMSO, anhydrous, 99.9%), selenium pellets (99.995%), cadmium sulfate hydrate (99.996%), thiourea (>99%), dimethyl sulfoxide-D_6 (99.96 atom % D), 1,2-dichlorobenzene-D_4 (98 atom % D), chloroform-D (99.96 atom % D), toluene-D_8 (99.6 atom % D), ethylene carbonate (99.96%), copper (II) acetylacetonate (99.9%), indium (III) acetylacetonate (99.99%), gallium (III) acetylacetonate (99.99%), sulfur (99.99%), and hexanethiol (95%) were purchased from Sigma Aldrich and used as received with the exception of OLA, which was degassed through successive freeze pump thaw cycles, and gallium, from which surface oxide was removed with a blade. Indium (99.999%), hexanes (mixture of isomers, 99%), isopropyl alcohol (IPA, 99.9%), acetone (99.5%), and ammonium hydroxide (28.0-30.0% in H_2O) were purchased from Fisher Scientific and used as received. All chemicals were stored and dispensed under an inert nitrogen environment with < 0.1 ppm H_2O and O_2. Ultrapure water was produced using a Millipore Direct-Q 3 (18.2 MΩ at 25°C).

4.2.2 Synthesis of Cu(In,Ga)S_2 (CIGS) Nanoparticles.

Nanoparticle synthesis was performed using a modified method from our previous report.[23] Briefly, separate Cu_2S and In/Ga precursor solutions were prepared. Propylamine and 1,2-ethanedithiol were added (2:1 mol:mol) to Cu_2S powder to form a 1.79 M (with respect to copper) solution, and to Ga and In (Ga/(In+Ga) ratio of 0.3) to form a 1.01 M solution. The Cu_2S solution was dissolved in a glovebox at room temperature overnight and the In/Ga solution was dissolved at 45°C on an argon purged Schleck line for several days. The transparent homogenous In/Ga solution was mixed with the transparent yellow/brown Cu_2S solution such that the Cu/(In+Ga) ratio was 0.92, yielding a homogenous transparent yellow/brown solution. Note: Extremely careful mixing of the two solutions is needed to obtain the proper Cu/(In+Ga) ratio. Due to the viscosity of the two solutions, repeated washing of their containing vessel with oleylamine to be used in the reaction mixture is needed to collect all of each solution. The two solutions were transferred to a 100 mL

three neck reaction flask, diluted with 5.86 mL of OLA per mmol of In + Ga and connected to an argon purged Schlenk line. Typically, a total reaction volume of 22-24 mL was targeted to reproduce the heating rates accurately. The solution was heated to 285°C over the course of approximately 40 minutes. After 16 minutes, condenser cooling water was removed to allow for removal of excess propylamine and 1,2-ethanedithiol, which was captured in a secondary air-cooled trap to prevent amine-thiol from collecting in the schlenk line. After reaching reaction temperature, the reaction mixture was allowed to dwell at reaction temperature for 90 minutes followed by natural cooling to room temperature, all with vigorous stirring using a pyrex magnetic stir bar. The reaction mixture was transferred to three fluorinated ethylene polymer (FEP) 30 mL centrifuge tubes was then precipitated with excess IPA and centrifugation at 14000 rpm for 5 minutes. The supernatant was decanted and the nanoparticles were redispersed in 4 mL of hexanes at approximately 75 mg/mL per tube followed by precipitation with IPA and centrifugation. The suspension and precipitation cycle was repeated two more times to remove all free OLA (as determined by ^{1}H-NMR, Figure 4.8). Prior to the final wash, the suspension of nanoparticles was combined to a single tube using a total of 4 mL of hexanes. After precipitation and decantation of the supernatant, the final pellet was dried under argon flow and stored under an inert atmosphere for further use. Approximately 1 gram of CIGS nanoparticles were obtained from a single synthesis. For nanoparticle synthesis using metal acetylacetonate salts and sulfur in OLA, previous literature methods were used.[6,24]

4.2.3 Ligand Exchange

Pyridine ligand exchanges were performed by first dispersing the dry CIGS nanoparticles in toluene at 100 mg/mL using sonication. The dispersed nanoparticle ink was transferred into a borosilicate glass microwave reaction vial with a polytetrafluoroethylene (PTFE) coated magnetic stir bar and diluted with pyridine at a 9:1 pyridine:toluene vol:vol ratio. The microwave reaction vial was crimp sealed with an aluminum cap over a PTFE coated silicone septa. The microwave vial was heated using a Biotage Initiator EXP 400W microwave reactor, equipped with an in-situ IR temperature sensor and pressure gauge. The microwave vial was heated to 150°C for 30 minutes with magnetic stirring, followed by natural cooling to room temperature. The nanoparticles were then precipitated using excess hexanes and centrifugation. The supernatant was decanted. If additional pyridine cycles were performed, the pellet was redispersed in pyridine and again

transferred to a microwave vial. The aforementioned procedure was repeated up to three times for successive pyridine cycles.

The final pyridine exchanged CIGS pellet was then dispersed in 10:1 vol:vol NMF:DAS at approximately 20 mg/mL through vortex mixing in a fluorinated ethylene propylene (FEP) vessel (significant particle adsorption to glass vessel walls was observed, thus the use of a polymer vessel enabled increased yields). An immiscible phase of hexanes of equal volume was added. The mixture was allowed to stir at room temperature for 90 minutes, after which, the polar NMF/DAS phase was removed and added to a clean vial. The liquid-liquid interface between the polar and non-polar phase was intentionally rejected to prevent collection of poorly exchanged particles which typically aggregated at the liquid-liquid interface. An equal volume of hexanes was again added to the mixture. The two-phase mixture was stirred for an additional 30 minutes to allow any residual native ligand in the polar phase to segregate to the hexanes. The polar phase was removed, rejecting the liquid-liquid interface, and transferred to a centrifuge tube. The nanoparticles were precipitated with excess acetone and centrifugation. The supernatant was decanted, and the pellet was redispersed in acetonitrile at approximately 15 mg/mL and precipitated with acetone. The decanting, suspension in acetonitrile, and precipitation with acetone and centrifugation was repeated one additional time. The supernatant was decanted, and the nanoparticles were dried under a nitrogen flow for 30 minutes. The dry particles were stored under nitrogen for further use.

Single step exchanges were performed by first dispersing the native ligand capped CIGS nanoparticles in hexanes at 20 mg/mL using sonication. Then, a 10:1 vol:vol mixture of NMF and DAS solution were added as an immiscible polar phase. The mixture was stirred for 16 hours, during which time CIGS nanoparticles migrated from the upper hexanes phase to the lower NMF/DAS phase. The polar phase was removed while rejecting the liquid-liquid interface and transferred to a fresh vial. An equal volume phase of hexanes was added and allowed to stir for 30 minutes. Finally, the polar phase was removed, rejecting the liquid-liquid interface, and washing was performed as described for the hybrid ligand exchange.

4.2.4 Nanoparticle Ink Preparation and Coating

The dry ligand-exchanged nanoparticles (from single step or hybrid ligand exchanges) were weighed and dispersed in DMSO at concentrations ranging from 150-250 mg/mL, typically at 225 mg/mL using sonication. The resulting viscous ink was then blade coated on soda lime glass or

molybdenum coated soda lime glass substrates using a multipass auto-blade coater constructed from a modified 3D printer (KClone K200). First, the blade coater stage and substrate were heated to 80°C and 12 µL of ink were dispensed on the edge of a 2"x1" substrate. A 100 µm blade gap and blade speed of 25 mm/s was used, with two passes down and up the substrate using a borosilicate glass rod as a blade. The film was allowed to dry for four minutes at 80°C. The film was then annealed at 300°C for 90 s in an inert atmosphere followed by quenching on a room temperature aluminum block. If higher annealing temperatures were used, for example, 400°C, 30 s of natural cooling on an aluminum foil rail was performed to prevent cracking of the glass due to temperature shock. At 225 mg/mL, each coating typically yielded a 300 nm thick layer when 12 µL of ink was used for a single coating. Successive coatings could be repeated for desired thickness. For preparing the conventionally prepared nanoparticle thin films, dry particles were dispersed in hexanethiol at 250 mg/mL. Coatings were performed and annealed in air as described in previous literature.[6,24,25]

4.2.5 Device Fabrication

Molybdenum was DC magnetron sputtered on soda lime glass substrates with a final thickness of 800 nm. Nanoparticle inks were coated with four layers as described previously. Following coating, 10 nm of NaF was evaporated onto the CIGS nanoparticle films using E-beam evaporation. The CIGS films were then selenized in a graphite box in a tubular furnace under an argon atmosphere with selenium pellets at 500-550°C for 10-20 minutes. After selenization, CdS (50 nm) was deposited by chemical bath deposition. Then, i-ZnO (80 nm) and ITO (220 nm) were deposited by RF sputtering. Finally, Ni/Al (100 nm/1.5 µm) grids and a MgF_2 (100 nm) antireflection coating were deposited by E-beam evaporation. Devices were isolated with mechanical scribing with a device total-area of approximately 0.47 cm^2 (exact areas determined by image analysis) and a grid shading of 4%.

4.2.6 Characterization

Capillary gas chromatography mass spectrometry (GC-MS) analysis was performed with an Agilent 5975C mass spectrometer with an electron energy of 70 eV, ion source temperature of 250°C, and 30-meter DB-5 capillary column (250µm i.d. X 0.25µm film thickness). OLA was diluted in dichloromethane for GC-MS measurements. X-ray diffractograms (XRD) were collected

on a Rigaku Smart Lab diffractometer with a Cu Kα (λ = 1.5406 Å) source operated at 40 kV/44 mA in in parallel beam (PB) mode at an angle of 0.5 degrees. Raman spectra were collected using a Horiba/Jobin-Yvon HR800 Raman spectrometer with a 632.8 nm excitation laser wavelength. Quantitative elemental composition measurements were taken on a Fisher XAN 250 X-ray Fluorescence (XRF) instrument at 50 kV voltage with a silicon drift detector, primary nickel filter, and flowing helium gas purge. ^{1}H-NMR spectra were collected with a Bruker AV-III-400-HD using a relaxation time of 6 seconds and 32 scans. Heat up ^{1}H-NMR was performed on a Bruker DRX500-2 NMR with a relaxation time of 6 seconds and 8 scans. DMSO-D6, 1,2-dichlorobenze-D4, and toluene-D6, and chloroform-D were used as deuterated solvents and quantitation was performed using ethylene carbonate as an internal standard. During *in-situ* heat up experiments, 1,2-dichlorbenzene-D4 was used as a solvent in a screw cap NMR tube, and the sample was allowed to equilibrate for approximately five minutes at each temperature prior to measurement. FTIR spectra were collected with a Thermo-Nicolet Nexus 670 FTIR in transmission mode using either NaCl crystal or soda lime glass as substrates. Thermogravimetric Analysis (TGA) was performed using a TA Instruments Q50 with an alumina pan and platinum holder at a heating rate of 10°C/min under an argon atmosphere. Scanning Electron Microscopy (SEM) images were taken using a FEI Quanta 3D FEG Dual-beam SEM with an Everhart-Thornley Detector at an accelerating voltage of 10kV and working distance of 10 mm. Profilometry was performed using a Dektak 6M stylus profilometer with a 12.5 μm diameter diamond tip stylus. Thickness measurements were taken using mechanically scribed trenches. X-ray Photoelectron Spectroscopy (XPS) was performed on a Kratos AXIS ULTRA DLD Imaging XPS with monochromatic Al Kα radiation (1486.6 eV). Peak fitting was performed on CasaXPS using Voigt peak profiles and linear backgrounds. The peak position of C 1s was set to 285 eV and for the S 2p photoelectron transition the doublet separation between S $2p_{1/2}$ and $2p_{3/2}$ was set at 1.20 eV. Capacitance-voltage measurements were collected using a Hewlett Packard 4284A LCR meter operated at 100 kHz. Transmission electron microscopy (TEM) images and scanning tunneling electron microscopy energy dispersive x-ray spectroscopy (STEM-EDS) measurements were taken on a Talos 200X TEM with four silicon drift detectors with lacey carbon grids for imaging and molybdenum grids for STEM-EDS. A FEI Helios 600 Dualbeam FIB with a gallium ion beam was used to prepare the FIB samples.

4.3 Results and Discussion

4.3.1 Nanoparticle Synthesis and Ligand Chemistry

A wide variety of synthetic methods have been developed for CIS and CIGS nanoparticles.[4] In this report we adapted a synthetic pathway from our previous work that makes use of high purity elemental indium (99.999%), gallium (99.99999%), and copper (I) sulfide (99.99%) as precursors in amine-thiol solutions.[23] A gram-scale one-pot heat up reaction was employed using OLA as a reaction solvent/ligand as described in the experimental section. The advantage of this synthetic pathway is that it eliminates potential anionic impurities present in commonly used metal salts such as halides, nitrates, sulfates, acetate, acetylacetonates, etc.[3,4] It is well known that anions from conventional metal salts can bind to nanomaterial surfaces and alter their growth and/or subsequent optoelectronic properties,[9] or in the case of oxygen containing anions, introduce high resistivity oxide secondary phases.[3,26] Using only Cu_2S, In, and Ga prevents the introduction of non-sulfide, contaminating anionic X-type ligands typically present in metal salts. XRF measurements of as synthesized nanoparticles typically revealed elemental ratios of 0.92 for Cu/(In+Ga) and 0.29-0.30 for Ga/(In+Ga). The particles were imaged as shown in Figure 4.1 and have an average size of approximately 10 nm.

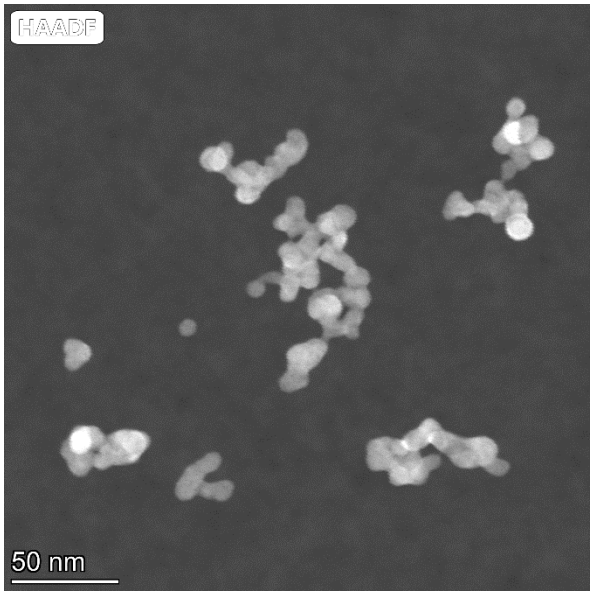

Figure 4.1. HAADF STEM image of as-synthesized CIGS nanoparticles with a 90-minute reaction time.

OLA has been widely employed as a solvent/ligand for the synthesis of CIS and CIGS nanoparticles due to the high colloidal stability it affords. OLA also exhibits favorable binding on indium (III) and gallium (III) surface sites due to favorable HSAB interactions.[3,4] However, OLA is almost always used as a technical grade mixture, a mixture of primary amines and other trace alkyl components. After degassing by successive freeze pump thaw cycles under vacuum (which removes more volatile components of the mixture), the technical grade OLA was run through GC-MS to identify the components of the degassed technical grade mixture. An understanding of this mixture is important for the design and characterization of adequate ligand exchange pathways. Table 4.1 details the compositional makeup of the technical grade OLA.

Table 4.1. GC-MS mixture composition of technical grade oleylamine after freeze-pump-thaw degassing, species identified via MS.

Molecule	**% Compound**
Oleylamine	82.7
Hexadecenylamine	4.6
Octadecylamine	4.1
Hexadecylamine	3.6
Trace Components (n-octylformamide, oleylanitrile, column bleed)	5

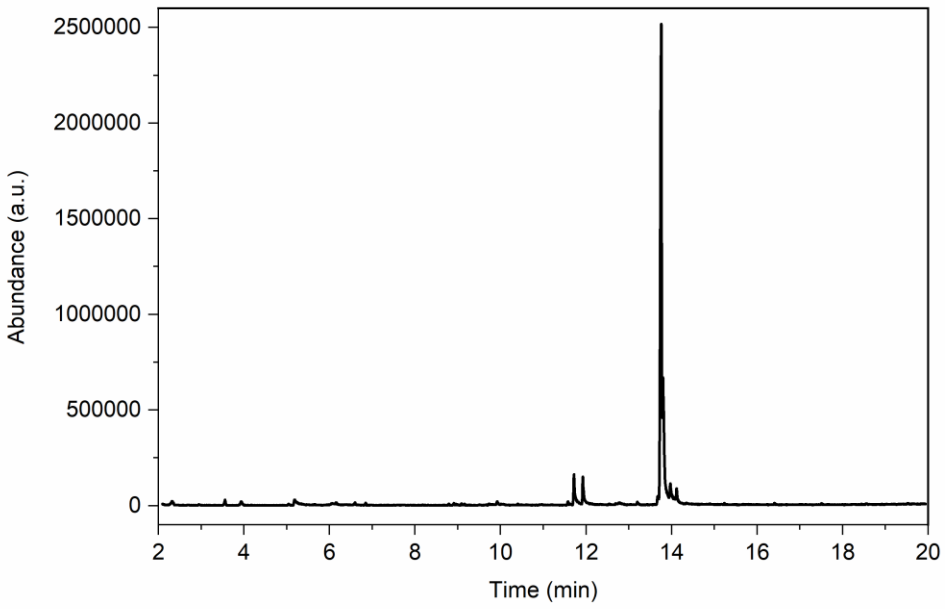

Figure 4.2. Gas chromatogram of the technical grade oleylamine in CH_2Cl_2.

Of the degassed mixture species, 87.3% contained a carbon-carbon double bond, either as OLA or hexadeceneylamine. Additionally, no X-type impurities were observed as is reported by others.[20] Using ^{1}H-NMR, the protons of the alkene region are distinctly separate from the alkyl chain and amine protons. As such, this provides a convenient means of quantifying the OLA molecules bound to the nanoparticle surface. Figure 4.3a shows the ^{1}H-NMR of OLA, as well as OLA capped CIGS nanoparticles. Distinct peak broadening and disappearance of the amine protons and CH_2 protons closest to the amine are observed which are all characteristic of surface bound OLA. The peak broadening is caused by immobilization of the ligand molecule at the nanoparticle surface and becomes more pronounced the closer the protons are to the bound polar head group. In the case of the amine and neighboring alkyl chain protons, the peak broadens so significantly that it becomes indistinguishable from the noise.[20] The amine is able to donate its lone pair electrons on the nitrogen atom to cationic metals on the nanoparticle surface. Typically, this binding is described as a weakly bound adsorption like process, and amines can be desorbed as simply as through dilution. This "weak" binding has been observed for binary metal chalcogenides such as CdTe and PbSe.[27] Interestingly, OLA and octadecylamine (ODA) have been shown to exhibit exceptionally tight binding to CIS nanoparticles in previous work by Diereck et al.[20] Conventional spontaneous desorption was not observed for OLA and ODA ligands at room temperature. Desorption was only

observed when the CIS nanoparticles were exposed to temperatures in excess of 110°C.[20] Due to differences in synthetic pathway and the inclusion of gallium (a harder acid than indium), we repeated their temperature dependent ^{1}H-NMR OLA binding study on CIGS nanoparticles synthesized via the amine-thiol precursor route.

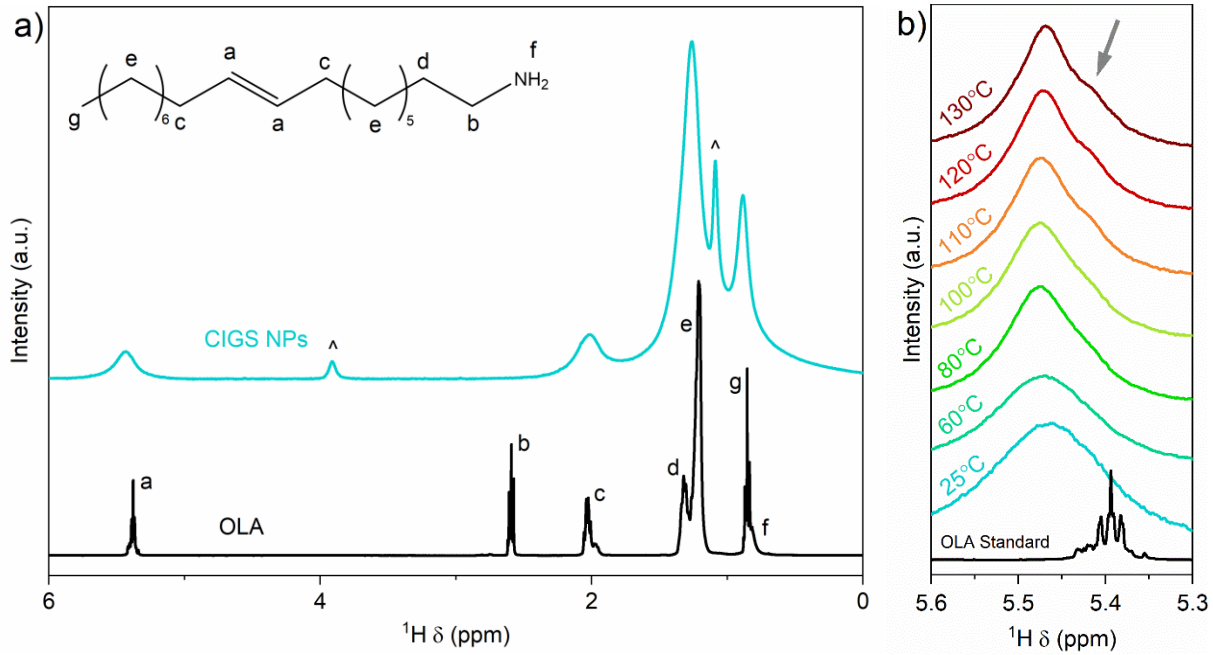

Figure 4.3 a) ^{1}H-NMR of OLA capped CIGS NPs as compared to neat OLA (^ denotes residual IPA from particle washing) and b) In-situ heat-up ^{1}H-NMR of OLA capped CIGS NPs from 25°C to 130°C as compared to neat OLA. Chloroform-D and 1,2-dichlorobenzene-D4 were used as deuterated solvents in a) and b) respectively.

As shown in Figure 4.3b, a shoulder peak emerges at 5.44 ppm, onset at approximately 110°C. This shoulder is attributed to dynamically absorbed/desorbed OLA, confirming similar results to what was observed by Diereck et al.[20] As a result, elevated temperature in the solution phase is needed to induce OLA desorption. Furthermore, the removal of OLA from a thin film was probed using FTIR. CIGS nanoparticles were dropcast from chloroform onto NaCl crystals and spectra were recorded at the same location (and thereby same pathlength) on the CIGS thin film before and after annealing at 300°C for 5 minutes in a nitrogen atmosphere. As shown in Figure 4.4, no appreciable change in the intensity of C-H stretches around 2924 cm^{-1} was observed, demonstrating the low volatility of OLA ligands in a thin film. Use of higher temperature annealing risks the decomposition of OLA into graphitic carbon under an inert atmosphere. While air annealing can

prevent the formation of graphitic carbon through the combustion of the organic species, it risks the oxidation of the nanoparticle precursor film.[1] Oxide containing precursor films generally require an additional reduction step,[28] otherwise residual oxide content can be observed in the final selenized film,[29] and could substantially increase series resistance.

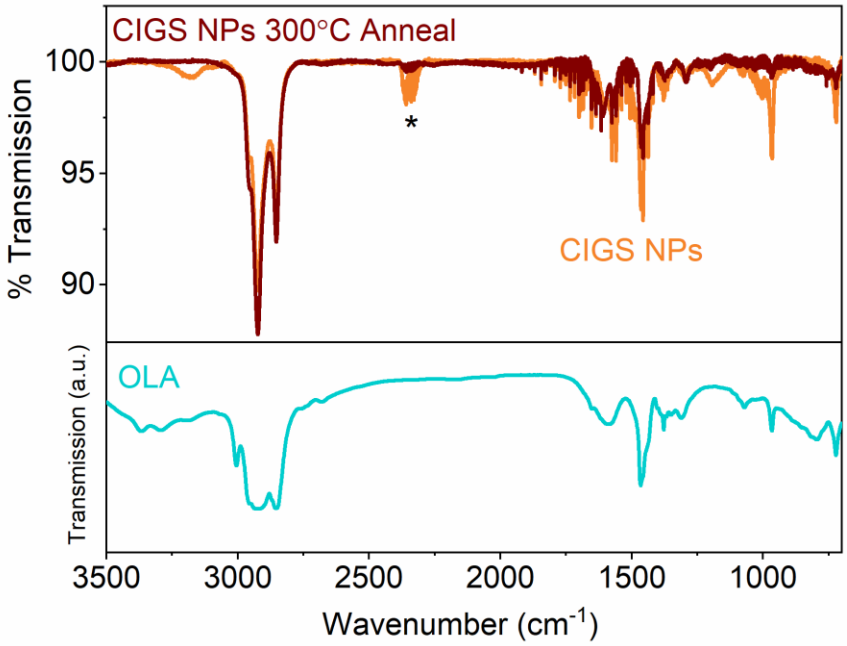

Figure 4.4. FTIR of neat OLA, and comparison of OLA capped CIGS NPs with OLA capped CIGS NPs annealed at 300°C for 5 minutes under nitrogen atmosphere (* donates atmospheric CO_2).

4.3.2 Developing Ligand Exchange Pathways

To remove the carbonaceous impurities stemming from native OLA ligands, a variety of ligand exchange pathways were investigated. Both volatile organic ligands and inorganic sulfide ligands were analyzed with respect to their ability to remove OLA, preserve nanoparticle stoichiometry, and retain colloidal stability at high mass concentrations. In order to quickly probe a variety of organic ligands, thermal lability experiments were performed by heating nanoparticles at 20 mg/mL in the desired organic species for exchange in a sealed microwave reaction vial. Temperatures between 100℃ and 130℃ were used depending on the boiling point of the ligand. Amines, thiols, and pyridines were investigated for oleylamine displacement. Following exchange and washing, the exchanged nanoparticles were redispersed in the organic species used for ligand

exchange and dropcast onto FTIR cards. The dropcast films were dried at 50°C for 5 minutes and FTIR data was collected. The same sample was then annealed at 300°C for 5 minutes and run again at approximately the same location of the film. While by no means an exhaustive or highly quantitative study, it gave insight into the ability to remove various organic ligands. It should be noted that after annealing at 300°C, residual C-H stretches can originate from either residual oleylamine or from non-volatalized new organic ligand. As such, comparisons between the C-H intensities of different organics cannot be directly made, but the ratio of C-H after to before exchange can be compared. Butylamine, tert-butylamine, ethylenediamine, butanethiol, tert-butylthiol, ethanedthiol, pyridine, 3,5-lutidine, and 4-tertbutyl pyridine were all investigated as candidate ligands due to varying functional groups, basicity, binding strengths, etc. Figure 4.5 shows the resulting FTIR spectra for each of the exchanges, showing the results from the highest boiling point species of the pyridines, amines, and thiols that were investigated.

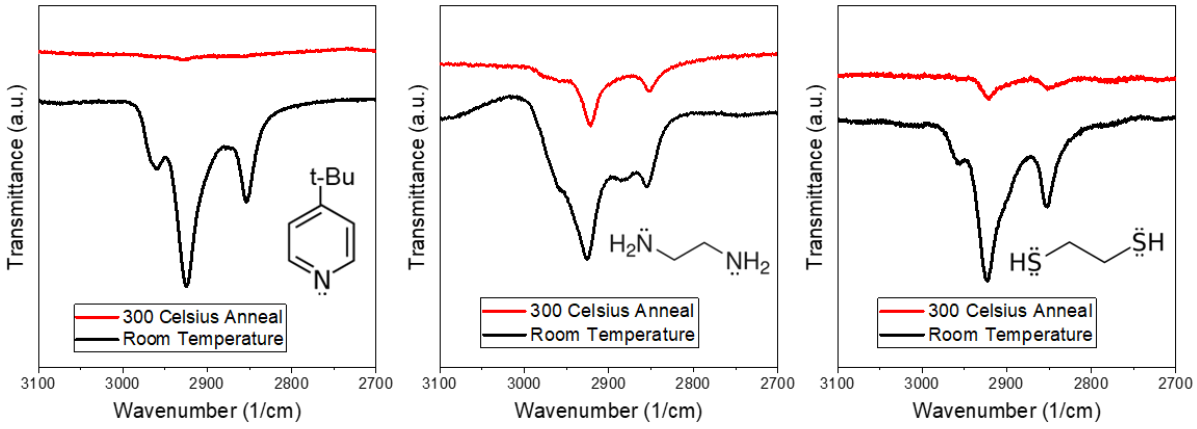

Figure 4.5. FTIR spectra of various organic ligand exchanges for tert-butylpyrdine, 1,2-ethylenediamine, and 1,2-ethanedithiol.

Of the organics investigated, ethylenediamine appeared to be the least effective, with the most residual C-H visible. 4 tert-butylpyrdine showed the smallest residual C-H peak intensity after the exchange. The other two pyridine species investigated showed similar thermal lability and oleylamine removal. The elemental ratios of each species were investigated via XRF to probe any potential etching of the nanoparticles and is shown in Table 4.2.

Table 4.2. Elemental ratios of cations as measured by XRF post ligand exchange with organics.

Ligand	Cu/(In+Ga)	Ga/(In+Ga)
As Synthesized	0.92	0.30
Pyridine	0.94	0.30
3,5-lutidine	0.92	0.29
4-tertbutyl pyridine	0.92	0.29
Butylamine	0.90	0.29
Ethylenediamine	0.94	0.30
Tert-butylamine	0.94	0.30
Butanethiol	0.93	0.28
Ethanedithiol	1.39	0.38

Of all the organic species investigated, only ethanedithiol induced any appreciable etching, substantially etching indium and gallium from the nanoparticle. The use of ethanedithiol allows for the formation of desorbed oleylamine-dithiol mixtures. Mixture of alkylamine and dithiols are known for their ability to dissolve pure metals and metal chalcogenides. As such this etching is consistent with the behavior of those mixtures. The other organic ligands alone, including the other thiols, were not capable of such etching.

Of all ligands used, butylamine and pyridine were investigated to their superior performance. Initial investigation of oleylamine removal using butylamine revealed that it was capable of displacing oleylamine at room temperature, therby removing the need for a higher temperature solvothermal exchange as shown previously. However, a side effect of room temperature exchange that was not observed with the solvothermal exchange previously used was significant selective etching of indium and gallium during successive exchange cycles. Figure 4.6 shows the FTIR of CIGS nanoparticles after two cycles of exchange and annealing at 200°C, along with the XRF of cation ratios after successive butylamine exchanges.

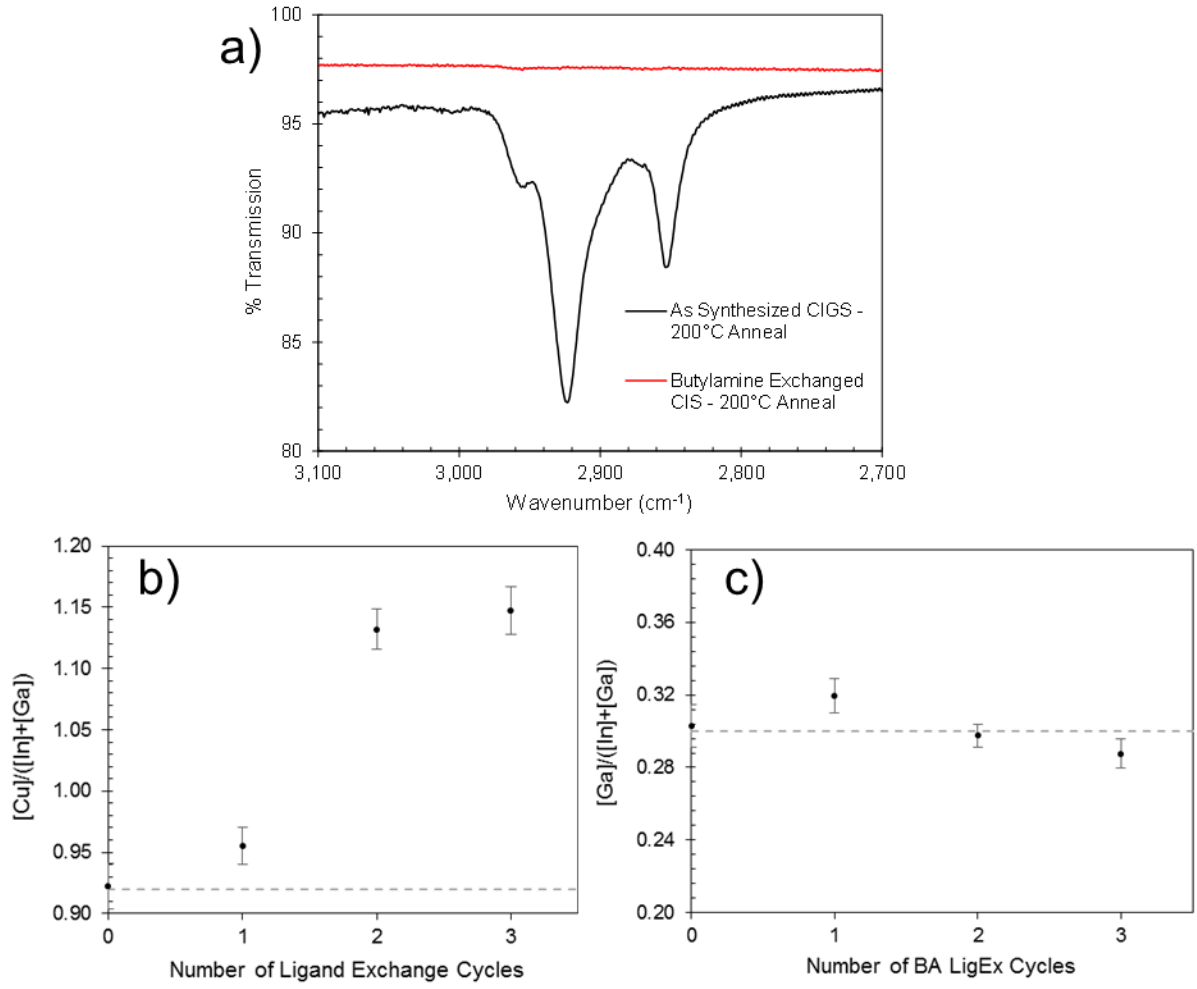

Figure 4.6. a) FTIR from CIGS nanoparticles after two successive cycles of room temperature butylamine exchanges and XRF cation ratios of successively room temperature butylamine exchanges CIGS nanoparticles showin b) Cu/(In+Ga) and c) Ga/(In+Ga) ratios.

After just a single cycle, the Cu/(In+Ga) ratio was increased to ~0.96. After two cycles, a Cu/(In+Ga) over 1.10 shows the selective etching of indium and gallium. Little change in the Ga/(In+Ga) ratio shows that butylamine doesn't have significant preference between the two cations. While the species formed during selective etching is not known, orange colored supernatants were observed in between butylamine cycles after precipitation with isopropyl alcohol. Interestingly, the butylamine etching observed at room temperature was not observed during the higher temperature solvothermal exchange shown in Table 4.2. It is possible that the complexes formed are thermally unstable, and at elevated temperatures are above their thermal decomposition

onset, thereby leaving the nanoparticle stoichiometry unchanged. However, to exhaustively avoid the possibility of etching, pyridine was investigated as an alternative organic species.

Pyridine was investigated as a target volatile organic species due to its weak basicity (therby reducing the chances of etching), relatively low boiling point, and previous success in ligand exchange for photovoltaics literature.[12] Similar to alkylamines, pyridine can bind to cationic surface atoms as an L-type ligand through its nitrogen lone pair electrons, thus native ligand desorption followed by pyridine adsorption was the targeted exchange mechanism, driven by a molar excess of pyridine. Traditionally, ligand exchanges with pyridine are performed at reflux conditions. However, due to the temperature-dependent nature of OLA desorption, pyridine's boiling point of 115°C barely enters OLA's thermal desorption regime as observed in heat up ^{1}H-NMR. As such, a microwave-assisted solvothermal approach was investigated as a means to bypass atmospheric pressure boiling point limits, while microwave radiation could selectively excite the polar head groups of the ligands to aid in exchange. Use of a sealed vessel allowed pressurized reaction conditions above the boiling point of pyridine, and farther into the desorption regime of oleylamine. A temperature and time of 150°C for 30 minutes was selected to facilitate ligand exchange, a temperature well above the OLA desorption onset. Due to pyridine's near universal miscibility, ligand exchange was performed in a single liquid phase. While OLA capped nanoparticles were readily dispersible in non-polar media such as hexanes, toluene, and chloroform, neat pyridine was observed to induce significant flocculation due to its relatively higher polarity ($\varepsilon = 12.4$). To bypass this, the particles were first suspended in toluene followed by dilution with pyridine (1:9 vol:vol toluene:pyridine) to allow for proper dispersion. To the best of our knowledge, this is the first report of microwave-assisted solvothermal ligand exchange reaction.

After the heating cycle and cooling of the dispersion back to room temperature, the pyridine exchanged particles would remain dispersed directly after exchange with the onset of settling observed after an hour with no agitation. The nanoparticles were precipitated with excess hexanes and centrifugation. Prior to the exchange, hexanes were a suitable solvent to disperse the nanoparticles, a qualitative indication of OLA removal by their action as an antisolvent post-exchange. However, after precipitation, the particles did not fully redisperse in additional pyridine, with many visible aggregates in solution. The significant decrease in observed colloidal stability is attributed to the significantly less bulky tail group of pyridine's ring, thereby providing less steric repulsion between adjacent nanoparticles and allowing for some degree of aggregation. To further

probe pyridine's ability to remove OLA ligands, successive pyridine exchange cycles were performed to assess the upper limit of its OLA removal ability. Due to the compromised colloidal stability and rapid settling, quantitative measurements of residual OLA in colloidal dispersions using ^{1}H-NMR were not feasible. In its place, TGA was used to probe the OLA removal capacity of pyridine as shown in Figure 4.7. Each of the pyridine exchanged nanoparticles were dried under vacuum prior to TGA. Note that TGA measurements were run under inert atmosphere to prevent particle oxidation (and thereby changing the mass of the CIGS nanoparticles), thus the mass loss at higher temperatures may not be fully representative of the total mass of OLA due to coke formation from incomplete pyrolysis of OLA.[1] Mass loss up to 500°C is shown in Figure 4.7, which is the maximum processing temperature used for later device fabrication.

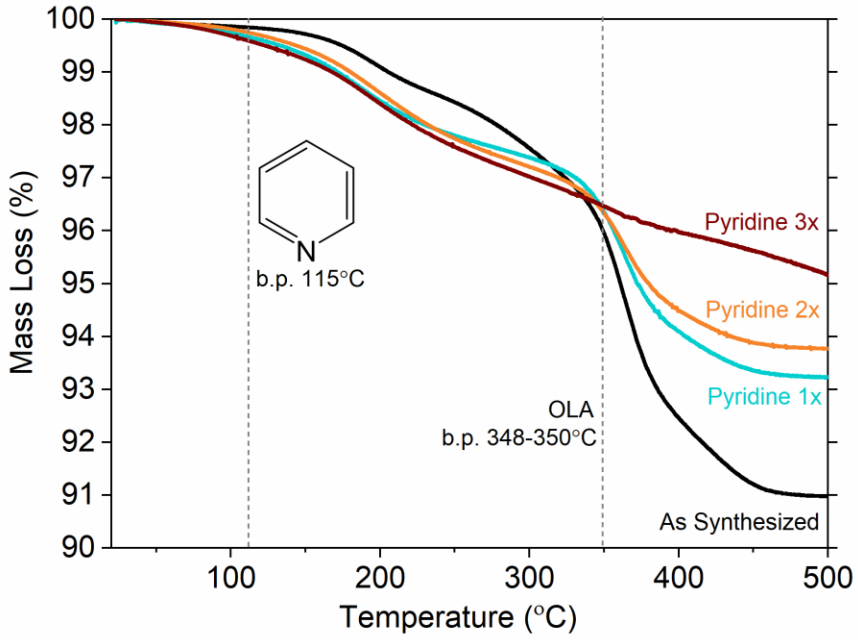

Figure 4.7**.** TGA of CIGS nanoparticles with as synthesized OLA ligands as compared to CIGS nanoparticle ligand exchanged with pyridine in 1, 2, and 3 successive cycles.

As shown in Figure 4.7, pyridine was able to begin OLA removal after a single cycle. However, even after up to three successive pyridine exchanges, a significant portion of OLA as denoted by the mass loss event around 350°C remains. This suggests that there is a critical amount of OLA that can be removed by pyridine-based ligand exchanges, implying there may be an equilibrium of pyridine/OLA capping as defined by their relative strength as ligands. Further, while pyridine is an

intermediate base as defined by HSAB theory, there may be some preference to specific metal surface sites, leaving native ligands on other surface sites bound. Interestingly, after three pyridine exchanges, the TGA mass loss was significantly more linear, not showing a discrete mass loss event at the boiling point of OLA. However, due to the lack of any discrete mass loss events in the three-pyridine exchange case, it is unclear if the observed mass losses are the result of solely pyridine evaporation, decomposition of the nanoparticle, and/or simply from atmospheric or cleaning procedure induced adsorbates on the alumina TGA pan decomposing during heat up. Future work aims to further clarify the TGA data for the three-pyridine exchange case. Further ink formulation of pyridine exchanged nanoparticles was marred by the poor colloidal stability and rapid settling of pyridine capped particles, thereby not meeting the need for high mass concentration inks suitable for blade and slot die printing methods. As such, pyridine exchanges alone were deemed to be a largely ineffective means of complete native ligand removal.

As a means to bypass the limitations of organic ligands such as pyridine, ligand exchange with inorganic sulfide ligands was investigated as an alternative. In the case of OLA to sulfide ligand exchange, sulfide anions bind to the cationic sites on the nanoparticle surface. To maintain charge neutrality, when the neutral L-type OLA ligand is displaced by an anionic sulfide ligand, counter cations of the sulfide salt must be retained to form a net charge neutral nanoparticle. If any X-type ligands are present on the nanoparticle surface (such as 1,2-ethanedithiol, which is a part of the reaction mixture during synthesis), a metathesis type ligand exchange is possible. In this exchange, the cation from the sulfide salt coordinates with a thiolate and induces desorption. The sulfide would then covalently bind to metal cations on the nanoparticle surface as an X-type ligand.[9] Of sulfide salts, sodium and DAS are the two most readily available. However, due to the possible retention of cationic species, sodium sulfide was avoided to prevent an excess of sodium from being retained in the film. While sodium is a favorable dopant species in CIGSSe photovoltaics, too much can harm optoelectronic properties.[30] Therefore, we opted to control sodium content post film deposition for more fine control and selected DAS as the ligand of choice. In the case of DAS, charged ammonium cations can be volatilized as ammonia gas, leaving just protons as a charge balancing cations. Further, during annealing or selenization, the DAS ligand could simply volatilize as ammonia and hydrogen sulfide gas.[31]

A two-phase ligand exchange was employed as is common in the literature.[18] First the nanoparticles were dispersed in non-polar hexanes. Then an immiscible polar phase of NMF and

aqueous DAS solution was added. With stirring, a gradual phase transfer of the nanoparticles in the upper non-polar phase to the polar phase was observed over the course of 16 hours. After purification and drying as described in the experimental section, the nanoparticles could be redispersed in deuterated DMSO forming colloids that did not settle for months. As such, ^{1}H-NMR quantitation of OLA removal was possible. Using ethylene carbonate as an internal standard, remaining OLA was quantified using peak fitting and integration of the alkene proton peak, which is distinctly separate from the chemical shift of other trace species such as washing solvents. As shown in Figure 4.9a, the sulfide exchange was observed to be extremely effective at removing OLA, removing 97.3% of the native ligands, determined through comparison of the as-synthesized and ligand exchanged alkene peak integration. This result is a substantial improvement on previous quantitative reports in the literature, whereby only ~50% of OLA was removed with DAS. In the previous literature report, pre-exchanged particles were observed to have a sharp peak at 5.35 ppm, slightly offset from the broadened bound alkene peak at approximately 5.4 ppm.[22] This sharp peak, likely being free OLA, may have inhibited their sulfide exchange by altering the equilibrium, highlighting the need for sufficient nanoparticle purification post-synthesis to remove free OLA. In this work, sufficient nanoparticle washing was determined through ^{1}H-NMR, where no free OLA resonance was observed after four successive precipitation/resuspension cycles with isopropyl alcohol and hexanes as antisolvent and solvent respectively as shown in Figure 4.8.

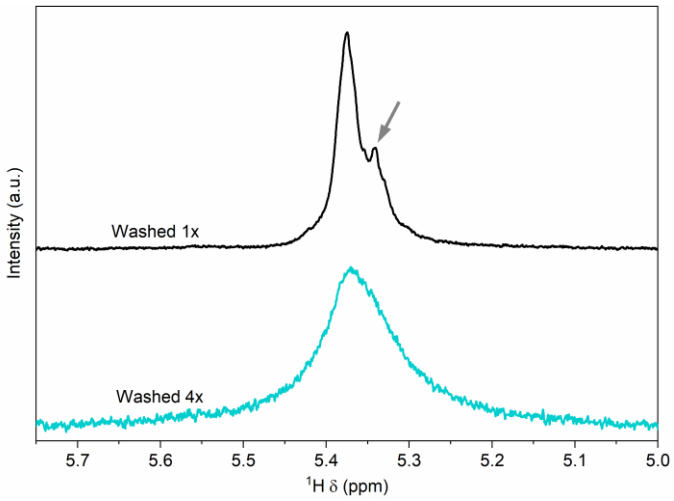

Figure 4.8. ^{1}H-NMR of the alkene proton resonance of oleylamine capped CIGS nanoparticles after being washed (as described in the experimental section) for one and four cycles. Arrow shows sharp resonance of free oleylamine, demonstrating underpurification. Chloroform-D was used as a deuterated solvent.

Additionally, we believe the longer duration of the sulfide exchange used in this report allowed for more complete exchange. However, this longer duration exchange also exposes the nanoparticles to the fairly aggressive DAS species for a longer time, raising concerns of nanoparticle surface etching. XRF measurements of DAS exchanged nanoparticles revealed that some copper was in fact etched from the nanoparticle during the exchange. DAS is known to dissolve certain metal chalcogenides such as copper selenide, so selective etching of copper from the chalcogenide nanoparticle is not unexpected and has been observed in previous reports.[32]

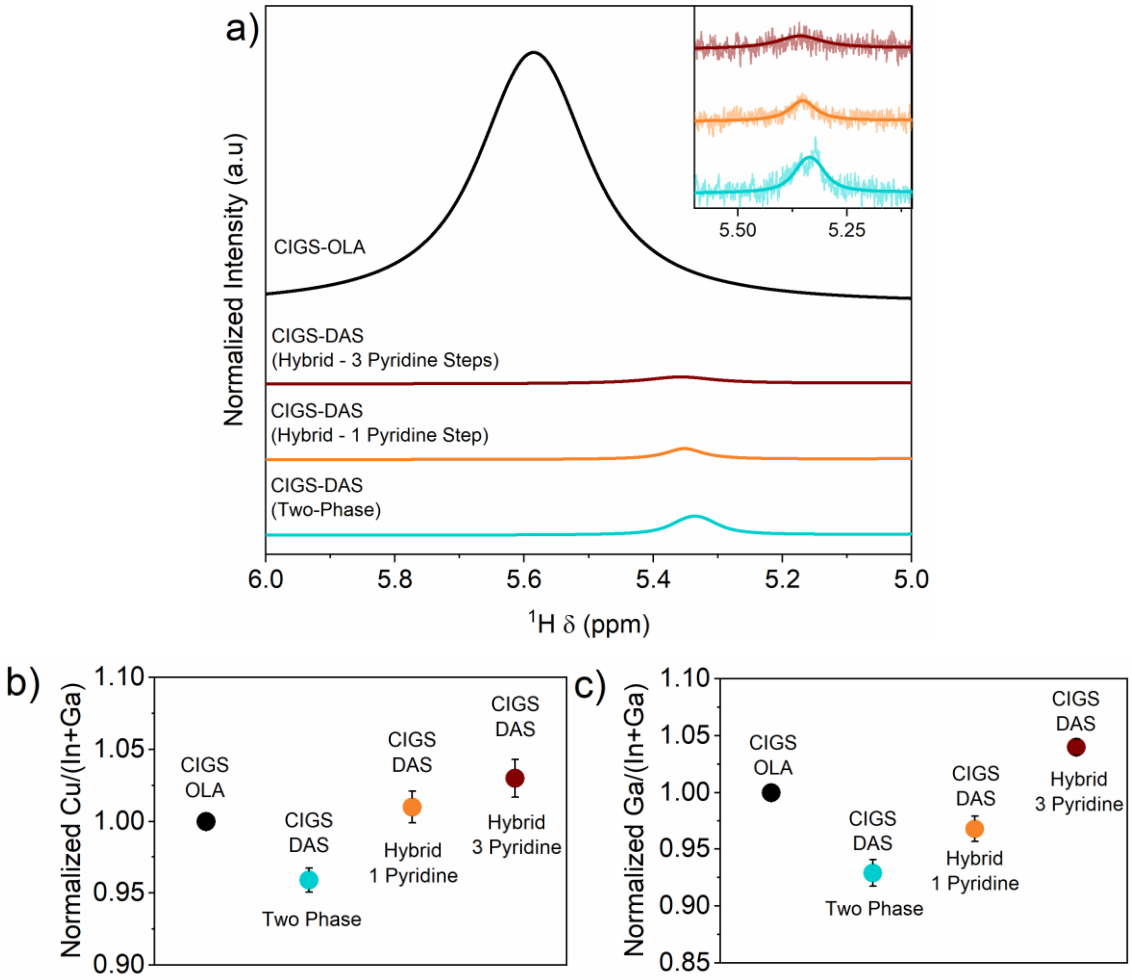

Figure 4.9 a) Fitted ^{1}H-NMR comparing alkene proton resonance on OLA capped CIGS nanoparticles and hybrid pyridine/DAS exchange and DAS exchange (inset shows fitted data superimposed on experimental data for each of the CIGS-DAS exchanges). The shift in the alkene peak positions between the CIGS-OLA spectrum and CIGS-DAS spectra are due to the use of different deuterated solvents, where Toluene-D8 and DMSO-D6 were used, respectively. b) Cu/(In+Ga) and **c)** Ga/(In+Ga) ratios normalized to 1 for the respective exchange methods measured by XRF (As synthesized CIG = 0.92 and GIG = 0.29).

Additionally, a corresponding drop in Ga/(In+Ga) ratio was observed, implying that Ga may also be selectively etched. While this copper and gallium etching could be compensated for by increasing the relative metal content of the original nanoparticle, one of the goals of solution processing is to increase materials utilization. Thus, it is advantageous to avoid this etching outright. It was hypothesized that the combination of the solvothermal pyridine exchange followed by the DAS exchange would allow for significantly reduced residence time in the DAS containing polar phase, thereby decreasing etching of metals while also substantially decreasing the total time required for the ligand exchange. The pyridine exchange is able to remove a portion of OLA, providing holes in the protective layer of sterically hindering and hydrophobic alkyl chains, allowing DAS to access the nanoparticle surface more readily. This sequential exchange was performed as described in the experimental section, where the pyridine-exchanged particles were directly dispersed in the NMF/DAS phase and allowed to stir for a total of 120 minutes and is referred to as the hybrid ligand exchange (hybrid LigEx). The resulting exchanged particles were purified and dried, followed by analysis by quantitative ^{1}H-NMR and XRF. The two-step hybrid organic-inorganic exchange was able to surpass the OLA removal attained by the single step two-phase method. No traces of pyridine were observed in the ^{1}H-NMR spectra, demonstrating its ease of displacement by DAS as shown in Figure 4.10.

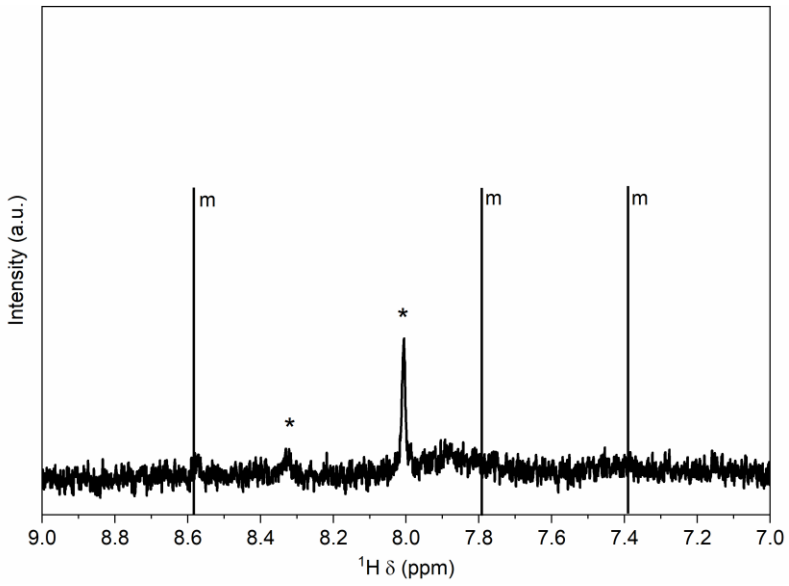

Figure 4.10. ^{1}H-NMR after hybrid ligand exchange showing no residual pyridine content (* denote trace impurities and black lines indicate the centers of the multiplet (m) peaks of pyridine in DMSO-d6). DMSO-D6 was used as a deuterated solvent.

Additionally, XRF confirmed negligible copper etching and substantially decreased gallium etching, confirming the hypothesis that decrease in DAS containing polar phase residence time can prevent metal etching. The removal of OLA could be further driven to completion by repeating the pyridine exchange several times. ^{1}H-NMR quantitation of hybrid exchanged nanoparticles with three pyridine exchanges show near complete removal of the alkene peak. For the hybrid LigEx with 1 pyridine cycle, 98.4% of the original alkene intensity was removed. For the hybrid LigEx with three pyridine cycles, quantitation was also performed yielding 98.4% removal again, however, we note that the very low signal to noises ratio at that level of OLA removal likely yields inaccurate quantitation for this sample. To confirm the hybrid LigEx did not alter crystalline phase or induce the formation of any amorphous phase material, XRD and Raman were run on nanoparticles exchanged with both the one-step, two-phase transfer method and hybrid LigEx as is shown in Figure 4.11.

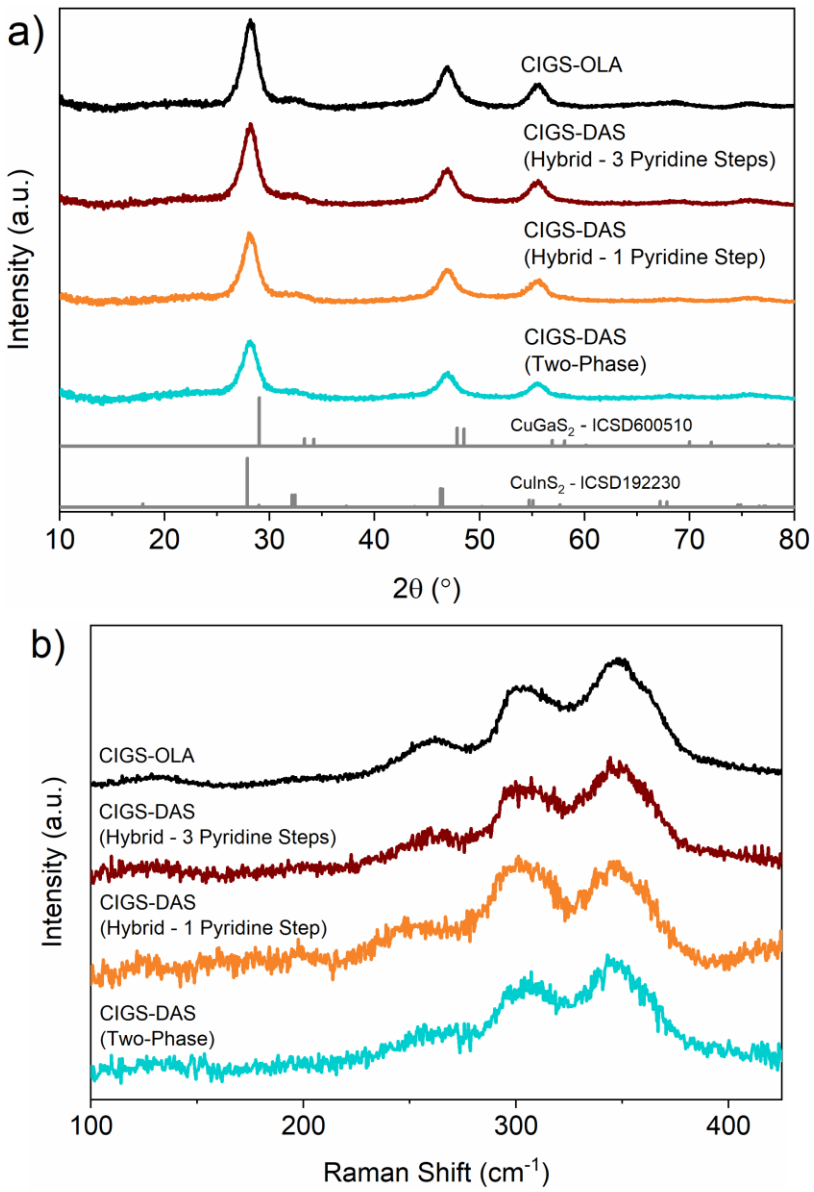

Figure 4.11. a) XRD and b) Raman of single step and hybrid ligand exchanged films with 1 and 3 pyridine cycles.

No changes in crystalline phases or evolution of secondary phase formation were observed via both XRD and Raman.

4.3.3 Ink Formulation

With near exhaustive OLA removal obtained by the rapid hybrid exchange method, ink formulation was explored with the goal to form stable inks with mass concentrations exceeding 200

mg/mL. As previously mentioned, these high mass concentration inks allow us to bypass non-scalable and low materials utilization coating techniques such as spin coating and enables scalable coating techniques such as blade coating. Various polar aprotic solvents were tested such as acetonitrile, DMF, NMF, formamide, and DMSO. Polar protic species such as alcohols and water (which were observed to disperse the ligand exchange nanoparticles well) were avoided due to their ability to bind as alkoxide and hydroxide ligands, which are known to decompose to metal oxides.[33] While all tested polar solvents could disperse the sulfide ligand exchanged nanoparticles to some extent, formamide, NMF, and DMSO were able to disperse the exchanged nanoparticles at mass concentrations exceeding 200 mg/mL without aggregates. Formamide has been previously investigated as a solvent for DAS exchanged $CuInS_2$ nanoparticles. However, in work by Dierick et al., it was observed that the use of formamide as a solvent was responsible for the oxidation of dropcast nanoparticle CIS thin films upon annealing in an inert atmosphere. They observed this oxidation in XPS via a transition of surface S^{2-} to positive oxidation state sulfur bonded to oxygen as SO_2, SO_3-, and/or SO_4^{2-} moieties. Furthermore, they observed that the surface oxidation inhibited sintering of the sulfide capped nanoparticles.[31] As such, we chose to avoid formamide and its derivatives, NMF and DMF, for ink formulation. Ideally, a solvent molecule that does not contain oxygen could completely avoid oxidation concerns. Acetonitrile is such a solvent, however, acetonitrile-based inks were only able to disperse a portion of the ligand exchanged nanoparticles and thereby contained a substantial amount of aggregates. DMSO was observed to disperse the sulfide-capped nanoparticles with ease, and formed stable inks at mass concentrations of up to 250 mg/mL without gelling. These inks were stable for over two months when stored in an inert atmosphere without settling and for several days when stored in air. However, as an oxygen containing molecule, oxidation of the nanoparticle films similar to what had been observed with formamide was a concern. To test if DMSO based inks could induce particle oxidation, XPS was performed on two dropcast thin films, one containing DMSO and sulfide exchanged CIGS, and a control of sulfide exchanged CIGS in the non-oxygen-containing solvent, acetonitrile. Both films were coated and annealed at 300°C for 90s in a nitrogen filled glovebox. As shown in Figure 4.12 a) through d), both films appeared identical under XPS and neither contained the Sulfur IV oxidation state peak observed at 169.5 eV in Dierick et al.'s previous report that made use of formamide as a solvent.[31] Furthermore, analysis of gallium, which forms the most stable oxide of the cations in CIGS did not show any discernable oxide content, only exhibiting a single gallium

peak as is commonly observed or CIGS/CIGSSe.[34] This lack of oxidation and the high stability of DMSO based inks coupled with its low toxicity made for an attractive ink for device fabrication.

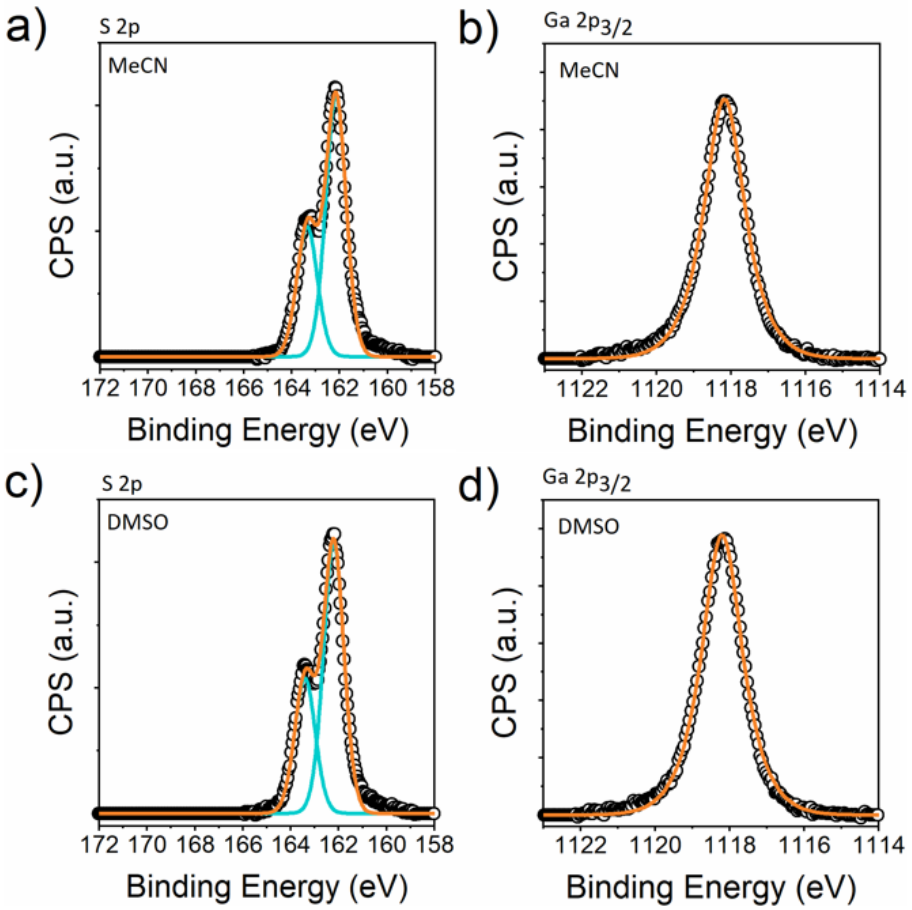

Figure 4.12. a) and **c)** XPS of sulfur 2p peak showing absence of any sulfoxide (169.5 eV) and b) and d) XPS of gallium $2p_{3/2}$ peak showing absence of any gallium oxide species for both the control acetonitrile and DMSO inks demonstrating absence of solvent induced oxidation. Circles, blue lines, and orange lines denote experimental data points, individual peak fits, and overall fit, respectively.

4.3.4 Film Coating

Blade coating was selected as a scalable coating method for ligand exchanged inks and was performed using a custom-built automated blade coater based on a KClone K200 3D printer with controllable substrate-blade gap, coating speed, coating pattern, and substrate temperature. DMSO was observed to dewet from the edges of both soda-lime glass and molybdenum coated soda lime glass substrates during long drying periods at room temperature. A heated bed was found to be effective in enabling rapid drying prior to edge dewetting. A bed temperature of 80°C was found to

be most effective. Using the conditions described in the experimental section, highly uniform coatings at thicknesses of approximately 300 nm per coating were obtained. Sequential coatings could be performed by annealing the films at a minimum of 300°C for 90 s between coatings. If not sufficiently annealed between coatings, it was observed that subsequent coatings would redisperse underlying layers and yield rough and discontinuous films. After four successive coatings, remarkably smooth films with an average and RMS roughness of 5.07 and 6.25 nm, respectively, were obtained at thicknesses of approximately 1200 nm as shown in the SEM cross section in Figure 4.13a. Additionally, the films were free of any microcracks as evidenced by SEM plan view as shown in Figure 4.13b.

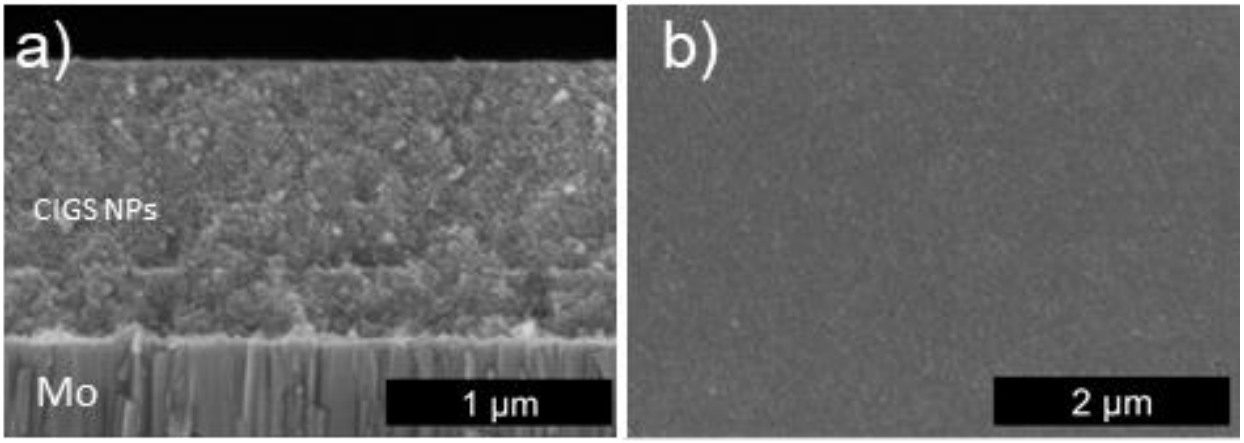

Figure 4.13. a) SEM Cross-section and b) plan view of hybrid ligand exchange nanoparticle film coated by blade coating.

A larger area optical micrograph and profilometry scan are shown in Figure 4.14, further demonstrating the high quality of the coated films.

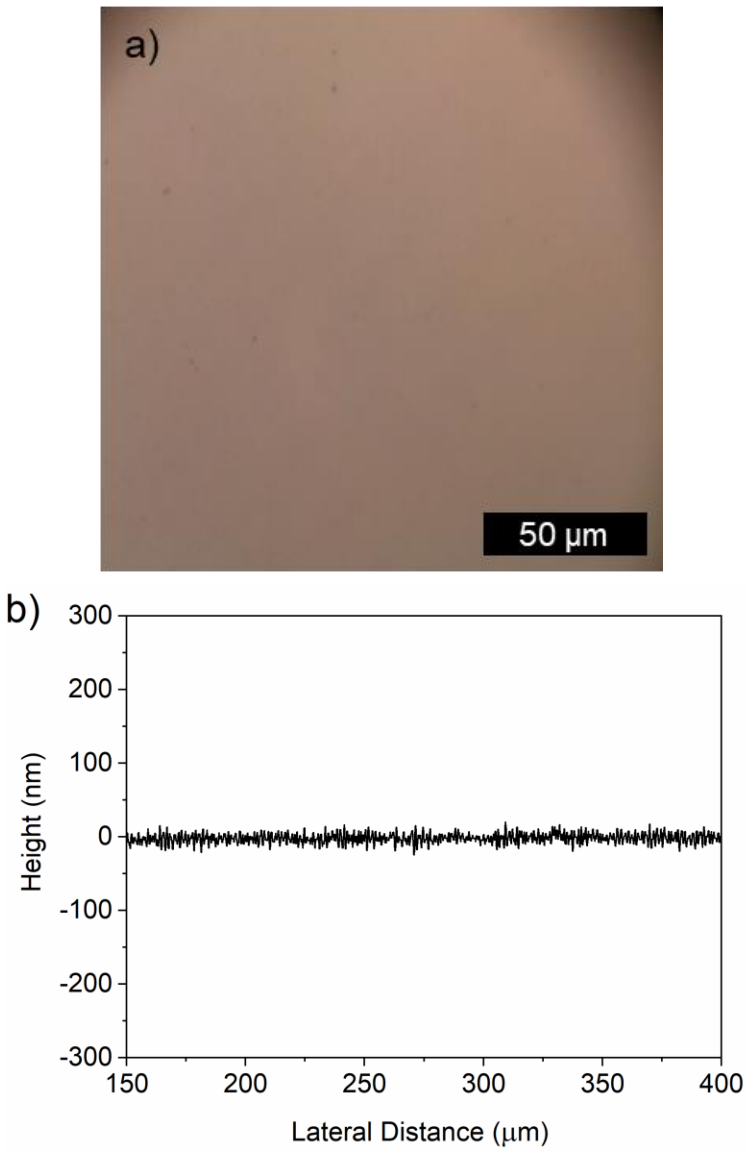

Figure 4.14. a) Optical microscope image of coated ligand exchanged film and **b)** profilometry demonstrating low surface roughness and lack of microcracks.

The hybrid LigEx films were uniquely resistant to microcracking, which has been a significant concern and the topic of entire research articles in other nanoparticle-based coating methods. In these reports, additional carbonaceous long chain surfactants, DDT or OLA, were incorporated in the ink through either reduced nanoparticle washing, or direct addition, counterproductive to the goal of removing carbon contamination.[35,36]

4.3.5 Selenization and Device Fabrication

Selenization of coated nanoparticle films was performed using a tubular furnace with ~300 mg of elemental selenium pellets under an argon atmosphere at 500°C. XRD and Raman analysis of the selenized films reveal conversion of the original CIGS nanoparticles to sulfur depleted CIGSSe with improved crystallinity. Conversion from sulfide to selenide is clearly visible in the shift in XRD peaks, as well as reduction in intensity of the sulfide CIGS A1 Raman peak, centered at approximately 300 cm^{-1}, and the emergence of a sharp A1 Raman peak of selenide $Cu(In,Ga)Se_2$ at approximately 178 cm^{-1}. Additionally, no secondary phases were found, notably residual elemental selenium or $Cu_{2-x}Se$ as shown in Figure 4.15 (however, it should be noted that Raman spectroscopy is surface sensitive, thus may not be representative of the back of the absorber layer). As such, no pre or post selenization treatment in highly toxic potassium cyanide were needed, reducing the toxicity and number of steps in film processing. XRF measurements showed post-selenization elemental ratios of 0.92 for Cu/(In+Ga) and 0.28 for Ga/(In+Ga).

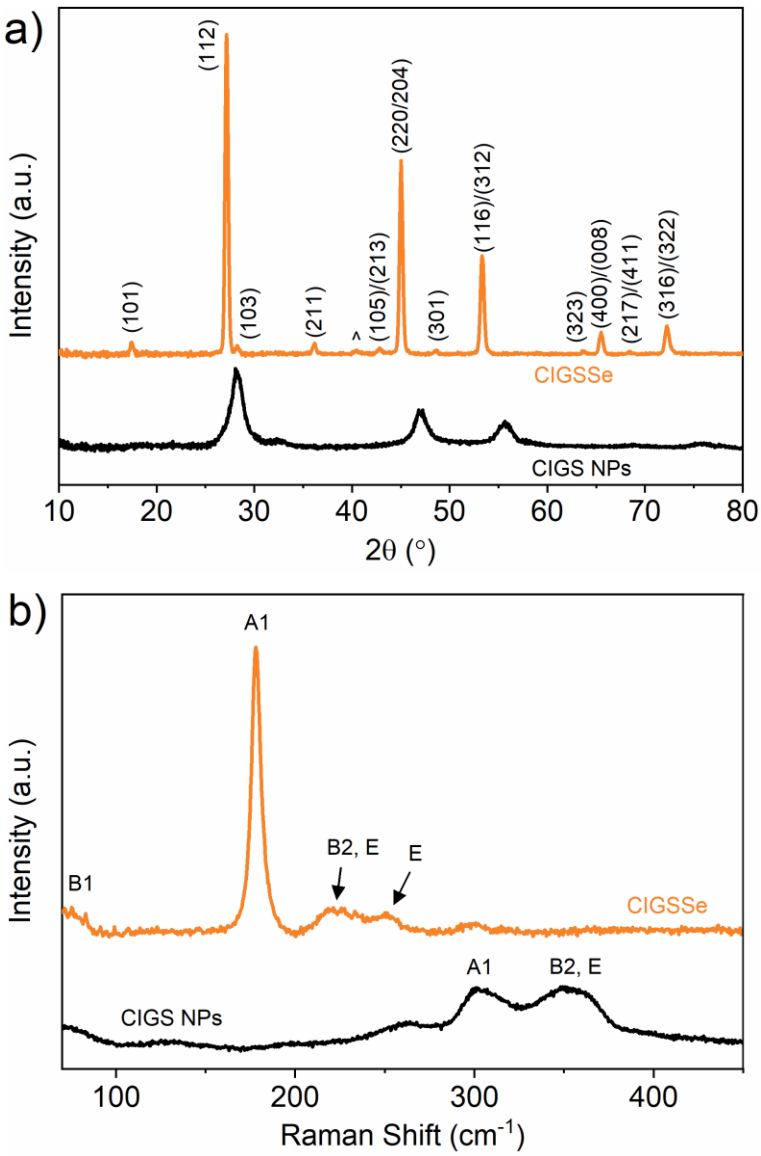

Figure 4.15. a) XRD and b) Raman of CIGS nanoparticles and selenized CIGSSe from hybrid ligand exchanged ink (^ denotes the molybdenum substrate's XRD peak).

Further analysis of the carbon content was performed on the coated and selenized films using FTIR and Raman spectroscopy. A thickness normalized (profilometry calibrated) comparison of an annealed unexchanged nanoparticle film, annealed ligand exchanged nanoparticle film coated from DMSO, and selenization of the ligand exchanged nanoparticle film was performed using FTIR on soda lime glass substrates. As shown in Figure 4.16, a significant reduction in C-H stretch intensity is observed when comparing unexchanged nanoparticle films with ligand exchanged nanoparticle films.

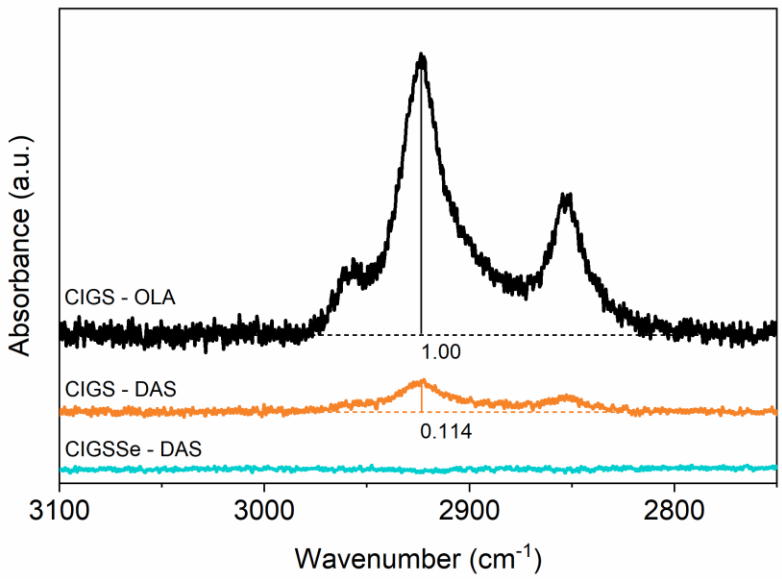

Figure 4.16. Thickness normalized FTIR on blade coated nanoparticles films of CIGS – OLA (coated from hexanethiol), Hybrid CIGS – DAS (coated from DMSO), and selenized hybrid CIGS – DAS (CIGSSe, 500°C, 10 min) on sodalime glass.

After selenization, there is a complete absence of C-H stretches. If all C-H intensity is attributed to residual OLA, there is a small discrepancy between the quantitative ^{1}H-NMR and the FTIR of the coated CIGS – DAS film. It is believed this discrepancy is due to the entrainment of coating solvent in the annealed nanoparticle film, which has been observed in other solution processed literature.[37] While selenized films of ligand exchanged CIGS nanoparticle films were free of C-H stretch in FTIR, Raman spectroscopy was used to probe graphitic carbon-carbon bonds. Due to Raman's low penetration depth of only a few hundred nanometers, a thin ~300 nm thick film was used. Miniscule, but discernable peaks were observed in Raman corresponding to graphitic carbon-carbon bonds as shown in Figure 4.17.

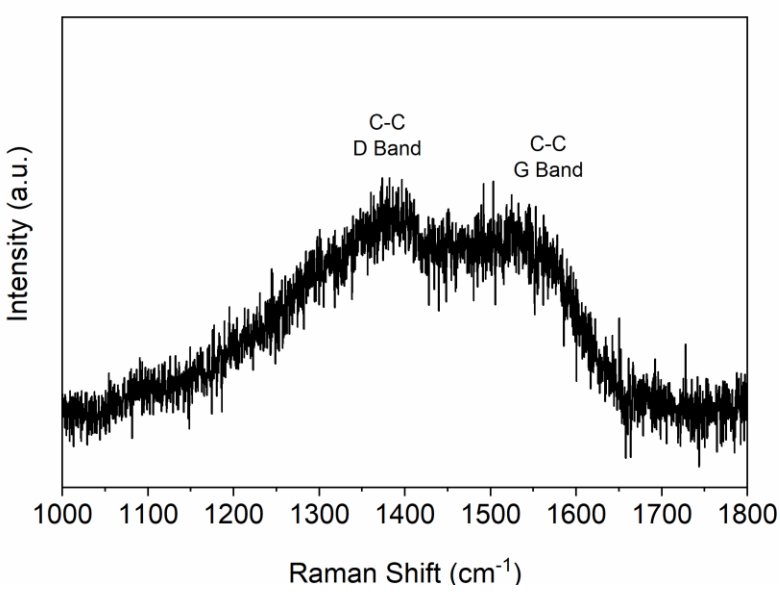

Figure 4.17. Raman spectrum of a thin selenized hybrid LigEx nanoparticle film showing trace graphitic carbon content persisting in the absorber.

We believe this residual signal is from the remaining ~1% of initial OLA, and potentially some of the entrained solvent decomposing during selenization.

Selenization of hybrid exchanged CIGS nanoparticles on molybdenum substrates for device fabrication was performed and compared with selenized CIGS nanoparticle films from conventional methods (OLA ligands, acetylacetonate salts for synthesis, hexanethiol as a coating solvent, coating and annealing in air). Sodium for both films was provided from soda lime glass substrates or by using 10, or 15 nm of electron beam evaporated sodium fluoride. All films were selenized at 500°C for 20 minutes. Cross-sections of all films is shown in Figure 4.18.

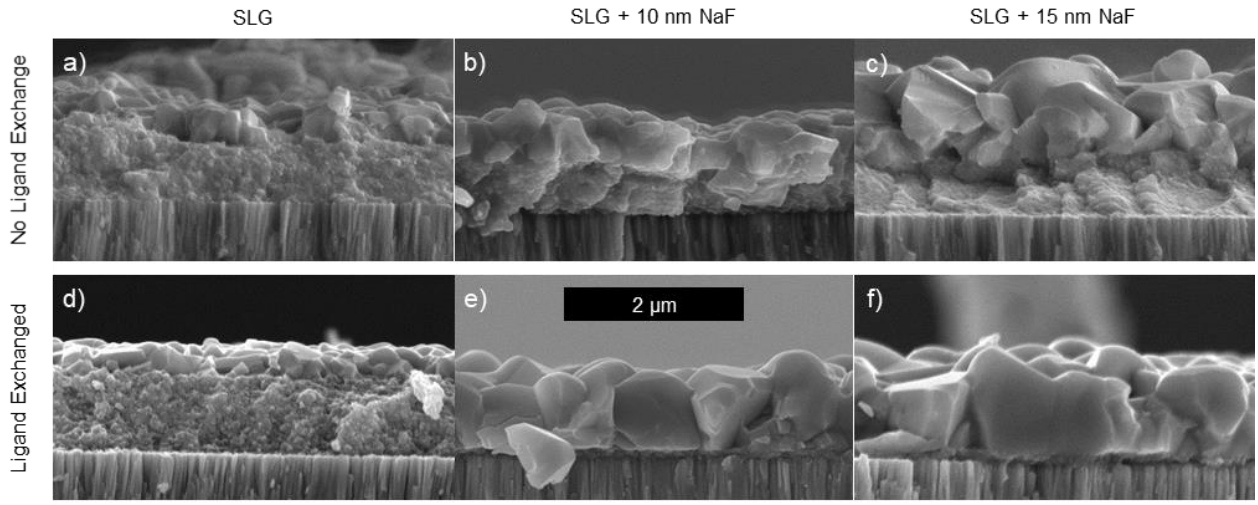

Figure 4.18. SEM cross-sections of non-ligand exchanged films selenized with a) no added sodium, b) 10 nm of NaF, c) 15 nm NaF as well as SEM cross sections of hybrid LigEx films slenized with d) no added sodium, e) 10 nm NaF, and f) 15 nm NaF.

Conventional and hybrid LigEx films subjected to the aforementioned selenization conditions began to grow from their original nanocrystalline size in all cases. However, in both cases, sodium from only the soda lime glass was not sufficient for large grain growth. Only a thin upper crust of small sub-micron grains appeared at the upper surface, with a large unsintered underlayer. With just 10 nm of NaF, the hybrid LigEx film was able to grow large micron size grains that nearly spanned the entire film laterally. For the conventional film with 10 nm of NaF, an improvement in grain growth over the soda lime glass alone was observed, however, grains only spanned about half the thickness of the film and remained significantly smaller than in the hybrid LigEx film. With the addition of further sodium content, no appreciable change in the hybrid LigEx film was observed. The additional sodium helped the conventional film leading to further increases in grain size. However, the unsintered fine grain layer remained about one third of the film thickness, due to the retention of significant carbon impurity from OLA ligands.

While containing much larger grains, a small nanoparticle like layer is also observed for the ligand exchanged film. This layer was further probed using STEM-EDS to elucidate the species present along with comparison to a conventional film as shown in Figure 4.19.

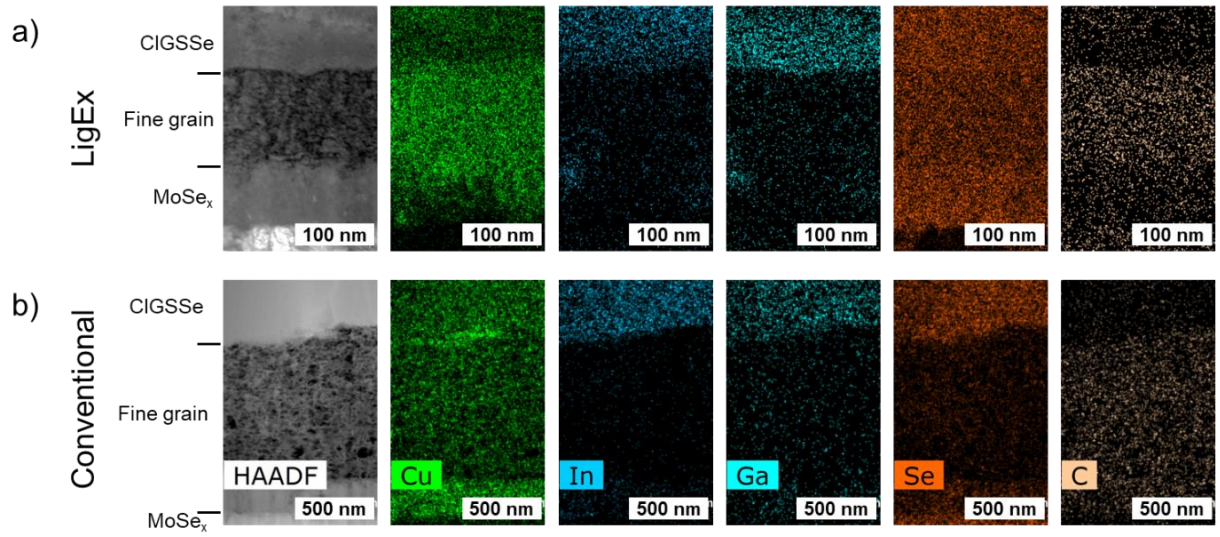

Figure 4.19. STEM-EDS of residual unsintered layer on a a) hybrid ligand exchanged film b) conventional non-ligand-exchanged film. Note the difference in scale bars between images.

Table 4.3. Atomic percent of various species present in the fine grain layer for both hybrid LigEx films and conventional films.

Atom	**LigEx (at%)**	**Conventional (at%)**
Cu	41.10	23.02
In	1.21	0.60
Ga	1.24	1.81
S	2.40	2.34
Se	35.83	16.12
C	8.11	34.35
O	2.14	14.07
Na	3.63	5.78
Mo	4.34	1.91

The conventional films have a predominantly carbon-based fine grain layer with significantly higher carbon content than the hybrid LigEx film. Additionally, a "sponge" like morphology can be observed for the conventional film's carbon-based fine grain layer whereas the for the hybrid LigEx film, a more nanocrystalline appearance is observed. A slight increase in carbon content as compared to the bulk background is observed for the hybrid LigEx film (possibly due to the ~1.4% native ligand remaining as well as potentially decomposed entrained solvent). However, the residual unsintered layer is composed almost entirely of copper and selenium, devoid of gallium and indium. As mentioned in the text, a C/(Cu+Se) ratio of 0.10 is observed for a ~100 nm thick fine grain whereas for the conventional film a C/(Cu+Se) ratio of 0.88 is observed for a substantially thicker layer. For the hybrid LigEx, this suggests that this unincorporated layer is a function of the selenization reaction mechanism as opposed to carbon entrainment. We hypothesize that the similar ratio of copper and selenium, or a CuSe like material, is the result of the high selenium vapor pressure present during selenization. This may cause copper to maintain a +2 oxidation state, thereby preventing its incorporation into the $Cu(In,Ga)(S,Se)_2$ lattice in the +1 oxidation state. More fine control of selenium may be needed to generate fully laterally spanning grains using techniques such as flow RTP, where selenium temperature can be controlled independently of the substrate as is shown in previous reports. However, existing results show promise, nearly removing unsintered/carbon residue layers and significantly improving grain growth due to the absence of carbon impurity.

Since potassium cyanide was not needed for the hybrid LigEx films to correct elemental ratios, remove surface oxide or $Cu_{2-x}Se$ secondary phases, potassium cyanide was also not used in the conventional device as has been used prior to selenization in our group's previous reports.[24,25] This allowed for direct comparison between the two devices, decoupling any effects that residual potassium could have on the electronic or morphological properties. Devices were prepared from both the conventional unexchanged and hybrid ligand exchanged methods with varying sodium content and is shown in Table 4.4, no antireflection coatings were used.

Table 4.4. Comparison of device characteristics without antireflective coatings for conventional and hybrid LigEx based devices at varying sodium contents.

Film	NaF (nm)	J_{sc} (mA/cm^2)	V_{oc} (V)	FF (%)	η (%)
Conventional	0	21.5	0.55	62.3	7.36
	10	24.2	0.58	63.7	8.93
	15	27.4	0.58	60.1	9.67
Hybrid LigEx	0	17.1	0.38	53.1	3.44
	10	27.0	0.60	67.3	10.90
	15	24.4	0.58	60.4	8.53

The conventional films exhibit continued improvements in efficiency as more sodium is added, peaking at 9.67%. However, in the hybrid LigEx case, the efficiency peaks at 10.90% with 10 nm of NaF added. For the conventional film, larger amounts of sodium are required to facilitate the necessary grain growth to adequately collect current, as shown by the increasing J_{sc}. However, for the hybrid LigEx devices, lack of carbon content allows for rapid selenization with only 10 nm of external NaF. This allows the hybrid LigEx devices to decouple the grain growth enhancing effects of sodium with the optoelectronic effects. An overabundance of sodium is known to degrade device performance and is exemplified by the decrease in efficiency of the hybrid LigEx device with 15 nm of NaF. The ability to optimize sodium content by optoelectronic properties as opposed to morphological properties allows for more fine-tuned control and higher efficiencies. However, it should be noted that some sodium is needed to induce grain growth in the hybrid LigEx films. It is hypothesized that the anionic surface of the sulfide capped nanoparticles may not wet liquid selenium, the primary flux medium in selenization. Addition of sodium changes the wetting properties due to formation of Na_xSe species which can act as flux.

The best hybrid ligEx efficiency device was reproduced with 10 nm NaF and an antireflection coating was added to enhance current collection. An identically fabricated (also with 10 nm NaF) conventional film was prepared for direct comparison. A notably higher efficiency of 12.0% was obtained as compared to the non-ligand exchange device with an efficiency of 9.2 %. As shown in Figure 4.20 and Table 4.5 and 4.6, nearly all device parameters have improved with the implementation of the hybrid ligand exchanged methods.

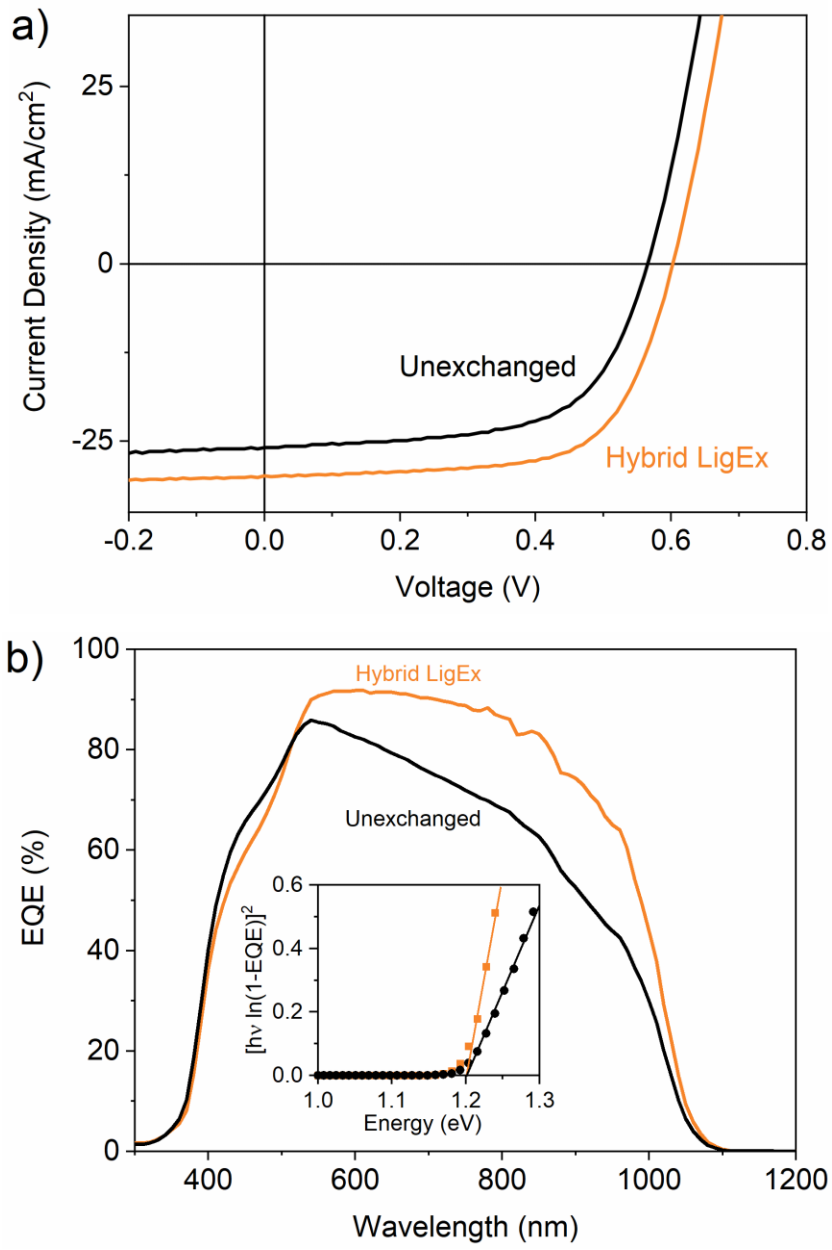

Figure 4.20. a) J-V curve for champion devices prepared from selenized conventional unexchanged nanoparticle films compared to selenized hybrid ligand exchange nanoparticle films b) and corresponding EQE from each device.

Notably, we observe a 14.2% increase in J_{sc} which is attributed to the significantly enhanced grain growth of selenized hybrid ligand exchanged nanoparticle films as compared to the conventional unexchanged film, yielding thicker, high-quality grains of CIGSSe to absorb incident photons.

Table 4.5. Device parameters of the cells on the hybrid LigEx device (Cell 2). Device characteristics reported from total area which was determined from image analysis (A = 0.451, 0.458, and 0.454 cm^2 for cells 1,2 and 3 respectively).

	η (%)	**V_{oc} (V)**	**J_{sc} (mA/cm^2)**	**FF (%)**	**R_s (Ω cm^2)**	**R_{sh} (Ω cm^2)**	**n**
1	11.8	0.60	29.7	66.1	1.22	576	1.55
2	12.0	0.60	29.7	67.5	1.00	605	1.59
3	11.9	0.60	29.5	67.1	0.93	502	1.48
Average	11.9	0.60	29.6	66.9	1.05	561	1.54

Table 4.6. Device parameters of the cells on the conventional device. Device characteristics reported from total area which was determined from image analysis (A = 0.510, 0.514, and 0.515 cm^2 for cells 1,2 and 3 respectively).

	η (%)	**V_{oc} (V)**	**J_{sc} (mA/cm^2)**	**FF (%)**	**R_s (Ω cm^2)**	**R_{sh} (Ω cm^2)**	**n**
1	9.2	0.57	26.0	62.1	0.9	554	1.71
2	9.0	0.58	25.8	60.3	1.04	476	1.58
3	8.3	0.57	23.1	62.8	1.13	297	1.55
Average	8.8	0.57	25.0	61.7	1.02	442	1.61

Capacitance-voltage measurement of the hybrid ligand exchanged device revealed a majority carrier concentration of $1.30*10^{16}$ as shown in Figure 4.21.

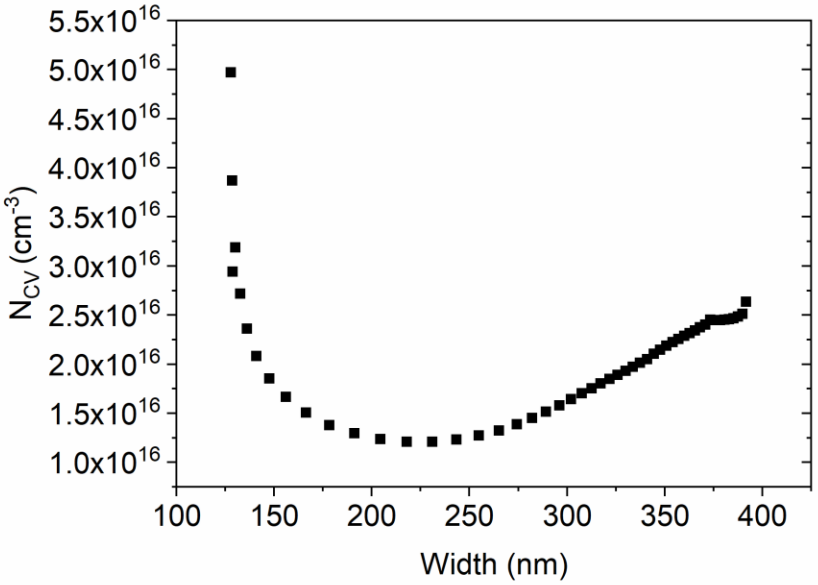

Figure 4.21. N_{CV} versus width extracted from capacitance-voltage measurements on cell 3 for the hybrid LigEx device.

While promising initial efficiencies were obtained with selenized hybrid LigEx nanoparticle films, further optimization of selenization with thicker films may be a pathway to higher J_{sc}. Additionally, the incorporation of heavier alkali to improve V_{oc} and the incorporation of gallium grading to reduce interface recombination are both areas of future study to improve device efficiency and verify if such ligand exchange methods are more effective than the current record carbonaceous ligand containing nanoparticle films at reaching high efficiencies.[24] Nevertheless, removal of carbonaceous impurities represents a forward step in replicating the existing carbon-free, vacuum-based absorbers using highly scalable, solution processed colloidal nanoparticles.

4.4 Conclusions

A rapid and exhaustive ligand exchange making use of sequential organic/inorganic exchanges was developed as a means to remove native oleylamine ligands and their resulting carbonaceous impurities in colloidal nanoparticle based $Cu(In,Ga)(S,Se)_2$ photovoltaics. Microwave-assisted solvothermal heating with pyridine enabled exposure of the nanoparticles to temperatures above oleylamine's desorption onset of 110°C-120°C and decreased the residence time needed for subsequent inorganic ligand exchange with the fairly aggressive species,

diammonium sulfide. This hybrid organic/inorganic method prevented etching of the nanoparticle surface, decreased the total time needed for exchange, and improved the net removal of oleylamine as compared to each of its individual steps yielding greater than 98% removal of native ligands with negligible impact to nanoparticle stoichiometry. The hybrid ligand exchanged nanoparticles could be dispersed in stable and benign inks of dimethyl sufoxide at mass concentration exceeding 200 mg/mL, enabling scalable coating techniques such as blade coating. High quality, crack free, and ultra-smooth nanoparticle films were obtained from the hybrid ligand exchanged inks. Significantly improved selenization and grain growth was observed as compared to selenized films of conventionally prepared, non-ligand-exchanged nanoparticles. Subsequent devices showed that selenized hybrid ligand exchanged nanoparticle films yielded a substantial increase in power conversion efficiency over the non-ligand-exchanged control, reaching a champion total-area efficiency of 12.0%. The enhancements afforded by the hybrid ligand exchange over conventional methods demonstrates the merit of the developed methods for fabrication of high-quality solution processed CIGSSe absorber layers.

4.5 Acknowledgments

This work was supported by funding from the National Science Foundation (NSF) under grants #1735282-NRT (SFEWS), #1534691-DMR (DMREF), and #10001536 (INFEWS). Research was carried out in part at the Center for Functional Nanomaterials, Brookhaven National Laboratory, which is supported by the U.S. Department of Energy, Office of Basic Energy Sciences, under contract no. DE-SC0012704. The authors would also like to acknowledge Joseph Andler and Xianyi Hu for their assistance in preparing molybdenum-coated soda lime glass substrates and Prof. Daniel Flaherty from the Department of Medicinal Chemistry and Molecular Pharmacology at Purdue University for allowing the use of his Biotage Initiator microwave reactor. Additionally, the authors would like to acknowledge Dr. Huaping Mo from Purdue University's Interdepartmental NMR Facility for operating the NMR during the in situ heat-up ^{1}H-NMR experiment, Dr. Dmitry Zemlyanov from Purdue University's Birck Nanotechnology for running XPS data collection, Connie Bonham from the Purdue University Mass Spectrometry Center for running GC–MS, and Kyle Weidman for collecting HAADF STEM images on as-synthesized nanoparticles.

4.6 References

(1) Martin, T. R.; Katahara, J. K.; Bucherl, C. N.; Krueger, B. W.; Hillhouse, H. W.; Luscombe, C. K. Nanoparticle Ligands and Pyrolized Graphitic Carbon in CZTSSe Photovoltaic Devices. *Chem. Mater.* **2016**, *28* (1), 135–145. https://doi.org/10.1021/acs.chemmater.5b03426.

(2) Rehan, S.; Kim, K. Y.; Han, J.; Eo, Y.-J.; Gwak, J.; Ahn, S. K.; Yun, J. H.; Yoon, K.; Cho, A.; Ahn, S. Carbon-Impurity Affected Depth Elemental Distribution in Solution-Processed Inorganic Thin Films for Solar Cell Application. *ACS Appl. Mater. Interfaces* **2016**, *8* (8), 5261–5272. https://doi.org/10.1021/acsami.5b10789.

(3) van Embden, J.; Chesman, A. S. R.; Jasieniak, J. J. The Heat-Up Synthesis of Colloidal Nanocrystals. *Chem. Mater.* **2015**, *27* (7), 2246–2285. https://doi.org/10.1021/cm5028964.

(4) Coughlan, C.; Ibáñez, M.; Dobrozhan, O.; Singh, A.; Cabot, A.; Ryan, K. M. Compound Copper Chalcogenide Nanocrystals. *Chem. Rev.* **2017**, *117* (9), 5865–6109. https://doi.org/10.1021/acs.chemrev.6b00376.

(5) Hages, C. J.; Koeper, M. J.; Miskin, C. K.; Brew, K. W.; Agrawal, R. Controlled Grain Growth for High Performance Nanoparticle-Based Kesterite Solar Cells. *Chem. Mater.* **2016**, *28* (21), 7703–7714. https://doi.org/10.1021/acs.chemmater.6b02733.

(6) McLeod, S.; Alruqobah, E.; Agrawal, R. Liquid Assisted Grain Growth in Solution Processed Cu(In,Ga)(S,Se)$_2$. *Sol. Energy Mater. Sol. Cells* **2019**, *195*, 12–23. https://doi.org/10.1016/j.solmat.2019.02.020.

(7) Wu, W.; Cao, Y.; Caspar, J. V.; Guo, Q.; Johnson, L. K.; Malajovich, I.; Rosenfeld, H. D.; Choudhury, K. R. Studies of the Fine-Grain Sub-Layer in the Printed CZTSSe Photovoltaic Devices. *J. Mater. Chem. C* **2014**, *2* (19), 3777–3781. https://doi.org/10.1039/c4tc00391h.

(8) Zhao, X.; Lu, M.; Koeper, M. J.; Agrawal, R. Solution-Processed Sulfur Depleted Cu(In,Ga)Se$_2$ Solar Cells Synthesized from a Monoamine–Dithiol Solvent Mixture. *J. Mater. Chem. A* **2016**, *4* (19), 7390–7397. https://doi.org/10.1039/C6TA00533K.

(9) Boles, M. A.; Ling, D.; Hyeon, T.; Talapin, D. V. The Surface Science of Nanocrystals. *Nat. Mater.* **2016**, *15* (2), 141–153. https://doi.org/10.1038/nmat4526.

(10) Lokteva, I.; Radychev, N.; Witt, F.; Borchert, H.; Parisi, J.; Kolny-Olesiak, J. Surface Treatment of CdSe Nanoparticles for Application in Hybrid Solar Cells: The Effect of Multiple Ligand Exchange with Pyridine. *J. Phys. Chem. C* **2010**, *114* (29), 12784–12791. https://doi.org/10.1021/jp103300v.

(11) Anderson, N. C.; Hendricks, M. P.; Choi, J. J.; Owen, J. S. Ligand Exchange and the Stoichiometry of Metal Chalcogenide Nanocrystals: Spectroscopic Observation of Facile Metal-Carboxylate Displacement and Binding. *J. Am. Chem. Soc.* **2013**, *135* (49), 18536–18548. https://doi.org/10.1021/ja4086758.

(12) Panthani, M. G.; Kurley, J. M.; Crisp, R. W.; Dietz, T. C.; Ezzyat, T.; Luther, J. M.; Talapin, D. V. High Efficiency Solution Processed Sintered CdTe Nanocrystal Solar Cells: The Role of Interfaces. *Nano Lett.* **2014**, *14* (2), 670–675. https://doi.org/10.1021/nl403912w.

(13) Munro, A. M.; Bardecker, J. A.; Liu, M. S.; Cheng, Y. J.; Niu, Y. H.; Plante, I. J. La; Jen, A. K. Y.; Ginger, D. S. Colloidal CdSe Quantum Dot Electroluminescence: Ligands and Light-Emitting Diodes. *Microchim. Acta* **2008**, *160* (3), 345–350. https://doi.org/10.1007/s00604-007-0770-7.

(14) Dai, M. Q.; Yung, L. Y. L. Ethylenediamine-Assisted Ligand Exchange and Phase Transfer of Oleophilic Quantum Dots: Stripping of Original Ligands and Preservation of Photoluminescence. *Chem. Mater.* **2013**, *25* (11), 2193–2201. https://doi.org/10.1021/cm304136a.

(15) Luther, J. M.; Law, M.; Song, Q.; Perkins, C. L.; Beard, M. C.; Nozik, A. J. Structural, Optical, and Electrical Properties of Self-Assembled Films of PbSe Nanocrystals Treated with 1,2-Ethanedithiol. *ACS Nano* **2008**, *2* (2), 271–280. https://doi.org/10.1021/nn7003348.

(16) Webber, D. H.; Brutchey, R. L. Ligand Exchange on Colloidal CdSe Nanocrystals Using Thermally Labile Tert -Butylthiol for Improved Photocurrent in Nanocrystal Films. *J. Am. Chem. Soc.* **2012**, *134* (2), 1085–1092. https://doi.org/10.1021/ja208878h.

(17) Brown, P. R.; Kim, D.; Lunt, R. R.; Zhao, N.; Bawendi, M. G.; Grossman, J. C.; Bulović, V. Energy Level Modification in Lead Sulfide Quantum Dot Thin Films through Ligand Exchange. *ACS Nano* **2014**, *8* (6), 5863–5872. https://doi.org/10.1021/nn500897c.

(18) Nag, A.; Kovalenko, M. V; Lee, J.; Liu, W.; Spokoyny, B.; Talapin, D. V. Metal-Free Inorganic Ligands for Colloidal Nanocrystals: S^{2-}, HS^{-} , Se^{2-}, HSe^{-}, Te^{2-}, HTe^{-}, TeS_3^{2-} , OH^{-}, and NH_2^{-} as Surface Ligands. *J. Am. Chem. Soc.* **2011**, *133* (27), 10612–10620. https://doi.org/10.1021/ja2029415.

(19) Korala, L.; Braun, M. B.; Kephart, J. M.; Tregillus, Z.; Prieto, A. L. Ligand-Exchanged CZTS Nanocrystal Thin Films: Does Nanocrystal Surface Passivation Effectively Improve Photovoltaic Performance? *Chem. Mater.* **2017**, *29* (16), 6621–6629. https://doi.org/10.1021/acs.chemmater.7b00541.

(20) Dierick, R.; Van den Broeck, F.; De Nolf, K.; Zhao, Q.; Vantomme, A.; Martins, J. C.; Hens, Z. Surface Chemistry of $CuInS_2$ Colloidal Nanocrystals, Tight Binding of L-Type Ligands. *Chem. Mater.* **2014**, *26* (20), 5950–5957. https://doi.org/10.1021/cm502687p.

(21) Houck, D. W.; Korgel, B. A. Facile Exchange of Tightly Bonded L-Type Oleylamine and Diphenylphosphine Ligands on Copper Indium Diselenide Nanocrystals Mediated by Molecular Iodine. *Chem. Mater.* **2018**, *30* (22), 8359–8367. https://doi.org/10.1021/acs.chemmater.8b04016.

(22) Dilena, E.; Xie, Y.; Brescia, R.; Prato, M.; Maserati, L.; Krahne, R.; Paolella, A.; Bertoni, G.; Povia, M.; Moreels, I.; Manna, L. $CuIn_xGa_{1-x}S_2$ Nanocrystals with Tunable Composition and Band Gap Synthesized via a Phosphine-Free and Scalable Procedure. *Chem. Mater.* **2013**, *25* (15), 3180–3187. https://doi.org/10.1021/cm401563u.

(23) Deshmukh, S. D.; Ellis, R. G.; Sutandar, D. S.; Rokke, D. J.; Agrawal, R. Versatile Colloidal Syntheses of Metal Chalcogenide Nanoparticles from Elemental Precursors Using Amine-Thiol Chemistry. *Chem. Mater.* **2019**, *31* (21), 9087–9097. https://doi.org/10.1021/acs.chemmater.9b03401.

(24) McLeod, S. M.; Hages, C. J.; Carter, N. J.; Agrawal, R. Synthesis and Characterization of 15% Efficient CIGSSe Solar Cells from Nanoparticle Inks. *Prog. Photovoltaics Res. Appl.* **2015**, *23* (11), 1550–1556. https://doi.org/10.1002/pip.2588.

(25) Guo, Q.; Ford, G. M.; Agrawal, R.; Hillhouse, H. W. Ink Formulation and Low-Temperature Incorporation of Sodium to Yield 12% Efficient $Cu(In,Ga)(S,Se)_2$ Solar Cells from Sulfide Nanocrystal Inks. *Prog. Photovoltaics Res. Appl.* **2013**, *21*, 64–71. https://doi.org/10.1002/pip.

(26) Niederberger, M.; Garnweitner, G.; Buha, J.; Polleux, J.; Ba, J.; Pinna, N. Nonaqueous Synthesis of Metal Oxide Nanoparticles:Review and Indium Oxide as Case Study for the Dependence of Particle Morphology on Precursors and Solvents. *J. Sol-Gel Sci. Technol.* **2006**, *40* (2–3), 259–266. https://doi.org/10.1007/s10971-006-6668-8.

(27) Fritzinger, B.; Moreels, I.; Lommens, P.; Koole, R.; Hens, Z.; Martins, J. C. In Situ Observation of Rapid Ligand Exchange in Colloidal Nanocrystal Suspensions Using Transfer NOE Nuclear Magnetic Resonance Spectroscopy. *J. Am. Chem. Soc.* **2009**, *131* (8), 3024–3032. https://doi.org/10.1021/ja809436y.

(28) Duchatelet, A.; Sidali, T.; Loones, N.; Savidand, G.; Chassaing, E.; Lincot, D. 12.4% Efficient Cu(In,Ga)Se_2 Solar Cell Prepared from One Step Electrodeposited Cu-In-Ga Oxide Precursor Layer. *Sol. Energy Mater. Sol. Cells* **2013**, *119*, 241–245. https://doi.org/10.1016/j.solmat.2013.07.053.

(29) Uhl, A. R.; Fuchs, P.; Rieger, A.; Pianezzi, F.; Sutter-Fella, C. M.; Kranz, L.; Keller, D.; Hagendorfer, H.; Romanyuk, Y. E.; Lamattina, F.; Yoon, S.; Karvonen, L.; Magorian-Friedlmeier, T.; Ahlswede, E.; VanGenechten, D.; Stassin, F.; Tiwari, A. N. Liquid-Selenium-Enhanced Grain Growth of Nanoparticle Precursor Layers for $CuInSe_2$ Solar Cell Absorbers. *Prog. Photovoltaics Res. Appl.* **2015**, *23* (9), 1110–1119. https://doi.org/10.1002/pip.2529.

(30) Rockett, A.; Britt, J. S.; Gillespie, T.; Marshall, C.; Al Jassim, M. M.; Hasoon, F.; Matson, R.; Basol, B. Na in Selenized Cu(In,Ga)Se_2 on Na-Containing and Na-Free Glasses: Distribution, Grain Structure, and Device Performances. *Thin Solid Films* **2000**, *372* (1), 212–217. https://doi.org/10.1016/S0040-6090(00)01028-2.

(31) Dierick, R.; Capon, B.; Damm, H.; Flamee, S.; Arickx, P.; Bruneel, E.; Van Genechten, D.; Van Bael, M.; Hardy, A.; Detavernier, C.; Hens, Z. Annealing of Sulfide Stabilized Colloidal Semiconductor Nanocrystals. *J. Mater. Chem. C* **2014**, *2* (1), 178–183. https://doi.org/10.1039/c3tc31393j.

(32) Guo, J.; Wang, X.; Zhou, W. H.; Chang, Z. X.; Zhou, Z. J.; Wu, S. X. Efficiency Enhancement of Dye-Sensitized Solar Cells (DSSCs) Using Ligand Exchanged $CuInS_2$ NCs as Counter Electrode Materials. *RSC Adv.* **2013**, *3* (34), 14731–14736. https://doi.org/10.1039/c3ra41602j.

(33) Hassinen, A.; Moreels, I.; De Nolf, K.; Smet, P. F.; Martins, J. C.; Hens, Z. Short-Chain Alcohols Strip X-Type Ligands and Quench the Luminescence of PbSe and CdSe Quantum Dots, Acetonitrile Does Not. *J. Am. Chem. Soc.* **2012**, *134* (51), 20705–20712. https://doi.org/10.1021/ja308861d.

(34) Khatri, I.; Fukai, H.; Yamaguchi, H.; Sugiyama, M.; Nakada, T. Effect of Potassium Fluoride Post-Deposition Treatment on Cu(In,Ga)Se_2 Thin Films and Solar Cells Fabricated onto Sodalime Glass Substrates. *Sol. Energy Mater. Sol. Cells* **2016**, *155*, 280–287. https://doi.org/10.1016/j.solmat.2016.06.023.

(35) Barbé, J.; Eid, J.; Ahlswede, E.; Spiering, S.; Powalla, M.; Agrawal, R.; Del Gobbo, S. Inkjet Printed Cu(In,Ga)S_2 Nanoparticles for Low-Cost Solar Cells. *J. Nanoparticle Res.* **2016**, *18* (12), 379. https://doi.org/10.1007/s11051-016-3686-5.

(36) Harvey, T. B.; Bonafé, F.; Updegrave, T.; Voggu, V. R.; Thomas, C.; Kamarajugadda, S. C.; Stolle, C. J.; Pernik, D.; Du, J.; Korgel, B. A. Uniform Selenization of Crack-Free Films of Cu(In,Ga)Se_2 Nanocrystals. *ACS Appl. Energy Mater.* **2019**, *2* (1), 736–742. https://doi.org/10.1021/acsaem.8b01800.

(37) Perlich, J.; Metwalli, E.; Schulz, L.; Georgii, R.; Müller-Buschbaum, P. Solvent Content in Thin Spin-Coated Polystyrene Homopolymer Films. *Macromolecules* **2009**, *42* (1), 337–344. https://doi.org/10.1021/ma801878j.

5. LIGAND EXCHANGE FREE, DIRECT SYNTHESIS OF SULFIDE CAPPED NANOPARTICLES FOR CARBON FREE SOLUTION PROCESSED PHOTOVOLTAICS

5.1 Introduction

In the pursuit of carbon impurity removal as detailed in the previous chapter, ligand exchange reactions have drawn significant interest. By a post synthesis replacement of the long chain carbonaceous ligands with either volatile organics,[1–3] or non-contaminating inorganic species,[4,5] low-carbon nanoparticle thin films can be produced while retaining the benefits of the long chain ligands during synthesis. In the previous section,[6] we detailed a method whereby tightly bound oleylamine ligands on $Cu(In,Ga)S_2$ nanoparticles were removed via a two-step, hybrid organic/inorganic exchange with pyridine and diammonium sulfide. After ligand exchange, greater than 98% of the native ligands were successfully removed and highly stable sulfide capped nanoparticles were formulated into inks in dimethyl sulfoxide (DMSO). Selenization of ligand exchanged nanoparticle films exhibited significantly improved grain growth with little to no fine grain layer, and improved device performance as compared to an identically fabricated device from oleyalmine capped nanoparticles.[6] However, the ligand exchange process requires many additional processing steps and increases solvent usage substantially for the generally low mass concentration exchange steps,[5,6] hindering the potential cost advantage and simplicity solution processing aims to deliver. Several reports have attempted to synthesize nanoparticles that do not require post-synthetic ligand exchange using metal salts in glycol,[7] or metal salts in formamide with thioacetamide as a sulfide source.[8] However, in the case of glycol, formation of secondary oxide phases,[7] surface oxide during synthesis, or alkoxide ligand binding and decomposition can introduce hard to remove oxide phases that detriment device performance.[9] Further, poor colloidal stability from this method required addition of polymeric dispersants such as PVP, again introducing substantial carbon contamination.[7] Others have made use of low temperature syntheses from solubilized metal chalcogenide complexes, but resultant device performance remained poor.[10]

In this chapter, we develop a method to bypass the necessity of ligand exchange through the direct synthesis of $CuInS_2$ (CIS) nanoparticles (NPs) with a combination of inorganic sulfide ligands and thermally degradable thioacetamide ligands. To ensure high quality of nanoparticles

without any anionic impurities, Cu_2S or Cu with In metal were solubilized as precursors in amine-thiol mixtures removing anionic impurity concerns as described in our previous report.[11] Excess amine and thiols were removed[12] and isolated metal thiolate complexes then thermally decomposed via a hot injection reaction in sulfolane which acts as a non-binding polar-aprotic solvent with a thioacetamide and in-situ generated H_2S as a sulfide ligand source. The resulting CIS nanparticles were pure phase chalcopyrite and exhibited high colloidal stability in polar media such as DMSO. Inks with mass concentrations up to 200 mg/mL were prepared and highly uniform and crack free thin films were easily deposited using scalable blade coating, demonstrating the stability.

5.2 Experimental Section

5.2.1 Materials

Copper (I) sulfide (99.99%), copper (nanopowder, 99.5%), propylamine (PA; >99%), 1,2-ethanedithiol (EDT; 98%), sulfolane (99%), thioacetamide (99%), toluene (anhydrous , 99.8%), acetonitrile (99.9%, anhydrous), dimethyl sulfoxide (anhydrous, 99.9%), butylamine (99.5%), zinc (nanopowder, 99%), sodium fluoride (99.99%), cadmium sulfate hydrate (99.996%), and thiourea (>99%) were purchased from Sigma Aldrich and used as received with the exception of sulfolane, which was degassed using successive freeze-pump-thaw cycles under vacuum. Indium (99.999%), tin (99.999%), and ammonium hydroxide solution (28.0-30.0%) were purchased from Fisher Scientific and used as received. All chemicals were dispensed in an inert environment with O_2 and H_2 < 1 ppm, with the exception of cadmium sulfate hydrate, thiourea, and ammonium hydroxide. Ultrapure water was generated using a Millipore Direct-Q3 (18.2 MΩ at 25°C).

5.2.2 Synthesis of $CuInS_2$ and Cu_2ZnSnS_4 Nanoparticles.

All synthesis work was performed under inert nitrogen or argon atmospheres. Metal precursor solutions were prepared by co-dissolving Cu and In metals in PA-EDT mixtures at 0.4M. A 400% excess of EDT was used assuming a minimum stoichiometry of 2 EDT per In and a 150% excess of EDT was used for Cu. For CZTS, a 2 EDT per Zn and 2 EDT per tin were assumed. When Cu_2S was used in place of Cu, separate Cu_2S and In solutions were prepared at 0.4M and mixed after complete dissolution. CIS and CZTS precursor solution were then evaporated under vacuum,

leaving isolated metal thiolate complexes. The complexes were dissolved in 3 mL of degassed sulfolane after stirring for 30 minutes. For CZTS precursor solutions, 300 µL of proylamine was added to the sulfolane to help solubilize the metal thiolate complexes. Seperately, thioacetamide was dissolved in 7 mL of sulfolane, where a 6:1 TAA:In and 6:1 TAA:Zn molar ratio was used. The TAA/sulfolane solution was transferred to a 100 mL 3 neck flask with condenser, glass sheathed thermocouple port, and a rubber septa. The TAA/suflolane mixture was transferred to an argon purged Schlenk line where cooling water was attached to the condenser. Under stirring at 600 rpm, the TAA/sulfolane was brought to 80℃ under vacuum for 30 minutes to further degas the sulfolane and remove any trace moisture from the TAA. The reaction vessel was then backfilled with argon and brought to 200℃ for synthesis with Cu containing precursors, and 210℃ for Cu_2S containing precursors. Two mL of the metal thiolate in sulfolane solution was hot injected into the TAA/sulfolane solution, and the reaction was allowed to continue at the reaction temperature for 15 minutes (for Cu metal precursors), or 30 minutes (for Cu_2S precursors). The reaction mixture was naturally cooled to room temperature and precipitated using excess toluene and centrifugation. After decanting the supernatant, 4 mL of acetonitrile was used to redisperse the nanoparticles with vortex mixing. Four total centrifugation washing cycles were used, after which the supernatant was decanted, and the nanoparticles were dried under a flow of argon.

5.2.3 Film Coating

All coating was performed in an inert nitrogen environment. Nanoparticle thin films were prepared by dispersing the dry nanoparticles at 200 mg/mL in DMSO using sonication for 30 minutes. A dark viscous ink was obtained after sonication, which was then blade coated onto either soda lime glass or molybdenum coated soda lime glass using a custom automatic blade coater. First, 12 µL of ink was dispensed on the top edge of a 1” x 2” substrate on an 80℃ heated bed. Then two passes down and up the substrate were performed at 25 mm/s using a cylindrical glass rod as a blade with a 100 µm substrate-blade gap. The films were then dried for 2 minutes at 80℃ followed by annealing at 320℃ for 1-5 minutes. Each coating yielded an approximate thickness of 400 nm. Sequential coatings were performed to reach thicknesses just over a micron. Molecular precursor films were coated directly out of dissolved solutions of Cu_2S and In in butylamine-EDT mixtures using blade coating and annealing at 300℃.

5.2.4 Characterization

X-ray diffractograms were collected using a Rigaku SmartLab diffractometer with a 40 kV/44 mA Cu Kα (λ = 1.5406 Å) source operated at in 0.5° parallel beam (PB) mode. Raman spectra were collected on a Horiba/Jobin-Yvon HR800 Raman spectrometer at a 632.8 nm excitation laser wavelength. Transmission electron micrographs were collected using a Tecnai transmission electron microscope. Elemental ratios were determined using a Fisher XAN 250 X-ray fluorescence (XRF) instrument, running at 50 kV with a silicon drift detector, nickel filter, and helium gas purge. ^{1}H-NMR spectra were collected with a Bruker AV-III-400-HD using a relaxation time of 6 s and 32 scans. FTIR absorbance spectra were collected with a Thermo-Nicolet Nexus 670 FTIR in transmission mode on soda lime glass as substrates. Uniform coatings were used for absorbance measurements such that the pathlength between measurements was constant and therefore directly comparable before and after annealing samples. Profilometry was performed using a Dektak 6 M stylus profilometer with a 12.5 μm diameter diamond tip stylus. Thickness measurements were taken using mechanically scribed trenches. Scanning electron microscopy (SEM) images were taken using FEI Quanta 3D FEG dual-beam SEM with an Everhart− Thornley detector at an accelerating voltage of 10 kV and working distance of 10 mm.

5.3 Results and Discussion

Cu_2S or elemental copper along with indium were selected as precursors due to their ease of reactive dissolution in monoamine-dithiol mixtures. Separate Cu_2S and indium solutions or single solutions of Cu and In were prepared in propylamine/1,2-ethanedithiol mixtures. Within 12 hours, complete dissolution of the solids was observed yielding homogenous and transparent precursor solutions of metal thiolate complexes. The thermal decomposition of these species was investigated in our previous report, where only metal sulfides and volatile byproducts are formed (ethylene sulfide, alkylamine, and hydrogen sufide).[11] This removes the concern of anionic impurities typically present with the use of metal salts such as metal acetates, aceylacetonates, nitrates, halides, etc.,[13,14] which can bind to nanoparticle surfaces as ligands or directly incorporate into the crystal structure of the targeted material.[15] While anionic impurities are removed in this method, amines and thiols are known to bind strongly as either L or X type ligands (donation of two electrons from a neutral species to a cationic metal and donation of one electron from an

anionic species to a cationic metal respectively).[16] As such, isolation of the metal thiolate species from the bulk amine-thiol mixtures used for reactive dissolution as detailed in our previous report was performed to remove all free amine and thiol from the precursor, yielding isolated powder of copper and indium thiolate complexes as was explored in our previous report.[12]

The isolated metal thiolate precursor solids were readily soluble in a wide variety of polar solvents. However, careful selection of a reaction solvent was necessary to ensure high boiling point for synthesis, thermal stability, low reactivity with reaction mixture constituents, solubilization of all precursors, and sufficient polarity to disperse sulfide capped particles. Importantly, the bulk solvent should not bind to the nanoparticle surface as a ligand, introducing additional carbonaceous species that would necessitate removal. As such, aprotic solvents were initially selected to prevent the strong X-type ligand binding mechanism from occurring that has been observed for protic species such as alcohols.[9] Sulfolane emerged as an attractive solvent option with relatively low toxicity, good thermal and chemical stability at a variety of acidic and basic conditions, high polarity ($\mu = 4.7$ debye, $\varepsilon = 43.4$), and availability at low cost due to existing commercial use in the petrochemical industry for aromatics extractions and sour gas sweetening.[17–19] Unlike alternative high boiling polar aprotic solvents such as hexamethylphosphoramide (HMPA), sulfolane is not expected to be carcinogenic, clastogenic, mutagenic, or pose any developmental risks at moderate exposure levels.[20] While sulfolane has extremely low decomposition rates as operating temperatures between 180°C and 200°C (0.009%/h), further elevation of temperature in the presence of trace oxygen or moisture can induce decompositions where butadiene, sulfur dioxide, and carbon dioxide gasses are produced.[19] To avoid incorporation of oxygen containing species (sulfur dioxide) to the ligand shell or the core material, the sulfolane was degassed using successive freeze pump thaw cycles and verified to be free of moisture by ^{1}H-NMR. After degassing, no increase in pressure was observed when heating sulfolane at 225°C for 1 hour in a sealed vessel under nitrogen, demonstrating little to no decomposition after purification. This stability is advantageous over other organic species that have been previously used in the literature such as formamide,[8] which has been shown to induce surface oxidation during its thermal decomposition.[21] Further, an advantage of sulfolane over conventional ligands such as oleylamine is the low cost and availability of high purity (>99%) sulfolane, whereas oleylamine is generally only available as technical grade mixtures (~70%),[6,13,14] which can significantly detriment

reproducibility due to batch to batch variability and the important coordinating role oleylamine plays during colloidal syntheses.

An inorganic sulfide ligand was targeted during the synthesis, and thus required a source of sulfide. Conveniently, during the decomposition of the metal thiolate precursor complexes, H_2S gas is liberated into the reaction mixture as a byproduct, thus providing a source of potential H-S-Metal X-type ligand, or H_2S L-type binding, similar to the stabilization mechanism that diammonium sulfide uses.[6,11] However, this H_2S alone was not enough to properly stabilize the nanoparticles. An additional ligand, thioacetamide was added to the reaction mixture. Thioacetamide undergoes thermal decomposition in an inert environment forming H_2S and acetonitrile (b.p. 82℃). This decomposition is reported to take place beginning around 180℃, taking approximately 25 minutes to reach completion during a temperature hold at 186℃.[20] Slightly different reactivities were observed for Cu/In precursors and Cu_2S/In precursors, where reaction times of 200℃/15 minutes and 210℃/30 minutes were used respectively to obtain particles with the correct stoichiometry. Due to sulfolane's miscibility with non-polar aromatic organics, toluene was selected as an antisolvent for nanoparticle washing with centrifugation to separate the particles. After decanting the supernatant, acetonitrile was used to disperse the nanoparticles for subsequent washes. Four total washes were used to exhaustively remove any residual reaction mixture, followed by drying with flowing argon at room temperature. The use of non-coordinating washing solvents such as acetonitrile and toluene further aids in the prevention of impurity oxide forming from alkoxide binding which can occurring during washing with alcohols.[9]

The resulting nanoparticles exhibited chalcopyrite phase and did not contain any crystalline or amorphous secondary phases, as determined by XRD and Raman as shown in Figure 5.1 a) and b).

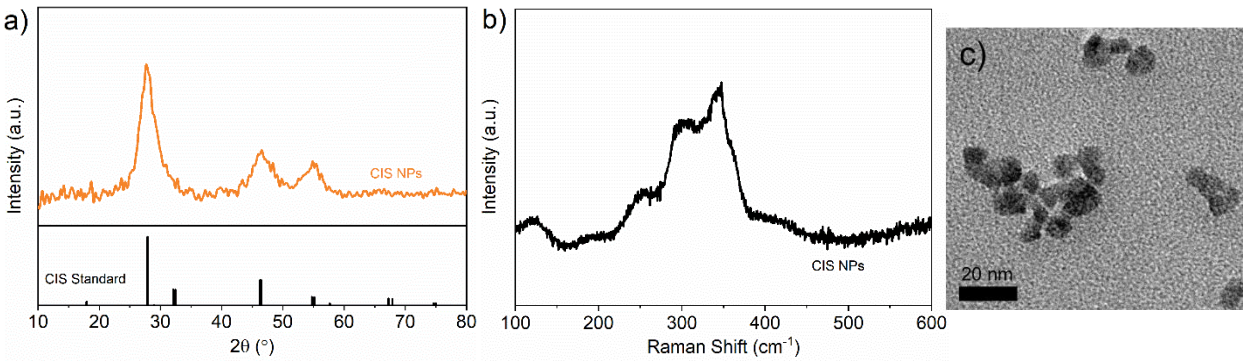

Figure 5.1. a) XRD, b) Raman, and c) TEM of CIS nanoparticles synthesized in this work.

A nanoparticle size of approximately 8 nm was observed in transmission electron microscopy as shown in Figure 5.1 c). XRF revealed a Cu/In ratio of 0.95, slightly above the charged Cu/In of 0.92 for both nanoparticles synthesized using Cu and Cu_2S precursors, however, particles synthesized using Cu_2S generally showed smaller size and more aggregation. HRTEM of CIS nanoparticles synthesized using Cu_2S is shown in Figure 5.2.

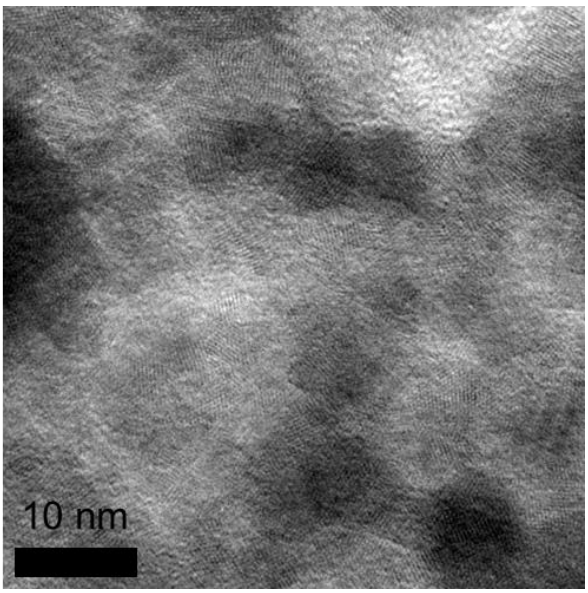

Figure 5.2. HRTEM of CIS nanoparticle synthesized using Cu_2S as a precursor.

To determine the ligand shell of the nanoparticles, ^{1}H-NMR and FTIR were employed. Qualitative ^{1}H-NMR of the $CuInS_2$ nanoparticles, thioacetamide, and sulfolane standards are shown in Figure 5.3, where all sharp peaks can be attributed to the DMSO-d6 residual, and trace amounts of the washing solvents toluene and acetonitrile.

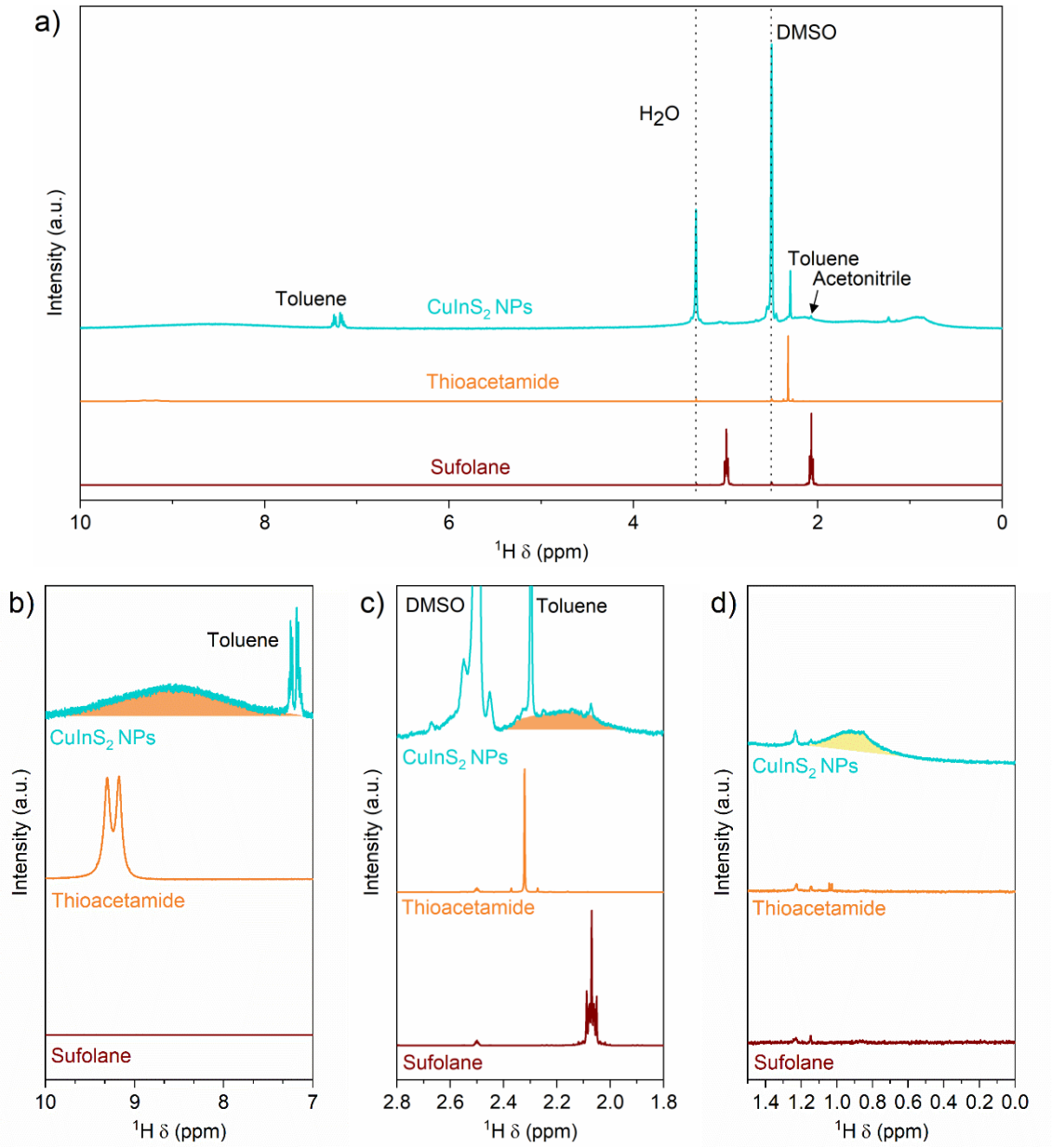

Figure 5.3. a) Full spectrum ^{1}H-NMR of neat sulfolane, thioacetamide, and $CuInS_2$ nanoparticles. b) Zoom in of region from 7 to 10 ppm, c) 1.8 to 2.8 pp, and d) 0 to 1.5 ppm. Broad peaks assigned to bound thioacetamide are shown in orange and the hypothesized surface H-S-/H_2S peak is highlighted in yellow. Note that Y-scaling is performed per curve and per panel for clarity.

Three broad peaks were observed across the spectrum are indicative of surface bound species due to surface immobilization, causing peak shift and broadening. Zoomed in ^{1}H-NMR spectra around each of the broadened peaks are shown in Figure 5.3 b), c) and d). The broad peaks at centered at

8.57 and 2.19 are attributed to thioacetamide's NH_2 and CH_3 protons respectively, shifted to lower ppm as is often observed for ligand peak shift. The broad peak centered around 0.9 ppm is hypothesized to be X-type surface H-S- or L-type surface H_2S. Generally, the H-S on thiols is observed as low as 1.2 ppm. The lower shift observed in Figure 5.3 d) is likely due to bound surface immobilization. The other peaks observed in Figure 5.3 d) are attributed to trace impurities in the deuterated DMSO, as evidenced by their appearance is all spectra. Neat deuterated DMSO was run to verify that all non-identified peaks were attributable to trace contamination in the deuterated DMSO, as shown in Figure 5.4.

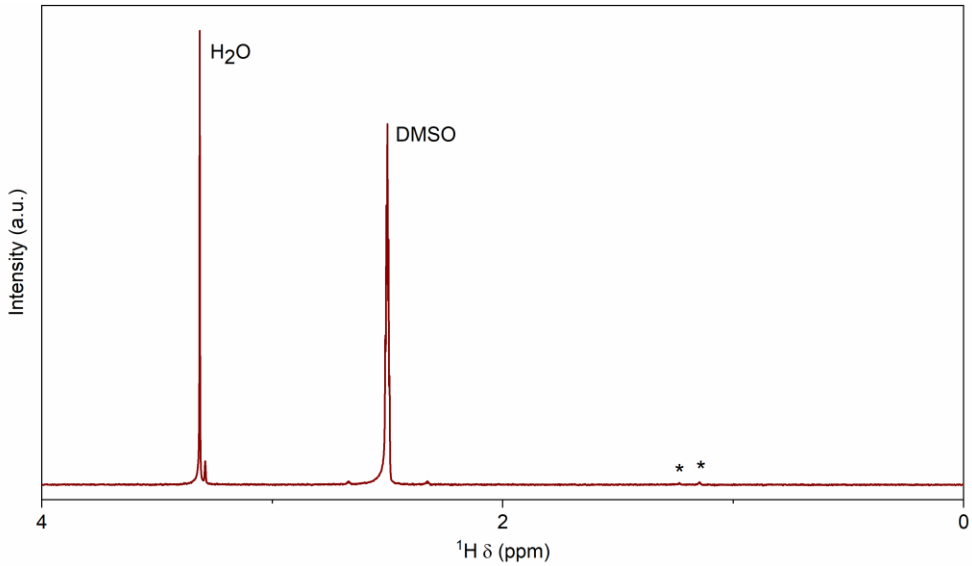

Figure 5.4. ^{1}H-NMR of neat as received DMSO-d6. Impurity water and residual non-dueterated DMSO are labelled along with other trace impurities marked with asterisks.

All broad peaks have extremely low intensities, as is expected for bound short chain species, where protons closest to the bound groups peak broaden the most significantly.[6] The lack of any appreciable sharp signals of sulfolane and thioacetamide in the nanoparticle spectrum verify that the washing is sufficient to remove all unreacted precursors and reaction solvent. FTIR was performed on films blade coated from a DMSO ink at 200 mg/mL on soda lime glass to yield uniform thickness films. These films were dried at 100°C for 5 minutes to remove residual coating solvent. Transmission FTIR was performed on the C-H region (where soda lime glass is IR transparent) of the dried CIS film. The film was then annealed at 320°C for 5 minutes in a nitrogen atmosphere and FTIR was run again. Because the blade coated film was uniform in thickness,

direct comparison can be made between the pre-annealed and post-annealed films due to identical path length across the thickness of the film as shown in Figure 5.5.

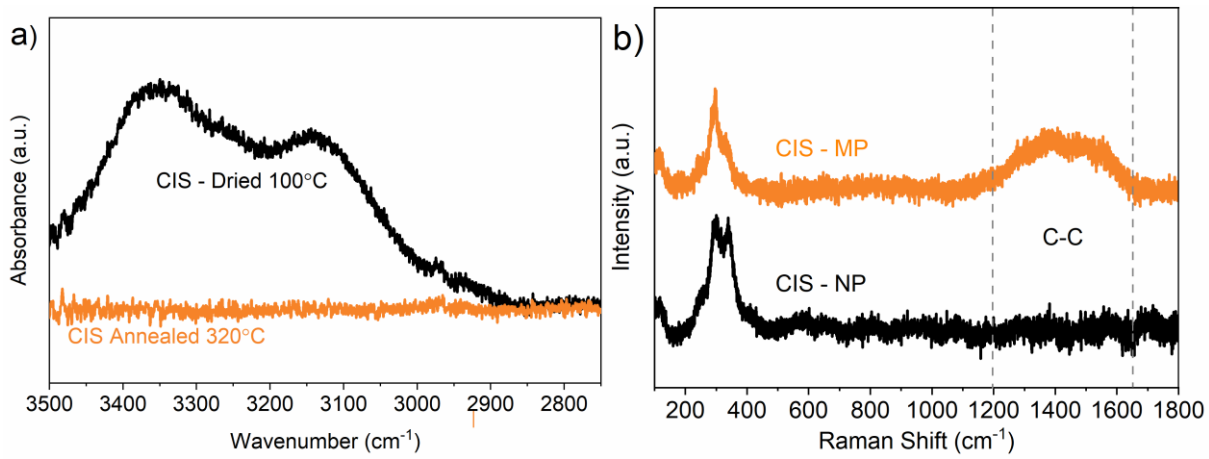

Figure 5.5. a) FTIR on CIS nanoparticles before and after annealing at 320°C, showing removal of surface bound thioacetamide and b) Raman spectroscopy showing graphitic carbon-carbon region of CIS nanoparticles compared to a molecular precursor (MP) film from Cu_2S and In in n-butylamine-1,2-ethanedithiol after annealing at 320 and 300 °C respectively.

In the pre-annealed film several broad peaks, attributed to are observed at wavenumbers greater than 3000, and small C-H stretches are observed at approximately 2950. These peaks are assigned to thioacetamide; however, the observed broadening suggests thioacetamide is surface bound. After annealing at 300°C, all signals are removed to the detection limit of FTIR, verifying a clean decomposition of surface bound thioacetamide. While the reaction was performed above the thermal decomposition onset of thioacetamide, the presence of potential thioacetamide peaks in both ^{1}H-NMR and FTIR show that residual bound thioacetamide exists. While contradictory to previous work showing decomposition above 180°C, a change in the chemical environment and/or surface binding may play a stabilizing role preventing complete decomposition. Longer reaction times may facilitate complete thioacetamide decomposition, however, the ease of thermal decomposition of thioacetamide during annealing already used in the film coating processes as evidenced by FTIR accomplishes the same goal without unnecessarily increasing the net thermal energy needed for the process. Further analysis was performed using raman spectroscopy to probe any residual C-C bonds, which often occur from coke like pyrolysis by-products. Films from the nanoparticle synthesis were compared to films directly cast from molecular precursors of Cu_2S

and In thiolate precursors in amine-thiol solution. Interesting, significant C-C bonding is observed from the molecular precursor, but not in the case of the sulfide capped nanoparticles, potentially providing a method to bypass carbon impurities often observed from molecular precursor approaches from either metal thiolate decomposition or bulk amine and thiol decomposition.[22]

Inks consisting of the nanoparticle were easily prepared at mass concentrations exceeding 200 mg/mL in DMSO. DMSO was selected due to its low toxicity as well as its lack of oxide inducing ability as demonstrated in our previous work.[6] Using blade coating on a preheated substrate at 80°C, high quality thin films were prepared with low surface roughness as shown in Figure 5.6.

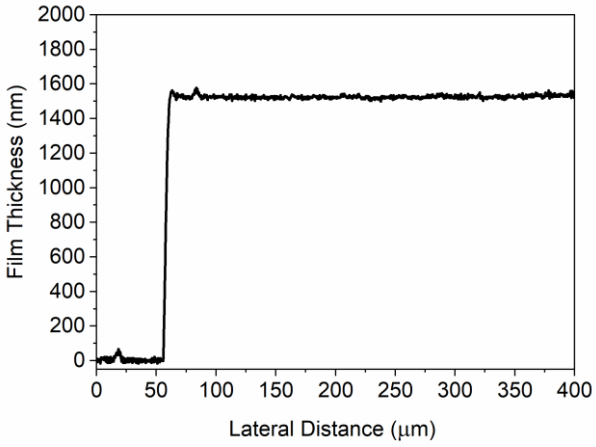

Figure 5.6. Profilometry scan of a CIS thin blade coated from a DMSO ink on molybdenum with a mechanically scribed trench for thickness and roughness measurement. Four successive coatings were used to reach the thickness shown.

To further explore the potential of this system, the significantly more complex quaternary material, Cu_2ZnSnS_4, known for its difficulty of synthesis and ease of secondary phases formation,[23] was prepared by first dissolving Cu, Zn, and Sn metals in propylamine-dithiol solutions followed by isolation of the thiolate complexes. The resulting complexes showed lower solubility in sulfolane than their CIS counterpart, so a few hundered microliters of propylamine were added to increase solubility. Again, hot injection into thioacetamide containing sulfolane at 200°C was performed. Wurzite CZTS nanoparticles were obtained as evidenced by XRD as shown in Figure 5.7 a). Raman spectroscopy was also performed showing no clear secondary phases were formed as shown in Figure 5.7 b).

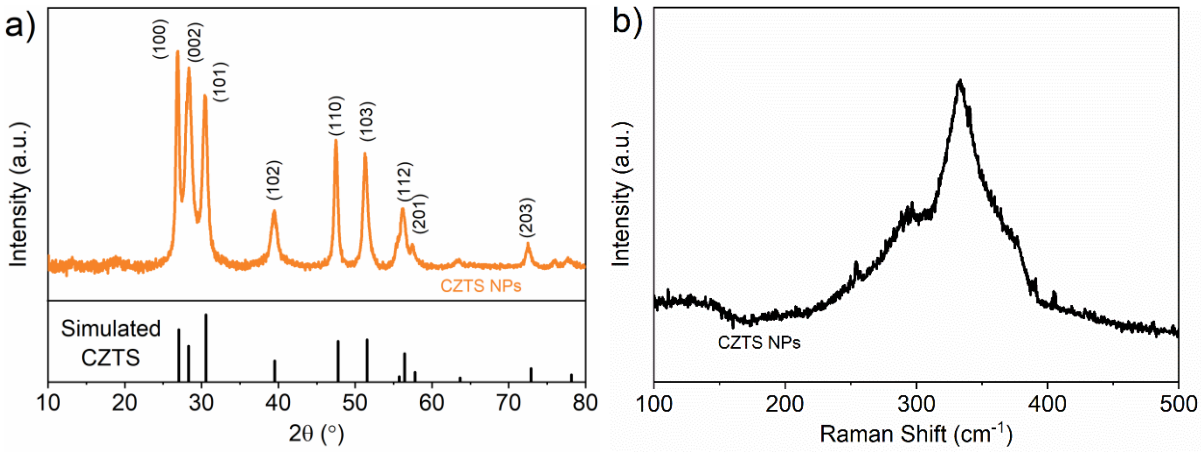

Figure 5.7. a) Simulated wurtzite CZTS standard as compared to CZTS nanoparticles as synthesized in this work, b) Raman spectrum of CZTS nanoparticles.

All major peaks were labelled, matching completely to wurtzite CZTS synthesized previously in our group using metal salts, sulfur, and oleylamine.[24] We believe that these methods can be easily adapted to other metal sulfide materials, opening a new avenue to high quality carbon free thin films from colloidal nanoparticles without the need for ligand exchange.

In summary, we have developed a novel method of nanoparticle synthesis in which metal sulfide nanoparticles can be synthesized with inorganic sulfide and thermally degradable thioacetamide ligands directly, bypassing the need for complex and solvent intensive ligand exchange procedures. Pure phase $CuInS_2$ and Cu_2ZnSnS_4 nanoparticles were demonstrated, and we believe these methods can easily be extended to other metal sulfide nanomaterials. Non-toxic ink formulation in dimethylsulfoxide and subsequent scalable blade coating yielded carbon free nanoparticle thin films, demonstrating the promise of this system for implantation into large scale, low toxicity photovoltaics manufacturing.

5.4 Acknowledgements

This work was supported by funding from the National Science Foundation (NSF) under grants #1735282-NRT (SFEWS), and #10001536 (INFEWS).

5.5 References

(1) Luther, J. M.; Law, M.; Song, Q.; Perkins, C. L.; Beard, M. C.; Nozik, A. J. Structural, Optical, and Electrical Properties of Self-Assembled Films of PbSe Nanocrystals Treated with 1,2-Ethanedithiol. *ACS Nano* **2008**, *2* (2), 271–280. https://doi.org/10.1021/nn7003348.

(2) Sayevich, V.; Guhrenz, C.; Dzhagan, V. M.; Sin, M.; Werheid, M.; Cai, B.; Borchardt, L.; Widmer, J.; Zahn, D. R. T.; Brunner, E.; Lesnyak, V.; Gaponik, N.; Eychmüller, A. Hybrid N-Butylamine-Based Ligands for Switching the Colloidal Solubility and Regimentation of Inorganic-Capped Nanocrystals. *ACS Nano* **2017**, *11* (2), 1559–1571. https://doi.org/10.1021/acsnano.6b06996.

(3) Gabka, G.; Bujak, P.; Giedyk, K.; Kotwica, K.; Ostrowski, A.; Malinowska, K.; Lisowski, W.; Sobczak, J. W.; Pron, A. Ligand Exchange in Quaternary Alloyed Nanocrystals - a Spectroscopic Study. *Phys. Chem. Chem. Phys.* **2014**, *16* (42), 23082–23088. https://doi.org/10.1039/c4cp03850a.

(4) Kovalenko, M. V.; Scheele, M.; Talapinl, D. V. Colloidal Nanocrystals with Molecular Metal Chalcogenide Surface Ligands. *Science (80-.).* **2009**, *324* (5933), 1417–1420. https://doi.org/10.1126/science.1170524.

(5) Nag, A.; Kovalenko, M. V; Lee, J.; Liu, W.; Spokoyny, B.; Talapin, D. V. Metal-Free Inorganic Ligands for Colloidal Nanocrystals: S^{2-}, HS^{-} , Se^{2-}, HSe^{-}, Te^{2-}, HTe^{-}, TeS_3^{2-} , OH^{-}, and NH_2^{-} as Surface Ligands. *J. Am. Chem. Soc.* **2011**, *133* (27), 10612–10620. https://doi.org/10.1021/ja2029415.

(6) Ellis, R. G.; Turnley, J. W.; Rokke, D. J.; Fields, J. P.; Alruqobah, E. H.; Deshmukh, S. D.; Kisslinger, K.; Agrawal, R. Hybrid Ligand Exchange of $Cu(In,Ga)S_2$ Nanoparticles for Carbon Impurity Removal in Solution-Processed Photovoltaics. *Chem. Mater.* **2020**, *32*, 5091–5103. https://doi.org/10.1021/acs.chemmater.0c00966.

(7) Jeong, S.; Lee, B. S.; Ahn, S.; Yoon, K.; Seo, Y. H.; Choi, Y.; Ryu, B. H. An 8.2% Efficient Solution-Processed $CuInSe_2$ Solar Cell Based on Multiphase $CuInSe_2$ Nanoparticles. *Energy Environ. Sci.* **2012**, *5* (6), 7539–7542. https://doi.org/10.1039/c2ee21269b.

(8) Huang, T. J.; Yin, X.; Tang, C.; Qi, G.; Gong, H. A Low-Cost, Ligand Exchange-Free Strategy to Synthesize Large-Grained Cu_2ZnSnS_4 Thin-Films without a Fine-Grain Underlayer from Nanocrystals. *J. Mater. Chem. A* **2015**, *3* (34), 17788–17796. https://doi.org/10.1039/c5ta03640b.

(9) Hassinen, A.; Moreels, I.; De Nolf, K.; Smet, P. F.; Martins, J. C.; Hens, Z. Short-Chain Alcohols Strip X-Type Ligands and Quench the Luminescence of PbSe and CdSe Quantum Dots, Acetonitrile Does Not. *J. Am. Chem. Soc.* **2012**, *134* (51), 20705–20712. https://doi.org/10.1021/ja308861d.

(10) Ritchie, C.; Chesman, A. S. R.; Jasieniak, J.; Mulvaney, P. Aqueous Synthesis of $Cu_2ZnSnSe_4$ Nanocrystals. *Chem. Mater.* **2019**, *31* (6), 2138–2150. https://doi.org/10.1021/acs.chemmater.9b00100.

(11) Deshmukh, S. D.; Ellis, R. G.; Sutandar, D. S.; Rokke, D. J.; Agrawal, R. Versatile Colloidal Syntheses of Metal Chalcogenide Nanoparticles from Elemental Precursors Using Amine-Thiol Chemistry. *Chem. Mater.* **2019**, *31* (21), 9087–9097. https://doi.org/10.1021/acs.chemmater.9b03401.

(12) Zhao, X.; Deshmukh, S. D.; Rokke, D. J.; Zhang, G.; Wu, Z.; Miller, J. T.; Agrawal, R. Investigating Chemistry of Metal Dissolution in Amine–Thiol Mixtures and Exploiting It toward Benign Ink Formulation for Metal Chalcogenide Thin Films. *Chem. Mater.* **2019**, *31* (15), 5674–5682. https://doi.org/10.1021/acs.chemmater.9b01566.

(13) van Embden, J.; Chesman, A. S. R.; Jasieniak, J. J. The Heat-Up Synthesis of Colloidal Nanocrystals. *Chem. Mater.* **2015**, *27* (7), 2246–2285. https://doi.org/10.1021/cm5028964.
(14) Coughlan, C.; Ibáñez, M.; Dobrozhan, O.; Singh, A.; Cabot, A.; Ryan, K. M. Compound Copper Chalcogenide Nanocrystals. *Chem. Rev.* **2017**, *117* (9), 5865–6109. https://doi.org/10.1021/acs.chemrev.6b00376.
(15) Marin, R.; Skripka, A.; Huang, Y. C.; Loh, T. A. J.; Mazeika, V.; Karabanovas, V.; Chua, D. H. C.; Dong, C. L.; Canton, P.; Vetrone, F. Influence of Halide Ions on the Structure and Properties of Copper Indium Sulphide Quantum Dots. *Chem. Commun.* **2020**, *56* (22), 3341–3344. https://doi.org/10.1039/c9cc08291c.
(16) Dierick, R.; Van den Broeck, F.; De Nolf, K.; Zhao, Q.; Vantomme, A.; Martins, J. C.; Hens, Z. Surface Chemistry of $CuInS_2$ Colloidal Nanocrystals, Tight Binding of L-Type Ligands. *Chem. Mater.* **2014**, *26* (20), 5950–5957. https://doi.org/10.1021/cm502687p.
(17) Hamid, S. H.; Ali, M. A. Comparative Study of Solvents for the Extraction of Aromatics from Naphtha. *Energy Sources* **1996**, *18* (1), 65–84. https://doi.org/10.1080/00908319608908748.
(18) Choi, Y. J.; Cho, K. W.; Cho, B. W.; Yeo, Y. K. Optimization of the Sulfolane Extraction Plant Based on Modeling and Simulation. *Ind. Eng. Chem. Res.* **2002**, *41* (22), 5504–5509. https://doi.org/10.1021/ie010435a.
(19) Bak, A.; Kozik, V.; Dybal, P.; Kus, S.; Swietlicka, A.; Jampilek, J. Sulfolane: Magic Extractor or Bad Actor? Pilot-Scale Study on Solvent Corrosion Potential. *Sustainability* **2018**, *10* (10), 3677. https://doi.org/10.3390/su10103677.
(20) Thompson, C. M.; Gaylor, D. W.; Tachovsky, J. A.; Perry, C.; Carakostas, M. C.; Haws, L. C. Development of a Chronic Noncancer Oral Reference Dose and Drinking Water Screening Level for Sulfolane Using Benchmark Dose Modeling. *J. Appl. Toxicol.* **2013**, *33* (12), 1395–1406. https://doi.org/10.1002/jat.2799.
(21) Dierick, R.; Capon, B.; Damm, H.; Flamee, S.; Arickx, P.; Bruneel, E.; Van Genechten, D.; Van Bael, M.; Hardy, A.; Detavernier, C.; Hens, Z. Annealing of Sulfide Stabilized Colloidal Semiconductor Nanocrystals. *J. Mater. Chem. C* **2014**, *2* (1), 178–183. https://doi.org/10.1039/c3tc31393j.
(22) Zhao, X.; Lu, M.; Koeper, M. J.; Agrawal, R. Solution-Processed Sulfur Depleted $Cu(In,Ga)Se_2$ Solar Cells Synthesized from a Monoamine–Dithiol Solvent Mixture. *J. Mater. Chem. A* **2016**, *4* (19), 7390–7397. https://doi.org/10.1039/C6TA00533K.
(23) Miskin, C. K.; Yang, W. C.; Hages, C. J.; Carter, N. J.; Joglekar, C. S.; Stach, E. A.; Agrawal, R. 9.0% Efficient $Cu_2ZnSn(S,Se)_4$ Solar Cells from Selenized Nanoparticle Inks. *Prog. Photovoltaics Res. Appl.* **2015**, *23* (5), 654–659. https://doi.org/10.1002/pip.2472.
(24) Yang, W.-C.; Miskin, C. K.; Hages, C. J.; Hanley, E. C.; Handwerker, C.; Stach, E. A.; Agrawal, R. Kesterite $Cu_2ZnSn(S,Se)_4$ Absorbers Converted from Metastable, Wurtzite-Derived Cu_2ZnSnS_4 Nanoparticles. *Chem. Mater* **2014**, *26*. https://doi.org/10.1002/pip.2472.

6. SLOT DIE COATING OF CIGS NANOPARTICLE INKS FOR SCALABLE SOLUTION PROCESSED PHOTOVOLTAICS

A version of this chapter has been published previously in conference proceedings: **Ellis, R. G**.; Vak, D.; Chesman, A. S. R.; Agrawal, R. Slot Die Coating of CIGS Nanoparticle Inks for Scalable Solution Processed Photovoltaics. In *Conference Record of the IEEE Photovoltaic Specialists Conference*; 2019; pp 1830–1833. https://doi.org/10.1109/PVSC40753.2019.8980504.

6.1 Introduction

$Cu(In,Ga)(S,Se)_2$ (CIGSSe) photovoltaics have emerged as a commercially viable thin film material with long term stability and power conversion efficiencies up to 23.35%.[1] However, current high efficiency devices are fabricated using three stage coevaporation or sputtered metallic precursor layers. These vacuum processes suffer from low materials utilization and low throughput. Solution processing is an attractive alternative fabrication method which has the potential to significantly reduce manufacturing costs through atmospheric pressure processing and high throughput roll-to-roll compatibility. However, high throughput coating techniques are relatively absent in the solution processed CIGSSe literature. A large amount of laboratory scale solution processing of CIGSSe photovoltaics is performed using non roll-to-roll compatible coating techniques such as spin coating, which has very poor materials utilization. Table 1 details a wide variety of solution processed CIGSSe devices and their fabrication methods.

Table 6.1. Power conversion efficiencies of various solution processing technologies with varying solvent systems and depositions methods. Asterisks denote active area efficiencies; all other reported efficiencies are total area efficiencies.

Power Conversion Efficiency (%)	Solvent System	Deposition Method	Reference
18.1%	Hydrazine	Spin Coating	2
15.85%*	Thiol-Amine	Spin Coating	3
10.5%	Aqueous	Spray Pyrolysis	4
15.2%*	Dimethyl Formamide	Spin Coating	5
15.0%	Hexanethiol	Blade Coating	6
11.3%	Ethylene glycol	Inkjet Printing	7

Power conversion efficiencies up to 18.1% have been demonstrated using a hydrazine based molecular precursor approach using spin coating.[2] However, hydrazine is extremely toxic and explosive posing significant challenges for scale up. Spray coating, while roll-to-roll compatible, is known for poor film quality and lower materials utilization. Currently, a colloidal nanocrystal ink using hexanethiol as a solvent has reached the highest solution processed, non-hydrazine total area efficiency of 15% using blade coating.[6] Roll-to-roll compatible inkjet analogues of this system have yielded power conversion efficiencies of 11.3%, however, the formation of an oxide precursor film and lack of a reduction step will likely keep this system from reaching higher power conversion efficiencies as discussed in Chapter 2.[7] In this work we adapt the colloidal nanoparticle approach for use with the scalable coating technique, slot die coating. Slot die coating offers high throughput with virtually 100% materials utilization and has been used extensively with a number of other photovoltaic technologies.

For example, recent work with state-of-the-art polymer solar cells has been able to achieve efficiencies of 13.5% using single-junction ternary polymer absorbers fabricated via slot die coating.[8] Impressively, using perovskite absorber layers also coated by slot-die, efficiencies up to 18.0% have been achieved.[8] Both of these examples demonstrate the promise of slot die coating as a scalable method to coat high efficiency devices. However, both perovskites and organic photovoltaics suffer from poor long-term stability, putting their use in commercial modules into question. As such, slot-die coating of an existing commercialized material such as CIGSSe is an attractive option to lower manufacturing costs while increasing throughput and materials utilization.

A custom built slot die coater based off of a commercial 3D printer was used to screen used to screen a wide variety of ink compositions and coating conditions.[9] The flexibility of the coater allowed for rapid screening a wide variety of coating conditions without the need for system redesign, and allowed for coating using an ink volume under 1 mL. This reduced the demand for nanoparticles for initial optimization increases optimization throughput and reduces materials consumption. A wide variety of non-polar solvents were screened, including toluene, chlorobenzene, and 1,2-dichlorobenzene. Optimized coatings were developed using a chlorobenzene/dichlorobenzene solvent mixture. Devices were fabricated from such coatings yielding active area efficiencies up to 11.7% (10.7% total area) on small area cells (0.47 cm^2). To

the best of our knowledge, this is the first report of slot die coated CIGSSe absorber layers demonstrating a path to low-cost large-scale fabrication of CIGSSe photovoltaics.

6.2 Experimental

$Cu(In,Ga)S_2$ nanoparticles were fabricated as described in a previous report [6]. Nanoparticles were purified using three successive suspension and precipitation cycles with hexane, isopropyl alcohol, and centrifugation. The nanoparticles were then dried under argon flow and suspended in toluene, chlorobenzene (CB), 1,2-dichlorobenzene (DCB), or a 1:1 vol:vol mixture of CB and DCB at a mass concentration of 250 mg/mL using sonication for 1 hour. Prior to coating, the ink was filtered through a 1 μm syringe filter to remove any aggregates. Coating was performed using a batch slot die coater fabricated from a modified 3D printer. Details of the fabrication and use of the slot die coater are described in a previous report.[9] Briefly, the lab scale slot die coater was based off a KClone K200 3D printer. The original extruder head, heater, and cooling fan were removed. The extrusion stepper was rewired to control a screw driven custom designed syringe pump manufactured by 3D printing. A custom slot die head consisting of two die ends, a 50 μm spacer foil, and meniscus guide were machined from 316 stainless steel by CNC machining. The printer had the capability of heating the slot die heat, the substrate bed, and had variable slot die gap in 10 μm increments. The coating speed could be varied from 1 mm/s to 150 mm/s over a bed area of 200 mm x 200 mm. The substrate temperature was varied between room temperature and 65°C during coatings. For all trials, the slot die gap, ink concentration and dispense rate were set at 100 μm, 250 mg/mL, and 1μL/cm^2 respectively. Absorbance measurements were taken using EPSON Perfection V600 and V700 scanners in transmission mode at 700 dpi. Devices were fabricated on soda lime glass substrates coated with 800 nm of molybdenum via sputtering. The CIGS ink was slot die coated in 13 mm wide stripes. Sodium doping was supplied by electron beam evaporation of ~22.5 nm of NaF. Nanoparticle films were cut to ~1/2" x 1" samples and annealed under an argon/selenium atmosphere at 500°C for 15-25 minutes (selenized). Devices were finished with 50 nm of CdS by chemical bath deposition. ZnO (80 nm) and ITO (220 nm) were deposited via sputtering. Finally, Ni (100 nm) and Al (1.5 μm) grids were deposited by E-beam evaporation. Devices were isolated using mechanical scribing with a cell area of 0.47 cm^2 and tested under AM 1.5 simulated light.

6.3 Results and Discussion

6.3.1 Coating Optimization

The tested inks wet clean soda-lime glass and molybdenum similarly, thus initial coatings were performed on transparent glass substrates to enable optical absorption measurements in transmission mode using a commercial photo film scanner. Absorbance was correlated to thickness using scribed step height measurements from a Dektak 6M Stylus Profilometer to generate a calibration curve. The as-synthesized particles contained ~8 wt% oleylamine as a surface ligand as determined by TGA and quantitative ^{1}H-NMR measurements. As such, colloidal stability was observed in non-polar solvents with dielectric constants ranging from ~2-10. Toluene, chlorobenzene, and dichlorobenzene were screened as solvents. Conventional slot die coating is considered a pre-metered process in which the coating thickness is set by the ink dispense rate. However, the small-scale lab coater operates in a hybrid of pre-metered and self-metered regimes whereby there is some film thickness dependence on both ink flow rate and coating parameters such as coating speed and substrate temperature. As such, various substrate temperatures and coatings speeds were iterated for each solvent system. The parameter space explored is shown in Table 6.2.

Table 6.2. Parameter space explored for ink composition and coating parameters for nanoparticle inks in this study.

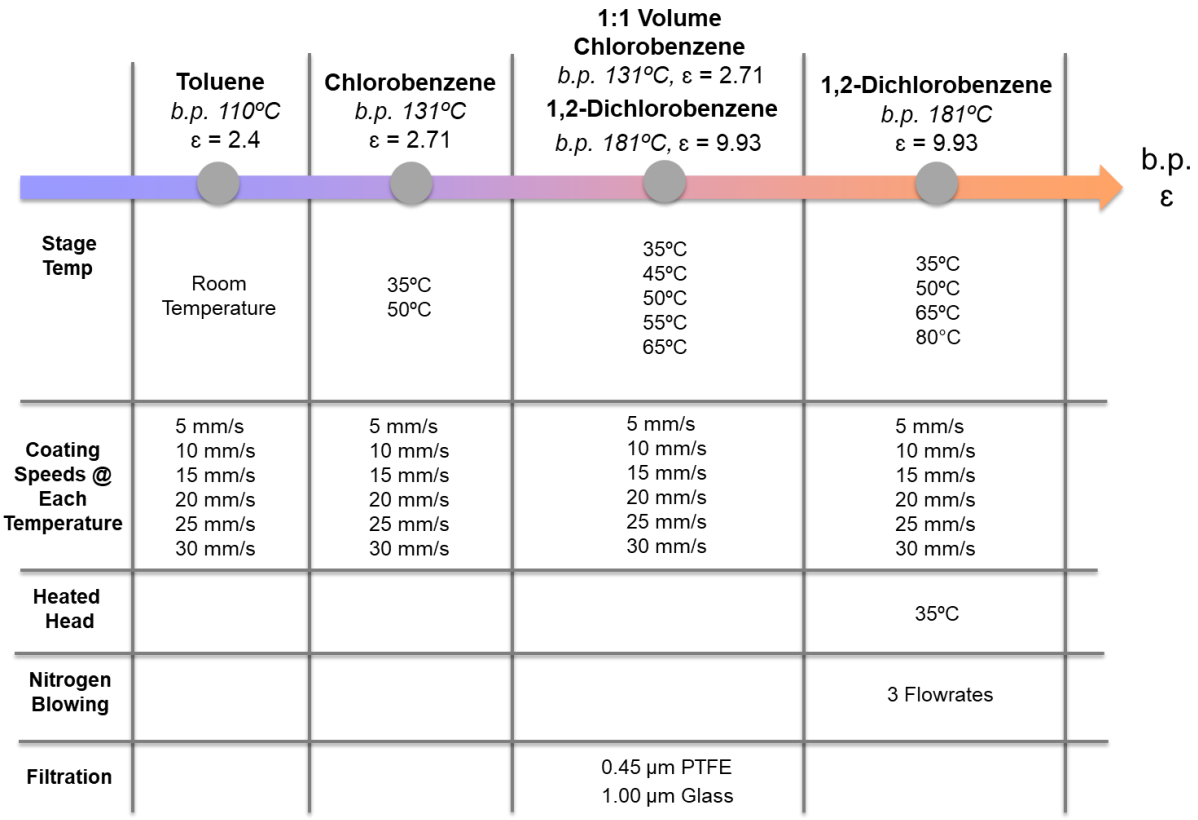

Toluene was quickly observed to poorly suspend the particles over the time scale of an hour resulting in nanoparticle settling in the syringe pump. This caused time variant coatings, and toluene was not considered further. Figure 6.1 shows the time dependence of toluene-based coatings as a result of poor colloidal stability.

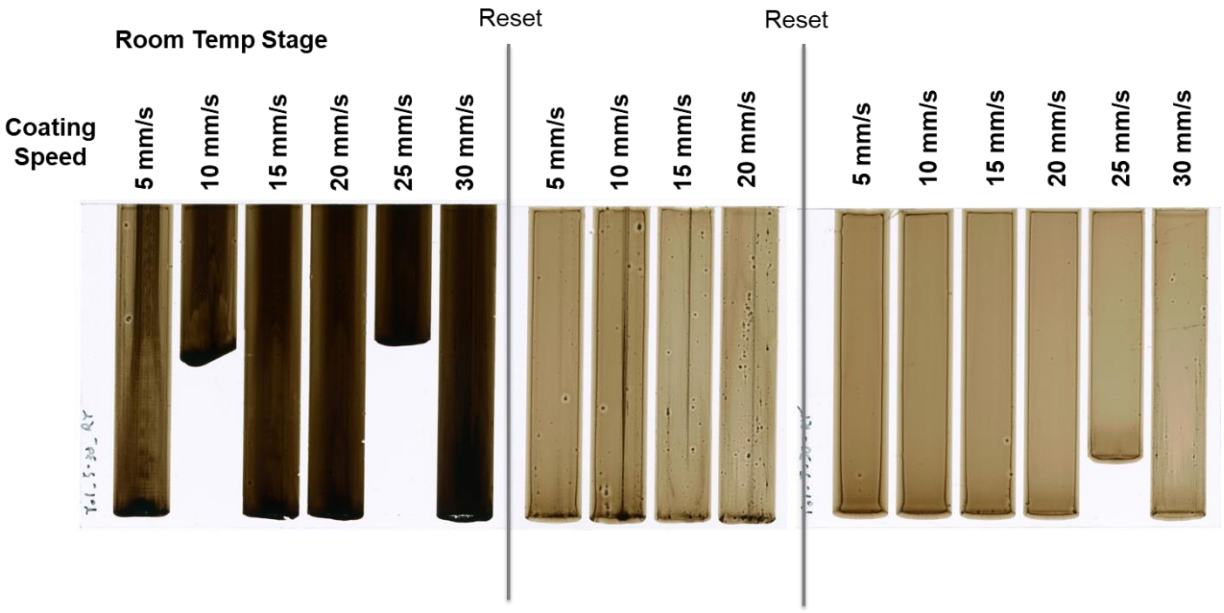

Figure 6.1. Color scans of toluene based coatings performed sequentially at various coating speeds. Reset denotes where a new substrate was loaded and coating was restarted.

CB and DCB were observed to provide significantly more stable colloidal suspensions. Coatings performed using dichlorobenzene were immediately observed to contain substantial coffee ring patterns, characterized by two large and thin increases in thickness at the edges of the coating. The effect became more pronounced for thicker films deposited at higher speeds as shown in the absorbance scan in Figure 6.2, where red areas are thicker parts of the film.

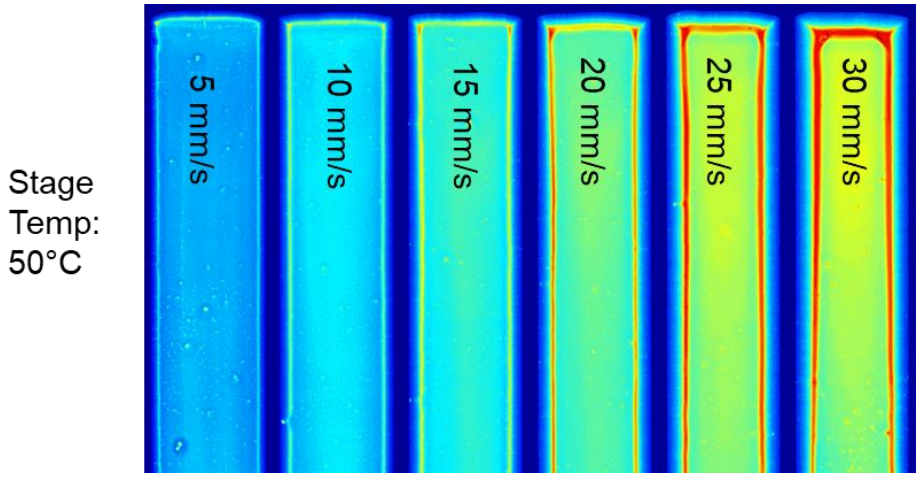

Figure 6.2. Absorbance image of the coffee ring pattern from slow drying dichlorobenzene based inks at a stage temperature of 50°C.

To help alleviate the coffee ring effects, a number of techniques were employed to assist in faster drying. The first method investigated was the use of a heated stage at various temperatures. Color scans of the films and reconstructed lateral thickness profiles are shown in Figure 6.3.

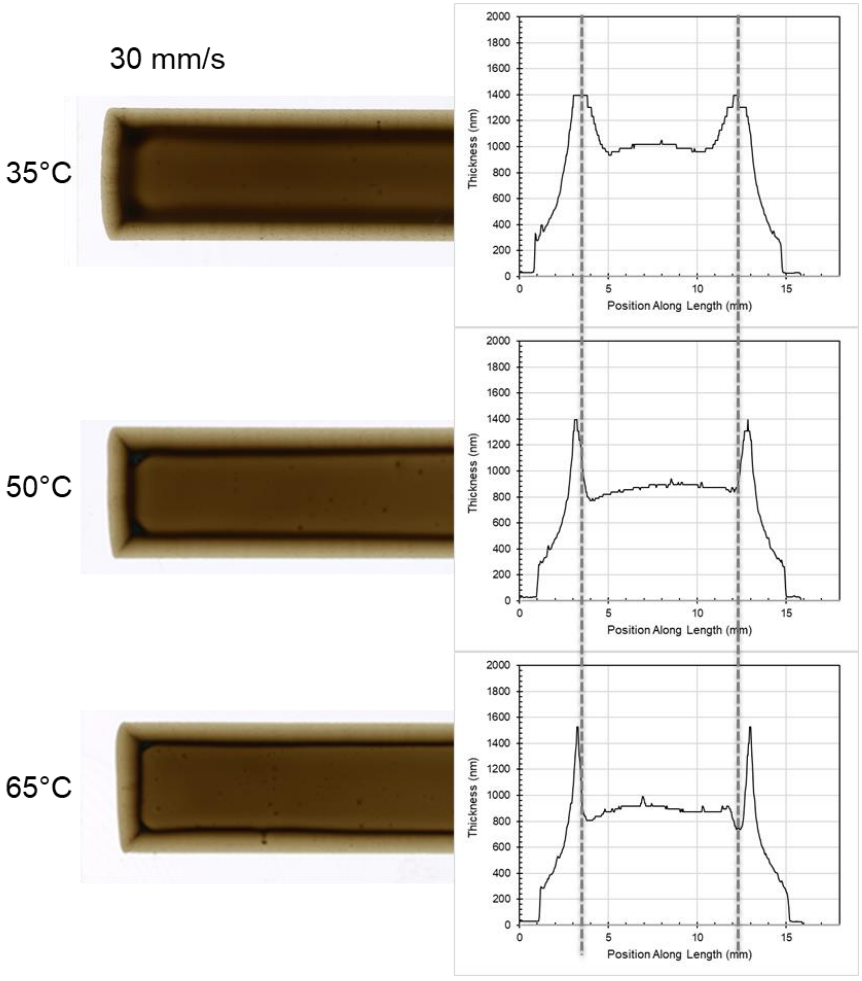

Figure 6.3. The dependence of the coffee ring pattern on the bed temperatures. Dashed lines show the peak of the coffee ring position.

While the width of the coffee ring decreased and the uniform center area increased slightly, the coffee ring pattern was largely unaffected by changing the bed temperature above 50°C. Another method was employed to reduce the drying time and therefore the time for the coffee ring pattern to developed was investigated, using a secondary slot die head to blow a stream of nitrogen over the wet film just after leaving the coating head. A diagram of the setup is shown in Figure 6.4.

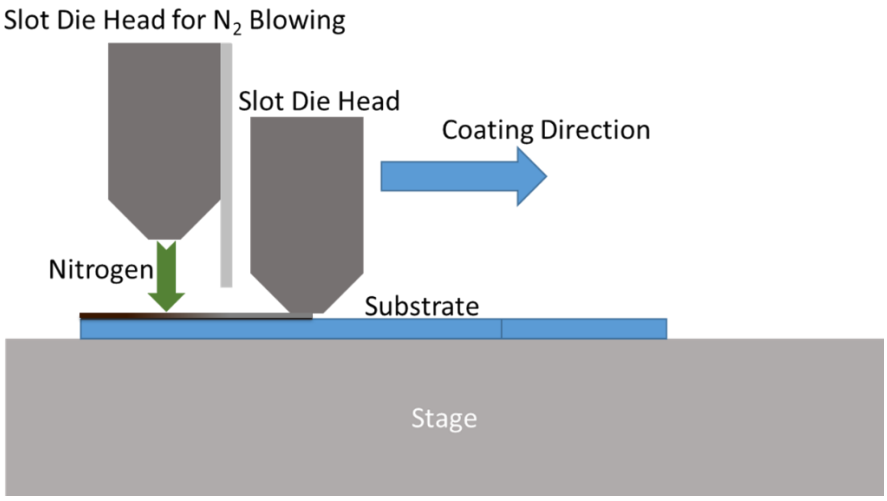

Figure 6.4. Nitrogen blowing setup using the custom slot die printer.

Films coated out of dichlorbenzene were explored at various flowrates (in approximate sccm) as shown in Figure 6.5, where the width of the nitrogen blowing slot was varied.

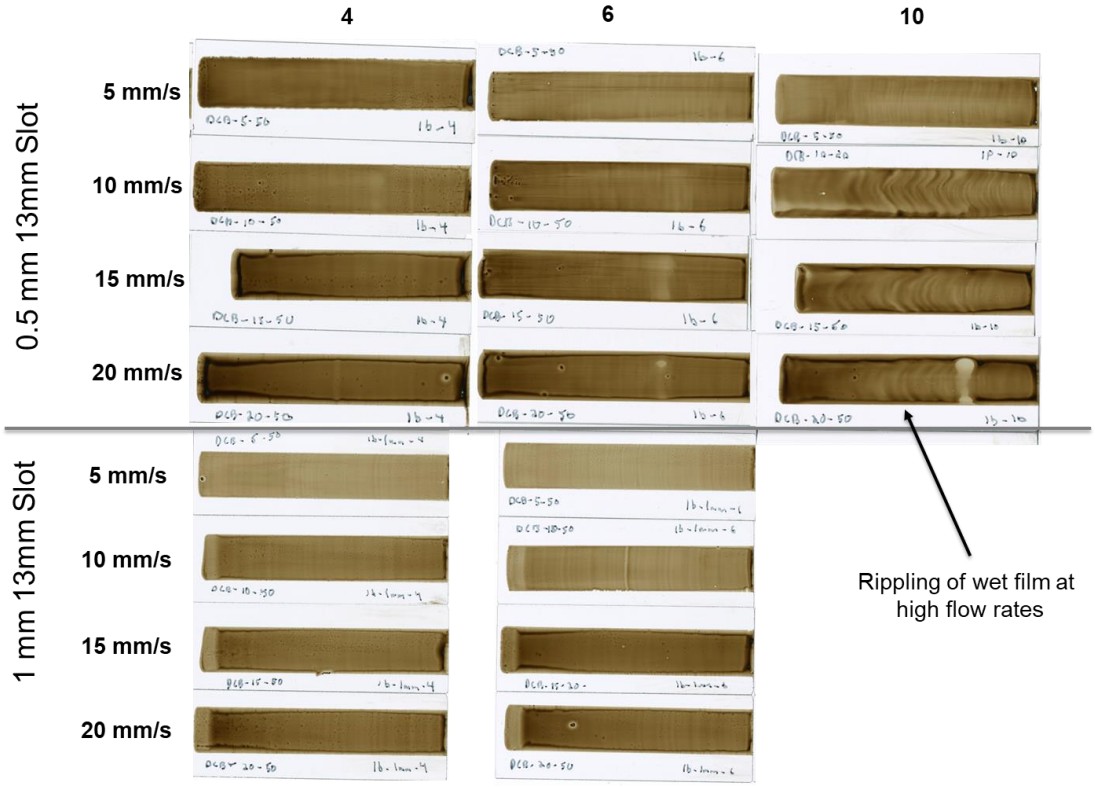

Figure 6.5. Color scans of films coated from dichlorobenzene inks at different speeds and nitrogen flowrates.

While coffee ring was largely suppressed for thinner films, a major drawback of the nitrogen blowing method was the rippling of the film. The force of the nitrogen likely imparted turbulence on the surface of the wet film, which then dried with ripple patters. While this method has some promise, a diffuser would be needed to prevent the rippling effect observed.

Another method to induce faster drying while simultaneously altering the wetting properties was the use of a low boiling co-solvent. Chlorobenzene was selected to its similarity to dichlorobenzene, but with a lower boiling point. A 1:1 mixture of chlorobenzene and dichlorobenzene was selected and compared to films coated at identical conditions from neat chlorobenzene and dichlorobenzene as shown in Figure 6.6.

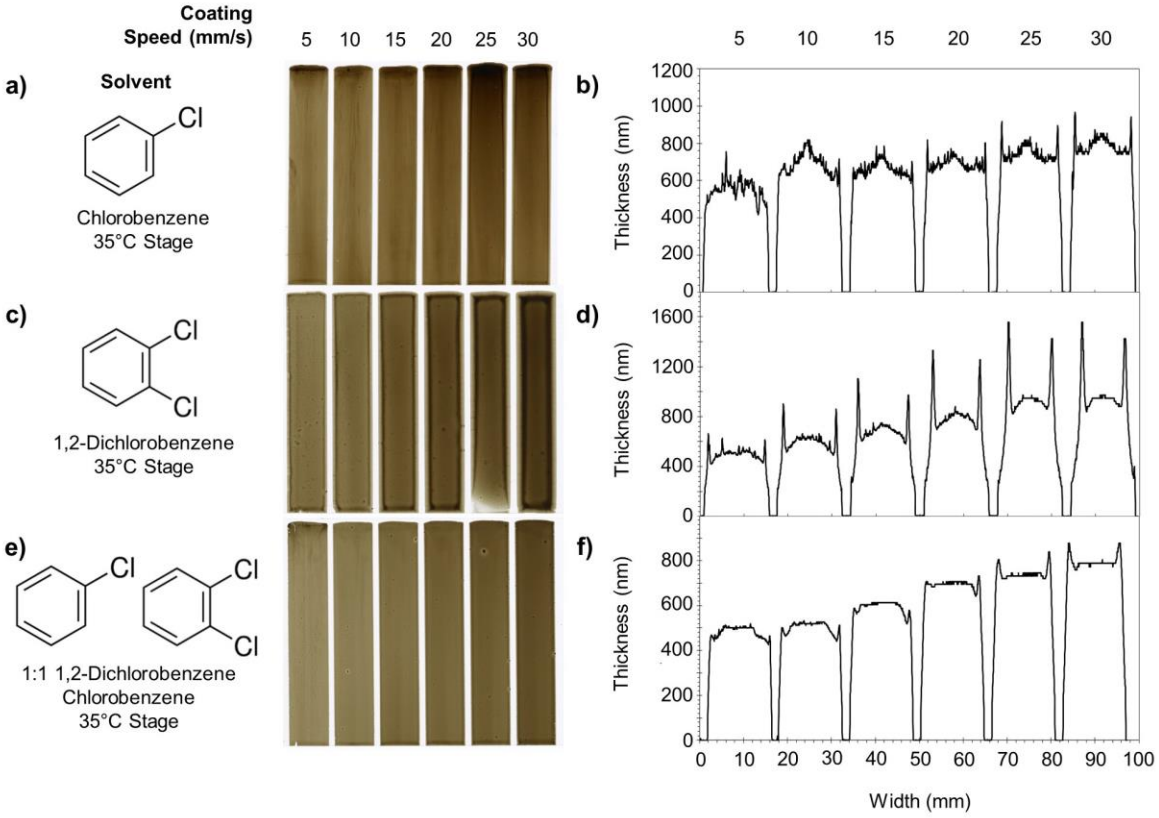

Figure 6.6. Color scans and generated width profiles from CIGS nanoparticle inks with various solvents. a) Color scans of chlorobezene ink films and b) their generated thickness profiles across the width. c) Color scans of 1,2-dichlorobenzene ink films and d) their generated thickness profiles across the width. e) Color scans of chlorobenzene/1,2-dichlorobenzene cosolvent ink films and f) their generated thickness profiles across the width.

The CB coatings appeared significantly more matte as opposed to the high shine of DCB coatings. This was attributed to small aggregate formation in the ink due to the nanoparticles' lower colloidal

stability in CB as compared to DCB. This resulted in significant surface roughness, as can be seen in Fig. 6.6 b). The surface roughness was accompanied by streak like structures along the length of the film. DCB yielded the best colloidal stability of the tested solvents, however, the aforementioned “coffee ring” like pattern was observed on the edges of each coating, increasing in prevalence for thicker films. The mixture immediately showed near complete removal of the persistent coffee ring pattern. The surface roughness of a chlorobenzene ink was also suppressed using the co-solvent method as shown in the width profile in Fig. 6.6 f). A three-dimensional reconstruction of the films using absorbance measurements shows improved width and length uniformity of the coatings using the co-solvent ink as shown in Figure 6.7.

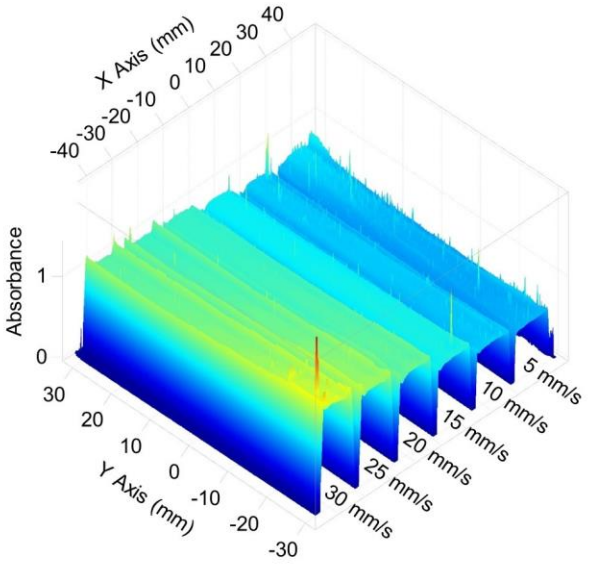

Figure 6.7. 3D film reconstruction via absorbance scanning showing minimal “coffee ring” and increased width and length uniformity using the CB/DCB co-solvent.

When coated as sequential stripes, superb length uniformity could be obtained after the first stripe. Additional substrate temperature optimization was performed starting at 35℃, up to 65℃, as shown in Figure 6.8.

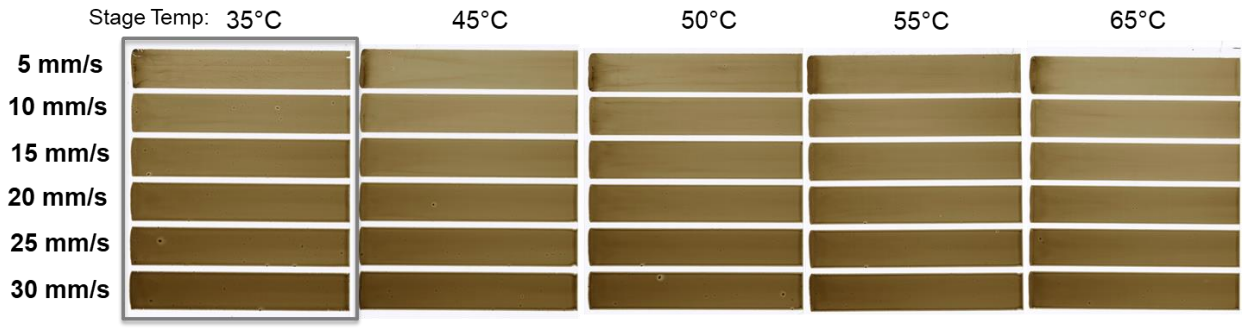

Figure 6.8. Stage temperature optimization for the 1:1 CB:DCB ink formulation at various coating speeds.

No substantial difference was observed between the various stage temperatures. As such, the lowest stage temperature was selected to reduce the thermal energy needed for the process, helping to reduce costs if the system were to be scaled.

6.3.2 Device Fabrication

The optimized co-solvent ink conditions were transferred to molybdenum substrates to enable device fabrication. Films on molybdenum substrates were coated from a single pass coating at 30 mm/s and a 35°C stage temperature yielding a ~830 nm thick nanoparticle film. Residual solvent was removed using a two-step annealing procedure under ambient conditions followed by natural cooling yielding largely crack free films as shown in Figure 6.9.

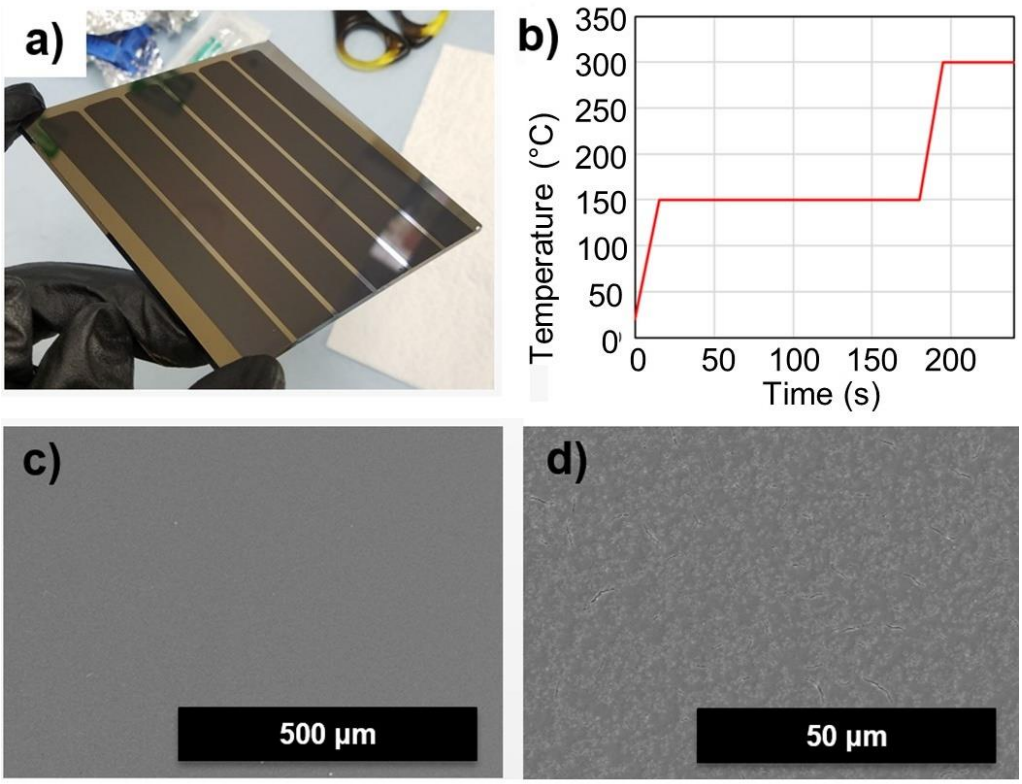

Figure 6.9. a) An image of a molybdenum coated substrate with stripes of CIGS nanoparticles b) A representative annealing profile to prevent cracking c) / d) SEM micrographs of the nanoparticle film surfaces showing largely microcrack free films.

Devices were finished as described in the experimental section. Full films divided into small area cells by using mechanical scribing yielding a device area of 0.47 cm^2 A finished device cross section and J-V curve is shown in Fig. 6.10 and Fig. 6.11 respectively. Active area efficiencies of up to 11.7% were achieved without the use of an antireflective coating, demonstrating the feasibility of the slot die coating technique for the fabrication of CIGSSe absorber layers.

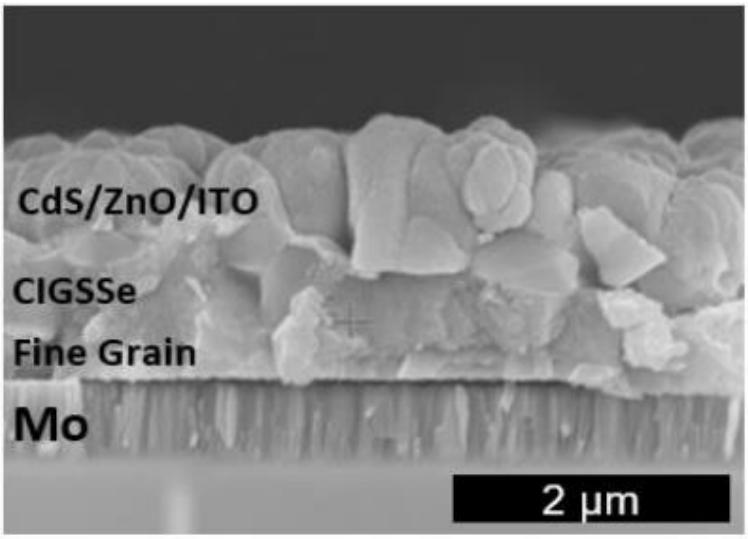

Figure 6.10. SEM cross-section of a completed device from slot die coating.

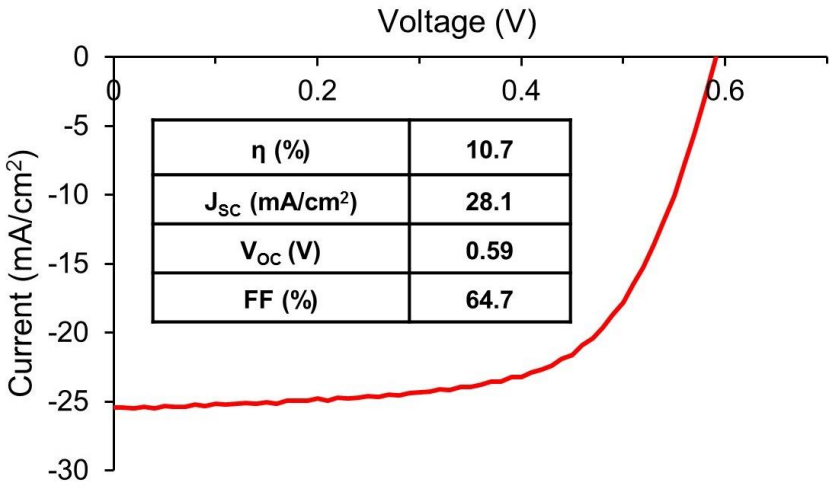

Figure 6.11. J-V curve from the light sweep of the champion cell with a total area efficiency of 10.7%.

To test the scalability of the process, the optimized ink was transferred from a batch slot die coater to roll-to-roll system. Proof of concept on PET film was performed to assess if large area uniformity could be obtained from the optimized inks. Ten meters of PET film was coated at a web speed of 1 mm/s. The laboratory scale roll-to-roll coater is shown in Figure 6.12 along with the coated film with high uniformity.

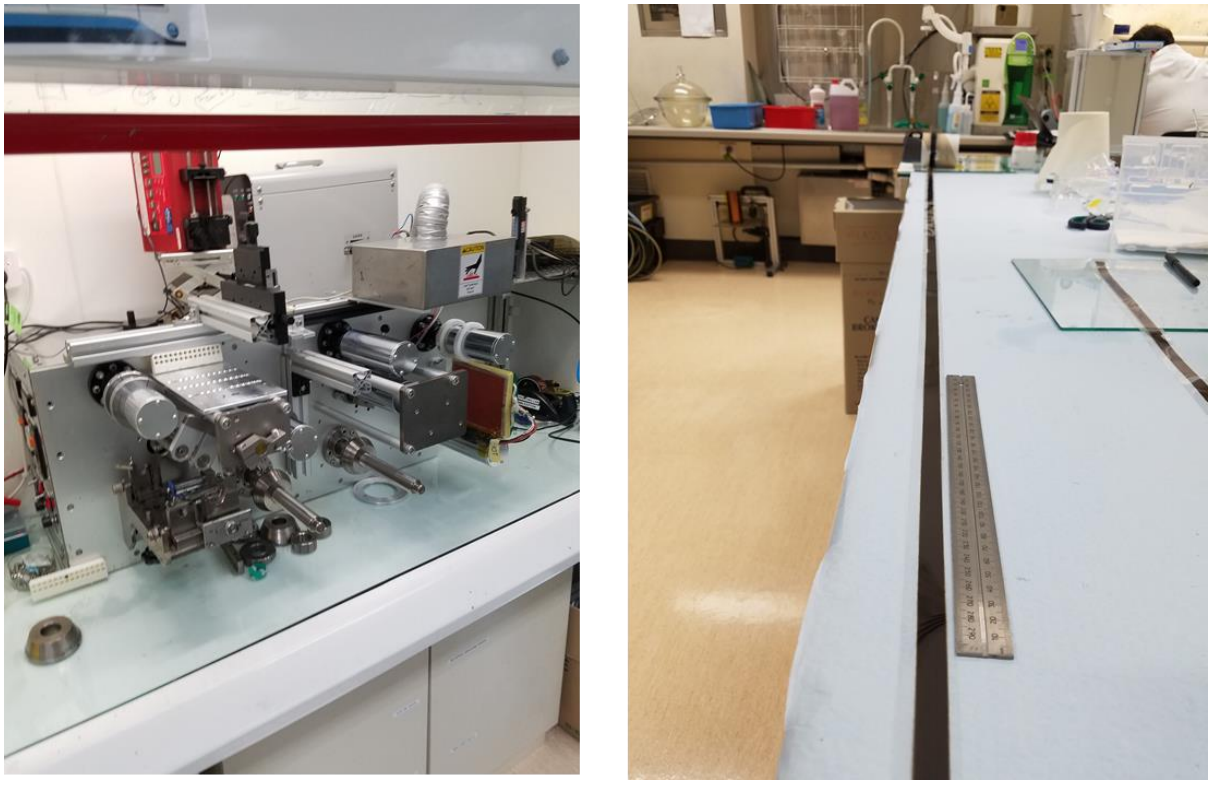

Figure 6.12. Roll-to-roll coater and section of CIGS nanoparticles coated from the optimized ink The proof of concept roll-to-roll coating demonstrates the high uniformity over large lengths that the optimized ink and slot-die coater is able to provide.

6.4 Conclusions

A wide variety of coating conditions were explored to obtain uniform thin films of CIGS nanoparticles using slot die coating. It was found 1,2-dichlorobenzene exhibited the best colloidal stability of the solvents tested, but the high boiling point and slow drying caused a “coffee ring” pattern to appear on the films. Adding a lower boiling co-solvent, chlorobenzene, suppressed the formation of “coffee rings” while maintaining the good colloidal stability of DCB. Through gentle solvent removal, virtually crack free films of nanoparticles could be obtained at thicknesses approaching a micron in a single coating pass. Devices fabricated from these films showed active area efficiencies up to 11.7% demonstrating the feasibility of slot die coating for the fabrication of CIGSSe absorber layers.

6.5 Acknowledgments

This work was supported by the NSF through the NRT program under award 1735282 and funding from the Australian Centre for Advanced Photovoltaics (ACAP). Ryan Ellis would also like to acknowledge Essam AlRuqobah, David Rokke, and Swapnil Deshmukh for their assistance in preparing nanoparticles as well as Joseph Andler, and Xianyi Hu for preparing Mo coated soda lime glass substrates.

6.6 References

(1) Nakamura, M.; Yamaguchi, K.; Kimoto, Y.; Yasaki, Y.; Kato, T.; Sugimoto, H. Cd-Free Cu(In,Ga)(Se,S)2 Thin-Film Solar Cell with Record Efficiency of 23.35%. *IEEE J. Photovoltaics* **2019**, *9* (6), 1863–1867. https://doi.org/10.1109/JPHOTOV.2019.2937218.

(2) Zhang, T.; Yang, Y.; Liu, D.; Tse, S. C.; Cao, W.; Feng, Z.; Chen, S.; Qian, L. High Efficiency Solution-Processed Thin-Film Cu(In,Ga)(Se,S) $_2$ Solar Cells. *Energy Environ. Sci.* **2016**, *9* (12), 3674–3681. https://doi.org/10.1039/C6EE02352E.

(3) Zhao, Y.; Yuan, S.; Kou, D.; Zhou, Z.; Wang, X.; Xiao, H.; Deng, Y.; Cui, C.; Chang, Q.; Wu, S. High Efficiency CIGS Solar Cells by Bulk Defect Passivation through Ag Substituting Strategy. *ACS Appl. Mater. Interfaces* **2020**, *12* (11), 12717–12726. https://doi.org/10.1021/acsami.9b21354.

(4) Fan, Q.; Tian, Q.; Wang, H.; Zhao, F.; Kong, J.; Wu, S. Regulating the Starting Location of Front-Gradient Enabled Highly Efficient Cu(In,Ga)Se $_2$ Solar Cells *via* a Facile Thiol–Amine Solution Approach. *J. Mater. Chem. A* **2018**, *6* (9), 4095–4101. https://doi.org/10.1039/C7TA10889C.

(5) Jiang, J.; Giridharagopal, R.; Jedlicka, E.; Sun, K.; Yu, S.; Wu, S.; Gong, Y.; Yan, W.; Ginger, D. S.; Green, M. A.; Hao, X.; Huang, W.; Xin, H. Highly Efficient Copper-Rich Chalcopyrite Solar Cells from DMF Molecular Solution. *Nano Energy* **2020**, *69*, 104438. https://doi.org/10.1016/j.nanoen.2019.104438.

(6) McLeod, S. M.; Hages, C. J.; Carter, N. J.; Agrawal, R. Synthesis and Characterization of 15% Efficient CIGSSe Solar Cells from Nanoparticle Inks. *Prog. Photovoltaics Res. Appl.* **2015**, *23* (11), 1550–1556. https://doi.org/10.1002/pip.2588.

(7) Barbé, J.; Eid, J.; Ahlswede, E.; Spiering, S.; Powalla, M.; Agrawal, R.; Del Gobbo, S. Inkjet Printed Cu(In,Ga)S2 Nanoparticles for Low-Cost Solar Cells. *J. Nanoparticle Res.* **2016**, *18* (12), 379. https://doi.org/10.1007/s11051-016-3686-5.

(8) Lee, J.; Seo, Y.; Kwon, S.; Kim, D.; Jang, S.; Jung, H.; Lee, Y.; Weerasinghe, H.; Kim, T.; Kim, J. Y.; Vak, D.; Na, S. Slot-Die and Roll-to-Roll Processed Single Junction Organic Photovoltaic Cells with the Highest Efficiency. *Adv. Energy Mater.* **2019**, *9* (36), 1901805. https://doi.org/10.1002/aenm.201901805.

(9) Vak, D.; Hwang, K.; Faulks, A.; Jung, Y. S.; Clark, N.; Kim, D. Y.; Wilson, G. J.; Watkins, S. E. 3D Printer Based Slot-Die Coater as a Lab-to-Fab Translation Tool for Solution-Processed Solar Cells. *Adv. Energy Mater.* **2015**, *5* (4). https://doi.org/10.1002/aenm.201401539.

7. INITIAL WORK TOWARDS FUTURE RESEARCH DIRECTIONS

7.1 Additional Improvements for Colloidal Nanoparticle Based CIGSSe Photovoltaics -

While the work detailed in the previous sections presents a method in which anionic impurities and carbonaceous impurities can be removed through the use of amine-thiol chemistry, exhaustive hybrid ligand exchange pathways, and/or ligand exchange free synthesis of metal chalcogenide nanoparticles, there is a remaining hurdle to overcome on the materials chemistry of the system. Even in low or no carbon containing nanoparticle films, selenization often leaves a residual fine grain layer. While no longer carbon containing, this fine grain layer is rich in copper and selenium, and devoid of indium and gallium. Again, this layer must be conductive in order for the devices fabricated in Chapter 4 to have functioned properly. However, the segregation of a copper selenide like material, if segregated to grain boundaries to any extent, would decrease the shunt resistance of a device substantially due to the high conductivity of $Cu_{2-x}Se$ materials. The origin of this material was speculated to arise from the sulfide to selenide reaction that occurs when selenizing pure sulfide materials.[1] As such, direct use of selenide nanoparticles could prevent the incomplete reaction and subsequent fine grain layer formation.

7.1.1 Antisolvent Precipitation as a Method to Prepare Thiol Free Selenide Precursors for Thin Film Fabrication

Introduction

In initial work in our group by Deshmukh et al., fabrication of selenide films using amine-thiol molecular precursors with excess selenium was able to form largely selenide $CuIn(S,Se)_2$ precursor films with an approximate Se/(Cu+In) of 0.9. When these films were selenized, no traditional fine grain layer was observed, showing that removing the sulfide to selenide transition may be responsible for fine grain layer formation.[2] It is hypothesized that primarily selenide precursor film will not undergo the traditional breakdown mechanism in selenization, where liquid selenium dissolves copper from the nanoparticle forming a $Cu_{2-x}Se$ intermediate. The sulfur is then replaced with selenium and the Cu_2-xSe then reacts with remaining indium and gallium to reconstitute as large grains of $Cu(In,Ga)(S,Se)_2$. In the case of a primarily selenide precursor film,

it is hypothesized that a bulk solid-state sintering mechanism is dominant due to the existing coordination of Cu with Se, preventing nanoparticle breakdown and $Cu_{2-x}Se$ formation as an intermediate species during selenization. The selenization may still be liquid fluxed, where ions may have improved mobility in a liquid selenium medium, however, this remains largely unclear at this stage. However, the prevention of $Cu_{2-x}Se$ formation and suppression of top down growth in favor of bulk growth is likely to prevent formation of residual fine grain layers rich in copper and selenium. As such, the colloidal nanoparticle equivalent method would be to synthesize $Cu(In,Ga)Se_2$ nanoparticles for use as precursors to be subjected to selenization. However, using the methods discussed in Chapter 3, the incorporation of sulfur is an inevitability unless large excesses of selenium are used to drive the reaction towards selenide. While $CuIn(S,Se)_2$ was synthesized in Chapter 3, elemental copper was used as a precursor, which was found to be heavily contaminated with oxide (~2%). The fate of this oxygen is still unknown, but to exhaustively avoid its incorporation into the film, Cu_2S (99.99%) was used as an alternative copper source.[3] However, due to the sulfur content of Cu_2S, its use further adds to sulfur content, likely requiring additional excess selenium addition to the reaction mixture to compensate. Another unintended side effect of using Cu_2S as a copper source is secondary phase formation during heat up with excess selenium. A competing reaction forming $Cu_{2-x}(S,Se)$ was observed in initial attempts to repeat the $CuIn(S,Se)_2$ nanoparticle synthesis of Chapter 3 (200% selenium case) using Cu_2S as a copper precursor, where large micron sized aggregates of $Cu_{2-x}(S,Se)$ were observed, increasing in prevelance as reaction times increased from 1 to 4 hours. Both spherical aggregates and plate like structures were observed. This phenomenon was observed with and without gallium addition, so it is unique to Cu_2S as a precursor. TEM images of the nano and microstructures from the aforementioned synthesis is shown in Figure 7.1.

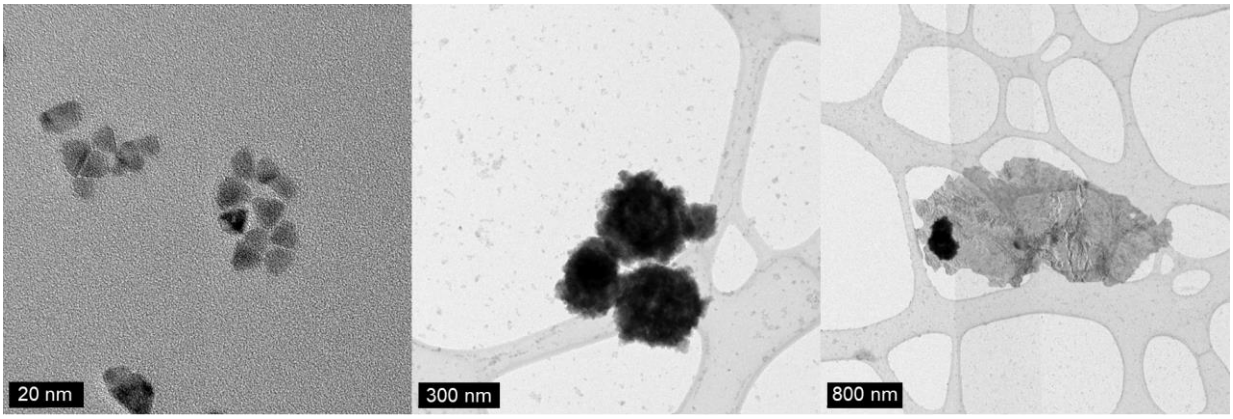

Figure 7.1. TEM of $Cu(In,Ga)(S,Se)_2$ nanoparticles synthesized using Cu_2S and "200%" selenium as described in Chapter 3 showing a) well dispersed nanoparticles, b) large aggregates of nanoparticles, and c) large plate like structures

While easily separated out using a 0.45 μm filter, the resulting well dispersed particles were then significantly deficient in copper. For a charge of Cu/(In+Ga) of 0.92, the product of filtration was generally Cu/(In+Ga) of 0.8. Further, Se/(Cu+In) was reduced to 0.7 as opposed to the 0.9 obtained in Chapter 3, due to the incorporation of sulfur from Cu_2S. As such, sulfide containing precursors such a Cu_2S introduce a number of challenges that hinder synthesis.

To avoid sulfur containing precursors, use of full selenide precursors such as Cu_2Se, and In_2Se_3 may allow for synthesis of nearly pure selenide CIGSe nanoparticles. However, for pure metal dissolution, metal thiolate (metal-sulfur bonding) is generally observed. Further, excess 1,2-ethanedithiol in the reaction mixture will likely contribute towards sulfide content. As such, a novel antisolvent precipitation method for isolation of Cu_2Se, In_2Se_3, and Se complexes (and mixtures of $Cu_2Se + In_2Se_3$, $Cu_2Se + Se$, $In_2Se_3 + Se$, and $Cu_2Se + In_2Se_3 + Se$) were developed to remove excess amines and thiol without the need for vacuum based evaporation techniques, while simultaneously changing the metal-sulfur coordination in the complexes to metal-selenium.

Antisolvent Precipitation Experimental

Materials

Copper (I) selenide (99.95% trace metals basis), selenium (99.99% trace metals basis, powder), toluene (99.9%, anhydrous), cyclohexane (99.9%, anhydrous), 1-methyl-2-pyrrolidinone (NMP, 99.5%, anhydrous), propylamine (99%), and oleylamine (70% technical grade) were

purchased from Sigma Aldrich and used as received with the exception of oleyamine, which was degassed using successive freeze pump thaw cycles under vacuum. Indium (III) selenide (99.95% trace metals basis) was purchased from Fisher Scientific and used as received.

Antisolvent Precipitation Method

All work was performed in a nitrogen atmosphere with <0.1 ppm O_2 and <0.1ppm H_2O. First, 0.4 to 0.8 M (indium basis or copper basis for solution not containing indium) solutions of $Cu_2Se + In_2Se_3$, $Cu_2Se + Se$, $In_2Se_3 + Se$, and $Cu_2Se + In_2Se_3 + Se$ of varying Se quantities were prepared by dissolving solid Cu_2Se, In_2Se_3, Se, and mixtures thereof in propylamine-1,2-ethanedithiol mixtures. Ratios of amines and thiols could be altered, but generally, 2 dithiols per indium and 1 dithiol per copper was the minimum amount of thiol used, where excess propylamine was used to determine concentration. Further, other amine thiol dissolutions such as ethylenediamine + 1,2-ethanedithiol + Ga + Se, propylamine + 1,2-ethanedithiol + Cu_2S, and propylamine + 1,2-ethanedithiol along with pure metals such as In, Zn, and Sn could be used. It is recommended that dissolution near their solubility limit are prepared to prevent losses in the supernatant during precipitation. As a specific example, a 0.8M solution (indium basis) of mixed Cu_2Se and In_2Se_3 was prepared in propylamine/1,2-ethanedithiol mixtures (1.53:1 propylamine:1,2-ethanedithiol mol:mol). After about 24 hours of stirring at room temperature a homogenous solution free of solids was obtained.

For antisolvent precipitation, 0.5 mL of the concentration Cu_2Se/In_2Se_3 solution was pipetted into a fluorinated ethylene propylene (FEP) centrifuge tube. Next 24 mL of anhydrous toluene was added immediately nucleating crystals of Cu_2Se and In_2Se_3 complexes. The mixture was vortex mixed for two minutes. Alternatively, a 1:4 vol:vol mixture of cyclohexane:toluene could be used to further drive the precipitation by reducing complex solubility further. After vortex mixing, the centrifuge tube was placed in a refrigerated centrifuge at 5°C and centrifuged at 5000-8000 rpm for 10 minutes. After centrifugation, a solid pellet was observed on the bottom of the centrifuge tube, and a clear supernatant was observed. The supernatant was decanted and the solid was dried under vacuum for 1 minute to remove any residual solvent. The solid precipitate was then redissolved in either propylamine or NMP at 0.16 M (250 µL added) with vortex mixing. Then 24 mL of toluene or 1:4 vol:vol cyclohexane:toluene was added followed by vortexing for two minutes. The mixture was centrifuged again at 5°C and 5000-8000 rpm. The clear supernatant

was decanted and the solid product was dried under vacuum for 5 minutes to remove antisolvent. We note that the redissolution after the first precipitation is not needed and addition of antisolvent alone should be sufficient for the second purification. The final dry product could be redissolved in oleylamine for nanoparticle synthesis. Butylamine, propylamine, dimethyl sulfoxide, and NMP were also observed to readily solubilize this complex mixture.

Nanoparticle Synthesis

For a typical nanoparticle synthesis with isolated Cu_2Se and In_2Se_3 complexes, the precipitated complexes were redissolved in 5 mL oleyalmine at 0.0572 M. The mixture was transferred to a microwave reaction vial (2-5 mL size) along with a polytetrafluoroethylene (PTFE) coated magnetic stir bar. The vial was crimp sealed with aluminum crimp seal with an inner PTFE coated silicone septa. The vial was loaded into a Biotage Initiator 400W EXP microwave reactor and heated to 250℃ and held at that temperature for 22 minutes. The vial was cooled to room temperature naturally. The reaction mixture was pipetted into an FEP centrifuge tube where ~ 20 mL of isopropyl alcohol was added along with centrifugation to precipitate the nanoparticles. The supernatant was discarded and the nanoparticles were redispersed in 4 mL of hexanes. The precipitation cycle was repeated 2 additional times, for a total of three washes. The particles were either dried under argon flow or dispersed in hexanes after the reaction.

Ligand Exchange with Precipitated Selenium Complex

A 4M selenium solution in butylamine/ethanethiol was precipitated with toluene using the precipitation methods previously described. The isolated complex was redissolved in formamide at an approximate concentration of 1M. $Cu(In,Ga)S_2$ nanoparticle synthesized with Cu_2S, In, and Ga precursors were synthesized as described in Chapter 3 and 4. The oleylamine capped nanoparticles were dispersed in toluene at 20 mg/mL. An equal volume of the immiscible non-polar toluene/CIGS phase was added to the polar formamide/Se complex phase. The two-phase mixture was transferred to a microwave vial and sealed as described in the previous section. The mixture was heated at 50℃ for 30 minutes. Complete transfer of the nanoparticle from the non-polar phase to the polar phase was observed suggesting some extent of ligand exchange. The nanoparticles were washed by removing the polar phase and adding excess pyridine. Through

centrifugation, the nanoparticles were isolated and could be redispersed in moderately polar solvents such as DMSO and acetonitrile. Additional washing cycles were attempted by redispersing the particles in acetonitrile and precipitating with excess pyridines and centrifugation again. However, significant losses were observed due to retention of a significant amount of nanoparticles in the supernatant. Further optimization is needed in selection or washing solvents.

Results and Discussion

A 4M selenium solution was precipitated using the precipitation procedure as described in the experimental section. The relatively simple procedure was able to remove all free amine and thiol species as verified by ^{1}H-NMR. Slight quantity of residual toluene can be removed by extending the duration of the vacuum dry after isolating the solid complexes. Various precipitations are shown in Figure 7.2 directly after antisolvent addition and cold centrifugation for the first and second washes (before supernatant removal).

Figure 7.2. Antisolvent precipitation of various complexes one first and second purification cycles respectively.

An interesting side effect of the precipitation is the change in coordination environment of the complexes. With solution of butylamine, 1,2-ethanedithiol, and Cu_2Se + Se or In_2Se_3 + Se, the nearest neighbor atom was probed using x-ray absorption spectroscopy (XAS). The complexes were observed to initially have metal sulfur coordination in bulk amine-thiol solvent. However, after antisolvent precipitation and redissolution in NMP, the coordination changed, where metal selenium coordination was observed as shown in Figure 7.3 and Table 7.1.

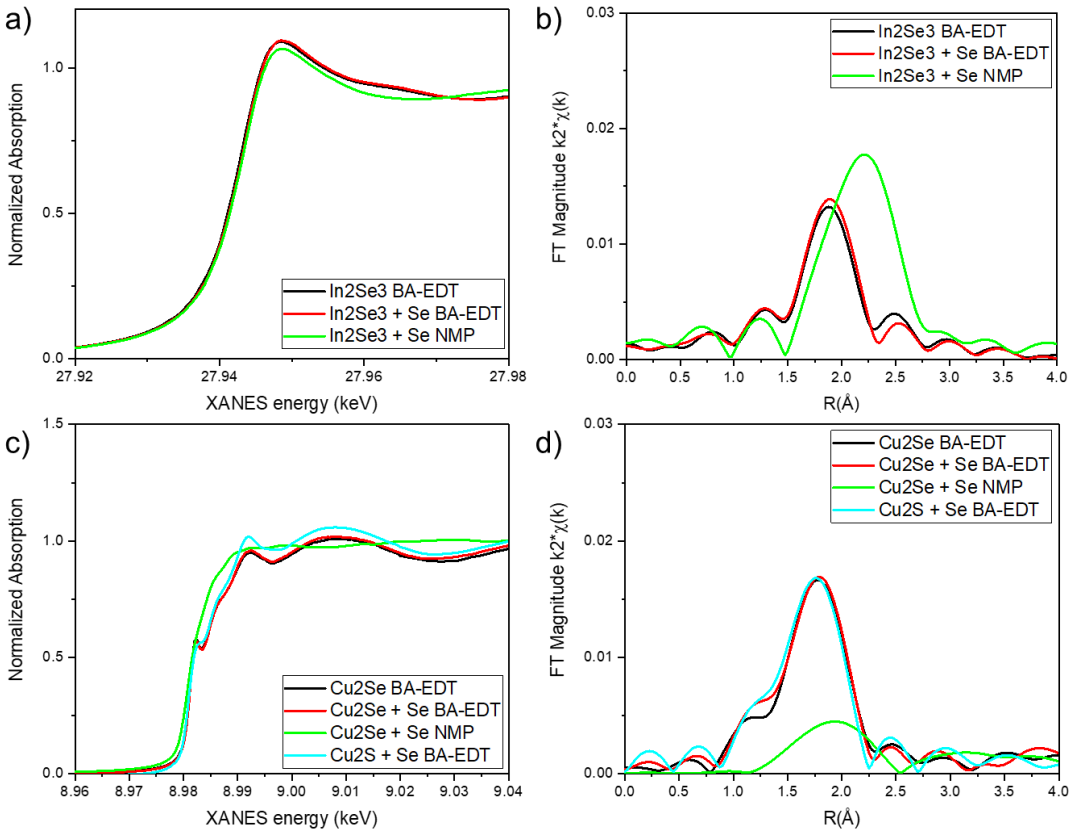

Figure 7.3. a) K-edge XANES for a) indium and c) copper solutions respectively. The magnitude of the Fourier transforms of the K-edge k^2 weighted EXAFS for b) indium and d) copper solutions respectively. Various solutions for both indium and copper were run as noted in the legends.

Table 7.1. Extracted scattering pairs, coordination numbers and bond length from XAS for copper in indium species respectively.

Sample	XANES Energy (keV)	Scattering Pair	CN	R (Å)
In_2Se_3 BA-EDT	27.9431	In-S	4.0	2.45
In_2Se_3 + Se BA-EDT	27.9431	In-S	4.0	2.45
In_2Se_3 + Se NMP	27.9431	In-Se	6.0	2.58

Sample	Preedge Energy (keV)	XANES Energy (keV)	Scattering Pair	CN	R (Å)	
Cu_2Se BA-EDT	8.9811	8.9847	Cu-S	4.0	2.23	Cu^{1+}
Cu_2Se + Se BA-EDT	8.9811	8.9847	Cu-S	4.0	2.23	Cu^{1+}
Cu_2Se + Se NMP		8.9807	Cu-Se	2.1	2.29	
Cu_2S + Se BA-EDT	8.9811	8.9847	Cu-S	4.0	2.23	Cu^{1+}

This side effect has large favorable implications for the synthesis of selenide materials, where previously, metal sulfides were likely to form first, followed by incorporation of excess selenium through an anion exchange at high temperature. Now, due to the metal selenium direct coordination, it is likely that metal selenides are the first species formed. The exact moment of metal sulfur coordination changing to metal selenium coordination during the various steps of antisolvent precipitation is not yet known, however this is currently under investigation.

Due to the favorable metal-selenium coordination in these complexes, initial fabrication of $CuInSe_2$ nanoparticles was proofed in oleylamine. Through a simple heat up microwave assisted solvothermal reaction, high quality $CuInSe_2$ nanoparticles were obtained without the use of excess selenium (selenium was only provided by the selenium in Cu_2Se and In_2Se_3). XRD and Raman from this synthesis are shown in Figure 7.4.

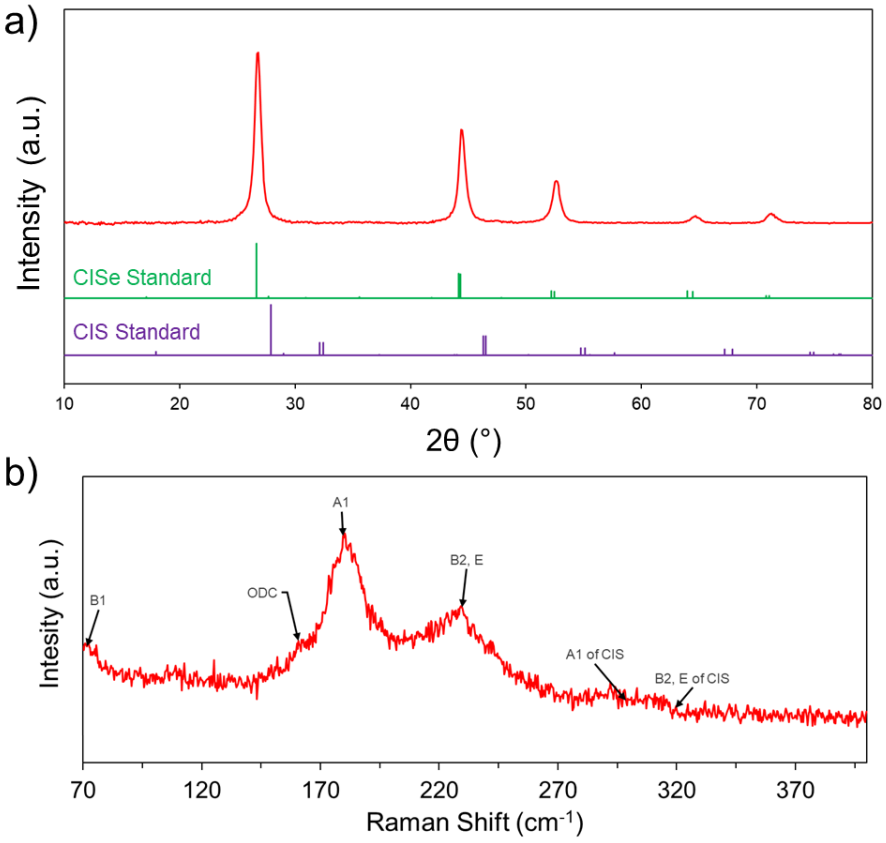

Figure 7.4. a) XRD and b) Raman spectroscopy of $CuIn(S,Se)_2$ nanoparticles from precipitated Cu_2Se and In_2Se_3 complexes

Notably, no secondary Cu_2-xSe secondary phase is observed in Raman. Minimal $CuInS_2$ is observed using Raman as evidenced by the low intensity of the CIS A1 and B2, E of CIS between

270 and 370 cm^{-1}. Further analysis using XRF shows a Se/(Cu+In) of approximately 0.98, a highly promising result for nearly complete selenide synthesis from these specialized precipitated precursors. While inclusion of gallium may pose a challenge due to the insolubility of Ga_2Se_3 and Ga_2Se_3 + Se in all amine thiol mixture attempted, Ga metal and elemental selenium can be codissolved in ethylenediamine/ethanedithiol mixtures. However, the sulfur content of nanoparticles made using that precursor is yet to be analyzed. Work on $Cu(In,Ga)(S,Se)_2$ nanoparticles from precipitated precursors in in progress. Beyond nanoparticle synthesis, these precipitated precursors may play a pivotal role in the development of molecular precursors, removing excess sulfur and reducing the toxicity and corrosive nature of amine-thiol precursor solutions. Further, because no excess amines and thiols are present, coating on underlying layers such as selenium becomes possible, due to the insolubility of selenium in solvents such as NMP, whereas previous the bulk amine-thiol solvent would dissolve any soluble species in layers below. Additionally, in the molecular precursor approach, coating with scalable coating techniques such as slot-die coating become available. While conventional amine-thiol mixtures may etch iron (a midgap defect inducing species in CIGSSe photovoltaics) from the stainless-steel slot die head, the lack of any excess amine and thiol reduces this possibility substantially.

In the case of a ligand exchange of the $CuIn(S,Se)_2$ nanoparticles, a sulfide ligand exchange pathway as developed in Chapter 4 may be counterproductive to the goal of largely pure selenide nanoparticles, due to the highly reactive and sulfurizing nature of diammonium sulfide.[4] In such a goal, a ligand exchange with a comparable selenide containing species would be an ideal case. However, diammonium selenide, which can be formed by addition of selenium to diammonium sulfide solution, is an unstable salt, potentially off gassing toxic H_2Se gas. As such, its use should be avoided due to safety concerns. Amine-thiol mixtures can be used to form sulfur free complexes with amines as shown in previous work by our group.[4,5] Using inspiration from ligand exchange pathways performed by Buckley et al., who performed ligand exchange with Sb_2S_3 dissolved in amine-thiol mixtures,[6] a selenium analog using alkylammonium polyselenide species formed from dissolution of Se in monoamine and monothiol mixtures may be an ideal ligand for CISe or CIGSe nanoparticles.[7] Using the previously described precipitation methods, large amounts of selenium complex can be isolated from 4M solutions of selenium in amine-thiol mixtures. Use of this ligand in identical methods to what was described in Chapter 4 may allow for alkylammonium polyselenide capped CIGSe nanoparticles, removing sulfur incorporation and potentially assisting

in selenization due to the presence of poylselenide surrounding every nanoparticle. One could imagine a selenization procedure in which very little or no external selenium is needed due to the excess of selenium surrounding each nanoparticle. Such a vision would further simplify processing due to the removal of selenium vapor delivery concerns. Initial work using this concept has been proofed, where an approximately 1M solution of precipitated selenium complex redissolved in formamide was used for a two-phase nanoparticle ligand exchange. $Cu(In,Ga)S_2$ nanoparticles dispersed in toluene were added to the formamide Se mixture to form a two phase mixture. Complete phase transfer of the nanoparticles was observed at the conditions described in the experimental section was observed. However, the limiting factor was a significant loss of particles due to unoptimized washing. There is a challenge in that excess selenium complex needs to be removed while simultaneously precipitating the nanoparticles. To do this, a non-polar antisolvent is needed to precipitate the now polar stable selenium capped nanoparticles. However, excess selenium complex is desirable to be removed, and non-polar solvents act as an antisolvent inducing selenium complex precipitation. Therefore, a non-polar solvent with some solubility of the selenium complex is needed to remove the excess. For this reason, pyridine was chosen as the non-polar antisolvent, however, significant retention of nanoparticles in the supernatant was observed when using pyridine as an antisolvent. An alternative method would be to directly use the polar phase as an ink; however, low nanoparticle mass concentration is a limitation of this method. Further optimization of this ligand exchange is certainly needed; however, it provides a promising route that could even be adapted to the Cu_2Se and In_2Se_3 based ligands.

7.1.2 Methods to Further Boost Efficiencies

While use of selenide nanoparticles may solve the residual fine grain layer formation problem, additional optimization of the absorber layer will certainly be needed in order to reach high efficiencies of 20% and beyond. Borrowing from vacuum processed CIGSSe, a number of processes have been developed to improve CIGSSe photovoltaics that could be implemented into solution processed CIGSSe absorbers. First, the use of thicker, > 2 μm absorbers is a commonality among most vacuum processed absorber layers.[8] While grain growth to this level has historically been a limitation with OLA capped CIGS nanoparticles, ligand exchange has provided a method to significantly boost grain growth.[1] We believe the use of ligand exchanged nanoparticles will provide a mode of reaching > 2 μm thin films. Initial work on this front using hybrid LigEx inks

coated with 6 blade coating cycles instead of 4 (as described in Chapter 4) were used to fabricated ~1.5 µm absorbers as shown in Figure 7.5.

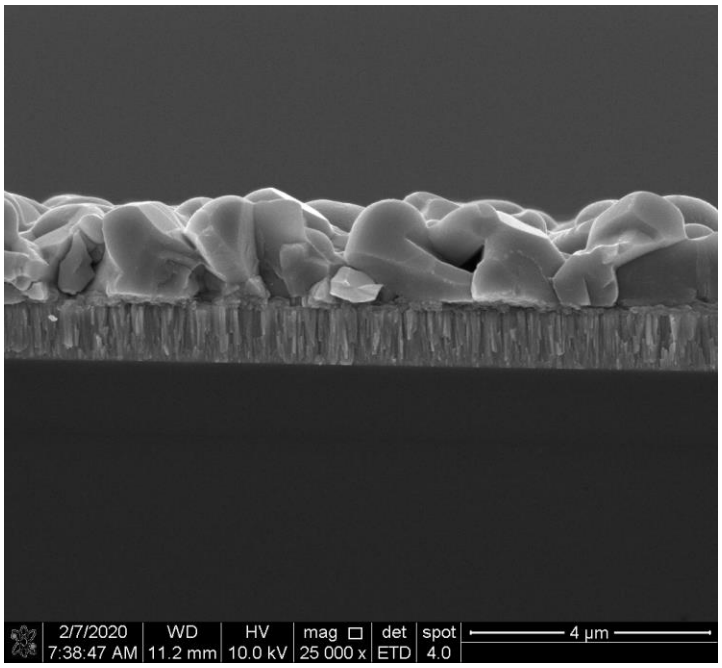

Figure 7.5. Approximately 1.5 µm thick $Cu(In,Ga)(S,Se)_2$ absorber layer from six blade coating cycles of hybrid LigEx nanoparticles

Additional selenization optimization will be needed, however, this represents a promising initial step. Further, use of selenide nanoparticles rather than sulfide will likely help prevent any fine grain formation which could otherwise thicken with increased absorber thickness.

Another commonality among high efficiency vacuum processed absorber layers is the use of a gallium grading, with higher gallium content towards the molybdenum back contact as well as a slight increase of gallium of the CIGSSe/CdS interface.[9,10] This prevents interfacial recombination and boost device performance significantly. The use of gallium gradings has been demonstrated for a number of solution processing routes and has generally increased efficiency compared to ungraded counterparts.[11,12] Alternatively, the front notch of increased gallium can be replaced using sulfurization to increase the surface bandgap. This is the method employed in the current world record vacuum processed CIGSSe device.[13] In solution processed methods, the surface sulfurization has yielded a substantial increase in device performance, mainly in an increased V_{OC}.[14] Designing a graded absorber from multiple coatings of compositionally varying

nanoparticles could be a path towards implementing a gallium grading in our solution processed absorbers.

The efficiency gains of vacuum processed CIGSSe over the last five years have been in large part due to the implementation of heavy alkali species. While sodium is commonly used to assist with grain growth and improve electrical properties as was demonstrated in Chapter 4, potassium, rubidium, and cesium all have been used to reach higher and higher efficiencies.[13,15,16] The benefits of potassium on solution processed devices has been investigated in our group by Alruqobah et al., showing clear improvements in device optoelectronic properties.[17] Implementation of these methods on ligand exchanged devices, sulfide or selenide would likely drastically improve device efficiency.

Lastly, the incorporation of silver into CIGSSe, forming $(Ag,Cu)(In,Ga)(S,Se)_2$, has been explored as a method to reduce the melting temperature of CIGSSe, reduce defect densities, and greatly improve grain growth.[18,19] This has been demonstrated for higher silver contents of 10-30% in vacuum processed absorbers, and at low silver contents around 1% in solution processed ACIGSSe absorbers.[20] Incorporation of silver has also been shown as a method to remove fine grain layer, likely through a modification of the selenization reaction pathway,[20] avoiding formation of a discrete $Cu_{2-x}Se$ like layer. If sulfide-based nanoparticles are used in the future, silver may be an optimal method of avoiding fine grain layer formation, reducing defects, selenization temperature, and boosting efficiencies.

Finally, slot die coating methods were demonstrated in Chapter 6, however, they were not extended to larger photovoltaics, namely minimodules. The nature of slot die coating allows for series interconnected cells using closely spaced striped patterns. This eliminates the need for laser scribing as pattering is facilitated by layer placement thereby further reducing processing costs. The envisioned architecture of both minimodules and large area cells are shown in Figure 7.1.

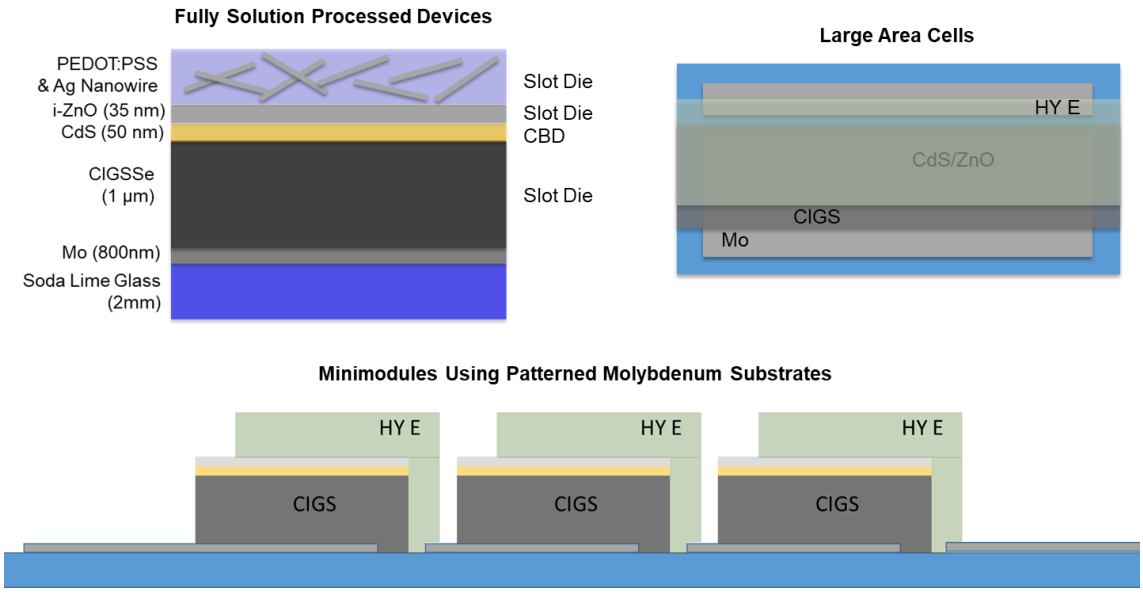

Figure 7.6. Fully solution processed CIGSSe device architecture cross-section, top down view of a large area cell making use of a patterned molybdenum substrate, and cross-section of series interconnected cells for minimodule fabrication.

The implementation of the aforementioned improvements are all methods that could greatly increase the efficiencies of solution processed absorber layers and help the transition from lab scale to commercial module scale. It is likely a majority of the methods discussed in this section will be needed. It can be highlighted that if high efficiency solution processed absorbers over 20% can be realized, a paradigm shift in photovoltaics manufacturing will also have been realized. A method of low-cost manufacturing of stable CIGSSe photovoltaics could change our existing energy landscape and help humanity transition into a renewable energy future. It is my hope that the work presented in this dissertation may aid in the journey towards that goal.

7.2 References

(1) Ellis, R. G.; Turnley, J. W.; Rokke, D. J.; Fields, J. P.; Alruqobah, E. H.; Deshmukh, S. D.; Kisslinger, K.; Agrawal, R. Hybrid Ligand Exchange of Cu(In,Ga)S_2 Nanoparticles for Carbon Impurity Removal in Solution-Processed Photovoltaics. *Chem. Mater.* **2020**, *32* (12), 5091–5103. https://doi.org/10.1021/acs.chemmater.0c00966.

(2) Deshmukh, S. D.; Rokke, D. J.; Kisslinger, K.; Agrawal, R. Investigating the Potential of Amine-Thiol Solvent System for High-Efficiency CuInSe2 Devices. In *47th IEEE PVSC*; 2020.

(3) Deshmukh, S. D.; Ellis, R. G.; Sutandar, D. S.; Rokke, D. J.; Agrawal, R. Versatile Colloidal Syntheses of Metal Chalcogenide Nanoparticles from Elemental Precursors Using Amine-Thiol Chemistry. *Chem. Mater.* **2019**, *31* (21), 9087–9097. https://doi.org/10.1021/acs.chemmater.9b03401.

(4) Zhang, H.; Solomon, L. V.; Ha, D. H.; Honrao, S.; Hennig, R. G.; Robinson, R. D. $(NH4)_2S$, a Highly Reactive Molecular Precursor for Low Temperature Anion Exchange Reactions in Nanoparticles. *Dalton Transactions*. The Royal Society of Chemistry August 13, 2013, pp 12596–12599. https://doi.org/10.1039/c3dt50803j.

(5) Walker, B. C.; Agrawal, R. Contamination-Free Solutions of Selenium in Amines for Nanoparticle Synthesis. *Chem. Commun.* **2014**, *50* (61), 8331–8334. https://doi.org/10.1039/c4cc02379j.

(6) Buckley, J. J.; Greaney, M. J.; Brutchey, R. L. Ligand Exchange of Colloidal Cdse Nanocrystals with Stibanates Derived from Sb2S3 Dissolved in a Thiol-Amine Mixture. *Chem. Mater.* **2014**, *26* (21), 6311–6317. https://doi.org/10.1021/cm503324k.

(7) Deshmukh, S. D.; Easterling, L. F.; Manheim, J. M.; Libretto, N. J.; Weideman, K. G.; Miller, J. T.; Kenttämaa, H. I.; Agrawal, R. Analyzing and Tuning the Chalcogen-Amine-Thiol Complexes for Tailoring of Chalcogenide Syntheses. *Inorg. Chem.* **2020**, *59* (12), 8240–8250. https://doi.org/10.1021/acs.inorgchem.0c00597.

(8) Heriche, H.; Rouabah, Z.; Bouarissa, N. High-Efficiency CIGS Solar Cells with Optimization of Layers Thickness and Doping. *Optik (Stuttg).* **2016**, *127* (24), 11751–11757. https://doi.org/10.1016/j.ijleo.2016.09.071.

(9) Dullweber, T.; Hanna, G.; Shams-Kolahi, W.; Schwartzlander, A.; Contreras, M. A.; Noufi, R.; Schock, H. W. Study of the Effect of Gallium Grading in $Cu(In,Ga)Se_2$. *Thin Solid Films* **2000**, *361*, 478–481. https://doi.org/10.1016/S0040-6090(99)00845-7.

(10) Schleussner, S.; Zimmermann, U.; Wätjen, T.; Leifer, K.; Edoff, M. Effect of Gallium Grading in $Cu(In,Ga)Se_2$ Solar-Cell Absorbers Produced by Multi-Stage Coevaporation. *Sol. Energy Mater. Sol. Cells* **2011**, *95* (2), 721–726. https://doi.org/10.1016/j.solmat.2010.10.011.

(11) Zhang, T.; Yang, Y.; Liu, D.; Tse, S. C.; Cao, W.; Feng, Z.; Chen, S.; Qian, L. High Efficiency Solution-Processed Thin-Film $Cu(In,Ga)(Se,S)_2$ Solar Cells. *Energy Environ. Sci.* **2016**, *9* (12), 3674–3681. https://doi.org/10.1039/C6EE02352E.

(12) Fan, Q.; Tian, Q.; Wang, H.; Zhao, F.; Kong, J.; Wu, S. Regulating the Starting Location of Front-Gradient Enabled Highly Efficient Cu(In,Ga)Se2 Solar Cells: Via a Facile Thiol-Amine Solution Approach. *J. Mater. Chem. A* **2018**, *6* (9), 4095–4101. https://doi.org/10.1039/c7ta10889c.

(13) Nakamura, M.; Yamaguchi, K.; Kimoto, Y.; Yasaki, Y.; Kato, T.; Sugimoto, H. Cd-Free $Cu(In,Ga)(Se,S)_2$ Thin-Film Solar Cell with Record Efficiency of 23.35%. *IEEE J. Photovoltaics* **2019**, *9* (6), 1863–1867. https://doi.org/10.1109/JPHOTOV.2019.2937218.

(14) Yuan, S.; Wang, X.; Zhao, Y.; Chang, Q.; Xu, Z.; Kong, J.; Wu, S. Solution Processed CIGSSe Solar Cells with 15.25% Efficiency by Surface Sulfurization. *ACS Appl. Energy Mater.* **2020**. https://doi.org/10.1021/acsaem.0c00917.

(15) Lepetit, T.; Harel, S.; Arzel, L.; Ouvrard, G.; Barreau, N. Coevaporated $KInSe_2$: A Fast Alternative to KF Postdeposition Treatment in High-Efficiency $Cu(In,Ga)Se_2$ Thin Film Solar Cells. *IEEE J. Photovoltaics* **2016**, *6* (5), 1316–1320. https://doi.org/10.1109/JPHOTOV.2016.2589365.

(16) Kato, T.; Wu, J. L.; Hirai, Y.; Sugimoto, H.; Bermudez, V. Record Efficiency for Thin-Film Polycrystalline Solar Cells Up to 22.9% Achieved by Cs-Treated Cu(In,Ga)(Se,S)$_2$. *IEEE J. Photovoltaics* **2019**, *9* (1), 325–330. https://doi.org/10.1109/JPHOTOV.2018.2882206.
(17) Alruqobah, E. H.; Agrawal, R. Potassium Treatments for Solution-Processed Cu(In,Ga)(S,Se)$_2$ Solar Cells. *ACS Appl. Energy Mater.* **2020**, *3* (5), 4821–4830. https://doi.org/10.1021/acsaem.0c00422.
(18) Boyle, J. H.; McCandless, B. E.; Shafarman, W. N.; Birkmire, R. W. Structural and Optical Properties of (Ag,Cu)(In,Ga)Se$_2$ Polycrystalline Thin Film Alloys. *J. Appl. Phys.* **2014**, *115* (22), 223504. https://doi.org/10.1063/1.4880243.
(19) Edoff, M.; Jarmar, T.; Nilsson, N. S.; Wallin, E.; Hogstrom, D.; Stolt, O.; Lundberg, O.; Shafarman, W.; Stolt, L. High Voc in (Cu,Ag)(In,Ga)Se$_2$ Solar Cells. *IEEE J. Photovoltaics* **2017**, *7* (6), 1789–1794. https://doi.org/10.1109/JPHOTOV.2017.2756058.
(20) Zhao, Y.; Yuan, S.; Kou, D.; Zhou, Z.; Wang, X.; Xiao, H.; Deng, Y.; Cui, C.; Chang, Q.; Wu, S. High Efficiency CIGS Solar Cells by Bulk Defect Passivation through Ag Substituting Strategy. *ACS Appl. Mater. Interfaces* **2020**, *12* (11), 12717–12726. https://doi.org/10.1021/acsami.9b21354.

APPENDIX A. OTHER WORK – INVESTIGATING MOLECULAR PRECURSOR APPROACHES TO SOLUTION PROCESSED CDTE PHOTOVOLTAICS

A.1 Introduction

A.1.1 CdTe Photovoltaics

Cadmium Telluride is a II-VI semiconducting material with a zinc-blende crystal structure. A great deal of research has focused on CdTe PVs dating back to the 1950s,[1,2] when it was discovered that CdTe has a high absorption coefficient and bandgap of ~1.5eV (which closely matches the ideal solar photon distribution with respect to electricity generation) making it ideal for photovoltaic applications, with a theoretical max efficiency placed at 32.1%.[3] CdTe is usually p-type without dopants due to an abundance of cadmium vacancies in Te rich films. Between 1975 and 1992, there was consistent improvement of CdTe efficiencies, from ~8% to ~15%.[4] However, from 1992 to 2011, there was little improvement of device efficiencies. Additionally, open circuit voltages were relatively low, with research cells rarely breaking 800mV.[5] During this time, the viability of CdTe at a commercial scale was suspect due to low efficiencies relative to silicon. However, beginning in 2011, CdTe devices have made a surge in efficiency as a result of significant device and process optimizations.[6] Additionally, CdTe devices with open circuit voltages greater than 1V were fabricated in early 2016.[5] As of mid-2016, First Solar reported lab scale efficiencies of 22.1%.[4]

A typical fabrication scheme of CdTe involves the following steps: CdS is deposited from a chemical bath (or in some cases using vacuum deposition), annealing, CdTe is deposited using a high rate vapor transport system similar to closed space sublimation (CSS), $CdCl_2$ is deposited using vapor deposition or via dipping in saturated $CdCl_2$ solutions, a chemical etch, back metal contacts are deposited, and finally annealing completes the device.[6] Currently, CdTe makes up 5.9% of the PV market, constituting over half of the thin film market. Due the surge in recent efficiencies and lower production costs, cadmium telluride stands unique among other PV technologies, holding the shortest energy payback time of less than one year, the smallest carbon footprint, and the lowest water usage of any PV technology.[7–9]

Despite a low carbon footprint and low water usage, there is significant concern regarding the use of toxic cadmium and cadmium salts in the production of CdTe devices. However, industrial zinc refining produces a significant amount of cadmium independent of PV demands. CdTe PVs provide a safe usage of this otherwise hazardous waste cadmium due to the relatively low toxicity of CdTe, which has low acute oral, inhalation, and aquatic toxicity, and is not mutagenic.[10] Additionally, the common $CdCl_2$ post treatment (used to enhance grain growth) given to CdTe PVs has been shown to be replicable with a $MgCl_2$ post treatment, which is of significantly lower toxicity.[11] Beyond toxicity concerns, the relative rarity of Tellurium has raised questions about the mid to long range future of CdTe PVs. It is estimated that about 800 metric tons of Tellurium are available every year, almost exclusively as a byproduct of copper refining. It is estimated that by 2040, that 8.1 GW of CdTe could be installed annually relying on 90% recycled tellurium from end of life modules, with 97% of materials recovered in module recycling.[12] While long term solutions may require moving away from CdTe, there is still significant short/mid-term promise with CdTe to help displace fossil fuel technologies and enhance the penetration of solar energy due to its ever dropping cost of production.

To displace heavily rooted technologies such as coal, further reductions in price are needed. Solution processing of CdTe offers a method to significantly reduce production costs, providing a method to undercut fossil fuels in price. A fair body of work has been conducted regarding solution processing of CdTe. Early work dates back to the 1980s, when spray pyrolysis of CdTe was used to deposit CdTe films using a solution of TeO_2, $CdCl_2$ in water, ammonium hydroxide, hydrazine, and hydrochloric acid.[13,14] H. B. Serreze et. al successfully fabricated a CdS/CdTe device using this spray pyrolysis method, achieving an efficiency of 4.0%.[15]

More recent work has focused on colloidal nanoparticle suspension routes to CdTe photovoltaics. Nanoparticle synthesis are performed in a variety of methods. A common method uses Te dissolved in TOP, added to cadmium myrsitate and trioctylphosphine oxide at 220-300°C, and held for 30 minutes. The resulting nanoparticles are washed and suspended in pyridine and 1-propanol.[16–18] Another common method uses CdO, n-tetradecylphosphonic acid (TDPA), and 1-octadecene (ODE) heated to 300°C. Te dissolved in tributylphosphine (TBP) is added and the mixture is cooled to 250°C and held for a period of time before cooling.[19,20] A third route uses Te dissolved using sodium borohydride in water. This solution is mixed with $CdCl_2$ dissolved in water with mercaptoethanol as a stabilizing agent. The solution is heated to 100°C and nanoparticles

begin to nucleate.[21,22] At this point, with all synthesis, ligand exchange can be performed. Panthani *et al.* have achieved success using $CdCl_3^-$ as a capping ligand for CdTe nanoparticles, yielding a device with 10% efficiency and only 400nm of thickness.[19] The highest efficiency solution processed nanoparticle CdTe device was achieved by Panthani *et al.*, with a 12.3% efficient device and a J_{sc} of over 25 mA cm^{-2}.[17]

A.1.2 Molecular Precursor Routes to Solution Processed Photovoltaics

Despite reaching respectable efficiencies, the previous nanoparticle PV routes all have fairly complex nanoparticle syntheses, which often require ligand exchange to yield viable suspensions.[19] Additionally, nanoparticles are subject to compositional non-uniformity, and nanoparticle capping ligands can introduce carbonaceous impurities into the final film.[23] Molecular precursors offer a simplified route to solution processed PVs. In a molecular solution, precursors are dissolved yielding a molecularly homogenous solution which can be directly cast and heat treated to yield a semiconductor film.

Early work using molecular precursors relied on hydrazine as a solvent,[24] however, hydrazine is extremely reactive and toxic, making it difficult and dangerous to work with, and less than ideal for industrial scaling. In place of hydrazine, mixtures of amines and thiols have been shown to be able to dissolve a wide variety of metal salts and chalcogens.[25,26] In the case of chalcogens such as selenium and tellurium, the amine-thiol systems acts as a reducing agent, stabilizing the chalcogens in an anionic state in solution. CIGS devices with power conversion efficiencies of 12.2% have been made using amine-thiol mixtures, demonstrating the promise of the system from work in our group.[27]

A.1.3 Previous Work on Amine-Thiol CdTe Molecular Precursors

Due to the wide versatility of the amine thiol system, and the ability to dissolve chalcogens, a molecular precursor approach to cadmium telluride PVs becomes a possibility. Miskin *et al.* demonstrated such a molecular precursor, successfully fabricating a cadmium telluride PV device. The CdTe absorber layer was obtained using a molecular precursor solution containing elemental tellurium and $CdCl_2$ dissolved in Ethylenediamine (en) and propanethiol at volume ratios varying

between (2:1) and (3:1). The procedure used to fabricate a PV device is detailed in Appendix D, CdTe Amine-Thiol Molecular Precursor Route.[28]

This approach yields incredible grain growth in the as coated and post high temperature annealed films, without the use of a $CdCl_2$ post treatment. Despite the unprecedented grain growth and superb density of the film, only a modest power conversion efficiency of 0.54% was obtained. The low efficiency obtained is attributed to several factors.

The first such problem is due to the incorporation of sulfur into the CdTe film, with the thiol as a sulfur source (determined from films fabricated without CdS layers). This sulfur manifests as an even dispersion in the CdTe film as well as in larger CdS grains. Due to the n-type properties of CdS, incorporation of sulfur into the p-type CdTe layer disrupts charge separation which would normally be facilitated by a single p-n junction. A second problem that has been observed is an initial large excess of chlorine in the film, followed by a deficiency after high temperature annealing. Excess Cl acts as a shallow donor dopant, and significantly increases the resistivity of CdTe, however, too little can also substantially detriment device performance.[29]A third problem is the large amount of carbon incorporated into the film via the solvents. A fourth problem is the complete consumption of the CdS n-type window layer. CdS is likely partially dissolved by the amine-thiol molecular precursors, causing intermixing with the CdTe absorber layer. Additionally, the many high temperature drying and annealing steps causes thermal diffusion of the CdS layer into CdTe absorber layer, destroying the p-n junction of the device.[28]In this work, alternative and/or modified approaches were investigated to fabricate solution processed CdTe, addressing some of the limitations previously discussed.

A.2 Experimental

A.2.1 Materials

Te (99.997%, 30 mesh), En (≥99.5%), Butylamine (99.5%), $Cd(CH_3CO_2)_2$ (99.995%), and tetramethlammonium borohydride (TMAB, >95%) were purchased from Sigma Aldrich. $CdCl_2$ (99.995% anhydrous) was purchased from STREM. Et (99%+) was purchased from ACROS Organics.

A.2.2 Minimum Thiol Solution and Film Preparation

For the preparation of the minimum thiol, amine-thiol molecular precursor solutions, $CdCl_2$ (99.995% anhydrous, Strem) and Te (99.997%, 30 mesh, Sigma Aldrich) were weighed into a 20 mL scintillation vial on an analytical balance in an inert glovebox. The minimum thiol ratio was found to be 9:1 (volume) Ethylenediamine (En) to Ethanethiol (Et) through successive dilutions of En (≥99.5%, Sigma Aldrich) with Et (99%+, Acros) yielding a final concentration of 0.18M of Te and $CdCl_2$. The minimum thiol ratio solution was spin-coated on a CdS coated (chemical bath deposited) 1"x1" cleaned using the standard spin coating procedure for 30 coatings. The film was made into a device. Flourinated tin oxide (FTO) coated glass was coated in ~200nm of CdS using a chemical bath deposition. Next, the molecular precursor solution was spin coated onto the CdS coated FTO glass. Each coating was followed by a drying/annealing step where the film was baked at 500°C for one minute and 30 seconds. Thirty to 40 coating/anneal cycles are performed. A final, high temperature annealing is performed at 550°C for 30 minutes, with the sample sealed in a glass ampoule. Next, 4 nm of Cu and 250 nm of Au are deposited on the CdTe film using a thermal evaporator. The Cu is then diffused into the CdTe layer by heating between 120-190°C.

For the preparation of "thiol removed" molecular precursor solutions, $CdCl_2$ and Te were weighed on an analytical balance into a 150 mL three-necked flask with magnetic stir bar, condenser, and thermocouple port, inside an inert glovebox. En and Et were added in a 5:1 ratio to make 0.18 to 0.22 M solutions. The three necked flask was marked after the addition of En to denote the target volume after the removal of thiol. The flask was sealed, brought out of the glovebox and attached to a Schleck line. Tubing exposed to air was purged 3 times with vacuum and argon backfill. The three-necked flask was opened to the Schleck line, with a constant argon flow through. The solution was stirred for approximately 3 hours at 300 rpm.

Once all solids were dissolved, gentle vacuum was pulled on the 3-necked flask. Cold water was passed through the condenser to prevent removal of En. Mild heating was applied through a heating mantle and PID temperature controller set at 30°C. Gentle boiling was held until the thiol volume was completely removed. The three necked flask was sealed and brought into the glovebox. The thiol removed solution was spin-coated using the standard spin coating procedure

A.2.3 Alternating Layer Approach

Tellurium and $CdCl_2$ were weighed on an analytical balance in an inert glovebox into separate 20 mL scintillation vials. Butylamine (99.5%, Sigma Aldrich) was added to $CdCl_2$ to make a 0.24 M solution. After vortexing for ~30 seconds, the solution was completely dissolved. En and Et were added in a 4:1 ratio to Te to make a 0.24M solution. The solution was stirred for 3 hours using a magnetic stir bar at 300rpm. A cleaned 1"x1" piece of FTO glass was set on the spin coater chuck. An amine pretreatment of the FTO glass surface was performed to increase the wettability of the molecular precursor on the FTO glass. ~ 300 µL of En was pipetted onto the FTO glass surface, covering the entirety of the FTO glass surface. The surface was left to soak for 5 minutes. After 5 minutes, the En was spun off using the following recipe: 5 s at 500rpm followed by 35 s at 1200 rpm. This spin was repeated 3 times to remove the bulk of the en used for the surface soak. After the amine soak, 250 µL of molecular precursor solution was pipetted onto the surface of the FTO glass such that the molecular precursor covers the entirety of the surface. The molecular precursor was spun off using the previously described recipe. The sample was then removed from the spin coater and placed on a hotplate at 500°C for one minute and 30 seconds. The sample was then placed on two thin aluminum rails to cool for one minute. This cooling method prevents thermal shocking the glass. The sample is then placed directly on an aluminum block to further cool for an additional minute.

Next, 150 µL of the Te precursor was pipetted onto the substrate and spun off using the standard recipe (5 s at 500rpm followed by 35 s at 1200rpm). The sample was then dried/annealed at 500°C for 90 s under gentle vacuum (~660 torr). The sample was cooled for 1 minute on aluminum rails, and then for an additional minute on an aluminum block. The previous procedure was repeated for the $CdCl_2$ solution. This cycle was repeated 10 times. A high temperature anneal was performed on a preheated hotplate at 550°C under gentle vacuum (~660 torr) for 20 minutes and cooled using the aluminum rail and block method described above. Optimization of Te layer deposition was also performed. A coating optimization study was performed using both dynamic and standard spin coating on amine treated FTO glass 1"x1" substrates. Dynamic spin coating was used with speeds of 1500, 2000, 2500, and 3000 rpm. 50 µL of molecular precursor was dispensed while the substrate was already at max speed. The substrate was allowed to spin for an additional 30 seconds after the precursor solution was dispensed. Standard spin coating was performed using

the standard spin coating recipe, 800 rpm, 1500 rpm, and 2500 rpm. All films were dried for one minute and 30 seconds at 200°C.

A.2.4 Aqueous Borohydride Assisted Route

$CdCl_2$ or $Cd(CH_3CO_2)_2$ (Sigma, 99.995%) and Te/TMAB (1:2 molar ratio) was weighed into 20 mL separate scintillation vials in an inert glovebox. Degassed ultrapure H_2O was added to the vials to make solutions ranging from 0.15 M to 0.30 M. A 1/8" thick graphite plate was placed on top of a hotplate set at 130 °C. A clean 1"x1" piece of FTO glass (Appendix D, Glass Cleaning and Scribing) was placed on the hotplate and allowed to preheat for 3 minutes. Master Airbrushes (G233-SET) were used to spray coat the films for proof of concept experiments. Each solution was given its own airbrush, and 0.5 mL of each solution was loaded into the airbrush hopper and sprayed per layer. A layer of tellurium was sprayed onto the substrate on the hotplate, followed by a 2 minute dry. Next, a layer of $CdCl_2$ or $Cd(CH_3CO_2)$ was sprayed, followed by a 2 minute dry. The sample was then placed on a hotplate at 500°C for 90 s. This was repeated for 1-3 cycles. For films using $Cd(CH_3CO_2)$ as a cadmium source, a dilute $CdCl_2$ solution was sprayed over the surface, and heat treated at 300°C to promote grain growth. Final annealing was performed using a tube furnace at 550°C for 30 minutes with the sample sealed in an evacuated ampoule. Appendix C, Figure 1 shows a schematic of the experimental setup.

A.2.5 Characterization

X-ray diffraction (XRD) was performed using a Rigaku SmartLab Diffractometer in Briggs Brantano mode with a Cu Kα X-ray source. Scanning electron microscopy and energy dispersive X-ray spectroscopy (SEM, SEM-EDS) were performed using a Quanta 3D FEG electron microscope with an accelerating voltage of 20kV, and silicon drift detector for EDS.

A.3 Results and Discussion

A.3.1 Minimum Thiol Quantity Amine-Thiol Molecular Precursors and Films

Despite the phenomenal solvent properties of the amine-thiol system, the sulfur in the thiol presents difficulties when used to make CdTe PVs. While the thiol is essential to the dissolution

of $CdCl_2$ and Te, which are otherwise insoluble in diamine alone and thiol alone, sulfur incorporation in the CdTe film is detrimental to device performance. As such, minimizing the amount of thiol used in dissolution seems to be a reasonable approach to mitigating the thiol induced problems. Additionally, a more volatile thiol, ethanethiol (b.p. 35°C), was selected to aid in thiol removal during heating. Experiments were performed in which films were cast from molecular precursors using the minimum amount of thiol possible.

Initial experiments were performed to analyze the stability of the amine-thiol system as thiol was removed. Vacuum was pulled on the molecular precursor solution until precipitates were visible. Tellurium visibly crashed out after slightly more than the thiol volume was removed from the solution, and $CdCl_2$ did not crash out until approximately 2/3 of the total volume was removed. This implies that the Te^{2-} anion is loosely stabilized by the thiol in solution, with removal of the thiol causing the anionic tellurium to return to the 0-oxidation state. However, the cation bonds more strongly to sulfur, retaining Cd^{2+}'s solubility even after the entirety of the thiol volume has been removed. The cadmium chloride dissolution mechanism relies on sulfur acting as a nucleophile to stabilize the cationic cadmium in solution, likely forming cadmium thiolate species in solution. This stabilization is also a major factor in preventing CdTe formation in solution.

A device was fabricated using the minimum thiol ratio (9:1 volume ratio En:Et) using the experimental flow shown in Figure A.1

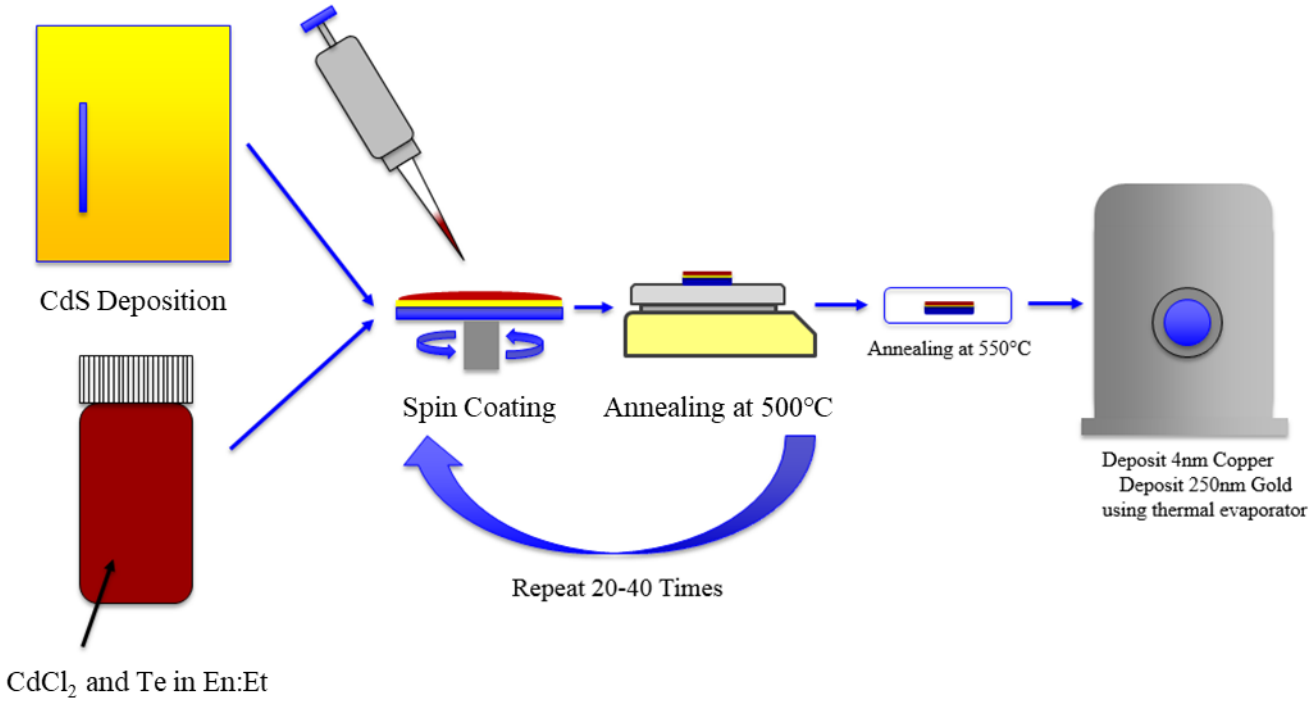

Figure A.1. Process flow of CdTe device fabrication from an amine-thiol molecular precursor, typically followed by a final anneal at 120-190°C to diffuse in copper.

X-Ray diffraction (XRD) was performed on the film prior to and after the high temperature anneal as shown in Figure A.2.

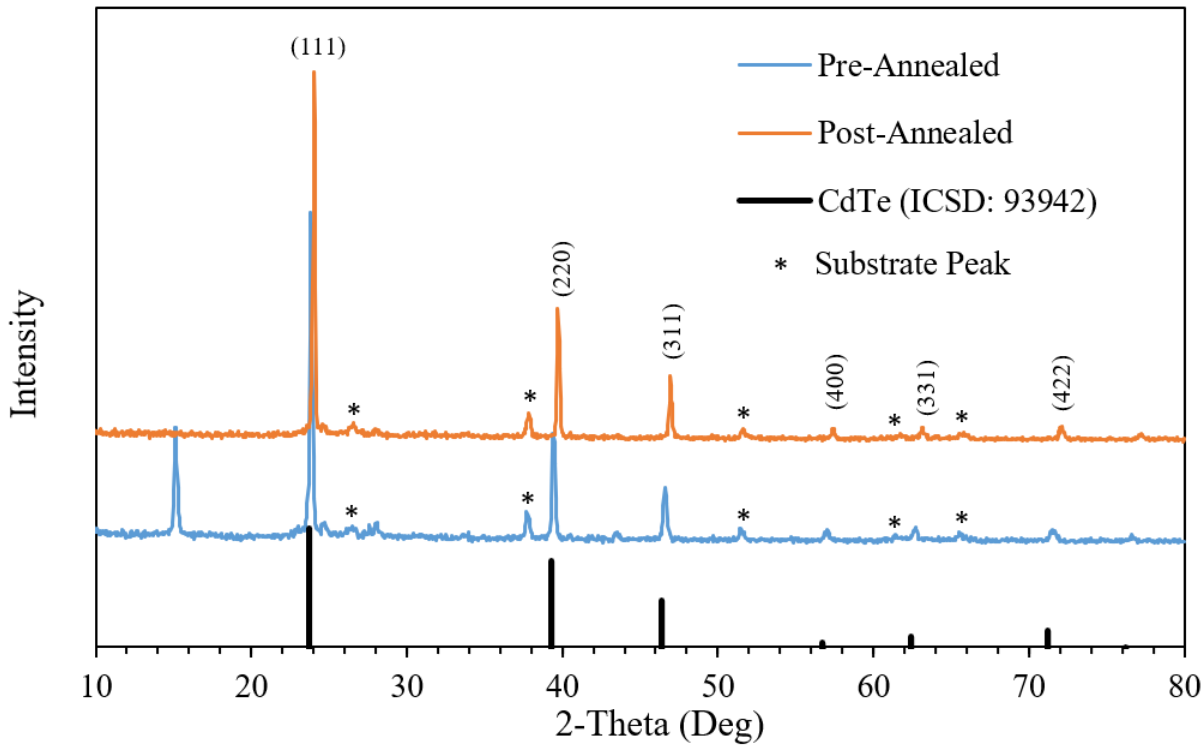

Figure A.2. XRD spectra of pre and post annealed films

CdTe formation was achieved, however apparent peak shifting is noted for the both films. The contaminant peak in the pre-annealed film at 15 2-theta is attributed to carbonaceous species, and is removed after annealing at 550°C, a typical result with amine-thiol films.[47] The peak shifting is characteristic of CdS intermixing with CdTe. Scanning electron microscopy (SEM) and energy dispersive x-ray spectroscopy (EDS) was performed pre annealing to obtain more in depth elemental analysis. Figure A.3 shows an SEM micrograph of the pre-annealed film, which exhibited grain growth and dense packing of grains.

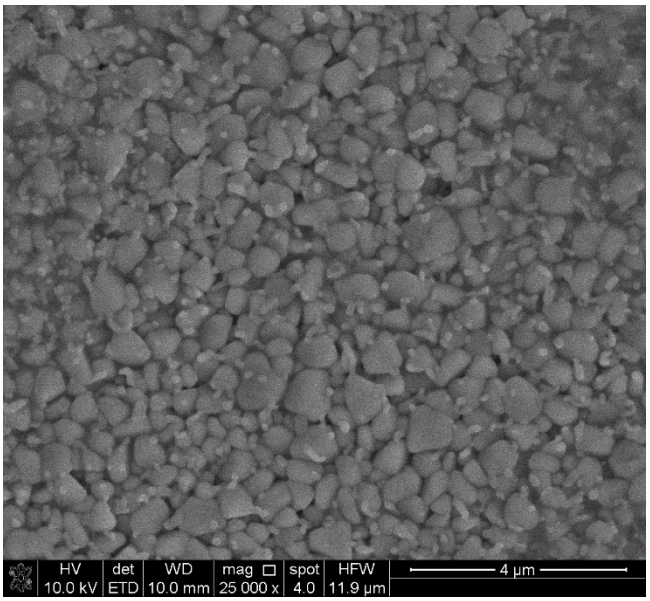

Figure A.3. SEM micrograph of the CdTe film surface after 500℃ anneals, but before high temperature 550℃

A Cd:Te:S elemental ratio of 1:0.88:0.11 was obtained in the center of the film, showing significant tellurium deficiency and sulfur incorporation. A macroscopic view of the film shows a unique "picture frame" outline of the film as shown in Figure A.4.

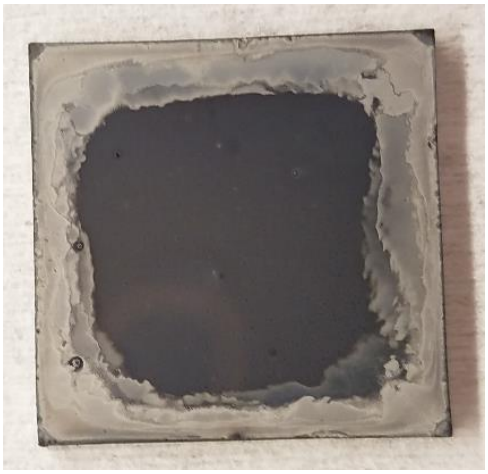

Figure A.4. Minimum thiol ratio (9:1 En:Et) CdTe film. Note the "picture frame" layer around the film edge.

EDS of the "picture frame" layer revealed a tellurium rich layer with a Cd:Te: ratio of 1:4.91. This result can be explained by the low amount of thiol used, and the high volatility of Et. When the precursor is spun on the spin-coater, ethanethiol evaporates first, and because the

absolute minimum amount of thiol is used, tellurium solid crash out of solution and is flung towards the edge of the film. This creates a tellurium deficiency in the center of the film. When heated, cadmium to reacts with any residual thiol, yielding a CdS rich, tellurium deficient CdTe film. This presented a counterintuitive result, where using less of a more volatile thiol increased sulfur incorporation in the film due to tellurium deficiencies in the center of the film. Due to these shortcomings, the fabricated device did not show diode behavior or an efficiency.

In order to obtain a compositionally homogeneous film, a comparable amount of thiol and amine of similar volatilities should be used to prevent compositional non-uniformities across the width of the film when using spin coating as a function of drying. While previous work has suggested heavier thiols tend to incorporate more carbon into the film, this could potentially be mitigated by drying the film at lower temperature to evaporate the solvent without decomposition. The current high temperature drying step (500°C) likely decomposes the carbonaceous solvents before they can entirely evaporate, leaving significant carbon reside. Based on the previously described minimum-thiol ratio experiment, increasing the thiol amount may actually reduce sulfur incorporation in the final film. Using doctor blading as alternative coating method may bypass the previous problems, however, preliminary work with doctor blading has yielded non-uniform depositions and poor film quality.

A.3.2 The Alternating Layer, Amine-Thiol Route to CdTe Thin Films

An alternative method to removing thiol from the molecular precursor solution is to remove thiol after the film is cast by separating the precursors into a thiol free $CdCl_2$ solution and an amine-thiol Te solution. Once the Te solution is cast, the loosely bound thiol can be removed through heated drying. To aid in the removal of thiol, Et was selected due to its high volatility. When the next layer of $CdCl_2$ in butylamine is cast, no thiol is present to contribute sulfur. Additionally, chlorine is able to leave the film from the surface rather than having to navigate through the bulk of the film. This method would allow for the potential of $CdCl_2$ to never contact sulfur, removing the possibility of forming CdS grains and incorporating sulfur into the CdTe film. A high temperature treatment is used to facilitate solid diffusion and ultimately the reaction of $CdCl_2$-amine complex thermal decomposition and reaction with Te to form CdTe. Proof of concept experiments have thus far shown successful formation of highly oriented CdTe with formation of large grains.

Both XRD and SEM-EDS were performed to confirm the formation of CdTe, and to analyze the suitability of the film for device fabrication. XRD spectra are shown in Figure A.5. The relative height of the (111) peak compared to the (220) in the CdTe standard shows that oriented growth was present. The oriented growth may be a result of vertical diffusion and reaction of the alternating layers to form CdTe, aligning to the (111) plane of the material.

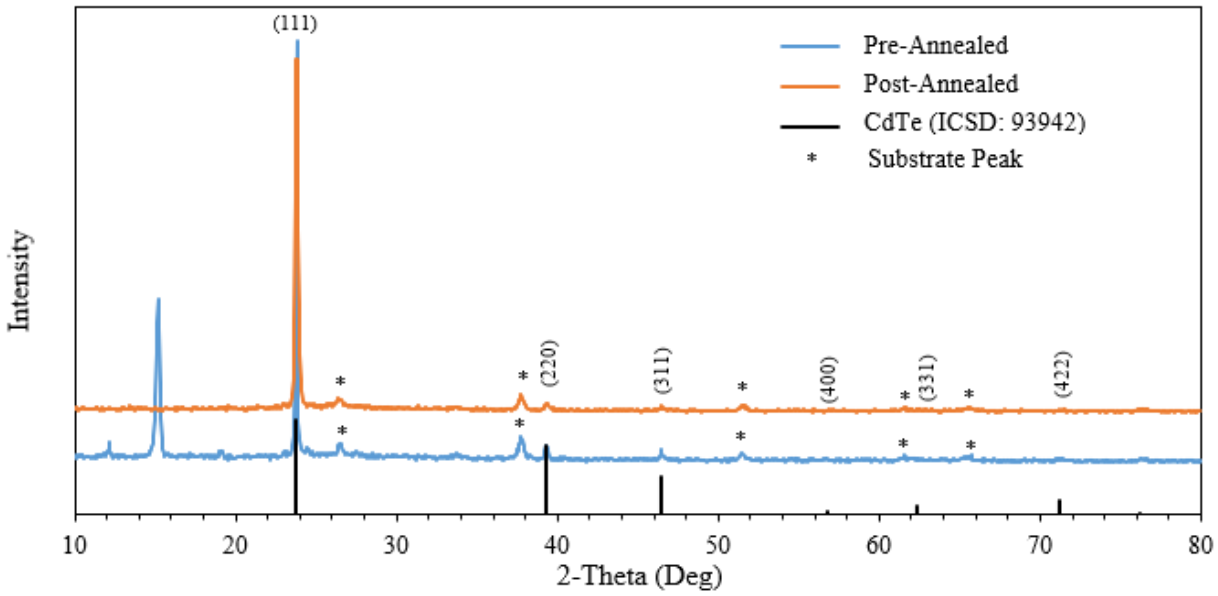

Figure A.5. XRD Spectrum of alternating layer amine-thiol CdTe film

The XRD confirms that CdTe was formed, and no contaminant peaks or residual Te or $CdCl_2$ are observed post-annealing meaning that all reactants are either consumed or volatilized during annealing, a promising result.

Further elemental analysis was performed using SEM-EDS. EDS revealed that the bulk film had non-negligible sulfur content with a Cd:Te:S atomic ratio of 1:0.84:0.07, also shown in the XRD peak shifting. While the alternating layer approach aimed to eliminate sulfur content, the result is not surprising based on observations during spincoating, with the $CdCl_2$ solution yielding visually thicker coatings. As such, cadmium was in excess and likely came into contact with sulfur via the thiol in the Te molecular precursor.

The film was visibly translucent after 10 cycles and showed a number of macroscale defects such as cracks and spots. Figure A.6 shows an image of the completed alternating layer CdTe film.

Figure A.6. Completed amine-thiol alternating layer CdTe film.

Additionally, there is apparent edge beading, implying that further optimization of the spin coating procedure is needed in order to obtain a more uniform film via spincoating. SEM imaging revealed grain density gradients across the width of the film, with a denser region towards the film edge, and a less dense region towards the center. The center of the film had an unsuitable density of grains for device fabrication as shown in Figure A.7

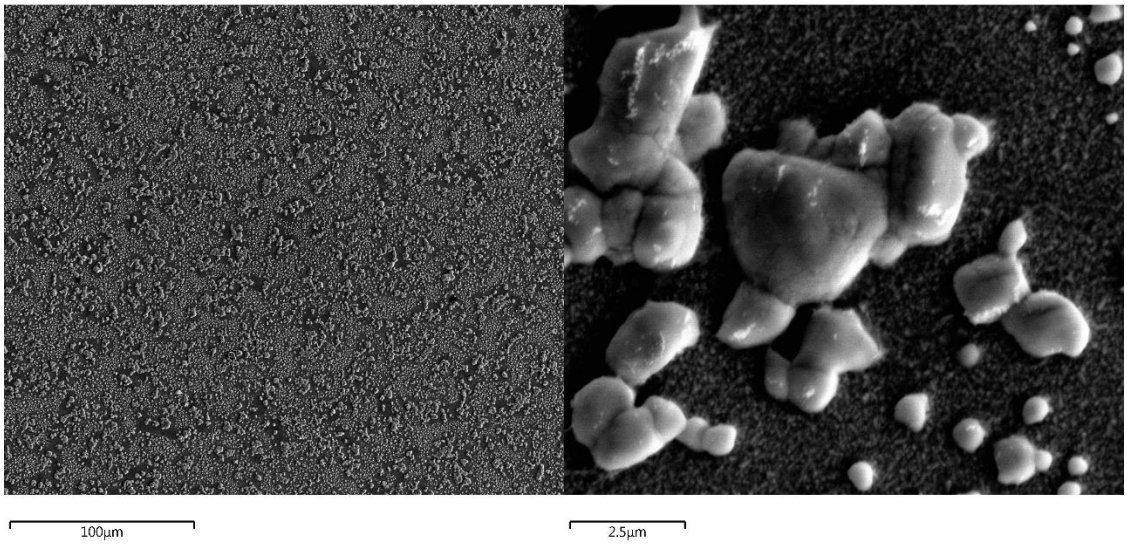

Figure A.7. SEM micrographs of the center of the alternating layer amine-thiol CdTe film. Dark regions in the SEM image are FTO glass showing through, and highlight the low density of CdTe grains. a) Bulk film appearance b) Close up of formed grains.

Despite the low grain density, large grains were still obtained between 0.5-5 µm. Figure A.8 shows the region towards the edge of the film with dense, but irregular sized grains.

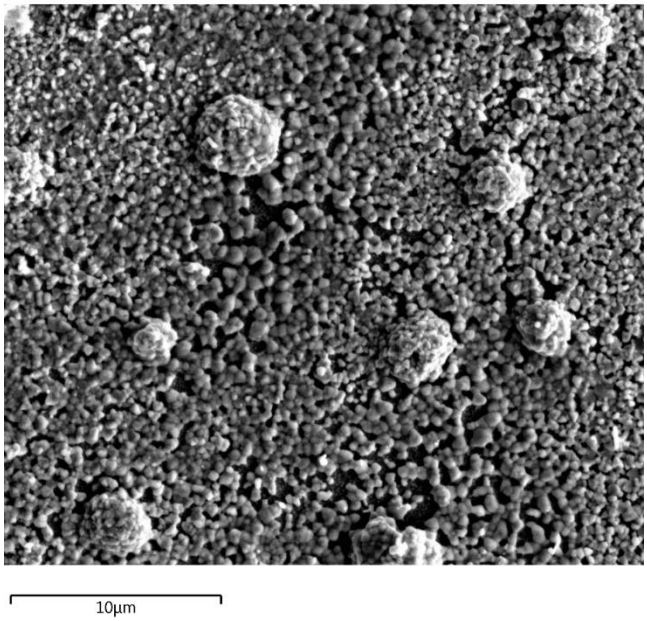

Figure A.8. SEM micrograph of alternating layer amine-thiol CdTe film. This image was taken at the edge of the film, showing the density, but smaller size of grains at the film edge.

The gradient in grain density highlights the need for further optimization of coating properties. Introductory coating optimization was performed. The spin coating of $CdCl_2$ was largely

Additional optimization is needed in order to obtain films with higher grain density. Initial coating optimization was performed to improve the quality of the difficult to coat Te layer, which was observed to rapidly crystallize into non-continuous films. Various contiditons used in the coating optimization and the resultant film quality is shown in Figure A.9 and A.10 for dynamic spin coating respectively and standard spin coating respectively. Dynamic spin coating differs from standard spin coating, where in dynamic spin coating, the solution is dispensed onto an already rotating substrate.

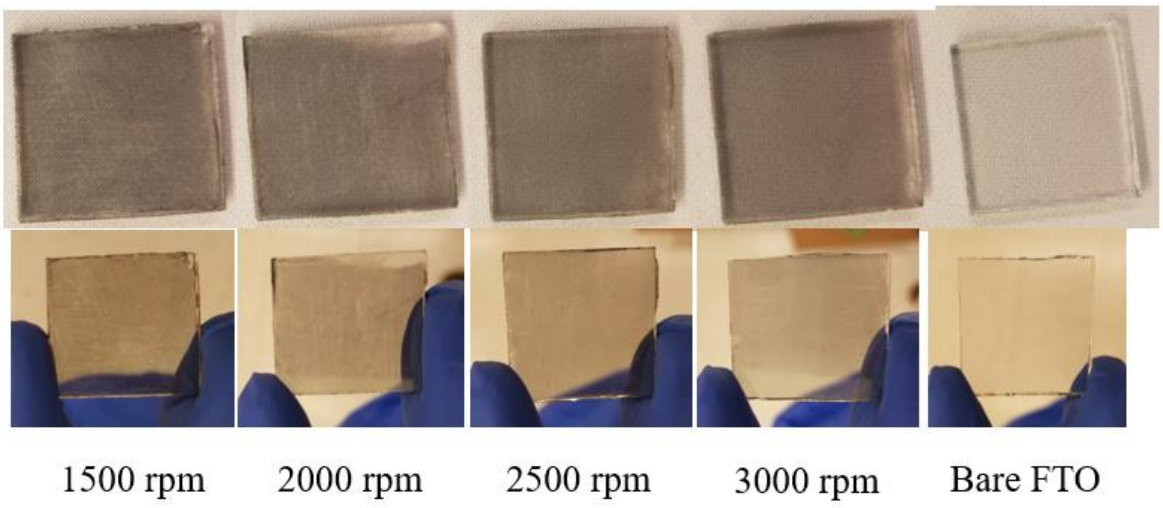

Figure A.9. Dynamic spin coating speed optimization, dried at 200°C. Top image is the film with a white background and bottom image is the film held up to the light.

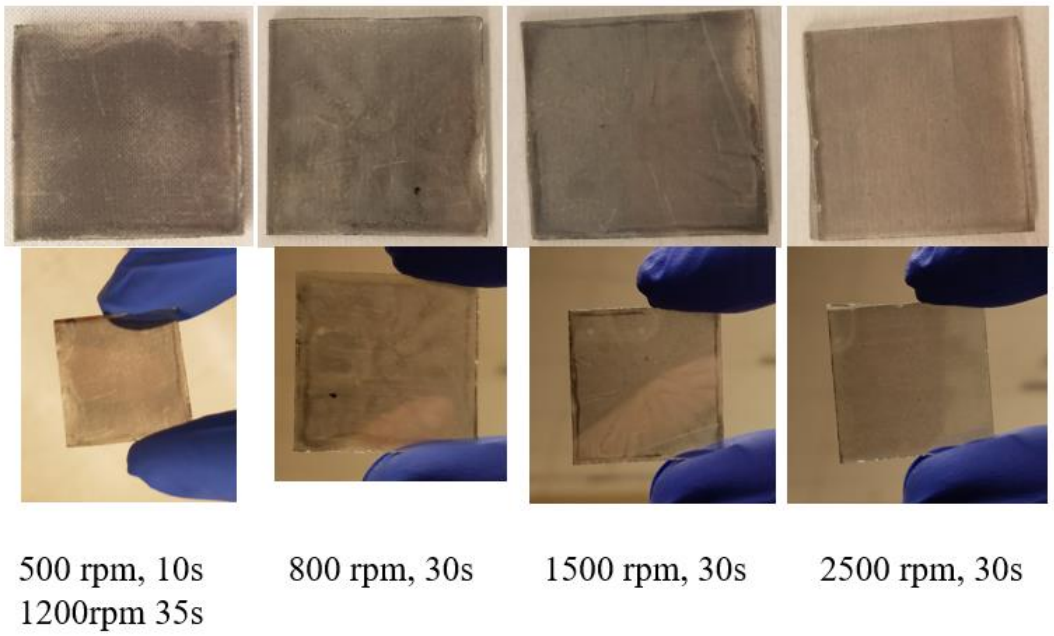

Figure A.10. Standard spin coating optimization, dried at 200°C. Top image is the film with a white background and bottom image is the film held up to light.

A low temperature drying to gently remove thiols can be implemented to remove decomposition and implementation of sulfur containing species. Further, removal of excess $CdCl_2$ between subsequent layers is likely needed to prevent contact of $CdCl_2$ with thiol containing solution and thereby prevent sulfur incorporation into the film. The envisioned modified procedure is shown in Figure A.11.

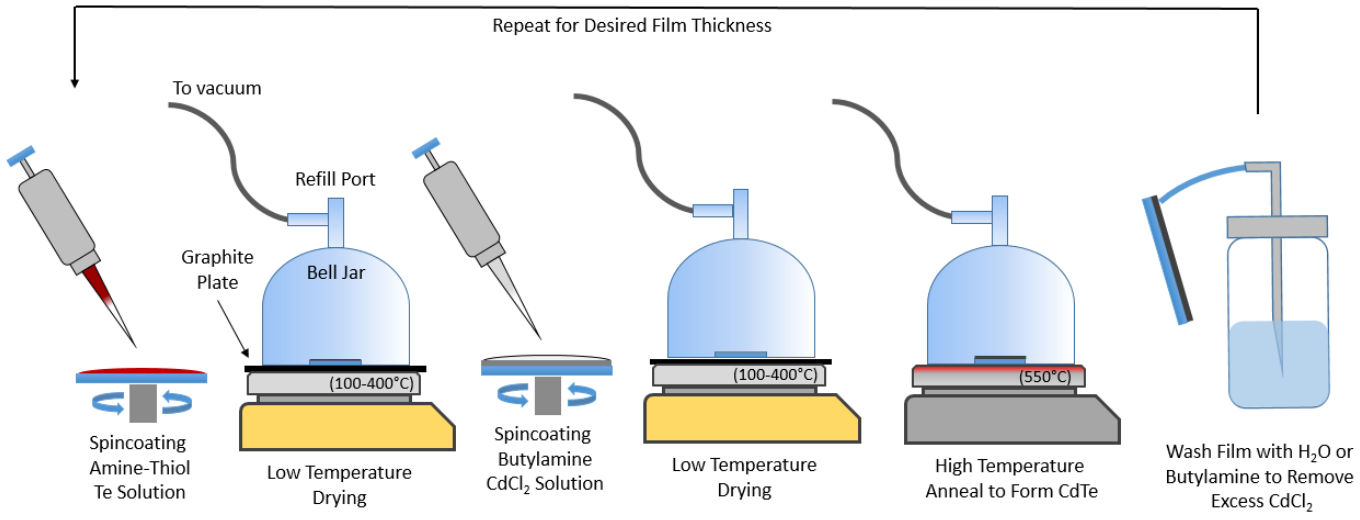

Figure A.11. Proposed modified procedure for alternating layer amine-thiol deposition of CdTe using amine-thiol Te and amine $CdCl_2$ solution with an added washing step.

A.3.3 An Aqueous Molecular Precursor Route to CdTe Thin Films

In the pursuit of eliminating sulfur incorporation into CdTe films, alternative solvent systems were investigated. Previous work has used sodium borohydride for the dissolution of in aqueous systems.[21] However, with the use of Sodium borohydride, potential sodium incorporation into the film could significantly reduce device performance. An alternative borohydride, tetramethylammonium borohydride (TMAB), was used to develop an aqueous molecular precursor route to CdTe thin films. However, due to the absence of a stabilizing nucleophile such as sulfur, a single molecular precursor solution could not be made without forming unstabilized nanoparticles, rather two separate solution deposited in alternating layers must be used. In this work a number of CdTe films deposited by this novel method are presented.

Films were sprayed using both $CdCl_2$ and $Cd(CH_3CO_2)_2$ as cadmium sources. A representation of the experimental setup is shown in Figure A.12.

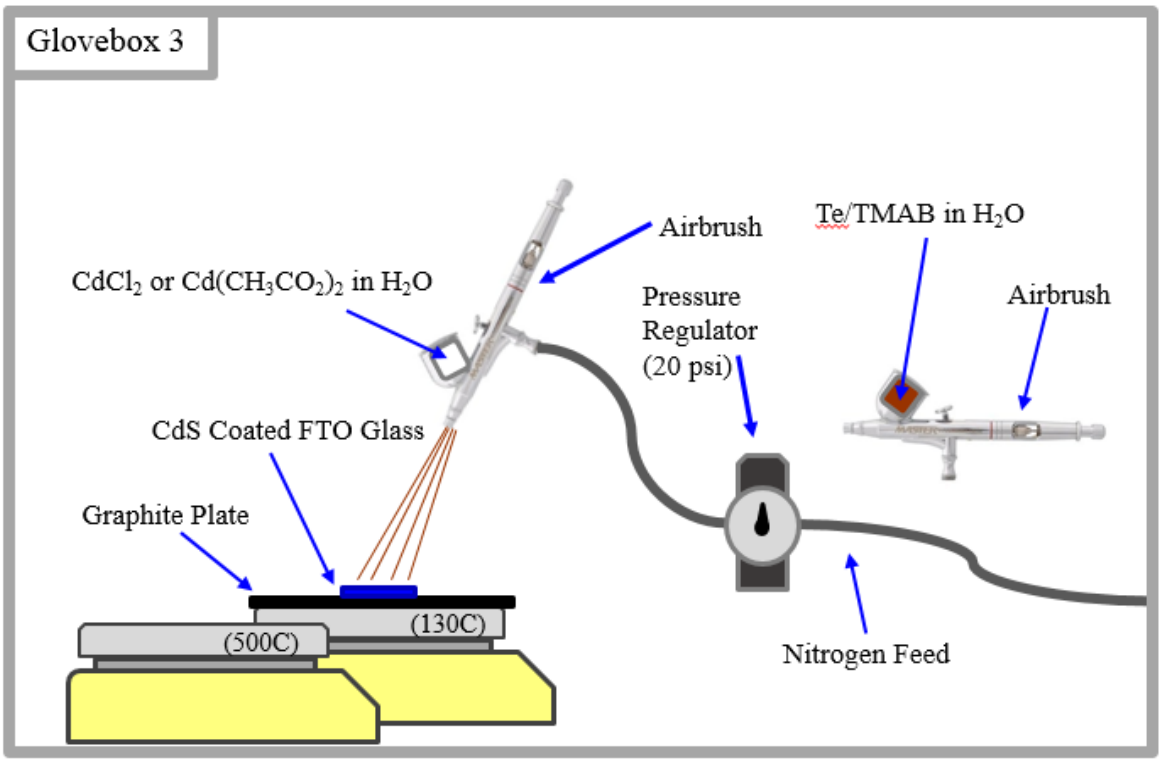

Figure A.12. Airbrush spray coating experimental setup.

XRD and SEM-EDS were performed. XRD of both films is shown in Figure A.13 and shows CdTe formation. However, a number of unidentified peaks are present.

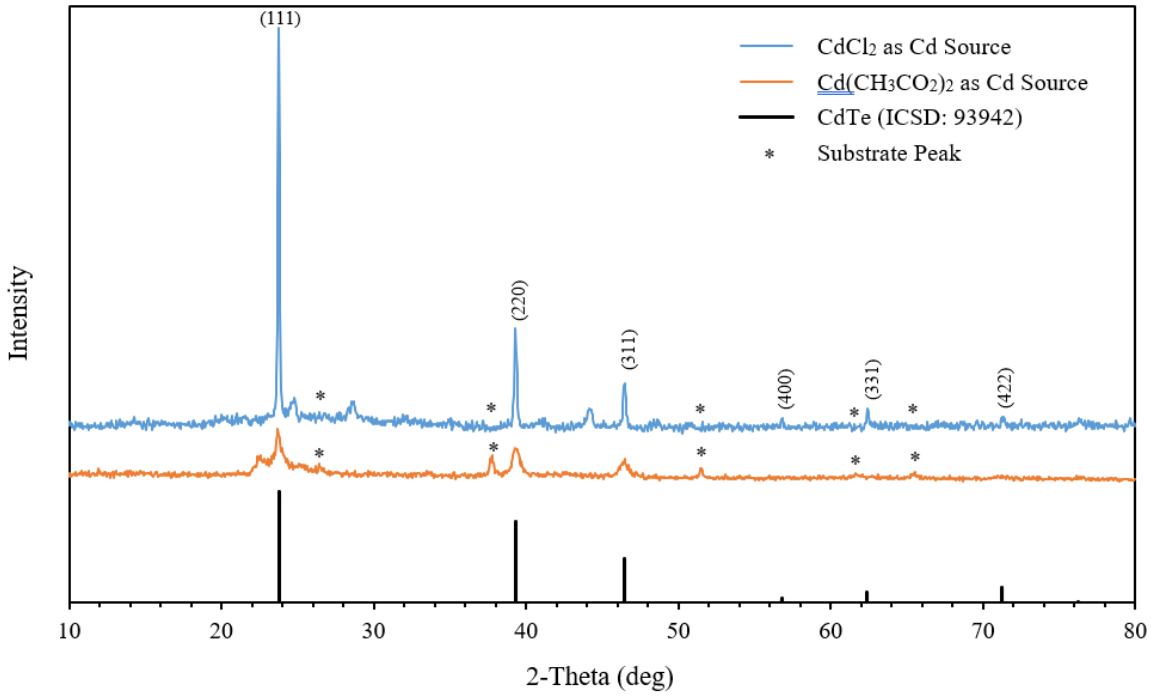

Figure A.13. XRD of the borohydride based molecular precursor method to CdTe thin films, showing films using $CdCl_2$ and $Cd(CH_3CO_2)_2$ as the cadmium precursor

A film grown using the $CdCl_2$ and Te precursor was imaged using SEM and is shown in Figure A.14. Minimal grain growth is observed for $CdCl_2$ deposited films.

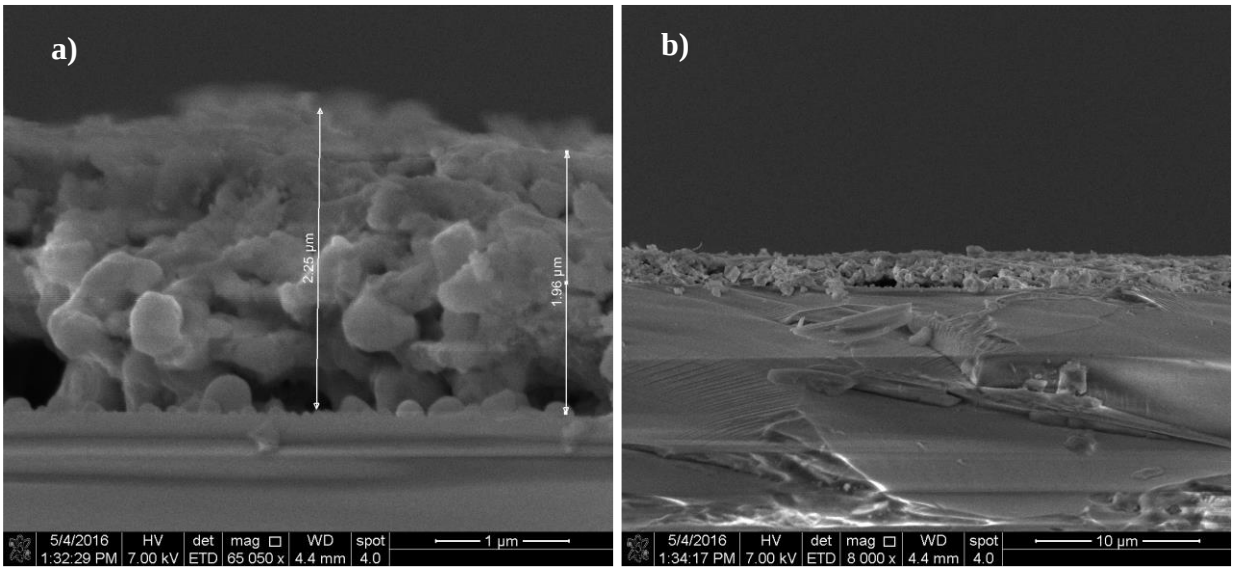

Figure A.14. Fracture cross-sections of a CdTe film deposited using aqueous borohydride molecular precursors. $CdCl_2$ was used as a cadmium precursor in this film. a) and b) show the film at different magnifications.

EDS of both films revealed the presence of large amounts of oxygen, 29.4 at% and 47.57 at% for $CdCl_2$ and $Cd(CH_3CO_2)_2$ respectively, in excess of what a cadmium salt hydrate would contribute (only $CdCl_2$ has a stable monohydrate above 500°C). This implies significant incorporation of the acetate into the film due to heightened oxygen content for the cadmium acetate precursor film. One other possible source of oxygen comes from the dissolution mechanism of Te using a borohydride. The proposed borohydride assisted dissolution mechanism is detailed below.

Proposed Borohydride dissolution mechanism:

$$[(CH_3)_4N]^+ [BH_4]^- (aq) + Te (s) \rightarrow [(CH_3)_4N]^+ [HTe]^- (aq) + BH_3 (g)$$

$$2BH_3(g) \rightarrow B_2H_6(g)$$

$$B_2H_6(g) + 6\ H_2O (l) \rightarrow 2\ B(OH)_3 (aq) + 6\ H_2 (g)$$

$$2H_3BO_3 \rightarrow 2HBO_2 + 2H_2O$$

$$2HBO_2 \rightarrow B_2O_3 + H_2O$$

$$[(CH_3)_4N]^+ [BH_4]^- (aq) + H_2O (l) \rightarrow [(CH_3)_4N]^+ [B(OH)_4]^- (aq) + H_2 (g)$$

The formation of B_2O_3, a water soluble, stable oxide is a byproduct of the reduction pathway in water. However, one caveat to this being the oxygen source in the film is that EDS would have detected some amount of Boron. While boron is on the lower end of the EDS detector's sensitivity limit, some signal should be detected. The lack of boron on the EDS spectrum implies that if B_2O_3 remains in the film, the boron is expelled by some unknown mechanism.

In order to remove the possibility of B_2O_3 formation, an organic system can be used in place of an aqueous one. Ethanol and N-methylformamide have shown promise in preliminary experiments with the ability to dissolve Te/TMAB and $CdCl_2$, albeit in very low concentration ($\leq$ 0.05M), making coating difficult. However, spray coating could provide a method to make low concentration coating viable.

A.4 Conclusions

Various molecular precursor approaches were investigated for the solution processing of CdTe thin films. Initial investigation into the reduction of sulfur contamination by removing excess thiol from the molecular precursor solution yielded films with a segregation of solid tellurium at

the edges of spin coated films, thereby depleting the center bulk region of tellurium and increasing the incorporation of sulfur as a counter anion. As such, an alternating layer approach was investigated whereby elemental tellurium was deposited from amine-thiol mixtures and annealed to remove all free thiol followed by thiol-less cadmium salt deposition. After a solid-state reaction, highly oriented CdTe was formed, however, sulfur incorporation was observed when multiple cycles were performed. A modified experimental procedure was proposed that should remove any possibility of sulfur incorporation. Finally, an aqueous borohydride approach was employed to remove all sulfur containing concerns. An alternating layer approach was employed and CdTe thin films were fabricated. However, significant oxygen incorporation was observed, hypothesized to originate from boron-oxygen containing species formed during the borohydride dissolution of tellurium. Non-aqueous systems are proposed to prevent these species from forming.

A.5 References

(1) Jenny, D. A.; Bube, R. H. Semiconducting Cadmium Telluride. *Phys. Rev.* **1954**, *96* (5), 1190–1191. https://doi.org/10.1103/PhysRev.96.1190.

(2) Cusano, D. A. CdTe Solar Cells and Photovoltaic Heterojunctions in II-VI Compounds. *Solid State Electron.* **1963**, *6* (3), 217–232. https://doi.org/10.1016/0038-1101(63)90078-9.

(3) Kirk, A. P.; Dinezza, M. J.; Liu, S.; Zhao, X. H.; Zhang, Y. H. CdTe vs. GaAs Solar Cells - A Modeling Case Study with Preliminary Experimental Results. In *Conference Record of the IEEE Photovoltaic Specialists Conference*; Institute of Electrical and Electronics Engineers Inc., 2013; pp 2515–2517. https://doi.org/10.1109/PVSC.2013.6744987.

(4) National Renewable Energy Laboratory. Best Research Cell Efficiencies https://www.nrel.gov/pv/assets/pdfs/best-research-cell-efficiencies.20200406.pdf (accessed Aug 7, 2020).

(5) Burst, J. M.; Duenow, J. N.; Albin, D. S.; Colegrove, E.; Reese, M. O.; Aguiar, J. A.; Jiang, C. S.; Patel, M. K.; Al-Jassim, M. M.; Kuciauskas, D.; Swain, S.; Ablekim, T.; Lynn, K. G.; Metzger, W. K. CdTe Solar Cells with Open-Circuit Voltage Breaking the 1V Barrier. *Nat. Energy* **2016**, *1* (4), 16015. https://doi.org/10.1038/NENERGY.2016.15.

(6) Ferekides, C. S.; Marinskiy, D.; Viswanathan, V.; Tetali, B.; Palekis, V.; Selvaraj, P.; Morel, D. L. High Efficiency CSS CdTe Solar Cells. *Thin Solid Films* **2000**, *361*, 520–526. https://doi.org/10.1016/S0040-6090(99)00824-X.

(7) De Wild-Scholten, M. J. Energy Payback Time and Carbon Footprint of Commercial Photovoltaic Systems. *Sol. Energy Mater. Sol. Cells* **2013**, *119*, 296–305. https://doi.org/10.1016/j.solmat.2013.08.037.

(8) Fthenakis, V.; Kim, H. C. Life-Cycle Uses of Water in U.S. Electricity Generation. *Renew. Sustain. Energy Rev.* **2010**, *14* (7), 2039–2048. https://doi.org/10.1016/j.rser.2010.03.008.

(9) Peng, J.; Lu, L.; Yang, H. Review on Life Cycle Assessment of Energy Payback and Greenhouse Gas Emission of Solar Photovoltaic Systems. *Renewable and Sustainable Energy Reviews*. Elsevier Ltd March 1, 2013, pp 255–274. https://doi.org/10.1016/j.rser.2012.11.035.

(10) Kacszmar, S. Evaluating the Read-across Approach on CdTe Toxicity for CdTe Photovoltaics. In *Society of Environmental Toxicoloy and Chemistry, 32nd Annual Meeting*; 2016.

(11) Major, J. D.; Treharne, R. E.; Phillips, L. J.; Durose, K. A Low-Cost Non-Toxic Post-Growth Activation Step for CdTe Solar Cells. *Nature* **2014**, *511* (7509), 334–337. https://doi.org/10.1038/nature13435.

(12) Marwede, M.; Reller, A. Future Recycling Flows of Tellurium from Cadmium Telluride Photovoltaic Waste. *Resour. Conserv. Recycl.* **2012**, *69*, 35–49. https://doi.org/10.1016/j.resconrec.2012.09.003.

(13) Boone, J. L.; Van Doren, T. P.; Berry, A. K. Deposition of CdTe by Spray Pyrolysis. *Thin Solid Films* **1982**, *87* (3), 259–264. https://doi.org/10.1016/0040-6090(82)90362-5.

(14) Lis, S.; Serreze, H.; Sienkiewicz, P. Method to Synthesize and Produce Thin Films by Spray Pyrolysis. US4327119A, 1981.

(15) Serreze, H. B.; Lis, S.; Squillante, M. R.; Turcotte, R.; Talbot, M.; Entine, G. Spray Pyrolysis Prepared CdTe Solar Cells. In *Photovoltaic Specialists Conference*; Kissimmee, 1981; pp 1068–1072.

(16) Sun, S.; Liu, H.; Gao, Y.; Qin, D.; Chen, J. Controlled Synthesis of CdTe Nanocrystals for High Performanced Schottky Thin Film Solar Cells. *J. Mater. Chem.* **2012**, *22* (36), 19207–19212. https://doi.org/10.1039/c2jm34280d.

(17) Panthani, M. G.; Kurley, J. M.; Crisp, R. W.; Dietz, T. C.; Ezzyat, T.; Luther, J. M.; Talapin, D. V. High Efficiency Solution Processed Sintered CdTe Nanocrystal Solar Cells: The Role of Interfaces. *Nano Lett.* **2014**, *14* (2), 670–675. https://doi.org/10.1021/nl403912w.

(18) Xie, Y.; Tan, Q.; Zhang, Z.; Lu, K.; Li, M.; Xu, W.; Qin, D.; Zhang, Y.; Hou, L.; Wu, H. Improving Performance in CdTe/CdSe Nanocrystals Solar Cells by Using Bulk Nano-Heterojunctions. *J. Mater. Chem. C* **2016**, *4* (27), 6483–6491. https://doi.org/10.1039/c6tc01571a.

(19) Zhang, H.; Kurley, J. M.; Russell, J. C.; Jang, J.; Talapin, D. V. Solution-Processed, Ultrathin Solar Cells from CdCl3--Capped CdTe Nanocrystals: The Multiple Roles of CdCl3- Ligands. *J. Am. Chem. Soc.* **2016**, *138* (24), 7464–7467. https://doi.org/10.1021/jacs.6b03240.

(20) Yu, W. W.; Qu, L.; Guo, W.; Peng, X. Experimental Determination of the Extinction Coefficient of CdTe, CdSe, and CdS Nanocrystals. *Chem. Mater.* **2003**, *15* (14), 2854–2860. https://doi.org/10.1021/cm034081k.

(21) Liang, Y.; Tan, J.; Wang, J.; Chen, J.; Sun, B.; Shao, L. Synthesis and Optimization of CdTe Quantum Dots with the Help of Erythorbic Acid and Ethanol. *RSC Adv.* **2014**, *4* (90), 48967–48972. https://doi.org/10.1039/c4ra07491b.

(22) Wang, T.; Jin, Z.; Shi, Y.; Li, W.; Yang, J. Kinetic Growth of One-Dimensional Zinc-Blende CdTe Nanocrystals by Aqueous Synthesis at Low Temperature. *Cryst. Growth Des.* **2009**, *9* (12), 5077–5082. https://doi.org/10.1021/cg900175x.

(23) Miskin, C. K.; Yang, W. C.; Hages, C. J.; Carter, N. J.; Joglekar, C. S.; Stach, E. A.; Agrawal, R. 9.0% Efficient $Cu_2ZnSn(S,Se)_4$ Solar Cells from Selenized Nanoparticle Inks. *Prog. Photovoltaics Res. Appl.* **2015**, *23* (5), 654–659. https://doi.org/10.1002/pip.2472.

(24) Todorov, T. K.; Tang, J.; Bag, S.; Gunawan, O.; Gokmen, T.; Zhu, Y.; Mitzi, D. B. Beyond 11% Efficiency: Characteristics of State-of-the-Art $Cu_2ZnSn(S,Se)_4$ Solar Cells. *Adv. Energy Mater.* **2013**, *3* (1), 34–38. https://doi.org/10.1002/aenm.201200348.
(25) Walker, B. C.; Agrawal, R. Contamination-Free Solutions of Selenium in Amines for Nanoparticle Synthesis. *Chem. Commun.* **2014**, *50* (61), 8331–8334. https://doi.org/10.1039/c4cc02379j.
(26) Webber, D. H.; Buckley, J. J.; Antunez, P. D.; Brutchey, R. L. Facile Dissolution of Selenium and Tellurium in a Thiol-Amine Solvent Mixture under Ambient Conditions. *Chem. Sci.* **2014**, *5* (6), 2498–2502. https://doi.org/10.1039/c4sc00749b.
(27) Zhao, X.; Lu, M.; Koeper, M. J.; Agrawal, R. Solution-Processed Sulfur Depleted Cu(In, Ga)Se2 Solar Cells Synthesized from a Monoamine-Dithiol Solvent Mixture. *J. Mater. Chem. A* **2016**, *4* (19), 7390–7397. https://doi.org/10.1039/c6ta00533k.
(28) Miskin, C. K.; Dubois-Camacho, A.; Reese, M. O.; Agrawal, R. A Direct Solution Deposition Approach to CdTe Thin Films. *J. Mater. Chem. C* **2016**, *4* (39), 9167–9171. https://doi.org/10.1039/c6tc02986h.
(29) Oba, F.; Choi, M.; Togo, A. What Causes High Resistivity in CdTe Related Content Point Defects in ZnO: An Approach from First Principles. https://doi.org/10.1088/1367-2630/14/6/063020.

VITA

Ryan Gupta Ellis was born in Saint Paul, MN on September 1st, 1993 to parents Abha Ellis, and Mark Ellis, both chemical engineers by education. Ryan has one older sister, Saarika Ellis. Throughout Ryan's early schooling he found an interest in science, mathematics, and the creative arts, namely music. Ryan attended Carver Elementary school in Maplewood, MN, Crosswinds Arts and Science School in Woodbury, MN, and attended high school at Central High School. Ryan's interests in math and science were heavily supported by his two engineer parents.

After graduation from high school in 2011, Ryan attended the University of Wisconsin – Madison, choosing to partially follow in the footsteps of his parents, double majoring in chemical engineering and chemistry. In his second year of undergraduate studies, Ryan joined the research group of Prof. Thomas F. Kuech. Ryan immediately found great satisfaction participating in higher level research, a method in which his interests in math, science, were combined with his creative interests in the arts. Research was a field in which technical prowess and creativity were needed in tandem to fuel discovery. Ryan worked on a number of projects such as chemical mechanical polishing and chemical polishing of GaAs and InP for quantum cascade laser applications, building high vacuum systems such as residual gas analyzer based leak checkers, and atomic layer deposition of Al_2O_3 and AlF_3 thin films for battery cathodes to improve charge capacity retention and overall battery longevity. This introduction to research was the catalyst from Ryan's desire to continue his studies in graduate school.

After graduating in 2015, Ryan began his graduate school career at Purdue University in the Ph.D. program at the Davidson School of Chemical Engineering. Ryan joined the research group of Prof. Rakesh Agrawal, working on the solution processing of photovoltaics. His research focused on the synthesis and subsequent ligand chemistry of metal chalcogenide nanomaterials for the fabrication of photovoltaics. Ryan finished his Ph.D. in August 2020, and joined AbbVie as a research scientist, where he hopes that he can continue research to aid in the betterment of mankind.

PUBLICATIONS

Jackson, D. H. K.; Laskar, M. R.; Fang, S.; Xu, S.; **Ellis, R. G.**; Li, X.; Dreibelbis, M.; Babcock, S. E.; Mahanthappa, M. K.; Morgan, D.; Hamers, R. J.; Kuech, T. F. Optimizing AlF3 Atomic Layer Deposition Using Trimethylaluminum and TaF_5 : Application to High Voltage Li-Ion Battery Cathodes. *J. Vac. Sci. Technol. A Vacuum, Surfaces, Film.* **2016**, *34* (3), 031503. https://doi.org/10.1116/1.4943385.

Ellis, R. G.; Fields, J. P.; Agrawal, R. Ligand Exchange of Copper Indium Gallium Sulfide Nanoparticles for Minimization of Carbonaceous Impurities in High Efficiency Solution Processed Photovoltaics. In *Conference Proceedings of the 2018 MRS Fall Meeting and Exhibit;* Boston, MA. November, 2018.

Ellis, R. G.; Vak, D.; Chesman, A. S. R.; Agrawal, R. Slot Die Coating of CIGS Nanoparticle Inks for Scalable Solution Processed Photovoltaics. In *Conference Record of the IEEE Photovoltaic Specialists Conference*; 2019; pp 1830–1833. https://doi.org/10.1109/PVSC40753.2019.8980504.

Miskin, C. K.; Li, Y.; Perna, A.; **Ellis, R. G.**; Grubbs, E. K.; Bermel, P.; Agrawal, R. Sustainable Co-Production of Food and Solar Power to Relax Land-Use Constraints. *Nat. Sustain.* **2019**, *2* (10), 972–980. https://doi.org/10.1038/s41893-019-0388-x.

Deshmukh, S. D.*; **Ellis, R. G.***; Sutandar, D. S.; Rokke, D. J.; Agrawal, R. Versatile Colloidal Syntheses of Metal Chalcogenide Nanoparticles from Elemental Precursors Using Amine-Thiol Chemistry. *Chem. Mater.* **2019**, *31* (21), 9087–9097. https://doi.org/10.1021/acs.chemmater.9b03401.

Ellis, R. **G.**; Agrawal, R. Synthesis and Ligand Engineering of Impurity Free $Cu(In,Ga)S_2$ Nanoparticles for Slot-Die Coated Photovoltaics. In *Conference Proceedings of the 2019 AIChE Annual Meeting*; Orlando, FL. November 2019.

Ellis, R. G.; Turnley, J. W.; Rokke, D. J.; Fields, J. P.; Alruqobah, E. H.; Deshmukh, S. D.; Kisslinger, K.; Agrawal, R. Hybrid Ligand Exchange of Cu(In,Ga)S2 Nanoparticles for Carbon Impurity Removal in Solution-Processed Photovoltaics. Chem. Mater. 2020, 32, 5091–5103. https://doi.org/10.1021/acs.chemmater.0c00966.

Ellis, R. G.; Alruqobah, E. H.; Turnley, J. W.; Agrawal, R. Improving Solution Processed CIGSSe Devices Through Colloidal Nanoparticle Ligand Exchange. In *Conference Record of the IEEE Photovoltaic Specialists Conference*; 2020.

Ellis, R. G.; Deshmukh, S. D.; Sutandar, D. S.; Fields, J. P.; Agrawal, R. Ligand Exchange Free, Direct Synthesis of Sulfide Capped Nanoparticles for Carbon Free Solution Processed Photovoltaics. *In preparation.*

Ellis, R. G.; Vak, D..; Chesman, A. S. R.; Agrawal, R. Fully solution processed $Cu(In,Ga)(S,Se)_2$ Photovoltaics by Slot Die Coating. *In preparation.*

Ellis, R. G.; Agrawal, R. Solution Processing of CIGSSe Photovoltaics from Colloidal Nanoparticles – A Review. *In preparation.*

* denotes equal contribution to the work